

Synthesis and Reactivity of a T-Shaped Phosphine and its Derivatives

Aaron J. King

Magdalen College

University of Oxford

Michaelmas 2024

A thesis submitted for the degree of

Doctor of Philosophy

Abstract

Synthesis and Reactivity of a T-Shaped Phosphine and its Derivatives

Aaron J. King Magdalen College

DPhil. Inorganic Chemistry Michaelmas 2024

This thesis describes the chemistry of a novel geometrically constrained phosphine and its derivatives.

Chapter 1. The chemistry of organophosphines is dominated by their typically strong Lewis basicity, resulting in their popular use as ligands to transition metals, or as nucleophiles in organic transformations. Their use in organic synthesis is driven by their tendency to form strong P=O double bonds, providing a thermodynamic sink towards alkene formation, as targeted in the Wittig reaction, or the nucleophilic deoxygenation of alcohols as performed in the Mitsonobu and Appel reactions. A common deviation in these reactivity pathways is accessed through the inclusion of a stoichiometric reducing agent (such as a silane) in these reactions, thus enabling phosphine-based organocatalytic reactions through reduction of the generated phosphine oxide. Alternatively, employing sterically bulky substituents permits the use of phosphines in Frustrated Lewis Pairs (FLPs), accessing further catalytic processes including imine hydrogenation. Geometric constraint in phosphines is achieved through tethering the substituents at phosphorus by the use of meridionally coordinating pincer ligands. This provides further deviation in the reactivity of phosphines by enhancing the Lewis acidity at phosphorus, thus enabling transition metal-like reactivity by co-localising electron acceptor and donor properties. This reactivity is utilised in the activation of E–H bonds for example, including those relevant to catalysis such as H_2 and the N–H bond of ammonia.

Chapter 2. Steric tuning of a tridentate, acridane-derived, NNN-pincer ligand was required to stabilise a highly constrained T-shaped phosphine. This species, **6**, exhibited ambiphilic reactivity, evidenced by its phosphorus-based reactivity with both electrophiles and nucleophiles. Furthermore, oxidation with chalcogens or azides provide the respective phosphorus(V) products, and was accompanied by a significant geometric distortion of the ligand backbone. Ligand-involvement was observed with the

cooperative activation of protic and hydridic E–H bonds, proceeding with the association of the negatively polarised substrate fragment to phosphorus, demonstrating its predominantly Lewis acidic nature.

Chapter 3. On complexation to transition metals, T-shaped phosphine **6** adopts a distorted trigonal pyramidal, or "bent", structure. A barrier to inversion of coordinated **6** of 19.3(5) kcal/mol was determined by variable-temperature NMR spectroscopy of gold(I) complex **19**. A combination of heteronuclear NMR spectroscopy, vibrational spectroscopy, SCXRD, and DFT calculations reveal **6** to be a moderate σ-donor with enhanced π-acceptor properties. Following coordination, **6** retains its ability to activate E–H bonds; doing so in a cooperative fashion across a ligand-based P–N bond without involvement of the metal centre. In the case of amine substrates, including ammonia, this process was reversible.

Chapter 4. The T-shaped phosphine **6** was shown to activate an ammonia N–H bond *via* redox-neutral cooperative addition, ultimately equilibrating in favour of the oxidative-addition product. This compound underwent reductive elimination upon heating, demonstrating the reversibility of ammonia activation at **6**. Methyl-phosphonium ion **7**, phosphine oxide **11**, and iminophosphorane **30**, each a derivative of **6** bearing reduced geometric constraint, were also shown to activate an ammonia N–H bond, in some cases more rapidly than **6**. DFT calculations and experimental observations support a mechanism involving the initial Lewis adduct formation between ammonia and the phosphorus centre in these compounds, followed by inter-/intra-molecular deprotonation of the now acidified N–H bond. These results highlight some alternative methodologies beyond geometric constraint for accessing phosphorus-based Lewis acidic reactivity which may be exploited towards desirable bond activation reactions.

Chapter 5. The synthesis of dihalophosphoranes derived from **6** was attempted. In the case of the difluoro- and diiodophosphoranes, these efforts provided only the respective HX-cooperative addition product. Conversely, the dichloro- and dibromophosphoranes were accessible. Photo-reduction of these phosphorus(V) species was achieved through LED irradiation targeting the Soret band in their UV-Vis spectra. The electronic transition responsible for this spectroscopic feature involved populating a $\sigma^*_{P–X}$

antibonding orbital, resulting in photo-elimination of halogen radicals from the phosphorus centre. This is supported by TD-DFT calculations and evidenced by heteronuclear NMR spectroscopy and SCXRD analysis. In support of this mechanism, radical elimination was observed upon heating **46** — a phosphorus(V) species bearing substituents at phosphorus which themselves are stable as free-radicals.

Acknowledgements

To Hannah: this has been just as much your journey as it has been mine. Thank you for all of your love and support throughout my D.Phil., I will cherish these years and always be grateful for our time together in Oxford. Thank you for introducing Thistle into our lives, she is the best four-legged friend anyone could ask for and always there to brighten my day.

To my family: I am incredibly lucky to have such a loving and supportive family. Your kindness and encouragement over the years has been invaluable, and I only hope I can support each of you half as much as you have supported me. I could not have done this without you.

To my colleagues: everything I know about research is thanks to the patience and guidance of my wonderful colleagues in the Goicoechea group. You made it a pleasure to go to work each day, offering great laughs and indispensable counsel to help me through my project. I am particularly grateful to Alex Mapp and Matthew Reveley who were with me through to the end; what should have been a stressful time was instead a time of great memories and friendship.

To my supervisor, Prof. Jose Goicoechea: thank you for the opportunity to work on such an engaging project. Your guidance over the years has been vital and I will always value everything I have learnt during my D.Phil..

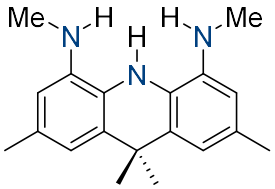
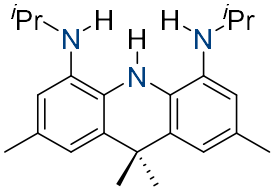
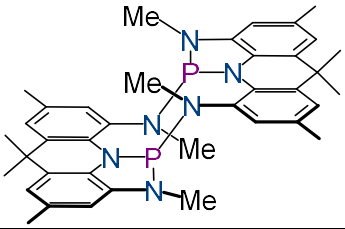
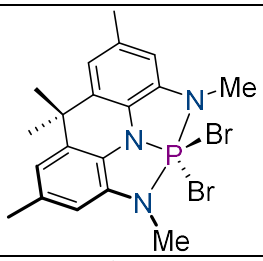
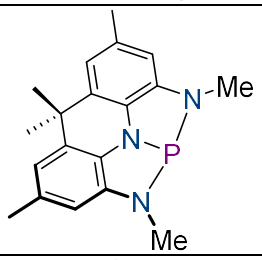
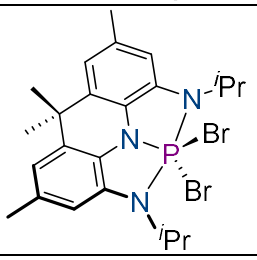
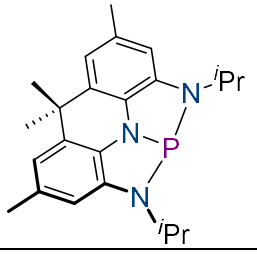
List of Abbreviations

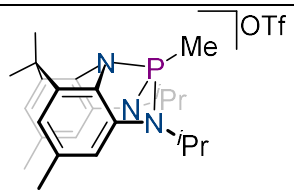
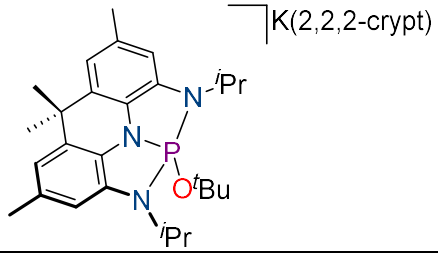
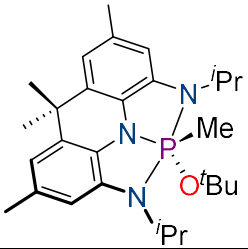
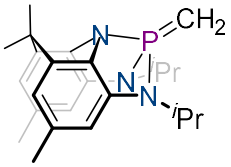
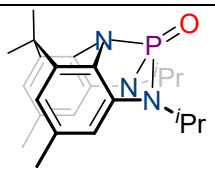
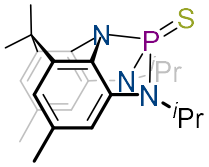
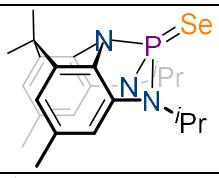
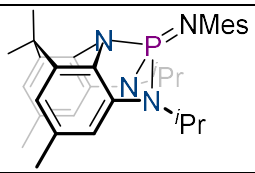
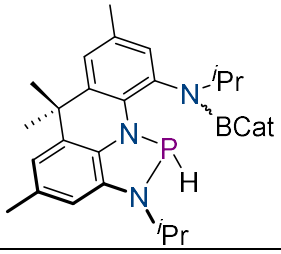
18-c-6	1,4,7,10,13,16-hexaoxacyclooctadecane
2.2.2-crypt	4,7,13,16,21,24-hexaoxa-1,10-diazabicyclo[8.8.8]hexacosane
2c-2e	2-centre 2-electron
3c-4e	3-centre 4-electron
Ar	aryl
Ar^F	3,5-bis(trifluoromethyl)phenyl
ATR	attenuated total reflectance
BDE	bond dissociation energy
BINAP	(2,2′-bis(diphenylphosphino)-1,1′-binaphthyl)
calcd.	calculated
Cat	catecholato
COD	1,5-cyclooctadiene
Cp	cyclopentadienyl
d	doublet
DFT	density functional theory
DiPAMP	(ethane-1,2-diyl)-bis((2-methoxyphenyl)(phenyl)phosphine)
Dipp	2,6-diisopropylphenyl
disp	dispersion
DME	1,2-dimethoxyethane
EDA	energy decomposition analysis
EPR	electron paramagnetic resonance
ESI	electrospray ionisation
Et	ethyl
eq	equivalent
FLP	frustrated Lewis pair
HAT	hydrogen atom transfer
HOMO	highest occupied molecular orbital
HRMS	high resolution mass spectrometry
IDipp	Dipp substituted unsaturated NHC 1,3-bis(2,6-diisopropylphenyl)imidazole-2-ylidene
imag	imaginary

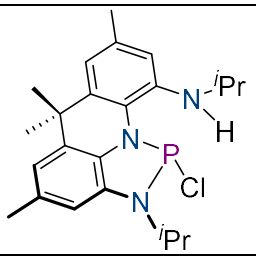
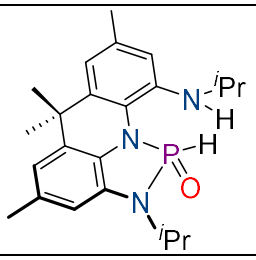
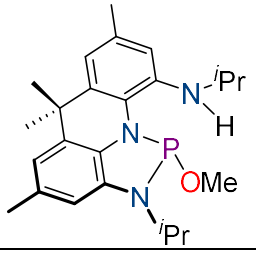
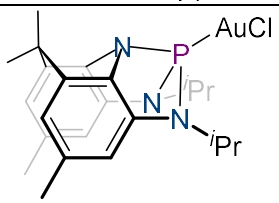
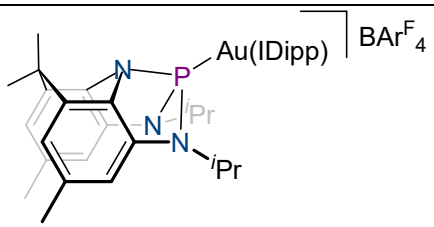
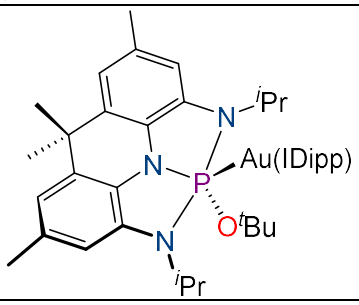
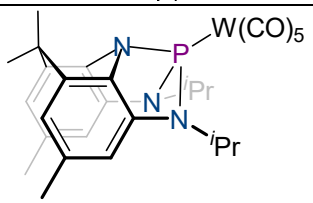
^{i}Pr	*iso*-propyl
IR	infrared
k	rate constant
L-DOPA	L-3,4-dihydroxyphenylalanine
LED	light emitting diode
LHS	left hand side
LMCT	ligand-to-metal charge-transfer
LUMO	lowest occupied molecular orbital
m	multiplet
m	*meta*-substituted
Me	methyl
Mes	mesityl 2,4,6-trimethylphenyl
min	minute
MMCT	metal-to-metal charge-transfer
^{n}Bu	*n*-butyl
^{n}Pr	*n*-propyl
NBO	natural bond orbital
NHC	N-heterocyclic carbene
NMR	nuclear magnetic resonance
NOCV	natural orbitals for chemical valence
Nu	nucleophile
o	*ortho*-substituted
oi	orbital interaction
PBE	Perdew-Burke-Ernzerhof
Ph	phenyl
Pin	pinacolato
Pn	pnictogen
Poly.	polynomial
ppm	parts per million
Py	pyridyl
q	quartet
RHS	right hand side

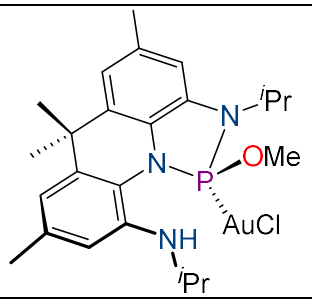
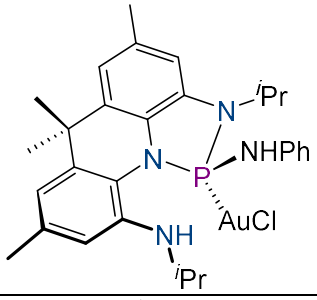
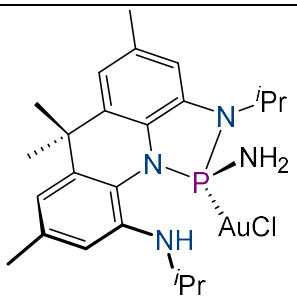
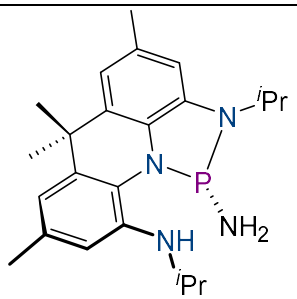
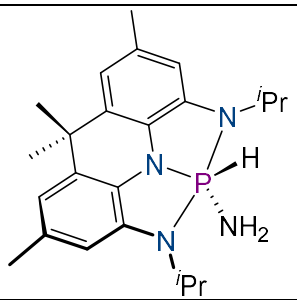
s	singlet
SARC	segmented all-electron relativistically contracted
SCXRD	single-crystal X-ray diffraction
sept	septet
SOMO	singly occupied molecular orbital
T	temperature
t	triplet
TASF	tris(dimethylamino)sulfonium trimethyldifluorosilicate
^{t}Bu	*tert*-butyl
TD-DFT	time-dependant density functional theory
TEMPO	(2,2,6,6-Tetramethylpiperidin-1-yl)oxyl
Tf	trifyl
TME	tetramethylethylene
tot	total
TZVP	triple-zeta valence with polarisation
THF	tetrahydrofuran
TS	transition state
UV	ultra violet
Vis	visible
XANES	X-ray absorption near-edge structure
ZORA	zeroth-order regular approximation

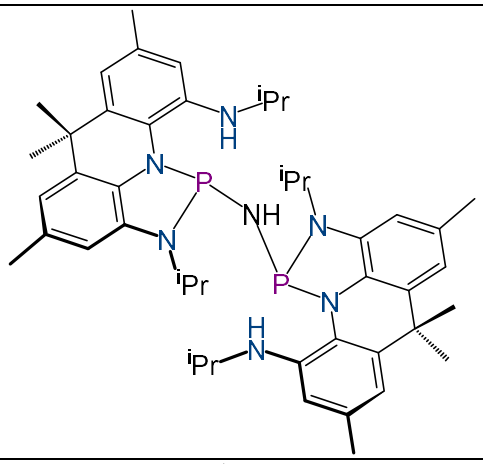
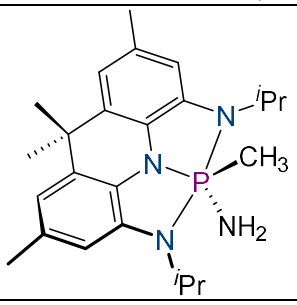
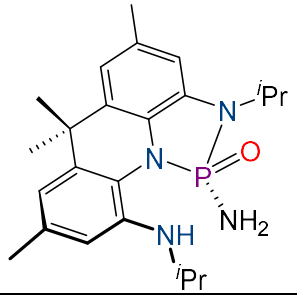
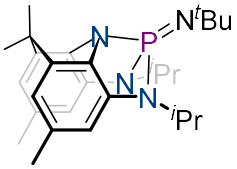
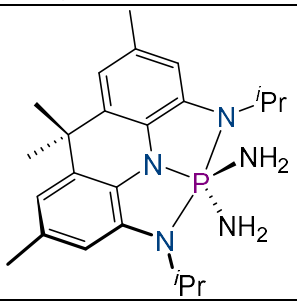
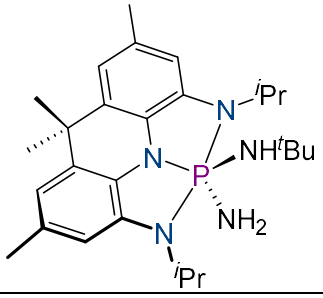
List of Compounds

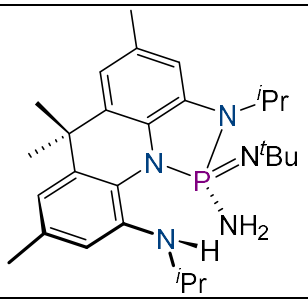
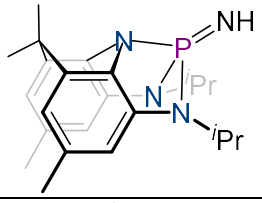
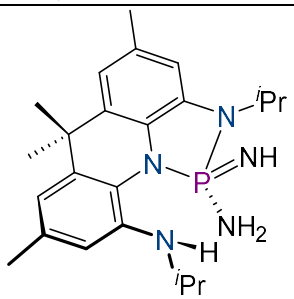
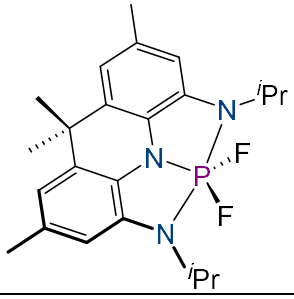
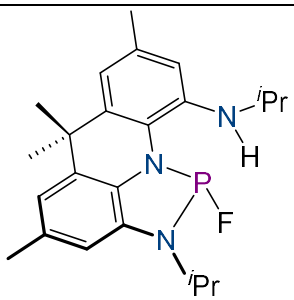
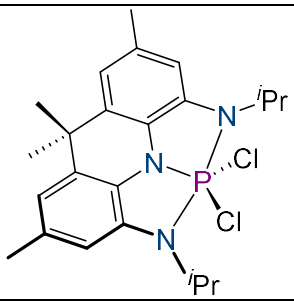
1^{Me}	
1^{iPr}	
2	
3	
4	
5	
6	

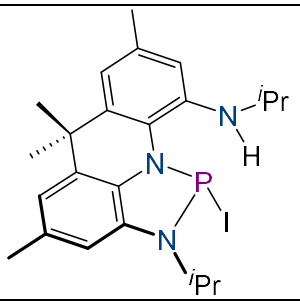
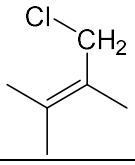
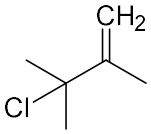
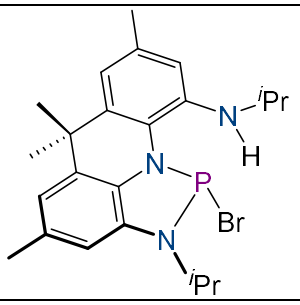
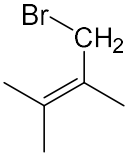
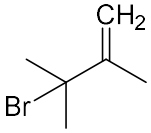
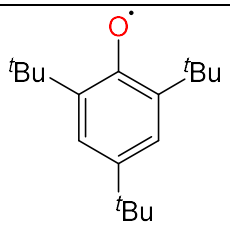
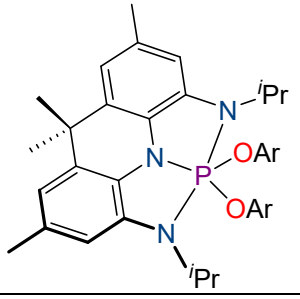
7[OTf]	
[K(2,2,2-crypt)]**8**	
9	
10	
11	
12	
13	
14	
15	

16	
17	
18	
19	
20[BAr^F_4]	
21	
22	

23	
24	
25	
26a	
26b	

27	
28	
29	
30	
31	
32	

33	
34	
35	
36	
37	
38	

39	
40	
41	
42	
43	
44	
45	
46	

Contents

Abstract i

Acknowledgements iv

List of Abbreviations v

List of Compounds viii

Introduction

1.1 Organophosphorus compounds 1

1.1.1 Reagents in organic transformations 1

1.1.2 Phosphines as ligands 4

1.1.3 Phosphorus-based catalysis 6

1.1.4 Phosphines in frustrated Lewis pairs 7

1.2 Geometrically constrained phosphines 8

1.3 The reactivity of geometrically constrained phosphines 12

1.3.1 Reactions with electrophiles and nucleophiles 12

1.3.2 Oxidation reaction 14

1.3.3 Reactions with E–H bonds 15

1.3.4 Catalysis 18

1.3.5 Reaction monitoring by NMR spectroscopy 19

1.4 Aims 20

1.5 References 21

Synthesis and Reactivity of a T-shaped Phosphine

2.1 Synthesis of geometrically constrained pnictogen compounds 26

2.2 Synthesis of acridane derived NNN pincer ligated phosphines and phosphoranes 29

2.2.1 Dimerisation of a sterically unprotected constrained phosphine 29
2.2.2 Steric tuning to afford a stable T-shaped phosphine, **6** 33
2.3 Reactivity of **6** 36
2.3.1 Reactions with electrophiles and nucleophiles 36
2.3.2 Two-electron oxidation reaction 42
2.3.3 Reactivity towards E–H bonds 46
2.4 Conclusions 51
2.5 Experimental section 52
2.6 References 72

Coordination Chemistry of a T-shaped Phosphine

3.1 The reactivity of coordinated phosphines 75
3.1.1 Phosphine-assisted reaction pathways 75
3.1.2 Geometrically constrained phosphines as ligands 76
3.2 Ligand properties of **6** 79
3.2.1 Coordination chemistry 79
3.2.2 σ-Donor ability of **6** 83
3.2.3 π-Acceptor ability of **6** 87
3.2.4 Ligand centred reactivity of **19** 95
3.3 Conclusions 99
3.4 Experimental section 100
3.5 References 110

Ammonia Activation at a T-shaped Phosphine and its Less Constrained Derivatives

4.1 The reaction of **6** with ammonia 113
4.2 The reactions of less constrained derivatives of **6** with ammonia 117
4.2.1 Phosphonium salt **7**[OTf] 118

4.2.2 Phosphine oxide **11** and iminophosphorane **30** 120

4.3 Conclusions 131

4.4 Experimental Section 132

4.5 References 139

Reductive Elimination from Phosphoranes Derived from a T-shaped Phosphine

5.1 HX-Splitting 140

5.2 Halogen photoelimination 141

5.2.1 Transition metal-based systems 141

5.2.2 Transition metal-main-group cooperative systems 144

5.2.3 Single-centre main-group systems 146

5.3 Synthesis of **6**-derived dihalophosphoranes 147

5.3.1 Difluorophosphorane, **36** 147

5.3.2 Dichlorophosphorane, **38** 149

5.3.3 Diiodophosphorane 150

5.4 Photoreduction of dihalophosphoranes 153

5.4.1 Dichlorophosphorane, **38** 153

5.4.2 Dibromophosphorane, **5** 160

5.5 Thermal reduction of bisaryloxyphosphorane, **46** 169

5.6 Conclusions 174

5.7 Experimental section 174

5.8 References 182

Conclusions and Future Work

6.1 Conclusions 184

6.2 Future work 186

Experimental and Computational Details

7.1 General experimental methods 187

7.1.1 Synthetic methods 187

7.1.2 Characterisation techniques 188

7.2 General computational methods 189

7.3 Single crystal X-ray diffraction data 191

7.3 References 203

Chapter 1

Introduction

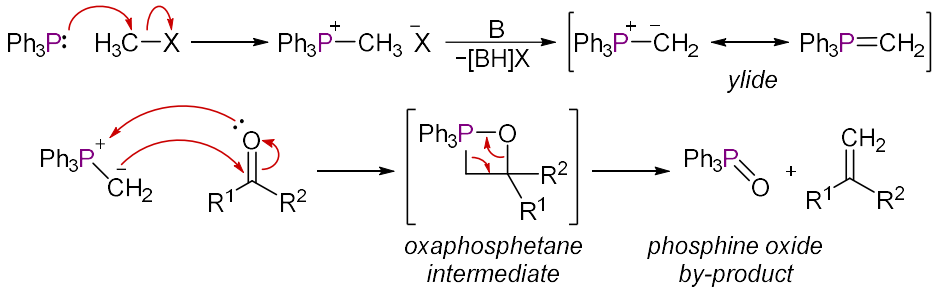
Abstract. The chemistry of organophosphines is dominated by their typically strong Lewis basicity, resulting in their popular use as ligands to transition metals, or as nucleophiles in organic transformations. Their use in organic synthesis is driven by their tendency to form strong P=O double bonds, providing a thermodynamic sink towards alkene formation, as targeted in the Wittig reaction, or the nucleophilic deoxygenation of alcohols as performed in the Mitsonobu and Appel reactions. A common deviation in these reactivity pathways is accessed through the inclusion of a stoichiometric reducing agent (such as a silane) in these reactions, thus enabling phosphine-based organocatalytic reactions through reduction of the generated phosphine oxide. Alternatively, employing sterically bulky substituents permits the use of phosphines in Frustrated Lewis Pairs (FLPs), accessing further catalytic processes including imine hydrogenation. Geometric constraint in phosphines is achieved through tethering the substituents at phosphorus by the use of meridionally coordinating pincer ligands. This provides further deviation in the reactivity of phosphines by enhancing the Lewis acidity at phosphorus, thus enabling transition metal-like reactivity by co-localising electron acceptor and donor properties. This reactivity is utilised in the activation of E–H bonds for example, including those relevant to catalysis such as H_2 and the N–H bond of ammonia.

1.1 Organophosphorus compounds

1.1.1 Reagents in organic transformations

Two modes of reactivity dominate the use of phosphines in organic synthesis. First, the Lewis basicity, or nucleophilicity, of the phosphorus-based lone-pair; and second, the tendency of these compounds to form strong P=O double bonds (bond dissociation energy (BDE) =130 kcal/mol). These reactivities are exploited most famously in the synthesis of alkenes, rendering organophosphorus compounds essential in the synthesis of natural products, pharmacological targets and agrochemicals.[1] A well-known (and

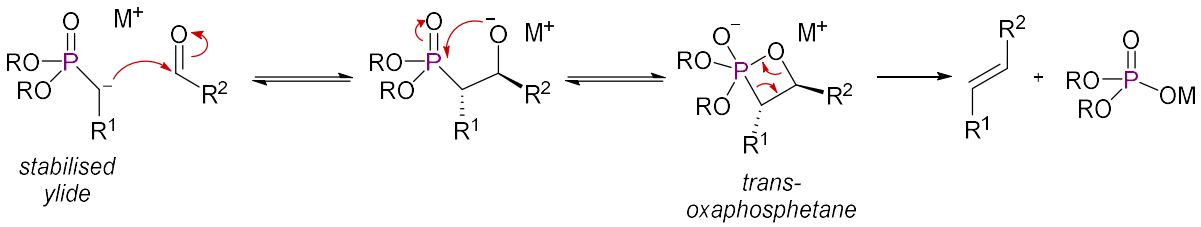
Nobel Prize winning) example of this is the Wittig reaction, which sees the use of an organophosphine, typically triphenylphosphine, PPh_3, in the synthesis of alkenes from carbonyls. This reaction is thermodynamically driven by the formation of a strong P=O double bond, and preceded by the nucleophilic attack of an organic halide by the phosphine to generate the reactive olefination ylide (Scheme 1.1).[2]



Scheme 1.1. The general mechanism of the Wittig reaction. A methyl derived ylide is used for simplicity. B represents a generic base required for ylide formation.

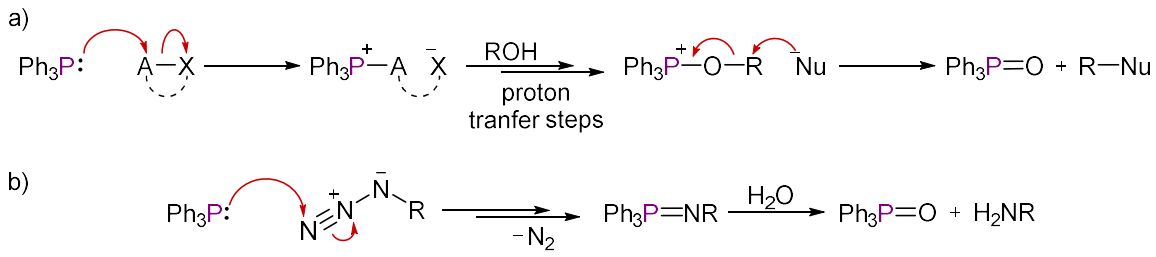
There are numerous theories regarding the mechanism of the Wittig reaction and the origin of its observed selectivity.[3] One such theory suggests that an essential factor dictating the stereochemical outcome (i.e. *E*- or *Z*-isomeric alkenes) is the degree of electronic delocalisation of the ylide, often written in its zwitterionic form to depict the relative polarity of the P–C bond.[4] Electron withdrawing groups at carbon, such as esters, provide "stabilised ylides", resulting in *E*-olefination. By contrast, "unstabilised ylides", such as those with alkyl substituents, result in *Z*-selective olefination. These selectivity arguments rely on a common substitution at phosphorus, with PPh_3 being the most popular phosphine for this reaction.[5]

Various modifications of the Wittig reaction utilise alternative organophosphorus reagents to further influence olefination selectivity.[6] For example, the Horner-Wadworth-Emmons reaction uses phosphonate esters to favour the formation of *E*-alkenes from aldehydes (Scheme 1.2). In this case the selectivity determining factor is the reversibility of oxaphosphetane formation enabled by the electron withdrawing phosphonate ester functionality, preferentially equilibrating to the thermodynamically favoured *trans*-isomer which eliminates towards the *E*-alkene.[7]



Scheme 1.2. The general mechanism of the Horner-Wadsworth-Emmons reaction, whereby R^1 is an electron withdrawing group and M^+ is the ylide counterion, typically an alkali metal ion.

Organophosphines play a similar role in the Mitsonobu and Appel reactions; methods of converting the –OH group of an alcohol into a leaving-group for nucleophilic substitution (Scheme 1.3a).[8,9] Both reactions use PPh_3 to activate the alcohol for nucleophilic attack through the generation of an electrophilic species of the type [R–O–PPh_3^+]. This rapidly combines with a nucleophile to generate the target compound and triphenylphosphine oxide, with the latter again providing the thermodynamic driving force for the reaction. Another reaction often used by organic chemists, and driven by P=O bond formation, is the Staudinger reduction.[10] In this reaction, an organic azide is reduced to its respective amine by reaction with a phosphine, usually PPh_3. This reaction proceeds with iminophosphorane formation by attack of the azide with PPh_3, with subsequent aqueous workup releasing the respective amine or amide, and generating the ubiquitous phosphine oxide (Scheme 1.3b).[10,11]



Scheme 1.3. a) The general mechanism of the Mitsunobu and Appel reactions. "A" represents an electrophile used to activate PPh_3 for nucleophilic attack – a diazo compound in the case of the Mitsunobu reaction, and carbon tetrachloride for the Appel reaction. b) General form of the Staudinger reduction.

The reactions discussed so far broadly utilise the same reactivity, however, there are several examples of deviations from trend, most notably the halogenation of alcohols using trihalophosphines.[12] These phosphines instead react primarily as Lewis acids on account of the electron-withdrawing nature of the

halogen substituents at phosphorus. Such reactions are still, however, driven by the strong affinity of phosphorus for bonding with oxygen.

1.1.2 Phosphines as ligands

Another widely adopted use of organophosphorus compounds is as ligands to transition metals (Figure 1.1). Phosphines appear in a vast number of catalytic reactions as spectator ligands; enhancing the solubility of the transition metal centre to which it is bonded, and modulating its electronics/sterics. Phosphines bond with metals primarily as a Lewis base – donating their lone-pair of electrons to the metal in an "L-type" fashion, however a varying degree of π-back-donation from the metal to the phosphorus centre occurs depending on the nature of the phosphine substituents.[13] As with organic transformations, PPh_3 is the most commonly used phosphine in transition metal chemistry. PPh_3 is both a moderate σ-donor and π-acceptor owing to the middling electron-withdrawing power of the phenyl substituents. This makes PPh_3 the ideal ligand for facilitating most catalytic processes, as neither the oxidised or reduced state of the transition metal is preferentially stabilised. As such, prominent palladium-catalysed cross-coupling reactions including the Suzuki, Heck and Negishi reactions (subjects of the 2010 Nobel prize for chemistry) were developed using PPh_3 as a ligand.[14–16] Further Nobel prize winning chemistry using phosphine ligands includes the rhodium-based "Wilkinson's catalyst" for alkene hydrogenation, and the ruthenium-based Grubbs catalysts for olefin metathesis, demonstrating their breadth and utility as ligands.[17–20]

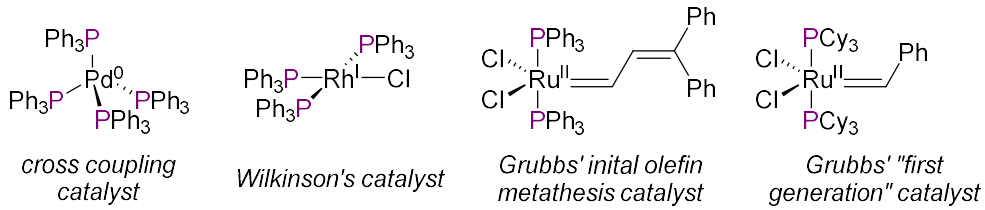


Figure 1.1. Notable examples of transition metal-based catalysts incorporating phosphine ligands. Note that Grubbs' initial, and first generation, olefin metathesis catalyst have been assigned as a "Fischer-type" carbene, though computational evidence supports their assignment as a "Schrock-type" carbene.[21]

In cases where further electronic or steric control is desirable, more complex phosphines have been developed to target specific outcomes of a reaction.[22] For example, dialkyl-biaryl phosphine **I** proved

to be a particularly effective ligand for the Suzuki cross-coupling of sterically bulky substates (Figure 1.2).[23] This was a result of the large steric bulk of **I** promoting ligand dissociation from the metal, generating a coordinatively unsaturated palladium centre susceptible to oxidative addition. A range of other dialkylbiaryl phosphines were developed for use as ligands in the Buchwald-Hartwig amination, similarly providing a marked increase in reaction rate owing to their electron-richness and large steric bulk.[24] Conversely, introducing electron-withdrawing substituents at phosphorus increases the rate of hydroformylation catalysis.[25] This is most often achieved by using phosphinite, phosphonite or phosphite ligands containing one, two, or three P–O bonds, respectively. Bridging-bidentate variations of these ligands, such as **II**, also favourably increases the ratio of linear:branched products through significant steric congestion, and disfavouring phosphine dissociation.[26–28]

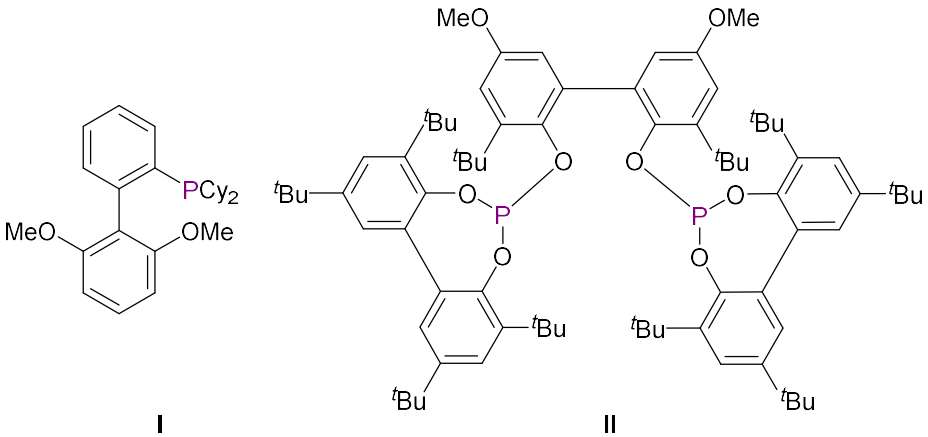


Figure 1.2. Dialkyl-biaryl phosphine **I** – an effective Suzuki cross-coupling ligand. Bridging bis-phosphite ligand **II** – an effective hydroformylation catalyst, known as BiPhePhos.

Phosphines bearing asymmetric substituents have been used to impart enantioselectivity upon catalytic processes, fulfilling a crucial requirement for natural product and pharmaceutical synthesis. This is an extensive topic, so only the most notable examples will be covered; namely those included in the 2001 Nobel prize in chemistry. (*S*)- and (*R*)-BINAP are bridging-bisphosphines related to one another through axial chirality; using an individual enantiomer of BINAP as a ligand to a transition metal enables asymmetric catalysis. For example, Noyori reported the use of an (*S*)-BINAP ligated rhodium(I) complex (*S*)-**III** for the asymmetric hydrogenation of amide-substituted alkenes (Figure 1.3).[29–31] An alternative asymmetric hydrogenation strategy includes the use of phosphines which are chiral at phosphorus by exploiting the stereogenic nature of its lone pair, as reported by Knowles and

co-workers.[32] Trisubstituted phosphines of the type P(R^1)(R^2)(R^3), where each substituent is different and comprises either; Me, Ph, $^{n/i}$Pr, cyclohexyl, or *o/m*-anisyl, were shown to catalyse the asymmetric hydrogenation of alkenes.[33,34] As shown by Noyori, Knowles also used bridging bis-phosphine ligands, in particular DiPAMP. Rhodium complex (*R*,*R*)-**IV** featuring this ligand was used in an enantioenriching hydrogenation step towards the industrial synthesis of L-DOPA (Figure 1.3).[35,36]

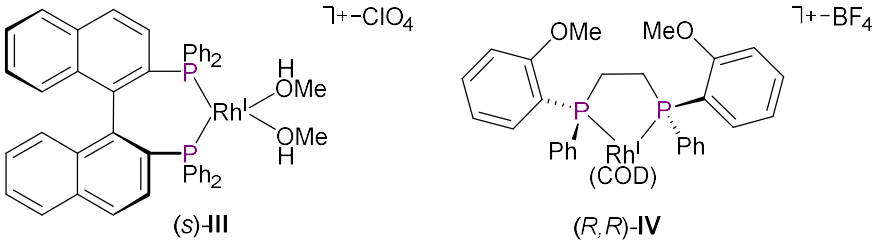


Figure 1.3. Structures of asymmetric hydrogenation catalysts (*S*)-**III** and (*R*,*R*)-**IV**. COD = 1,5-cyclooctadiene.

1.1.3 Phosphorus-based catalysis

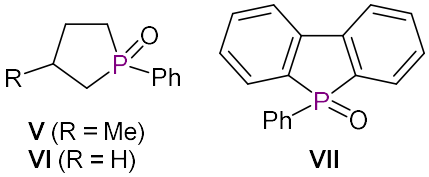
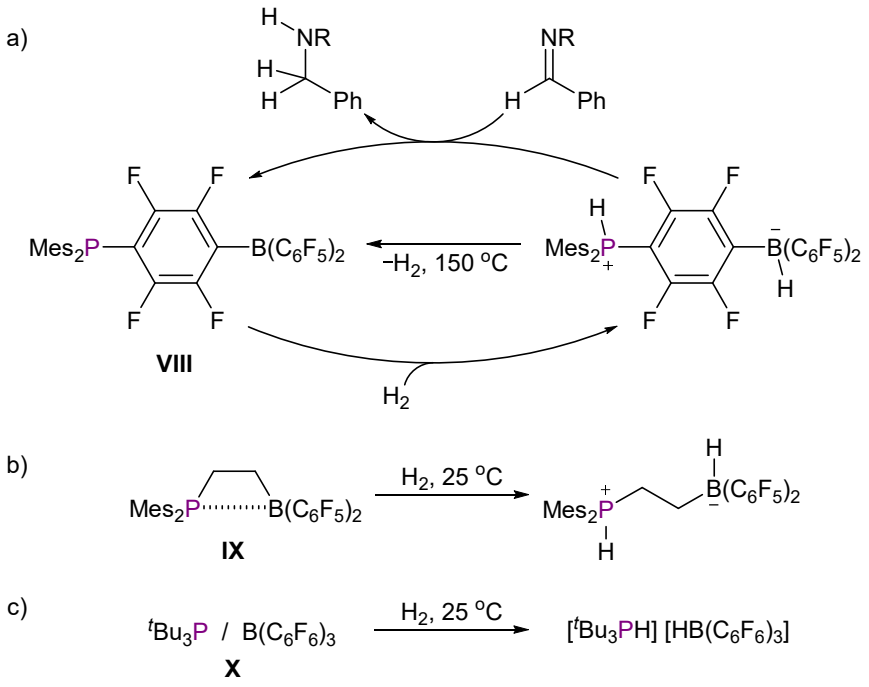


Figure 1.4. Phosphine oxide pre-catalysts used in the catalytic Wittig (**V**), Mitsunobu (**V**–**VII**), and Apell (**VII**) reactions, and the catalytic Staudinger reduction (**VII**).

Many of the reactions reviewed in Section 1.1.1 generate an equivalent of phosphine oxide waste per equivalent of product, thus limiting their application in certain industrial and academic settings. Attempts have been made to address this, particularly by performing these reactions catalytically with respect to the organophosphorus reagent.[37,38] A variant of the Wittig reaction catalytic in phosphine/phosphine-oxide (pre-catalyst) was developed in 2009 by O'Brien co-workers.[39] This reaction used cyclic 5-membered phosphine-oxide pre-catalyst **V** (Figure 1.4), chosen on account of strained phosphine-oxides being more readily reduced, and a silane as a stoichiometric *in-situ* reductant.[40] This reaction was conducted at 100 °C, but it was later found that including an acid additive enabled this reaction to occur at room temperature by promoting the silane mediated phosphine-oxide reduction.[41]

A similar approach led to the development of a catalytic Mitsunobu reaction using **V** as the pre-catalyst, as patented by O'Brien in 2009, again using a silane reductant for catalyst (re)generation.[42] Taking inspiration from this, Aldrich later reported a "fully catalytic" Mitsunobu reaction (i.e. also catalytic in the diazo "activator") using related cyclic phosphine-oxide **VI**, and a diazo reagent in catalytic amounts (Figure 1.4).[43] Dibenzo-fused phosphole-oxide **VII** also proved an effective pre-catalyst for this reaction, beneficial in that its increased ring-strain, and recovery of aromaticity upon reduction, promotes phosphine-oxide reduction. However, speculation regarding the catalytic nature of the diazo reagent prevents this reaction being deemed "fully catalytic".[44] The related Appel reaction can also be performed catalytically with respect to phosphole-oxide **VII** through the use of an *in situ* silane reductant, as developed by van Delft and co-workers.[45,46] Van Delft similarly used **VII** in formulating a catalytic Staudinger reduction. This protocol circumvented phosphine oxide formation by direct silane-induced reduction of the intermediate iminophosphorane species, preluding the need for aqueous work-up (Section 1.1.1, Scheme 1.3).[47]

1.1.4 Phosphines in frustrated Lewis pairs.



Scheme 1.4. Examples of hydrogen activation at; a) separated; b) weakly-interacting; and c) bimolecular FLPs.

The vast range of commercially available, variably substituted phosphines has led to them being a typical component of frustrated Lewis pairs (FLPs).[48] Stephan's seminal report of reversible hydrogen activation at an FLP (**VIII**) featured a mesityl substituted phosphine unit as the Lewis base component.[49] Since then, **VIII** has been shown to be a catalyst for the hydrogenation of imines to amines under an atmosphere of H_2 (Scheme 1.4a).[50] Bridged-FLPs such as **IX**, in which the formation of a weak Lewis adduct is enabled through flexibility, and bimolecular FLP mixtures containing bulky phosphines and boranes such as **X**, have also been shown to activate dihydrogen and be active hydrogenation catalysts (Scheme 1.4b and 1.4c).[51–54]

1.2 Geometrically constrained phosphines

This Section, and Section 1.3, introduces geometrically constrained, neutral phosphorus(III) compounds. The chemistry of geometrically constrained phosphenium cations falls outside the scope of this introduction. For examples of such systems, the reader is directed to the following references for further reading.[55–58]

Geometrically constrained phosphines are those which feature a non-trigonal geometry due to the nature of the substituents at phosphorus. Meridionally coordinating pincer ligands featuring three donor atoms are used to enforce this geometric constraint, with the resulting phosphines displaying C_s or C_{2v} symmetry and structures resembling the "edge-inversion" transition state of phosphines. Such compounds have been studied extensively on account of the divergent reactivity geometric constraint enables, namely the ability for phosphorus to not only donate electrons, as is typical for phosphines, but also accept electrons. This enhanced phosphorus-based Lewis acidity is attributed to orbital perturbations upon geometric constraint (Figure 1.5); experimentally and computationally validated by Radosevich, Daly, Keith, and co-workers.[59]

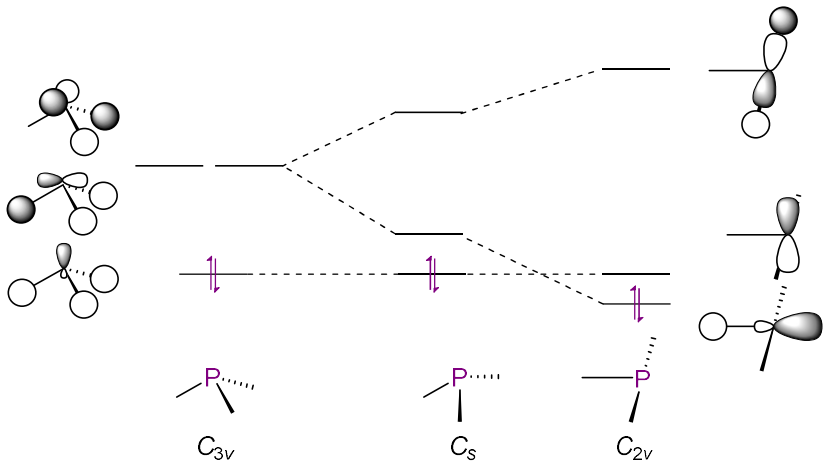
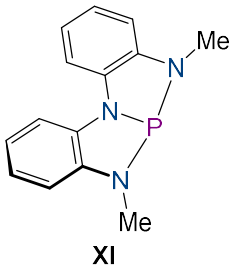


Figure 1.5. A qualitative Walsh diagram showing the frontier orbital perturbations of phosphines distorting from trigonal to planar geometries.

The frontier orbital arrangement of trigonal, C_{3v} symmetric, phosphines consist of a HOMO defined by a phosphorus-based lone-pair, and a high energy degenerate set of LUMO orbitals, which are antibonding with respect to the phosphorus–substituent bond (σ_{P-R}*). The effect of geometric constraint on these orbitals was probed through phosphorus K-edge X-ray absorption near-edge structure (XANES) – an experimental technique whereby a core phosphorus 1s electron is excited into unoccupied valence orbitals, with peak intensity correlated to the degree of p-orbital character of the acceptor orbitals.[60] The phosphorus K-edge XANES spectra of phosphines $P(NMePh)_3$ and **XI**, exhibiting C_3 and C_s symmetry respectively, were compared, chosen on account of their near identical local bonding *connectivity* (Figure 1.6). Comparison of the first pre-edge peak for $P(NMePh)_3$ and **XI** revealed that the latter was 1.1 eV lower in energy. These measurements were supported by DFT/TD-DFT calculations, which revealed that the lone-pair energy for both $P(NMePh)_3$ and **XI** only differed by 0.1 eV, therefore the large difference in transition energy was attributed to a reduced acceptor orbital energy for **XI**. This corresponds to a significant lowering of the LUMO in **XI** compared to $P(NMePh)_3$, comprised now of a non-bonding p-type orbital at phosphorus with concomitant lifting of LUMO degeneracy. Overall, these orbital perturbations provide a smaller HOMO-LUMO gap for geometrically constrained **XI**, resulting in enhanced Lewis acidity. With this, it would be expected that biphillic reactivity at phosphorus, i.e. co-localised electron accepting and donating properties, is promoted by geometric constraint. DFT calculations show that further constraining the C_s symmetric

XI to a fully planar structure bearing C_{2v} symmetry decreases the LUMO energy by a further 1.3 eV, suggesting that the degree of biphillicity is correlated to the extent of geometric constraint at phosphorus.



XI

Figure 1.6. Molecular structure of C_{2v} symmetric phosphine **XI**.

C_s symmetric phosphines typically have a small energy barrier to edge-inversion at phosphorus, so can access the planar C_{2v} symmetric state thermally and utilise its enhanced Lewis acidity without the need for rigid planarity within the ligand framework. The factors affecting the resulting geometry of pincer ligated phosphines are not immediately obvious, and were recently studied computationally by Chitnis and co-workers.[61] Qualitatively, trigonal phosphines see all three phosphorus p-orbitals engaged in σ-bonding with the substituents (net bond order = 3). On the other hand, highly constrained, planar (C_{2v}), phosphines invoke only two phosphorus p-orbitals for bonding; one engaged in a 2-centre-2-electron (2c-2e) bond with the central ligand donor atom, while the other is engaged in a 3c-4e bond with the flanking donors (net bond order = 2, Figure 1.7). The remaining phosphorus p-orbital is non-bonding and constitutes the LUMO of such compounds, as discussed. The lower bond order achieved in planar geometries results in them being destabilised on the grounds of σ-interaction strength.

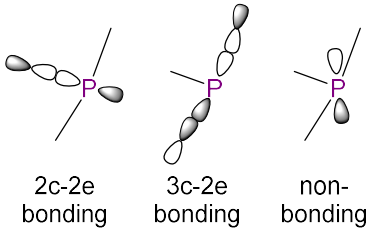


Figure 1.7. A qualitative description of the p-orbitals involved in bonding between phosphorus and its substituents in geometrically constrained phosphines.

Planarity is, however, stabilised through π-interactions on account of the vacant phosphorus p-orbital perpendicular to the molecular plane enabling π-delocalisation across the molecule. The interplay of σ and π effects influences the overall geometry, resulting in a continuum of structures from bent C_s symmetric to planar C_{2v} symmetry.[61] This trend is demonstrated by previously reported geometrically constrained phosphines **XII**–**XIV** (Figure 1.8).[62–64] Regarding **XII**, the unsaturated linkers between ligand donor atoms provides a platform for π-delocalisation across the whole molecule upon planarisation, hence stabilising this conformation. On the other hand, **XIII** adopts a bent geometry as competition between π-delocalisation of the phosphorus-containing 5-membered heterocycle and the existing aromaticity in the ligand-based arene unit destabilises the planar conformer. It is worth noting, however, that the energy difference between planar and bent geometries for **XIII** is small, highlighting that is only a subtle effect. For instance, tethering the backbone, as in **XIV**, pre-organises the ligand for π-delocalisation *via* phosphorus and overcomes this destabilisation, with the planar conformation persisting in the solid-state and in solution.

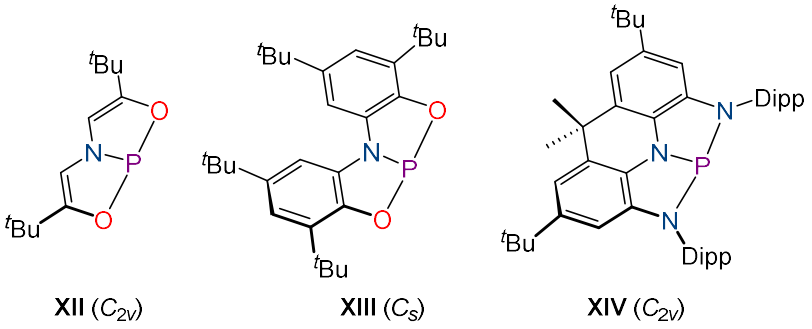


Figure 1.8. Example molecular structures of geometrically constrained phosphines **XII**–**XIV**.

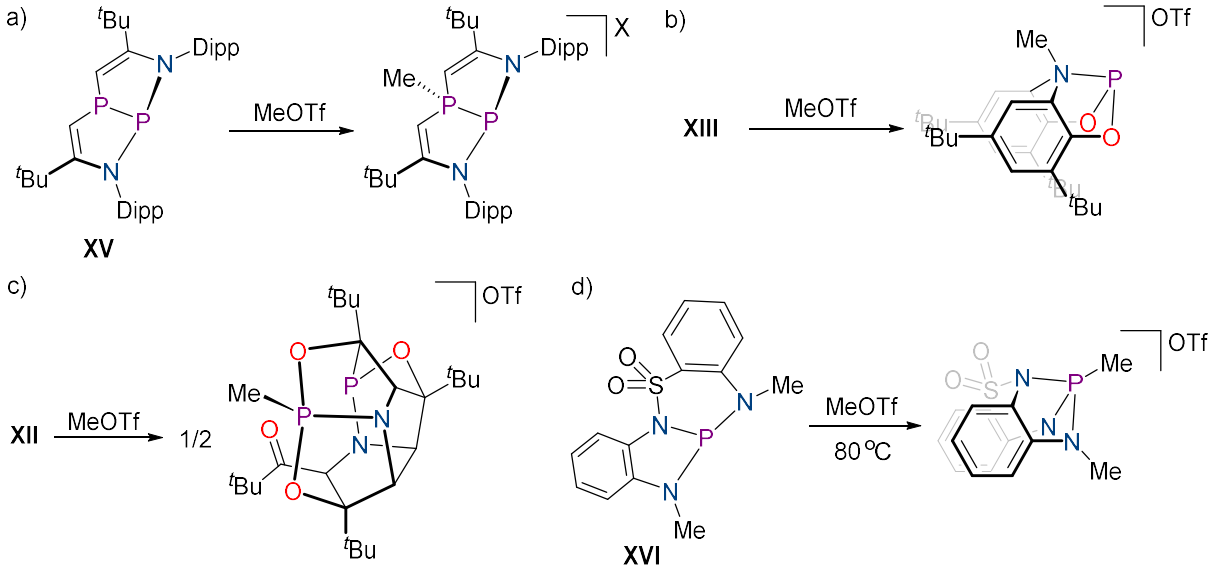
The aforementioned orbital perturbations result in unique redox properties for geometrically constrained phosphines. For instance, T-shaped phosphine **XIV** was originally synthesised by Wang and co-workers towards stabilising main-group radical anions.[64] Due to the non-bonding nature of the LUMO in geometrically constrained phosphines, one electron reduction was expected to provide a stable radical anion. For trigonal phosphines, on the other hand, the LUMO is best described as degenerate $\sigma^*_{P–R}$ antibonding orbitals, resulting in ligand fragmentation upon one-electron reduction. Cyclic voltammetry measurements on **XIV** revealed a reversible one-electron reduction at

$E_{1/2}$ = −2.28 V (versus Ag/Ag^+); synthetically accessible through reaction with elemental potassium to yield the respective radical anion salt. In the solid-state, this radical adopts a planar structure analogous to its neutral counterpart. The ligand-based C–N and C–C bond lengths were only slightly elongated compared to the parent phosphine, suggesting that the radical was predominantly phosphorus-based – an assertion supported by EPR spectroscopy and DFT calculations. This was further evidenced through an elongation in the P–N bonds – a result of decreased π-donation into a now partially occupied phosphorus p-orbital SOMO.

1.3 The reactivity of geometrically constrained phosphines

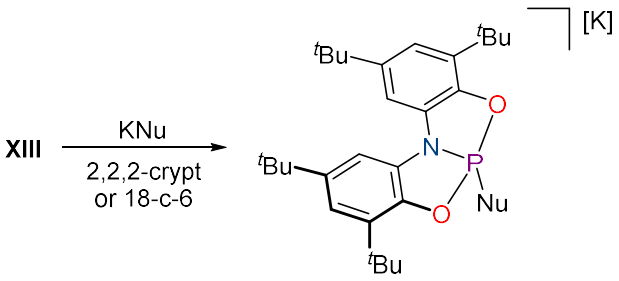
1.3.1 Reactions with electrophiles and nucleophiles

The electro/nucleophilicity of a compound is a strong indicator of its frontier orbital arrangement. Trigonal phosphines typically react rapidly with electrophiles on account of their strongly nucleophilic phosphorus lone pair (Section 1.1.1). Geometrically constrained phosphines, however, typically do not undergo phosphorus-based reactivity with electrophiles, for example **XI** did not react with benzyl bromide even on heating to 110 °C.[65] This is a result of the increased s-orbital character of the phosphorus lone-pair in these geometries, thus reducing its nucleophilicity. Instead, these species are most nucleophilic at the ligand-based heteroatoms and so react at these sites preferentially. This was observed in the reaction of C_s symmetric phosphines **XV** and **XIII**, whereby reaction with MeOTf resulted exclusively in methylation of a ligand-based donor atom (Scheme 1.5a and 1.5b).[66,67] Phosphorus-based reactivity was proposed for the reaction of T-shaped **XII** with MeOTf, however cyclodimerisation occurred due to the highly reactive enolate ligand backbone (Scheme 1.5c).[68] The reaction between **XVI**, bearing an unsymmetrical backbone, and MeOTf enabled the observation of phosphorus-methylation, presumably on account of the electron withdrawing sulfonamide functionality reducing the nucleophilicity of the ligand-based nitrogen centres (Scheme 1.5d).[69] Note that this last example was reported after the completion, and publication, of the results detailed in Chapter 2.



Scheme 1.5. Reactivity of some geometrically constrained phosphines with methyl triflate.

Nucleophiles react with geometrically constrained phosphines more readily, as demonstrated by the plethora of reactions with protic E–H containing substates; these reactions are discussed in detail in Section 1.3.3. Neutral nucleophiles, such as pyridine and PPh_3, do not react with C_s symmetric **XIII**, however anionic nucleophiles such as potassium *tert*-butoxide and potassium diphenylamide do so at room temperature, providing the respective anionic compounds (Scheme 1.6).[66] The difference in reactivity between electrophiles and nucleophiles at **XIII** demonstrates the enhanced electrophilicity and diminished nucleophilicity of phosphorus in geometrically constrained environments.



Scheme 1.6. Reactivity of geometrically constrained phosphine **XIII** with nucleophilic reagents. Nu = O^{t}Bu or NPh_2.

1.3.2 Oxidation reactions

For a discussion on phosphorus oxidation through the oxidative addition of E–H bonds, see Section 1.3.3.

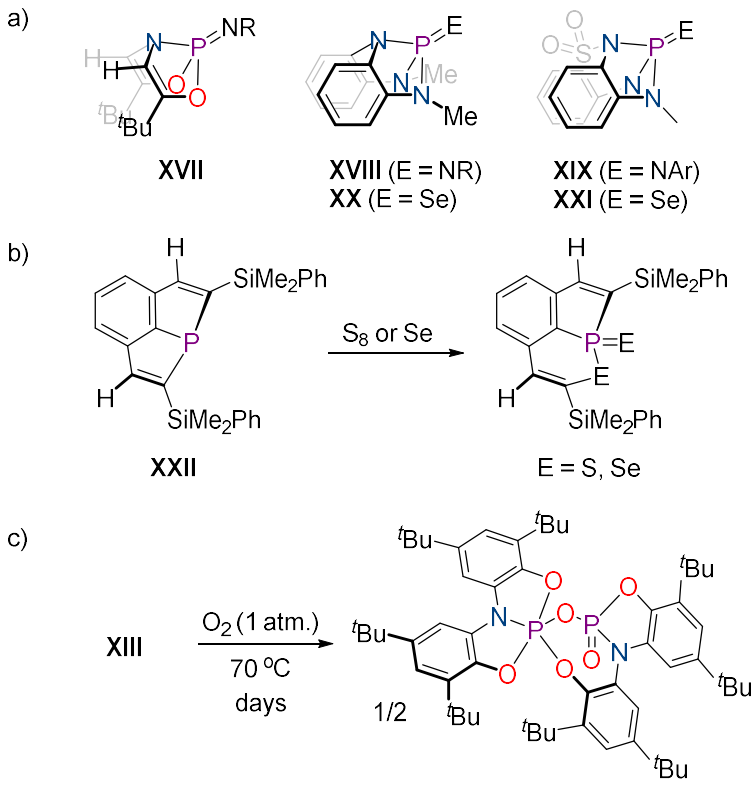


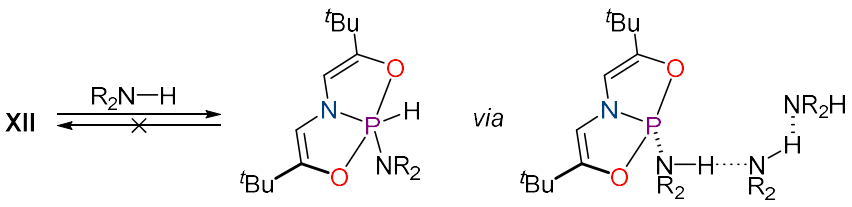
Figure 1.9. Phosphorus(V) derivatives of some geometrically constrained phosphines, including iminophosphoranes (R = various alkyl and aryl, Ar = *p*-OMe-Ph), selenophosphoranes, and those derived from ligand involvement in reactions of the parent phosphine with elemental chalcogens.

Phosphines readily access the phosphorus(V) oxidation state through reaction with a variety of two-electron oxidants. A well-established reactivity pathway is the formation of iminophosphoranes through reaction with organic azides *via* the Staudinger reaction.[70,71] This reactivity was demonstrated for C_{2v} symmetric **XII** and C_s symmetric **XI** and **XIII** to provide **XVII**, **XVIII** and **XIX**, respectively (Figure 1.9a). The resulting P=N bonds were shown to undergo 1,2-addition reactions with B–H and S–H bonds, or dimerisation *via* (2+2) cycloaddition reactions.[72] Regarding oxidations with chalcogens, constrained phosphines readily form selenophosphoranes such as **XX** and **XXI** through reaction with elemental (grey) selenium.[65,69] However, in the case of CCC-ligated phosphine **XXII**, reaction with either selenium or sulfur resulted in insertion to one of the ligand-based P–C bonds, driven by relief of

the highly strained fused ring system (Figure 1.9b).[73] Ligand involvement is also prevalent in reactions with oxygen as demonstrated by Goicoechea and Aldridge in the reaction of **XIII** and oxygen gas, whereby an oxo-bridged dimer forms *via* P–O_{ligand} bond cleavage (Figure 1.9c).[74]

1.3.3 Reactions with E–H bonds

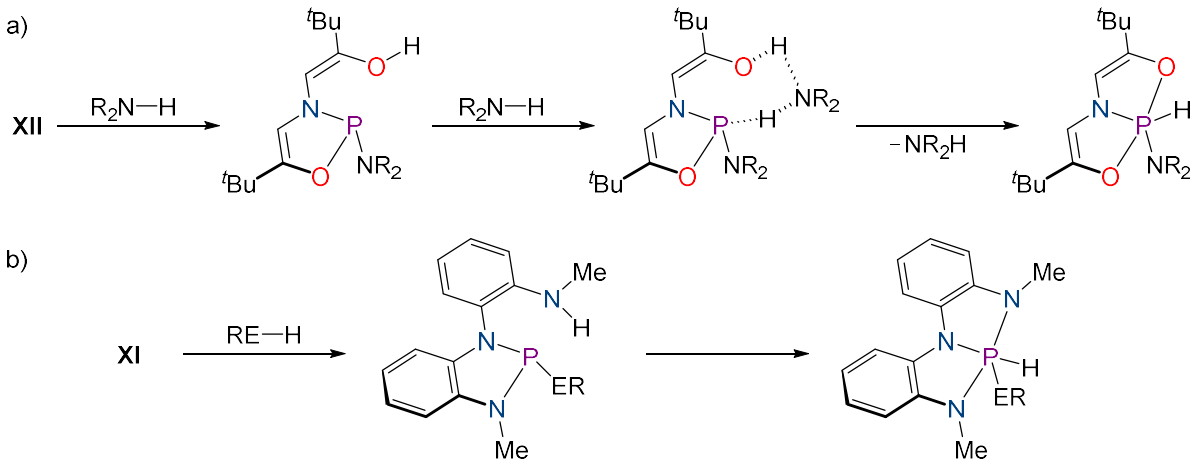
E–H bond activation (E = B, N and O) demonstrates the enhanced Lewis acidity of the phosphorus centre in constrained phosphines, akin to the analogous reactivity of carbenes as reported by Bertrand and Schoeller.[75] T-shaped phosphine **XII** reacts with N–H containing substrates such as ammonia and amines *via* oxidative addition, providing five-coordinate phosphorus species, which do not reductively eliminate on heating or on being subjected to vacuum (Scheme 1.7). Calorimetry measurements and DFT calculations suggest that a mechanism involving up to three molecules of substate is operative for this reaction.[76] Such a mechanism invokes the formation of a Lewis adduct between the N–H containing substrate and the electrophilic phosphorus centre, with the former then undergoing deprotonation by an additional molecule of substrate, itself in a hydrogen bonding network with a third. Proton transfer yields the product of oxidative-addition to phosphorus.



Scheme 1.7. N–H bond activation of ammonia, alkyl and aryl amines at **XII**. DFT calculations show that the reaction proceeds *via* base assisted bond activation involving three molecules of N–H containing substrate.

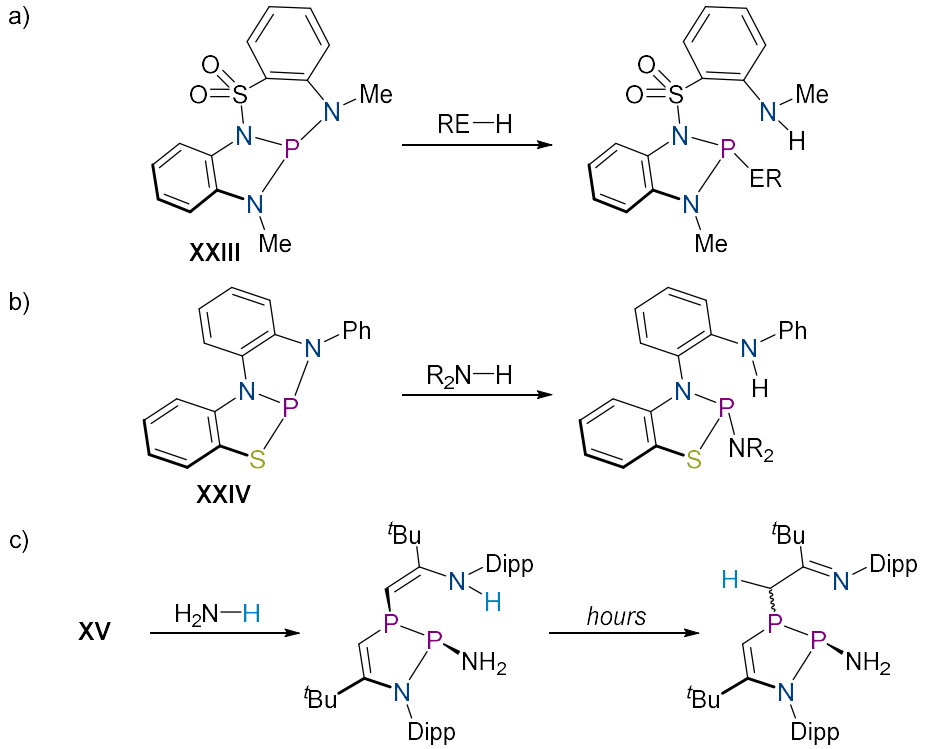
An alternative mechanism for the activation of N–H bonds at **XII**, based on DFT calculations, was proposed by Vanka and co-workers.[77] This mechanism invoked cooperativity between the phosphorus centre and a ligand-based oxygen atom towards initial N–H cleavage, with base-assisted proton transfer proving the final phosphorus(V) product (Scheme 1.8a). This mechanism is supported by observations of ligand cooperativity in N–H and O–H activation at C_s symmetric **XI**, whereby the initial phosphorus(III) reaction product is the result of cooperative addition with involvement of a pendant ligand nitrogen centre (Scheme 1.8b).[65] However, this intermediate product converted to the product

of a formal oxidative-addition under ambient conditions. Reductive elimination from this compound can be facilitated by heating under a dynamic nitrogen flow.



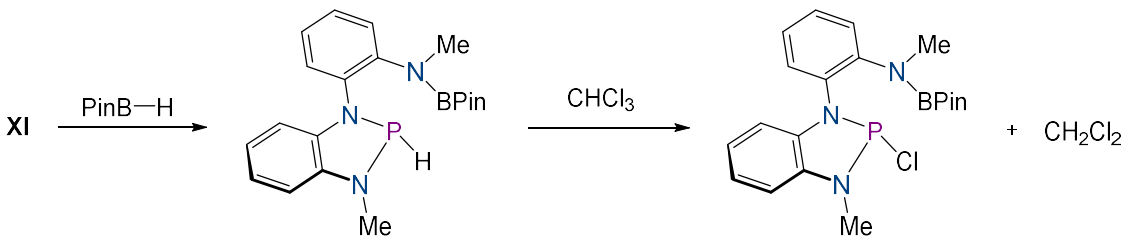
Scheme 1.8. a) Proposed mechanism for the activation of E–H bonds at **XII** based on DFT calculations. b) Activation of E–H bonds at **XI**. E = N and O. R = various alkyl and aryl substituents. Intermediate phosphorus(III) cooperative addition product was observed spectroscopically, for example for ER = O^{t}Bu.

Sole formation of a redox neutral, cooperative addition product can be promoted through inclusion of electron withdrawing substituents within the pincer ligand to destabilise the phosphorus(V) product. This was achieved for **XXIII**, whereby the central ligand nitrogen donor possessed sulfonamido functionality (Scheme 1.9a), and for **XXIV** which saw phosphorus bonded to sulfur — a soft donor atom, thus favouring the phosphorus(III) cooperative addition product on reaction with N–H bonds (Scheme 1.9b).[69,78] NPN-ligated **XV** also underwent cooperative activation of an ammonia N–H bond, however due to the reactive nature of its enamine-derived backbone, proton transfer resulted in ligand derivatisation (Scheme 1.9c).[79] This highlights the importance of an inert ligand scaffold for controlled bond activation, hence the prevalence of aromatic systems in such ligands.



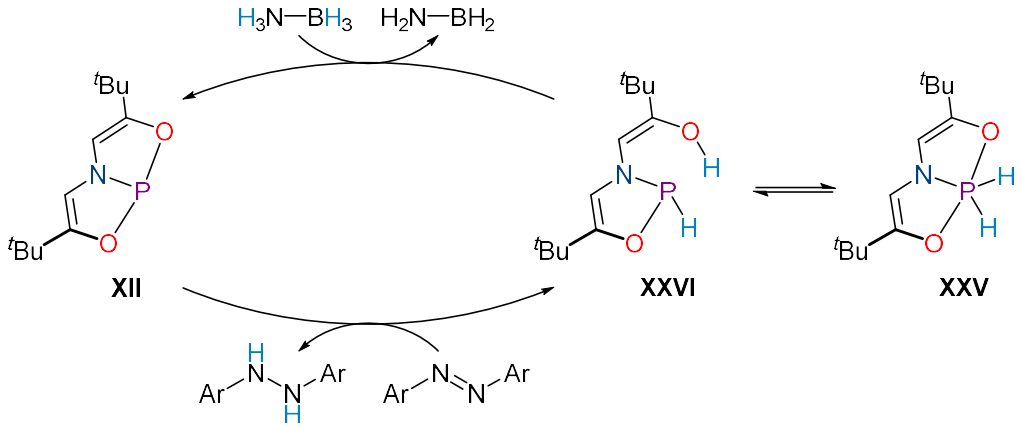
Scheme 1.9. Cooperative bond activation at geometrically constrained phosphines. E = N, O and S. R = various alkyl and aryl.

Cooperative B–H activation was also observed on addition of pinacol borane (HBPin) to **XI**, further substantiating the proposed redox-neutral mechanism of E–H activation at geometrically constrained phosphines (Scheme 1.10).[77,80] The resulting phosphorus(III) product features a new P–H bond, a result of the negatively polarised hydride unit associating with the Lewis acidic phosphorus centre in **XI**. This polarity was retained and utilised in the stoichiometric reduction of alkyl halides *via* hydrodechlorination, providing the respective chlorophosphine and C–H containing product. Generation of this chlorophosphine can be exploited in the catalytic C–H borylation of heteroarenes following the HBPin induced elimination of Cl–BPin.[81] Solely phosphorus-based catalytic transformations involving B–H activation is explored in Section 1.3.4.



Scheme 1.10. Cooperative B–H bond activation of HBPin at **XI**, and subsequent hydrochlorination of chloroform.

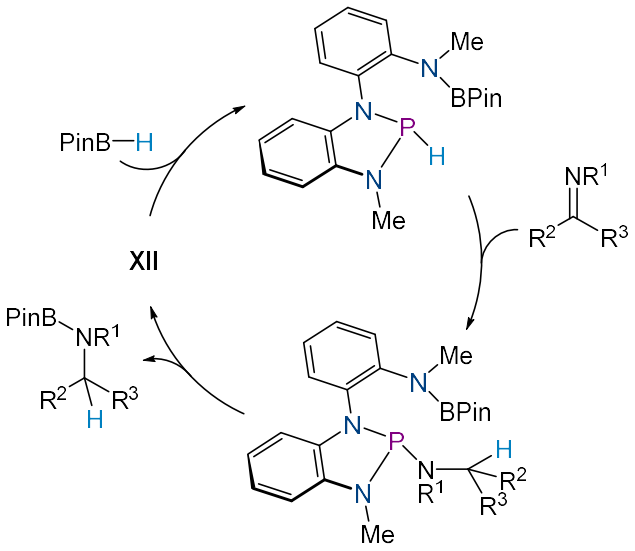
1.3.4 Catalysis



Scheme 1.11. Proposed mechanism of the catalytic transfer hydrogenation of azobenzene, using ammonia borane as the "H_2" source and T-shaped phosphine **XI** as the catalyst.

There have been several attempts to utilise the ability of geometrically constrained phosphines to activate E–H bonds to establish new catalytic processes. In a landmark report by Radosevich and co-workers, T-shaped phosphine **XII** was shown to be an active catalyst for the transfer-hydrogenation of azo-benzene, using ammonia borane as a "H_2" source (Scheme 1.11).[82] The mechanism of this reaction is contested in the literature, with a phosphorus(III/V) redox cycle proposed in the initial publication, evidenced by the observation of a dihydridophosphorane, **XXV**, itself catalytically competent. However, a P–O cooperative mechanism, *via* **XXVI**, has since been suggested based on DFT calculations by Sakaki and co-workers, whereby **XXV** was deemed to be an off-cycle intermediate.[83,84] Kinjo and co-workers reported the cooperative activation of ammonia borane at NPN-ligated phosphine **XV**, resulting in formal "H_2" addition across one of its constituent P–N bonds, supporting the aforementioned cooperative mechanism proposed by Sakaki.[67]

C_s symmetric phosphine **XI** was shown to be a viable catalyst for the hydroboration of imines (Scheme 1.12).[80] This reaction is initiated by cooperative B–H bond activation of HBPin at **XI**, as demonstrated stoichiometrically (Section 1.3.3, Scheme 1.10). Insertion of the resulting hydridic P–H unit into the N=C double bond of an imine provides a tri-amino phosphine which readily eliminates the amino-borane product, thus regenerating **XII**.



Scheme 1.12. The mechanism of the catalytic hydroboration of imines using **XII**. R^1 = benzyl or a variety of aryl substituents. R^2 = a variety of aryl substituents. R^3 = H, Me, Ph.

1.3.5 Reaction monitoring by NMR spectroscopy

NMR spectroscopy is often the choice method for monitoring the outcome of reactions involving geometrically constrained phosphines. This is on account of the $^{31}P\{^1H\}$ chemical shift for such compounds being highly sensitive to the environment and oxidation state of the phosphorus centre, thus providing a quick and reliable method for determining the outcome of a reaction.

Typically, geometrically constrained phosphines have a chemical shift within the range of *ca.* 100 – 200 ppm.[62–65,69,78,79] Phosphorus(III) derivatives of these, such as those resulting from the cooperative addition of an E–H bond, have a typical chemical shift range from *ca*. 70 – 120 ppm.[65,69,78,79] Phosphorus(V) species derived from geometrically constrained phosphines typically fall within two categories; four-coordinate species (i.e. those containing a P=E double bond) which have a chemical shift range of *ca.* 0 – 100 ppm;[65,69,72,73] and five coordinate species such as the result of E–H oxidative addition, or dihalogenation, which have a chemical shift range from *ca.* −250 – −20 ppm.[63,65,72,74,76,82] It should be noted, however, that this is not general for phosphines/phosphoranes as a whole, but specifically for geometrically constrained systems. Reference will be made to these chemical shift ranges throughout this thesis.

1.4 Aims

The initial target of this study was to *experimentally* validate the ambiphilic hypothesis attributed to T-shaped phosphines, thus addressing a gap in the literature pertaining to solely phosphorus-based reactivity of such highly constrained systems. Therefore, the first aim of this research project was to synthesise a phosphine whereby the T-shaped geometry is stabilised, and possesses an inert backbone to prevent its involvement in reactions. Chapter 2 explores these efforts, with the general reactivity of a novel T-shaped phosphine assessed by reaction with small molecules of varying polarity.

Phosphines are typically used as ligands to transition metals, prompting the question of how geometric constraint influences their electronic (and steric) properties. Complexes of the above T-shaped phosphine bearing indicative spectroscopic probes were therefore targeted to assess ligand properties, and to determine if the reactivity permitted by geometric constraint (such as the activation of E–H bonds) is maintained on bonding to a transition metal. Chapter 3 details this study.

The next target was to investigate whether enforcing a T-shaped geometry is a privileged means of promoting phosphorus-based Lewis acidic reactivity. Chapter 4 addresses this with an investigation of whether alternative means of phosphorus Lewis acidification, such as oxidation or methylation, were sufficient to promote ammonia activation in the absence of geometric constraint.

The research project was concluded with a study of the photochemical properties of derivatives of the title phosphine. Photoinduced reduction of phosphorus(V) species *via* the elimination of substituents at phosphorus is a mode of reactivity crucial in establishing photocatalytic reactions utilising phosphines. Therefore, Chapter 5 explores efforts towards the photo-induced reduction of dihalogenated, phosphorus(V), derivatives of the above phosphine; a critical step in photocatalytic HX-splitting.

1.5 References

[1] J. Clayden, N. Greeves, S. Warren, *Organic Chemistry. 2nd ed.*, Oxford University Press, Oxford, **2012**

[2] B. E. Maryanoff, A. B. Reitz, M. S. Mutter, R. R. Whittle, R. A. Olofson, *J. Am. Chem. Soc.* **1986**, *108*, 7664–7678.

[3] P. A. Byrne, D. G. Gilheany, *Chem. Soc. Rev.* **2013**, *42*, 6670–6696.

[4] R. Robiette, J. Richardson, V. K. Aggarwal, J. N. Harvey, *J. Am. Chem. Soc.* **2006**, *128*, 2394–2409.

[5] E. Vedejs, C. F. Marth, *J. Am. Chem. Soc.* **1988**, *110*, 3948–3958.

[6] B. E. Maryanoff, A. B. Reitz, *Chem. Rev.* **1989**, *89*, 863–927.

[7] I. Janicki, P. Kiełbasiński, *Ad. Synth. Catal.* **2020**, *362*, 2552–2596.

[8] K. C. K. Swamy, N. N. B. Kumar, E. Balaraman, K. V. P. P. Kumar, *Chem. Rev.* **2009**, *109*, 2551–2651.

[9] R. Appel, *Angew. Chem., Int. Ed.* **1975**, 14, 801–811

[10] C. Bednarek, I. Wehl, N. Jung, U. Schepers, S. Bräse, *Chem. Rev.* **2020**, *120*, 4301–4354.

[11] F. L. Lin, H. M. Hoyt, H. van Halbeek, R. G. Bergman, C. R. Bertozzi, *J. Am. Chem. Soc.* **2005**, *127*, 2686–2695.

[12] C. R. Noller, R. Dinsmore, *Org. Synth.* **1933**, *13*, 20.

[13] A. G. Orpen, N. G. Connelly, *Organometallics* **1990**, *9*, 1206–1210.

[14] Norio. Miyaura, Akira. Suzuki, *Chem. Rev.* **1995**, *95*, 2457–2483.

[15] I. P. Beletskaya, A. V. Cheprakov, *Chem. Rev.* **2000**, *100*, 3009–3066.

[16] D. Haas, J. M. Hammann, R. Greiner, P. Knochel, *ACS Catal.* **2016**, *6*, 1540–1552.

[17] J. A. Osborn, F. H. Jardine, J. F. Young, G. Wilkinson, *J. Chem. Soc. A* **1966**, 1711–1732.

[18] S. T. Nguyen, L. K. Johnson, R. H. Grubbs, J. W. Ziller, *J. Am. Chem. Soc.* **1992**, *114*, 3974–3975.

[19] P. Schwab, M. B. France, J. W. Ziller, R. H. Grubbs, *Angew. Chem., Int. Ed.* **1995**, *34*, 2039–2041.

[20] P. Schwab, R. H. Grubbs, J. W. Ziller, *J. Am. Chem. Soc.* **1996**, *118*, 100–110.

[21] G. Occhipinti, V. R. Jensen, *Organometallics* **2011**, *30*, 3522–3529.

[22] C. A. Tolman, *Chem. Rev.* **1977**, *77*, 313–348.

[23] T. E. Barder, S. D. Walker, J. R. Martinelli, S. L. Buchwald, *J. Am. Chem. Soc.* **2005**, *127*, 4685–4696.

[24] R. Martin, S. L. Buchwald, *Acc. Chem. Res.* **2008**, *41*, 1461–1473.

[25] C. K. Brown, G. Wilkinson, *J. Chem. Soc. A* **1970**, 2753–2764.

[26] M. P. Magee, W. Luo, W. H. Hersh, *Organometallics* **2002**, *21*, 362–372.

[27] G. Yagupsky, C. K. Brown, G. Wilkinson, *J. Chem. Soc. A* **1970**, 1392–1401.

[28] A. van Rooy, P. C. Kamer, P. W. M. van Leeuwen, K. Goubitz, J. Fraanje, N. Veldman, A. L. Spek, *Organometallics* **1996**, 15, 835–847.

[29] R. Noyori, M. Kitamura, T. Ohkuma, *Proc. of the Natl. Acad. Sci. U.S.A.* **2004**, *101*, 5356–5362.

[30] A. Miyashita, A. Yasuda, H. Takaya, K. Toriumi, T. Ito, T. Souchi, R. Noyori, *J. Am. Chem. Soc.* **1980**, *102*, 7932–7934.

[31] R. Noyori, *Angew. Chem., Int. Ed.* **2002**, *41*, 2008–2022.

[32] W. S. Knowles, *Angew. Chem., Int. Ed.* **2002**, *41*, 1998–2007.

[33] W. S. Knowles, M. J. Sabacky, *Chem. Commun. (London)* **1968**, 1445–1446.

[34] W. S. Knowles, M. J. Sabacky, B. D. Vineyard, *J. Chem. Soc., Chem. Commun.* **1972**, 10–11.

[35] B. D. Vineyard, W. S. Knowles, M. J. Sabacky, G. L. Bachman, D. J. Weinkauff, *J. Am. Chem. Soc.* **1977**, *99*, 5946–5952.

[36] W. S. Knowles, *Acc. Chem. Res.* **1983**, *16*, 106–112.

[37] C. Xie, A. J. Smaligo, X.-R. Song, O. Kwon, *ACS Cent. Sci.* **2021**, *7*, 536–558.

[38] H. Guo, Y. C. Fan, Z. Sun, Y. Wu, O. Kwon, *Chem. Rev.* **2018**, 118, 10049–10293.

[39] C. J. O'Brien, J. L. Tellez, Z. S. Nixon, L. J. Kang, A. L. Carter, S. R. Kunkel, K. C. Przeworski, G. A. Chass, *Angew. Chem., Int. Ed.* **2009**, *48*, 6836–6839.

[40] G. Keglevich, M. Fekete, T. Chuluunbaatar, A. Dobó, V. Harmat, L. Tőke, *J. Chem. Soc., Perkin Trans. 1* **2000**, 4451–4455.

[41] C. J. O'Brien, F. L. Lavigne, E. E. Coyle, A. J. Holohan, B. J. Doonan, *Chem. Eur. J.* **2013**, 19, 5854–5858.

[42] C. J. O'Brien, *Catalytic Wittig and Mitsunobu Reactions*, **2014**, US8901365B2.

[43] J. A. Buonomo, C. C. Aldrich, *Angew. Chem., Int. Ed.* **2015**, *54*, 13041–13044.

[44] D. Hirose, M. Gazvoda, J. Košmrlj, T. Taniguchi, *Org. Lett.* **2016**, *18*, 4036–4039.

[45] H. A. van Kalkeren, S. H. A. M. Leenders, C. R. A. Hommersom, F. P. J. T. Rutjes, F. L. van Delft, *Chem. Eur. J.* **2011**, 17, 11290–11295.

[46] H. A. van Kalkeren, F. L. van Delft, F. P. J. T. Rutjes, *Pure Appl. Chem.* **2012**, *85*, 817–828.

[47] H. A. van Kalkeren, J. J. Bruins, F. P. J. T. Rutjes, F. L. van Delft, *Adv. Synth. Catal.* **2012**, 354, 1417–1421.

[48] D. W. Stephan, *J. Am. Chem. Soc.* **2015**, *137*, 10018–10032.

[49] G. C. Welch, R. R. S. Juan, J. D. Masuda, D. W. Stephan, *Science* **2006**, *314*, 1124–1126.

[50] P. A. Chase, G. C. Welch, T. Jurca, D. W. Stephan, *Angew. Chem., Int. Ed.* **2007**, *46*, 8050–8053.

[51] P. Spies, G. Erker, G. Kehr, K. Bergander, R. Fröhlich, S. Grimme, D. W. Stephan, *Chem. Commun.* **2007**, 5072–5074.

[52] P. Spies, S. Schwendemann, S. Lange, G. Kehr, R. Fröhlich, G. Erker, *Angew. Chem., Int. Ed.* **2008**, *47*, 7543–7546.

[53] G. C. Welch, D. W. Stephan, *J. Am. Chem. Soc.* **2007**, *129*, 1880–1881.

[54] P. A. Chase, T. Jurca, D. W. Stephan, *Chem. Commun.* **2008**, 1701–1703.

[55] D. Bawari, D. Toami, K. Jaiswal, R. Dobrovetsky, *Nat. Chem.* **2024**, *16*, 1261–1266.

[56] D. Roth, A. T. Radosevich, L. Greb, *J. Am. Chem. Soc.* **2023**, *145*, 24184–24190.

[57] K. Chulsky, I. Malahov, D. Bawari, R. Dobrovetsky, *J. Am. Chem. Soc.* **2023**, *145*, 3786–3794.

[58] S. Volodarsky, D. Bawari, R. Dobrovetsky, *Angew. Chem., Int. Ed.* **2022**, *61*, e202208401.

[59] K. Lee, A. V. Blake, A. Tanushi, S. M. McCarthy, D. Kim, S. M. Loria, C. M. Donahue, K. D. Spielvogel, J. M. Keith, S. R. Daly, A. T. Radosevich, *Angew. Chem., Int. Ed.* **2019**, *58*, 6993–6998.

[60] C. M. Donahue, S. R. Daly, *Comments Inorg. Chem.* **2018**, *38*, 54–78.

[61] T. J. Hannah, T. Z. Kirsch, S. S. Chitnis, *Chem. Eur. J.* **2024**, e202402851.

[62] A. J. Arduengo, C. A. Stewart, *Chem. Rev.* **1994**, *94*, 1215–1237.

[63] T. P. Robinson, D. M. De Rosa, S. Aldridge, J. M. Goicoechea, *Angew. Chem., Int. Ed.* **2015**, *54*, 13758–13763.

[64] M. K. Mondal, L. Zhang, Z. Feng, S. Tang, R. Feng, Y. Zhao, G. Tan, H. Ruan, X. Wang, *Angew. Chem., Int. Ed.* **2019**, *58*, 15829–15833.

[65] W. Zhao, S. M. McCarthy, T. Y. Lai, H. P. Yennawar, A. T. Radosevich, *J. Am. Chem. Soc.* **2014**, *136*, 17634–17644.

[66] T. P. Robinson, S.-K. Lo, D. De Rosa, S. Aldridge, J. M. Goicoechea, *Chem. Eur. J.* **2016**, *22*, 15712–15724.

[67] J. Cui, Y. Li, R. Ganguly, R. Kinjo, *Chem. Eur. J.* **2016**, *22*, 9976–9985.

[68] M. Driess, N. Muresan, K. Merz, M. Päch, *Angew. Chem., Int. Ed.* **2005**, *44*, 6734–6737.

[69] N. Beims, T. Greven, M. Schmidtmann, J. I. van der Vlugt, *Chem. Eur. J.* **2023**, *29*, e202302463.

[70] Yu. G. Gololobov, I. N. Zhmurova, L. F. Kasukhin, *Tetrahedron* **1981**, *37*, 437–472.

[71] Y. G. Gololobov, L. F. Kasukhin, *Tetrahedron* **1992**, *48*, 1353–1406.

[72] Y.-C. Lin, J. C. Gilhula, A. T. Radosevich, *Chem. Sci.* **2018**, *9*, 4338–4347.

[73] A. Hentschel, A. Brand, P. Wegener, W. Uhl, *Angew. Chem. Int. Ed.* **2018**, *57*, 832–835.

[74] T. P. Robinson, D. De Rosa, S. Aldridge, J. M. Goicoechea, *Chem. Eur. J.* **2017**, *23*, 15455–15465.

[75] G. D. Frey, V. Lavallo, B. Donnadieu, W. W. Schoeller, G. Bertrand, *Science* **2007**, 316, 439–441

[76] S. M. McCarthy, Y.-C. Lin, D. Devarajan, J. W. Chang, H. P. Yennawar, R. M. Rioux, D. H. Ess, A. T. Radosevich, *J. Am. Chem. Soc.* **2014**, *136*, 4640–4650.

[77] A. Pal, K. Vanka, *Inorg. Chem.* **2016**, *55*, 558–565.

[78] J. Abbenseth, O. P. E. Townrow, J. M. Goicoechea, *Angew. Chem., Int. Ed.* **2021**, *60*, 23625–23629.

[79] J. Cui, Y. Li, R. Ganguly, A. Inthirarajah, H. Hirao, R. Kinjo, *J. Am. Chem. Soc.* **2014**, *136*, 16764–16767.

[80] Y.-C. Lin, E. Hatzakis, S. M. McCarthy, K. D. Reichl, T.-Y. Lai, H. P. Yennawar, A. T. Radosevich, *J. Am. Chem. Soc.* **2017**, *139*, 6008–6016.

[81] J. M. Lipshultz, Y. Fu, P. Liu, A. T. Radosevich, *Chem. Sci.* **2021**, *12*, 1031–1037.

[82] N. L. Dunn, M. Ha, A. T. Radosevich, *J. Am. Chem. Soc.* **2012**, *134*, 11330–11333.

[83] G. Zeng, S. Maeda, T. Taketsugu, S. Sakaki, *Angew. Chem., Int. Ed.* **2014**, *53*, 4633–4637.

[84] G. Zeng, S. Maeda, T. Taketsugu, S. Sakaki, *ACS Catal.* **2016**, *6*, 4859–4870.

Chapter 2

Synthesis and Reactivity of a T-Shaped Phosphine

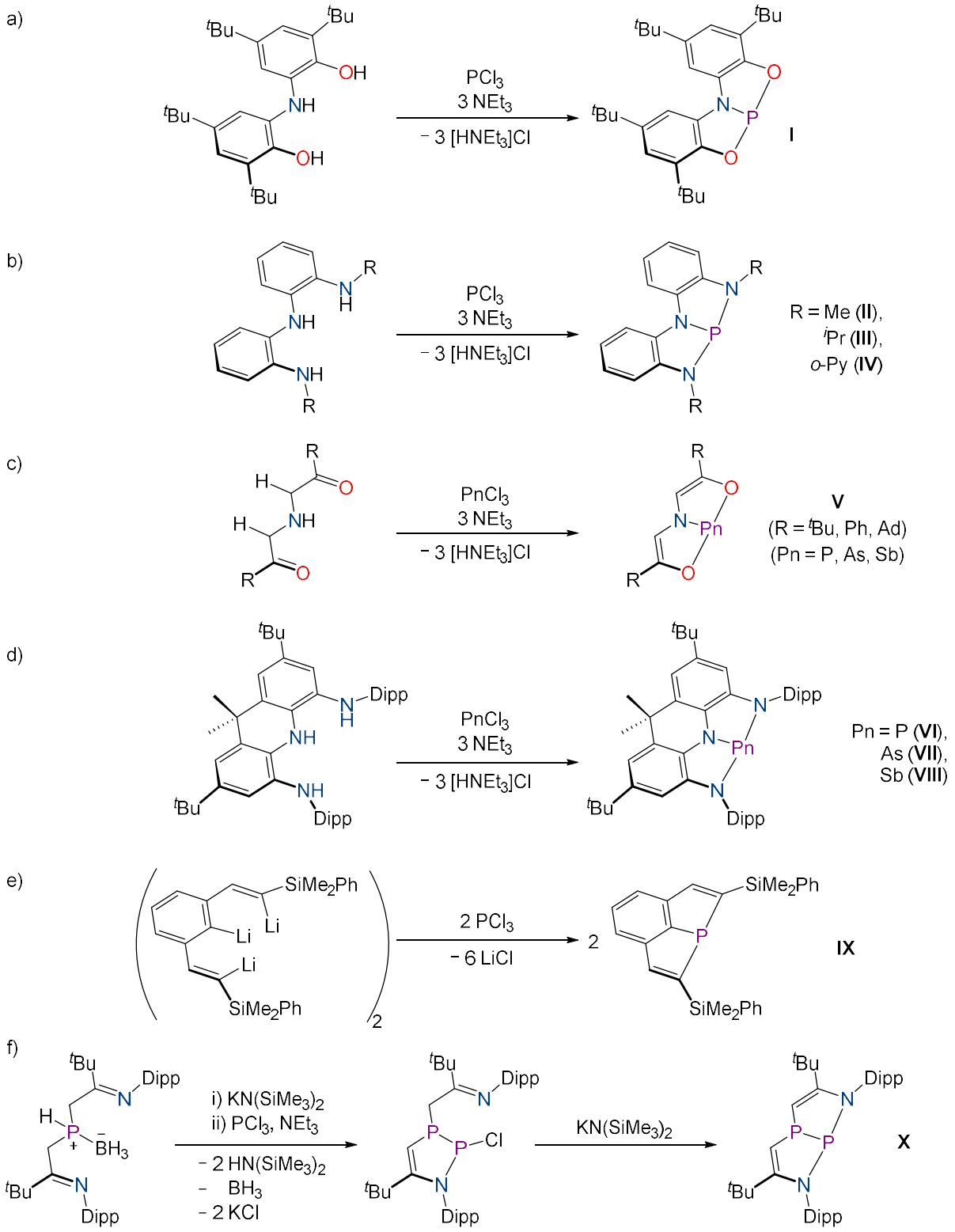
Abstract. Steric tuning of a tridentate, acridane-derived, NNN-pincer ligand was required to stabilise a highly constrained T-shaped phosphine. This species exhibited ambiphilic reactivity, evidenced by its phosphorus-based reactivity with both electrophiles and nucleophiles. Furthermore, oxidation with chalcogens or azides provide the respective phosphorus(V) products, and was accompanied by a significant geometric distortion of the ligand backbone. Ligand-involvement was observed with the cooperative activation of protic and hydridic E–H bonds, proceeding with the association of the negatively polarised substrate fragment to phosphorus, demonstrating its predominantly Lewis acidic nature.

2.1 Synthesis of geometrically constrained pnictogen compounds

Typically, geometrically constrained pnictogen compounds, including phosphines, are synthesised by reaction of a protonated pincer ligand with the respective trichloro-pnictogen in the presence of a weak base, e.g. triethyl amine.[1,2] This method was employed for both C_s symmetric phosphines, such as ONO- and NNN-ligated **I** and **II**–**IV**, and highly constrained, C_{2v} symmetric pnictogen compounds **V**–**VIII** (Scheme 2.1a–d).[3–7] The ligand scaffolds employed are often highly tuneable, and accessible from a common precursor, allowing steric modulation and installation of further donor atoms such as the pyridyl substituents present in **IV**.

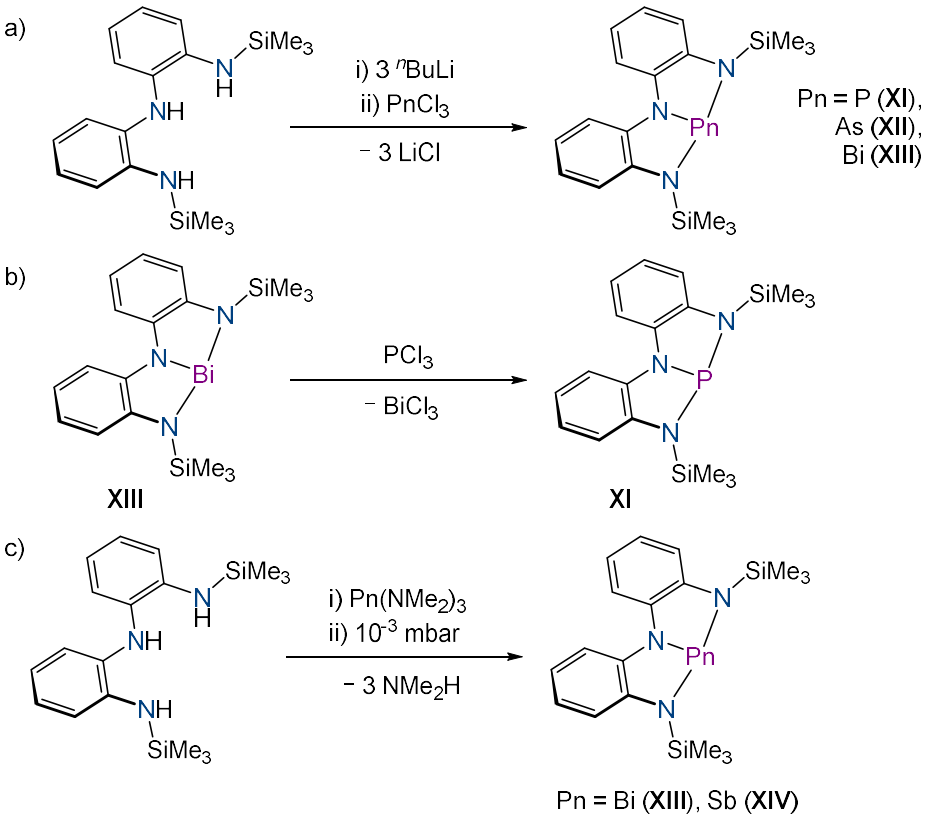
There are several examples of alternative methodologies. The synthesis of CCC-ligated phosphine **IX** required pre-lithiation of all three donor atoms of the respective pincer ligand (Scheme 2.1e).[8] These trilithiates were isolable as cage-like oligomers, and themselves synthesised by the reaction of ^{n}BuLi with a digallium complex of the ligand.[9] A multi-step process was required for the synthesis of NPN-ligated **X**, a rare example whereby only two P–D (D = ligand donor atoms) bonds were initially

formed to provide an isolable monocyclic species, with further deprotonation/dehalogenation required for ring closure (Scheme 2.1f).[10]



Scheme 2.1. Synthesis of geometrically constrained phosphines **I**–**X**.

Chitnis reported the synthesis of a range of pnictogen triamides based on a common NNN-pincer ligand (Scheme 2.2), shedding light on the various electronic and steric effects influencing their molecular structure.[11] Phosphine **XI**, arsine **XII** and bismuthine **XIII** were synthesised by deprotonation of the protio ligand with ^{n}BuLi, followed by addition of PCl_3, $AsCl_3$ or $BiCl_3$, respectively. Phosphine **XI** may also be synthesised by pnictogen exchange of bismuthine **XIII** with PCl_3, followed by $BiCl_3$ removal over Celite.[12] Alternatively, addition of $Pn(NMe_2)_3$ (Pn = Sb or Bi) to the protio ligand resulted in proton transfer to the dimethylamide fragments, such that the pnictogen resides within the pincer cavity whilst datively bound to two dimethylamine ligands. Application of vacuum to these complexes removes the volatile dimethylamine to provide **XIII** or **XIV**.



Scheme 2.2. Synthesis of constrained pnictogen compounds **XI**–**XIV**.

While **XI** and **XII** are monomeric in the solid-state, stibine **XIV** is dimeric. In the solution-state, monomeric and dimeric forms of **XIV** exist in equilibrium. This was attributed to insufficient steric bulk around the Lewis acidic antimony centre, which is electronically destabilised due to reduced covalency between antimony and the nitrogen atoms to which it is bonded (due to their large

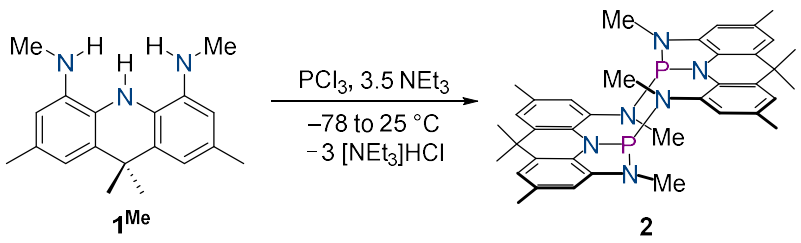
electronegativity difference). Based on a similar argument, it would be expected that bismuthine **XIII** would adopt a similar dimeric structure, however, this compound exists solely in its monomeric form. This was attributed to the large Pauli repulsion between the proposed bismuthine dimer subunits on account of the larger bismuth ionic radii.

2.2 Synthesis of acridane derived NNN pincer ligated phosphines and phosphoranes

2.2.1 Dimerisation of a sterically unprotected constrained phosphine

Herein begins the original work for this chapter.

In order to access phosphorus-based reactivity of a T-shaped phosphine, a ligand must be designed which is both inert, so as to avoid its participation in reactivity (as was observed for **V**), and possesses several spectroscopic handles to aid in determining the reaction outcome. With this brief, acridane derived ligands, as employed by Wang and co-workers for the synthesis of **VI**–**VIII**, were synthesised based on the 2,7,9,9-tetramethyl-9,10-dihydroacridane scaffold.[13] Reductive amination of the respective dinitro compound, 2,7,9,9-tetramethyl-9,10-dihydro-4,5-dinitroacridane, with paraformaldehyde provided the trisamine pincer ligand $\mathbf{1^{Me}}$ bearing methylamine side-arms in 79 % isolated yield. $\mathbf{1^{Me}}$ possesses C_{2v} symmetry on the ^{1}H NMR timescale, making it a suitable candidate for the synthesis of a T-shaped phosphine. In an attempt to incorporate phosphorus within the planar pincer cavity, $\mathbf{1^{Me}}$ was reacted with PCl_3 in the presence of NEt_3 (Scheme 2.3). However, rather than generating the targeted T-shaped phosphine, instead the dimeric bisphosphine **2** was formed (49% isolated yield).



Scheme 2.3. Synthesis of bisphosphine **2**.

2 exhibits a peak in its ^{31}P{^{1}H} NMR spectrum at 112.1 ppm, which is within the range expected of phosphorus(III) compounds derived from P–N rupture of geometrically constrained phosphines, while the ^{1}H NMR spectrum exhibits inequivalent acridane backbone signals. The SCXRD structure of **2**

reveals a ten-membered ring consisting of two distorted-pyramidal phosphorus atoms and two ligand units (Figure 2.1). The three P–N bonds about each phosphorus centre are of a similar length, implying that the dimer is tightly-bound; P1–N (Å) = 1.729(1) (N1), 1.746(1) (N2), 1.733(1) (N3).

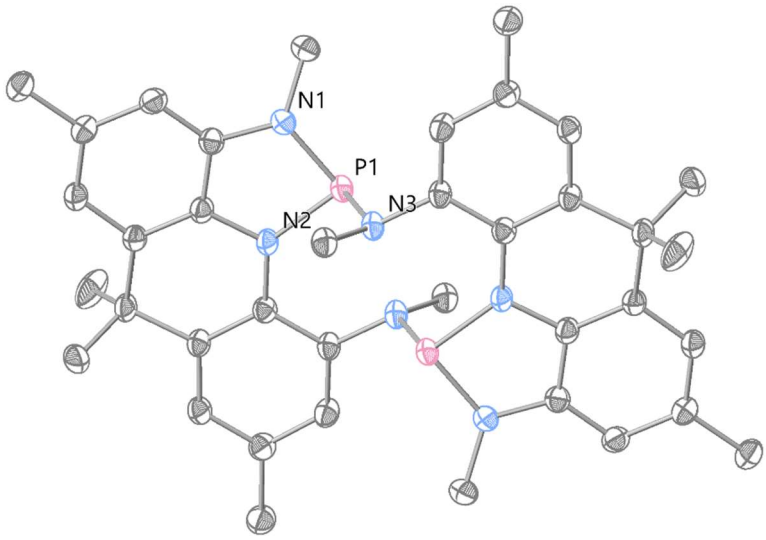


Figure 2.1. Solid-state structure of bisphosphine **2**. Thermal ellipsoids pictured at 50% probability level. Hydrogen atoms and solvent of crystallisation removed for clarity.

The dimeric structure of **2** does not dissociate into the respective monomeric phosphines upon heating, as revealed by variable-temperature NMR spectroscopy. The sample was heated in 20 °C increments from room temperature to 100 °C in d_8-toluene, with both $^{31}P\{^1H\}$ and ^1H NMR spectra collected at each interval (Figures 2.2 and 2.3, respectively). The $^{31}P\{^1H\}$ NMR spectrum remained constant, with the only appreciable change in the ^1H NMR spectrum being a slight temperature dependence on chemical shift, with the overall symmetry of the acridane backbone maintained.

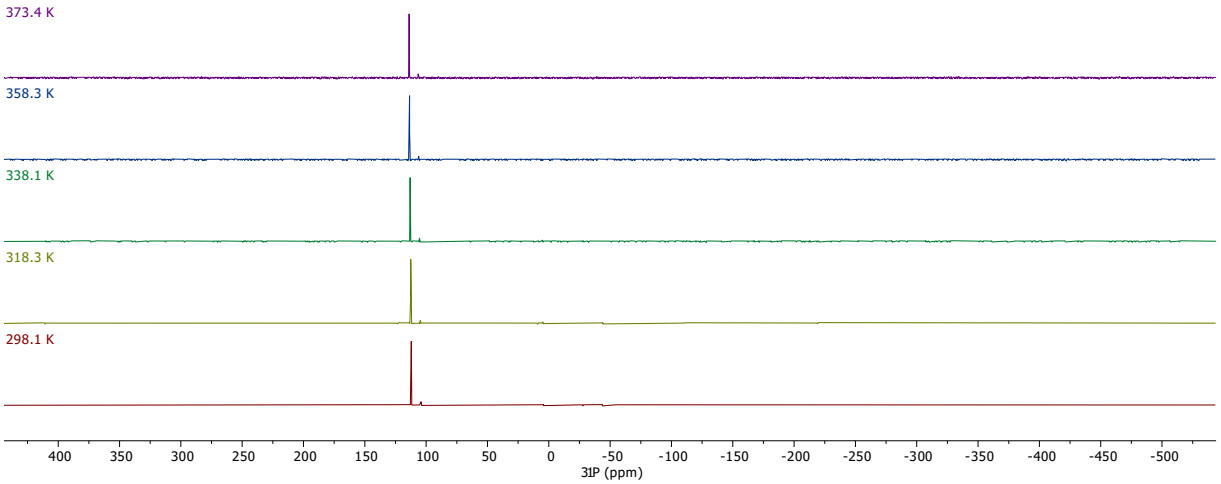


Figure 2.2. Stacked variable-temperature $^{31}P\{^1H\}$ NMR spectra of **2** in d_8-toluene.

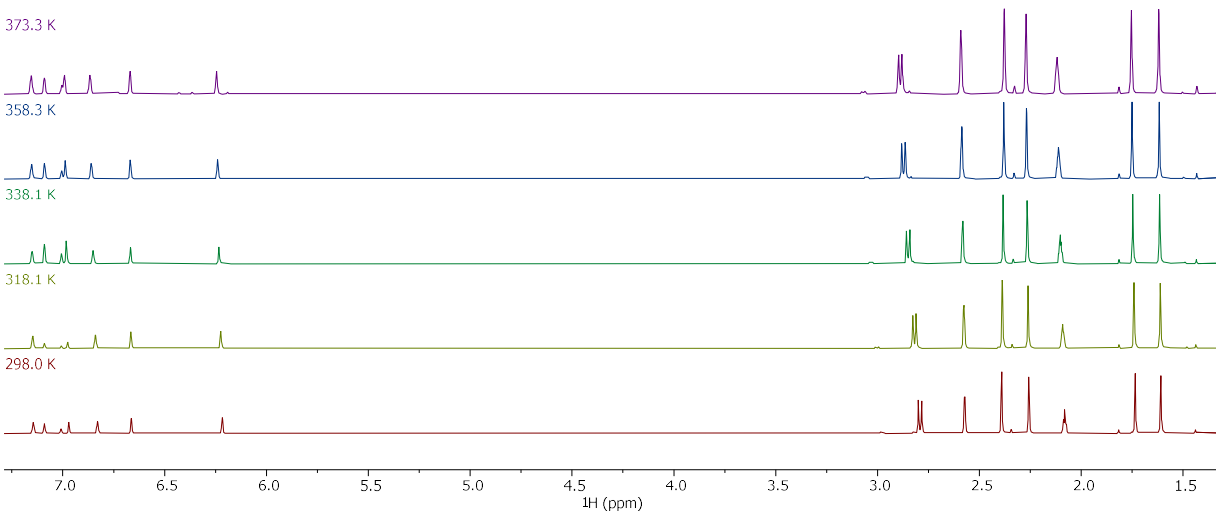
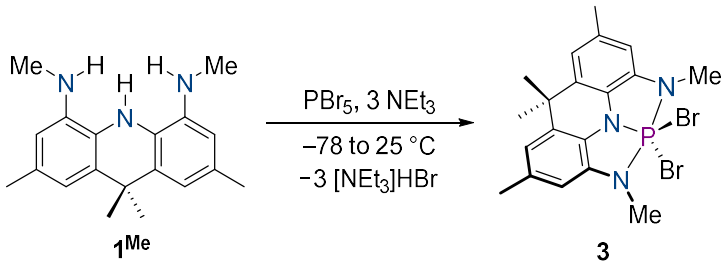


Figure 2.3. Stacked variable temperature ^{1}H NMR spectra of **2** in d_8-toluene.

It was suspected that **2** formed through the dimerisation of a transient T-shaped phosphine possessing a Lewis acidic vacant orbital and a Lewis basic lone pair of electrons co-localised at phosphorus.[11,14] To assess whether such a species may be observed spectroscopically, a phosphorus(V) precursor which can be reduced to the desired T-shaped phosphine *in situ* was targeted. The reaction between $\mathbf{1^{Me}}$ and PBr_5 in the presence of NEt_3 provides dibromophosphorane **3** in 64% isolated yield (Scheme 2.4). **3** is characterised by a peak at −107.6 ppm in its $^{31}P\{^{1}H\}$ NMR spectrum confirming its phosphorus(V) oxidation state - this is typically negative for 5-coordinate phosphoranes derived from geometrically constrained phosphines. The ^{1}H NMR spectrum exhibits equivalent backbone resonances as expected of a C_{2v} symmetric compound.



Scheme 2.4. Synthesis of dibromophosphorane **3**.

The SCXRD structure of **3** corroborates these spectroscopic data (Figure 2.4). The structure reveals a fully planarised acridane backbone, with meridionally coordinating nitrogen donor atoms occupying one equatorial and two axial positions about an overall trigonal bipyramidal phosphorus centre. The

P–N bond lengths are consistent with the formation of single bonds, suggesting that the redox non-innocent ligand does not undergo oxidation; P–N (Å) = 1.768(2) (N1), 1.653(2) (N2).

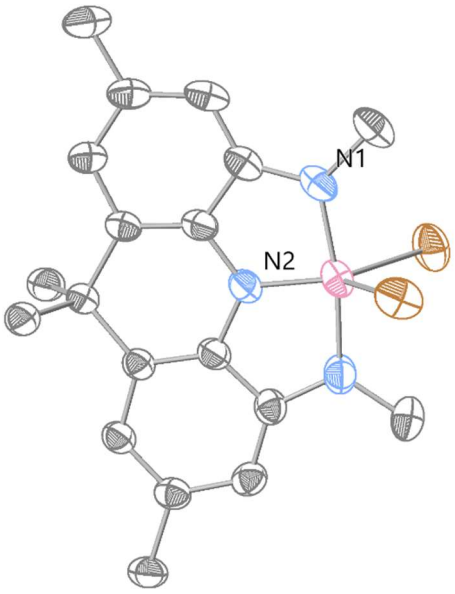
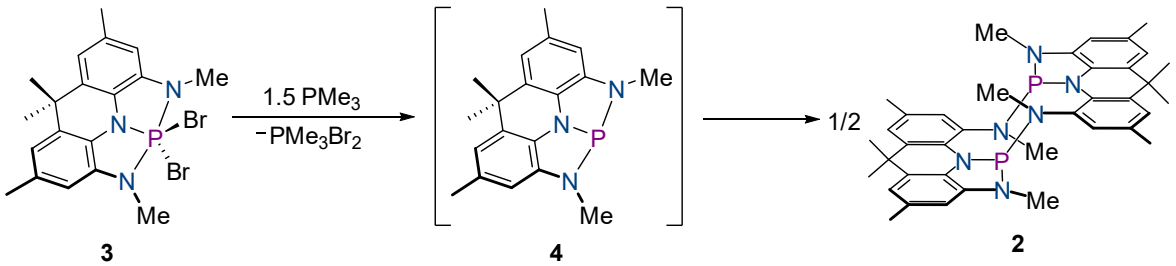


Figure 2.4. Solid-state structure of dibromo phosphorane **3**. Thermal ellipsoids pictured at 50% probability level. Hydrogen atoms and solvent of crystallisation removed for clarity.

Reduction *via* phosphine-induced dehalogenation was performed by the addition of PMe_3 (1.5 equivalents) to a benzene solution of **3**.[15–19] The reaction mixture turned bright orange and a colourless precipitate (PMe_3Br_2) formed. The $^{31}P\{^1H\}$ NMR spectrum acquired immediately after the addition of PMe_3 displays a signal at 150.9 ppm (br s). This chemical shift, and colour of the solution, strongly indicate the formation of T-shaped phosphine **4** (*vide infra*). However, over the course of minutes, the solution turns yellow and this NMR signal disappears, and is replaced by that corresponding to **2**. This data supports the hypothesis of **2** being formed through the dimerisation of transient **4** (Scheme 2.5).

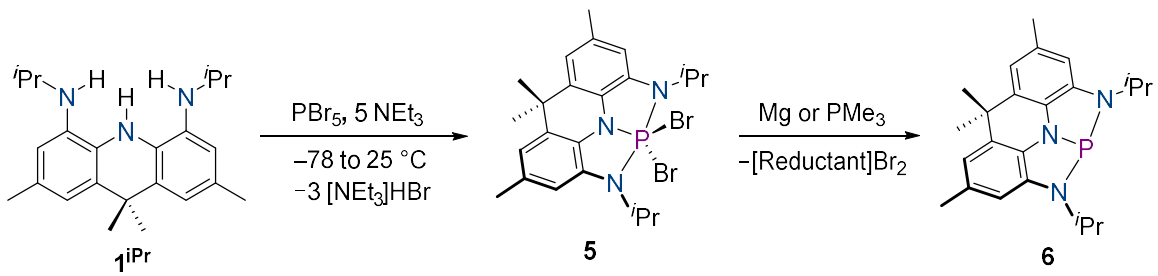


Scheme 2.5. Reduction of dibromophosphorane **3** towards transiently observed **4**, which dimerises to give **2**.

2.2.2 Steric tuning to afford a stable T-shaped phosphine, 6

Given the transient formation of **4**, it was suspected that an increase in bulk about the phosphorus centre would provide sufficient protection to avoid dimerisation. Installation of alternative nitrogen-based side-arms was possible *via* reductive amination from the ligand precursor 2,7,9,9-tetramethyl-9,10-dihydro-4,5-dinitroacridane. This strategy was employed previously by Goicoechea and Abbenseth for the synthesis of *iso*-propyl substituted derivative $\mathbf{1}^{\mathbf{iPr}}$, which possessed a greater degree of steric bulk about the pincer cavity.[20] However, reaction between $\mathbf{1}^{\mathbf{iPr}}$ (made according to the literature procedure) and PCl_3 in the presence of Et_3N did not proceed cleanly, giving rise to several phosphorus containing compounds as indicated by $^{31}P\{^1H\}$ NMR spectroscopy. Integration of this spectrum revealed that a product with a chemical shift of 145.0 ppm was most prominent; a value similar to those of previously reported geometrically constrained phosphines, and that attributed to **4**. Additionally, the ^1H NMR spectrum features prominent signals which correspond to a planar acridane backbone, suggesting that the target T-shaped phosphine was present in the mixture. Importantly, the aforementioned NMR resonances did not disappear over time, indicating that this compound was stable.

As described in Section 2.2.1, reduction of the respective dibromo phosphorane was pursued as an alternative route to the target phosphorus(III) compound. To this end, reaction of $\mathbf{1}^{\mathbf{iPr}}$ with PBr_5 and Et_3N provided **5** in 54% isolated yield (Scheme 2.6). The SCXRD structure and heteronuclear NMR spectra of **5** closely resemble that of **3** (Figure 2.5). Dehalogenation of **5** using either PMe_3 (5 equivalents) or magnesium powder (20 equivalents) resulted in the formation of a bright orange solution and a product with a single $^{31}P\{^1H\}$ NMR signal at 145.0 ppm corresponding to T-shaped phosphine **6** (90% isolated yield).



Scheme 2.6. Synthesis of dibromo phosphorane **5**, and its reduction to give T-shaped phosphine **6**.

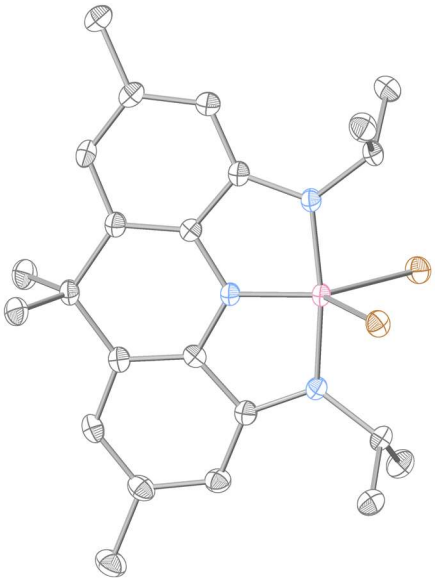


Figure 2.5. Solid-state structure of dibromophosphorane **5**. Thermal ellipsoids pictured at 50% probability level. Hydrogen atoms and solvent of crystallisation removed for clarity.

The ^{1}H NMR spectrum of **6** suggests C_{2v} symmetry across the acridane backbone (Figure 2.6). In solution, **6** may well be a rapidly inverting pseudo-trigonal phosphine featuring a bent acridane backbone, with signals averaging to those of the planar conformer on the NMR time scale. Variable temperature NMR measurements were conducted which showed that even on cooling the sample to −80 °C the signals corresponding to the planar structure are maintained. This, along with DFT calculations, suggest that the barrier to phosphorus inversion of **6** is too low for the bent conformation to be observed ($\Delta G^{\ddagger}_{DFT}$ = 3.8 kcal/mol at 298 K; $\Delta H^{\ddagger}_{DFT}$ = 2.9 kcal/mol; $\Delta S^{\ddagger}_{DFT}$ = −0.9 kcal/mol).[21]

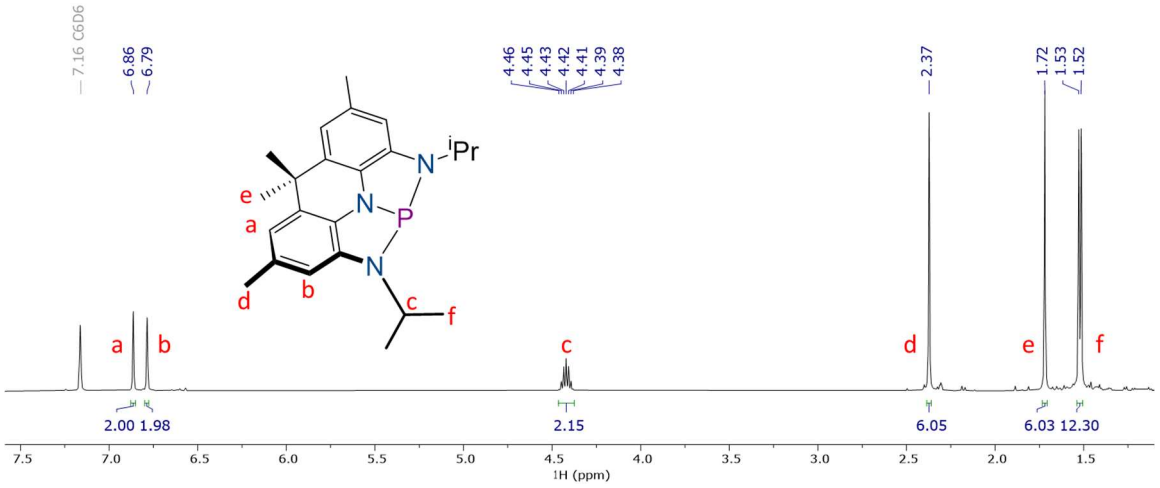


Figure 2.6. Room temperature ^{1}H NMR spectrum of **6**. Symmetrical environments across the centre of the acridane backbone (labelled) evidence a planar structure on the NMR time scale.

Regarding the stability of **6** in solution; only minor quantities (< 5% by $^{31}P\{^{1}H\}$ NMR integration) of additional phosphorus-containing compounds are generated several days after dissolution. The chemical shits of these products (111.0 and 103.8 ppm) are similar to that of dimeric **2** (112.1 ppm), therefore these new signals were assigned as isomeric forms of a dimer of **6**. Given that only trace amount of dimerisation occurred, the increased steric bulk going from methyl to *iso*-propyl substituents at the nitrogen side-arms was sufficient to stabilise a monomeric T-shaped phosphine.

SCXRD confirms that, in the solid-state, **6** adopts a planar conformation with bond angles around phosphorus summing to 360.3° (Figure 2.7). The P–N bond lengths are consistent with the formation of single bonds; P–N (Å) = 1.860(1) (N1/N1′), 1.710(2) (N2).[22] This was initially surprising given the energetically accessible π-symmetry orbital at phosphorus (*vide infra*) available for mesomeric stabilisation from the nitrogen lone-pairs. However, this may be accounted for by the redo non-innocent nature of the acridane ligand; a resonance form featuring an oxidised ligand and a reduced phosphorus centre exists.[13] This form results in the rupture of a side-arm P–N bond, hence their relative elongation despite any mesomeric stabilisation that may be occurring. This also resonance form invokes an aza-benzoquinone-type structure at the acridane ring-system, corroborated by the C–N1 bond lengths of **6** being between those of a single and double bond, and (slightly) shorter than those in **5**; C–N1 (Å) = 1.370(2) (**6**), 1.391(2) (**5**).[22]

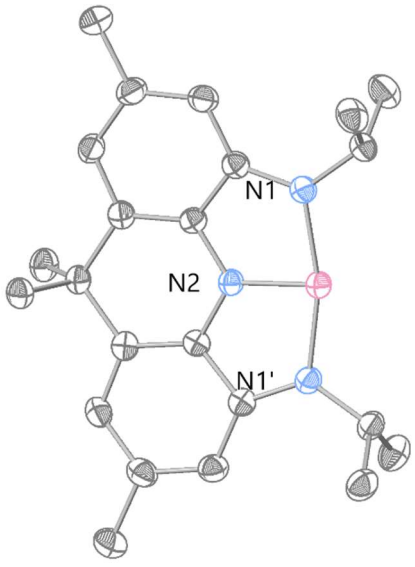


Figure 2.7. Solid-state structure of T-shaped phosphine **6**. Thermal ellipsoids pictured at 50% probability level. Hydrogen atoms and solvent of crystallisation removed for clarity.

2.3 Reactivity of 6

2.3.1 Reactions with electrophiles and nucleophiles

DFT calculations at the PBE0/DEF2-TZVP level of theory show that the HOMO−2 of **6** has phosphorus lone pair character, whilst the LUMO is predominantly a vacant p-type orbital situated at phosphorus, separated from the HOMO (delocalised ligand nitrogen lone-pairs) by only 3.87 eV (Figure 2.8). This HOMO–LUMO gap, which is significantly smaller than those of trigonal phosphines (calculated at the same level of theory), hints at the possibility of ambiphilic reactivity at **6**; HOMO–LUMO gap (eV) = 3.87 (**6**), 5.40 (PPh_3), 7.47 (PMe_3).

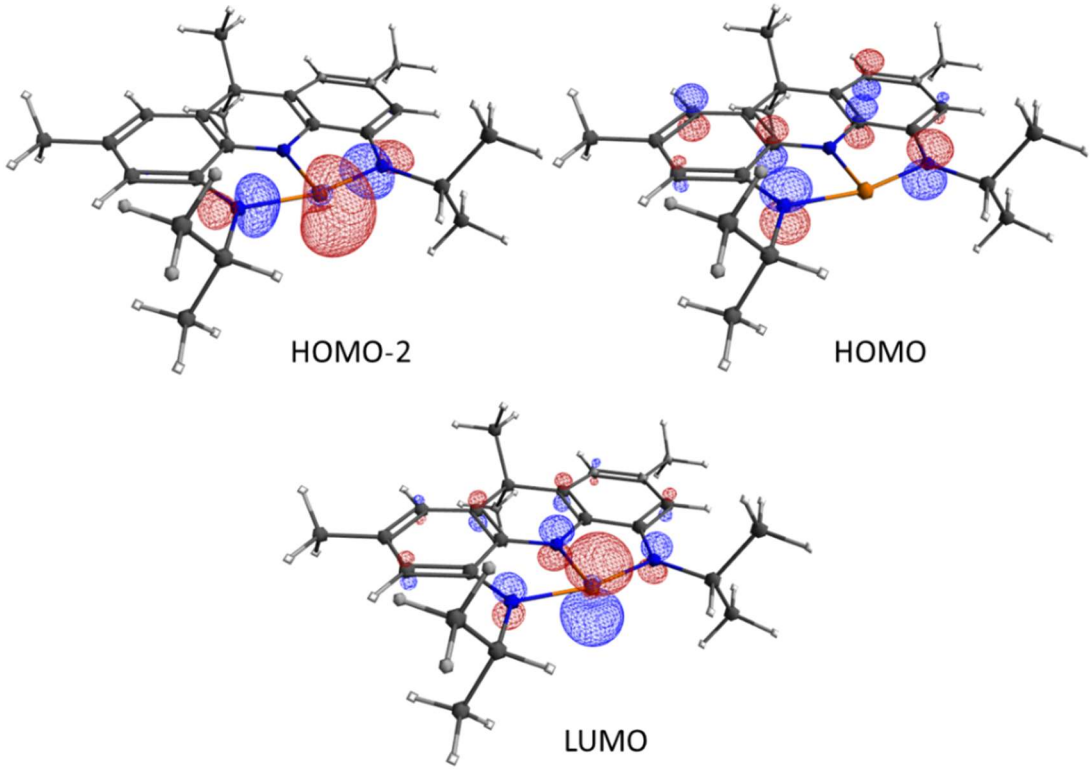
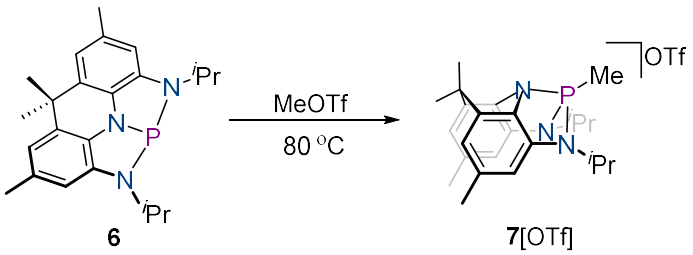


Figure 2.8. Kohn-Sham molecular orbitals of **6**. Isosurface values set to 0.07.

To address the electron donor properties of **6**, the strong electrophile methyl triflate was added, however, no reaction occurred at room temperature in benzene. This exemplifies the reduced accessibility of the phosphorus lone-pair in **6**. This is attributed to its high degree of s-orbital character in comparison with trigonal phosphines; 61% lone pair s-character for the bent conformation of **6**; 74% lone-pair s-character for the planar conformation of **6**, as revealed by NBO analysis. Elevated

temperatures (80 °C) were required to access phosphorus-based nucleophilic reactivity, generating phosphonium salt **7**[OTf] in 52% isolated yield (Scheme 2.7).



Scheme 2.7. Synthesis of phosphonium salt **7**[OTf].

The ^{31}P NMR resonance observed for **7**[OTf] displayed quartet-of-triplets multiplicity. The quartet was the larger of the two with a coupling constant of $^{2}J_{P–H}$ = 15.6 Hz, corresponding to a ^{1}H NMR signal at 3.13 ppm assigned as a P–CH_3 moiety (this ^{1}H NMR signal collapsed to a singlet upon ^{31}P-decoupling). The triplet multiplicity in the ^{31}P NMR spectrum was a result of coupling to the ligand-based *iso*-propyl side arms, a feature common amongst compounds derived from **6** which retain their bonds to each nitrogen atom of the acridane ligand. SCXRD of **7** reveals significant geometric distortion of the acridane backbone to accommodate the now cationic, four-coordinate phosphorus, featuring a bent geometry and shorted P–N bonds (Figure 2.9); N1–P–N1′ (°) = 131.2(4) (**7**); P–N1/N1′ (Å) = 1.860(1) (**6**), 1.660(1) (**7**); P–N2 (Å) = 1.710(2) (**6**), 1.658(2) (**7**). Together these data suggest that delocalisation of the ligand-based nitrogen lone pairs into the aromatic backbone (as depicted in the Kohn-Sham HOMO, Figure 2.8) quenched their usual nucleophilicity, thus precluding ligand methylation of **6** as observed for related compounds.[23,24]

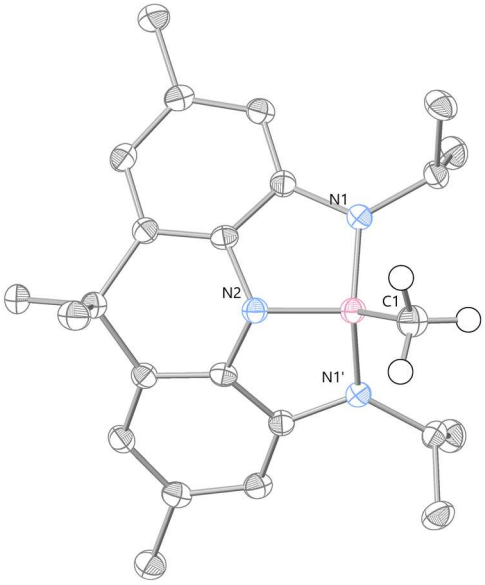
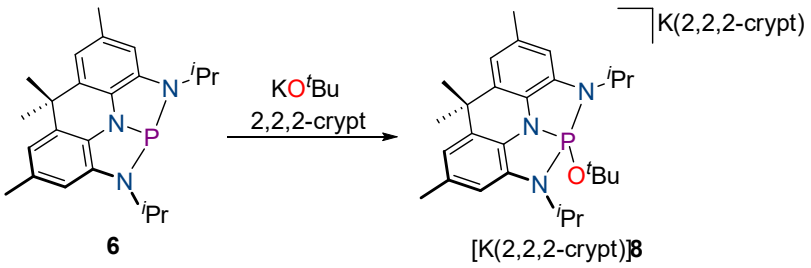


Figure 2.9. Solid-state structure of phosphonium salt **7**[OTf]. Thermal ellipsoids pictured at 50% probability level. Hydrogen atoms and triflate counterion removed for clarity.

To probe its electrophilic properties, **6** was reacted with potassium *tert*-butoxide in the presence of 4,7,13,16,21,24-hexaoxa-1,10-diazabicyclo[8.8.8]hexacosane (2,2,2-crypt). A reaction occurred upon addition at room temperature, evidenced by an immediate colour change from orange to yellow, to provide phosphorus-alkoxide salt [K(2,2,2-crypt)]**8** in 46% isolated yield (Scheme 2.8). This is in stark contrast to the reaction between **6** and an electrophile, suggesting that electrophilic reactivity pathways are the dominant mode of reactivity for **6**. [K(2,2,2-crypt)]**8** is characterised by a $^{31}P\{^{1}H\}$ NMR signal at 50.0 ppm, upfield shifted with respect to that of **6**, consistent with an increase in electron density at the phosphorus centre following association of the nucleophilic anion. ^{1}H NMR spectroscopy indicates a break of symmetry above/below the plane of the acridane ligand. A low-resolution SCXRD structure revealed the retention of planarity across the acridane backbone, with the P–O^{t}Bu moiety projecting out of the molecular plane (Figure 2.10).



Scheme 2.8. Synthesis of phosphorus-alkoxide salt [K(2,2,2-crypt)]**8**.

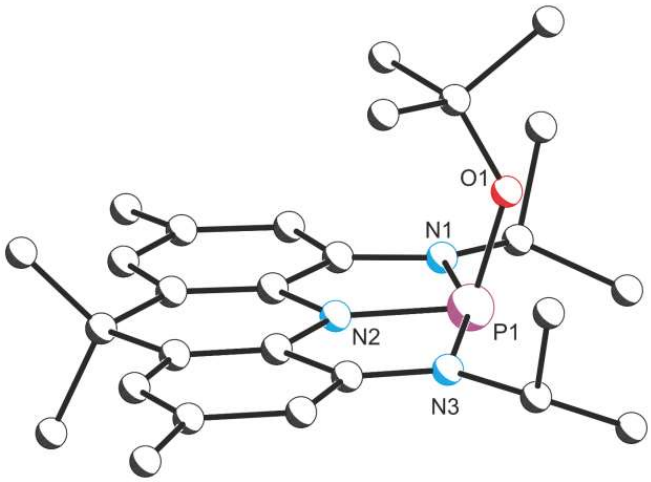
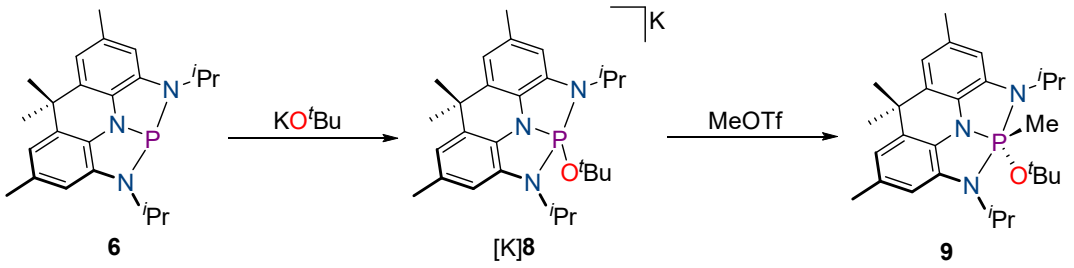


Figure 2.10. Ball-and-stick diagram of a low-resolution solid-state structure of phosphorus-alkoxide salt [K(2,2,2-crypt)]**8**. Hydrogen atoms, solvent of crystallisation and sequestered cation removed for clarity.

To establish whether the consecutive addition of a nucleophile and an electrophile at a single phosphorus centre was possible, **6** was reacted with each in tandem. First, the reaction of **6** with KO^{t}Bu to generate [K]**8**, followed by the addition of MeOTf (Scheme 2.9). In this order of addition, the reaction proceeds immediately with the generation of a colourless solution, and the formation of a single new product with a chemical shift at −39.4 ppm in the $^{31}P\{^1H\}$ NMR spectrum. Oxidation to a formally phosphorus(V) centre is evidenced by this chemical shift being in the range expected of phosphorus(V) derivatives of **6**. The ^1H NMR spectrum suggested a break in symmetry above/below the acridane backbone, consistent with a trigonal bipyramidal five-coordinate phosphorane featuring two different substituents in the equatorial plane (beyond those corresponding to the trisamine ligand). In the ^1H NMR spectrum, a signal at 1.63 ppm features coupling to phosphorus ($^2J_{P–H}$ = 16.6 Hz); a multiplicity reflected in the proton-coupled ^{31}P NMR spectrum, stemming from phosphorus-methylation. SCXRD confirms the formation of mixed phosphorane **9** (38% isolated yield, Figure 2.11). The immediate formation of **9** following the addition of MeOTf to [K]**8** demonstrates the enhanced nucleophilicity of the phosphorus centre in comparison to **6** which required heating to react with this strong electrophile (Scheme 2.7).



Scheme 2.9. Synthesis of mixed phosphorane **9**.

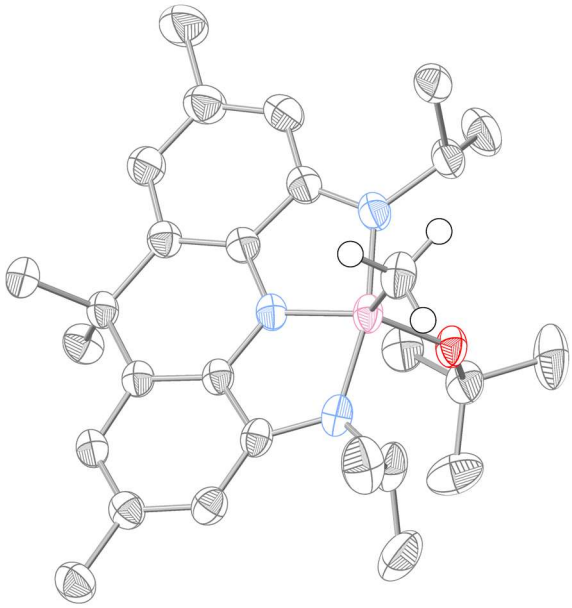
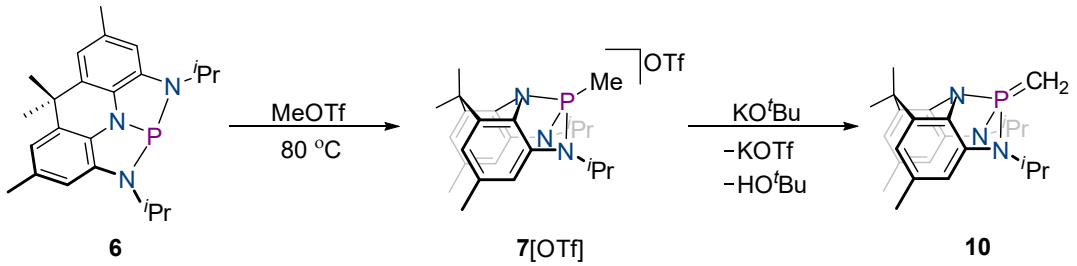


Figure 2.11. Solid-state structure of mixed phosphorane **9**. Thermal ellipsoids pictured at 50% probability level. Hydrogen atoms except for those at the phosphorus bound methyl group are removed for clarity.

Regarding the alternative order of addition of these reagents, reaction of potassium *tert*-butoxide with **7**[OTf] results in the generation of a new signal in the $^{31}P\{^{1}H\}$ NMR spectrum at 61.2 ppm, and the disappearance of the ^{1}H NMR resonance corresponding to the P–CH_3 group in the starting material. In its place, a signal at 1.20 ppm is observed, integrating to two protons and featuring doublet coupling to phosphorus ($^{2}J_{P-H}$ = 18.5 Hz). These data, and the observed lack of *tert*-butyl signals in the isolated product, suggest that C–H deprotonation has occurred (with the alkoxide reagent acting instead as a base) to provide the respective phosphorus ylide **10** (69% isolated yield, Scheme 2.10).



Scheme 2.10. Synthesis of ylide **10**.

SCXRD of **10** reveals a similar bent acridane backbone as present in **7**[OTf], and a P=C double bond is revealed by a shortened P–C interatomic distance (Figure 2.12); N1–P–N1′ (°) = 127.6(3) (**10**), 131.2(4) (**7**); P–C1 (Å) = 1.638(2) (**10**); 1.778(2) (**7**).

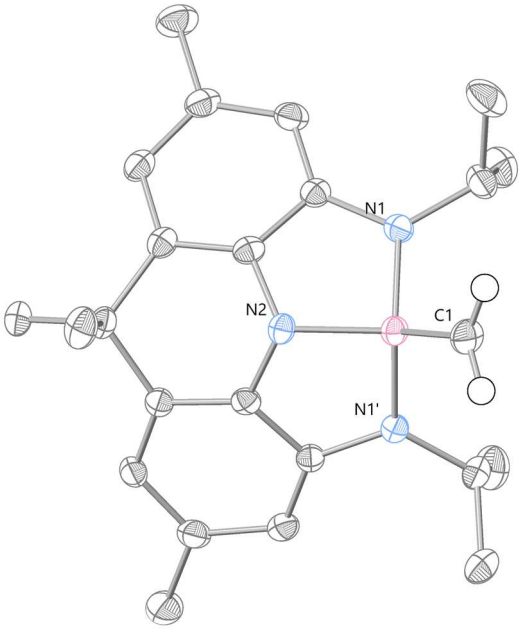
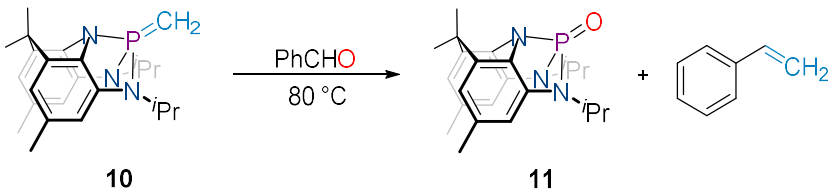


Figure 2.12. Solid-state structure of mixed ylide **10**. Thermal ellipsoids pictured at 50% probability level. Hydrogen atoms except for those in the ylide moiety are removed for clarity.

Given the ylide functionality present in **10**, its ability to perform the Wittig reaction was assessed through reaction with benzaldehyde (Scheme 2.11). The reaction was monitored by $^{31}P\{^1H\}$ NMR spectroscopy, revealing that no reaction occurred upon addition of benzaldehyde. Full consumption of **10** was observed upon heating at 80 °C for 1 hour. The $^{31}P\{^1H\}$ NMR spectrum contained two peaks, the minor of which (at 43.4 ppm) is unknown in origin (suspected of being the product of hydrolysis of **10** through water contamination in the benzaldehyde), while the major product (at 37.4 ppm) was identified as phosphine oxide **11** through independent synthesis (see Section 2.3.2). This, along with

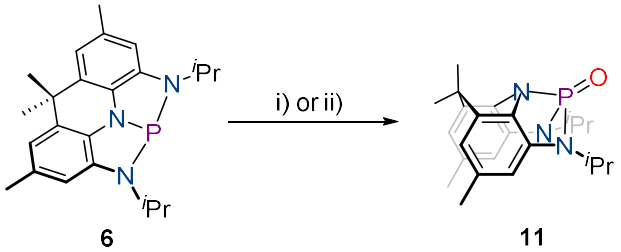
the observation of styrene in the ^{1}H NMR spectrum, confirms the possibility of Wittig-type reactivity from constrained phosphine derived ylides such as **10**.



Scheme 2.11. Wittig reaction between ylide **10** and benzaldehyde towards styrene and phosphine oxide **11**.

2.3.2 Two-electron oxidation reactions

The formation of a phosphine oxide is used as a driving force for several reactions in organic synthesis, such as the famed Mitsunobu and Wittig reactions. The latter of these was explored in Section 2.3.1, whereby phosphine oxide **11** was formed as the phosphorus containing by-product of this reaction, however this species could not be isolated from the reaction mixture. **11** was independently synthesised through the reaction of **6** with oxygen gas (Scheme 2.12). After addition at room temperature, ^{31}P{^{1}H} NMR spectroscopy revealed the formation of phosphine oxide **11**, along with two further signals at −1.2 (d, $^{2}J_{P-P}$ = 30.3 Hz) and −48.2 ppm (d, $^{2}J_{P-P}$ = 30.3 Hz) in a 1:1 ratio. These peaks indicate the formation of an oxo-bridged dimer featuring a phosphine oxide moiety, closely resembling the reaction product of a C_s symmetric phosphine with O_2 as reported by Goicoechea and co-workers (Chapter 1, Section 1.3.2).[25] This product mixture was maintained on stirring at room temperature, though heating the reaction to 60 °C for 16 hours results in the full conversion to phosphine oxide **11** (55% isolated yield), presumably through fragmentation of the proposed intermediate dimer. An alternative route to **11** is through the reaction of **6** with the oxygen-transfer reagent pyridine-N-oxide at room temperature (57% isolated yield, Scheme 2.12).



Scheme 2.12. Synthesis of phosphine oxide **11**. i) O_2, 60 °C. ii) Pyridine-N-oxide, 25 °C.

SCXRD of **11** reveals the presence of a P=O double bond and a bent acridane backbone isostructural to that present in ylide **10** (Figure 2.13); P=O (Å) = 1.468(2) (**11**), 1.484(1) (Ph_3PO).[22] The phosphorus centre in **11** adopts a geometry approaching tetrahedral, revealed through a τ'_4 value of 0.76, suggesting that very little geometric constraint is maintained upon oxidation.[26]

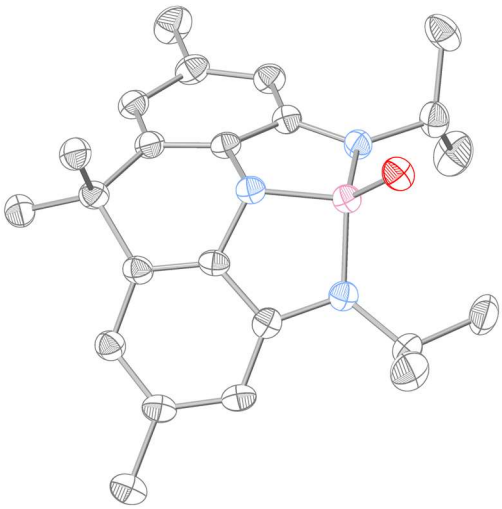
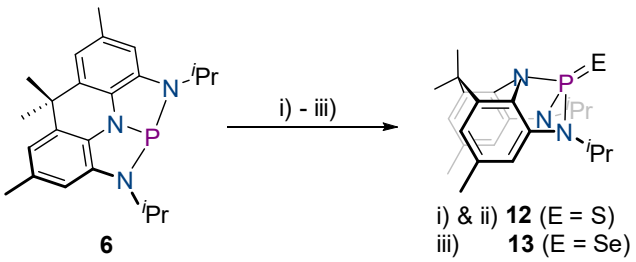


Figure 2.13. Solid-state structure of phosphine oxide **11**. Thermal ellipsoids pictured at 50% probability level. Hydrogen atoms and solvent of crystallisation removed for clarity.

Further oxidants were reacted with **6** to assess whether this structural change upon oxidation is a common reaction pathway, and to assess the effect of the phosphorus substituent on the overall structure of the resulting phosphorane (Scheme 2.13). Thiophosphorane **12** was synthesised through the reaction of **6** with an excess of elemental sulphur, or alternatively through reaction of **11** with Lawesson's reagent (54% isolated yield).[27] Similarly, selenophosphorane **13** was synthesised by addition of excess grey selenium to **6** (96% isolated yield). The synthesis of both of these phosphine chalcogenides proceeds cleanly with solely phosphorus-based reactivity, avoiding alternative P–N_{ligand} insertion reactions as observed for other pincer ligated phosphines.[8]



Scheme 2.13. Synthesis of phosphine chalcogenides **12** and **13**. i) 5 eq. S_8. ii) Pyridine-N-oxide to give **11**, then Lawesson's reagent. iii) 5 eq. Se.

SCXRD reveals that phosphoranes **11–13** are isostructural in the solid-state (Figure 2.14). The only significant deviation is the P=E bond length, which was shown to increase upon descending group 16 in accordance with the atomic radius of the respective chalcogen; P=E (Å) = 1.468(2) (**11**), 1.9272(6) (**12**), 2.0874(7) (**13**).

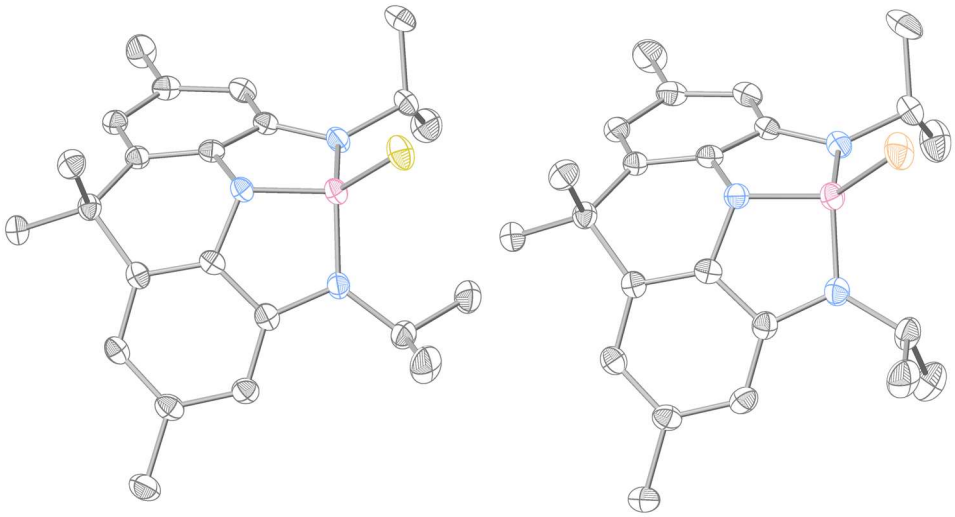


Figure 2.14. Solid-state structures of thiophosphorane **12** (left) and selenophosphorane **13** (right). Thermal ellipsoids pictured at 50% probability level. Hydrogen atoms removed for clarity.

The $^{31}P\{^{1}H\}$ NMR chemical shifts show significant variation (37.4 ppm (**11**); 83.8 ppm (**12**); 75.7 ppm (**13**)), while the ^{1}H NMR spectra of each are almost identical. Selenophosphoranes such as **13** have been used to determine the s-orbital character of the phosphorus-based lone-pair of the parent phosphine by comparison of the $^{1}J_{P–Se}$ coupling constant.[28] In the case of **13** (Figure 2.15), a value of $^{1}J_{P–Se}$ = 919 Hz suggests a high degree of lone-pair s-character, agreeing with electronic structure calculations of **6** (74% by NBO analysis, see Section 2.3.1).[29] However, on account of the geometric distortion that occurs on going from **6** to **13**, caution should be taken if using this value to describe the former.

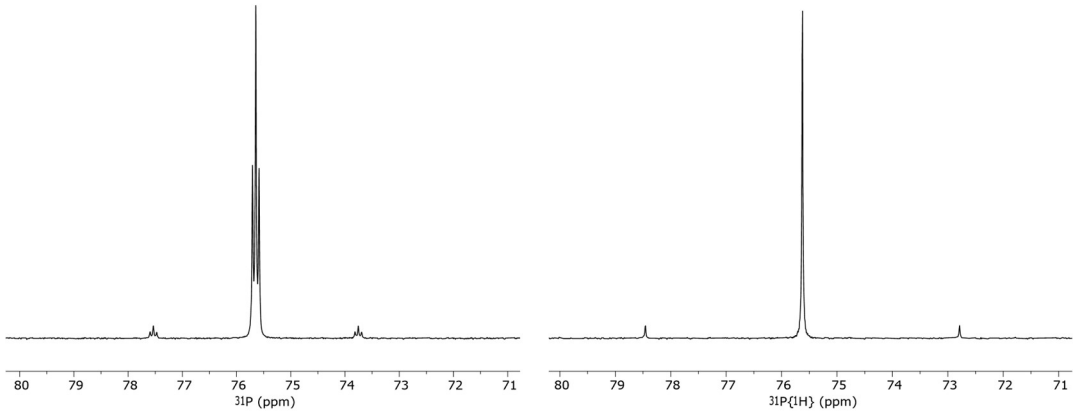
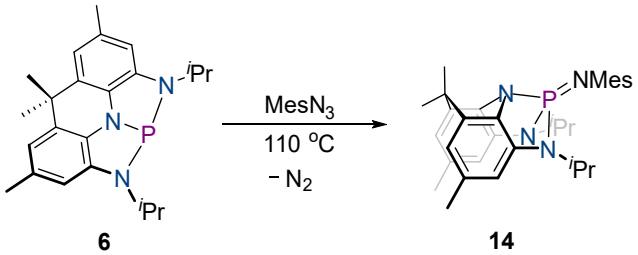


Figure 2.15. ^{31}P (left) and $^{31}P\{^{1}H\}$ (right) NMR spectra of **13**.

Beyond oxidation with chalcogens, such reactivity was also possible through the addition of azides to **6**. Iminophosphorane **14** was synthesised by reaction of **6** and mesityl azide at 110 °C (70% isolated yield, Scheme 2.14), with the elimination of dinitrogen.[30,31] In the $^{31}P\{^{1}H\}$ NMR spectrum, **14** displays a signal at 18.1 ppm, in the region expected of a tetra-aza phosphorane, while in the ^{1}H NMR spectrum signals for a bent, C_s symmetric backbone were present.[32] Additionally, a signal at 2.26 ppm corresponding to a mesityl-based methyl group was observed to couple to phosphorus (J_{P-H} = 2.8 Hz), confirming the formation of an iminophosphorane derived from mesityl-azide. In the solid-state, **14** adopts a bent acridane geometry isostructural to phosphoranes **11**–**13** (Figure 2.16), and features a P=N bond length of 1.533(1) Å — comparable to previously structurally authenticated iminophosphoranes derived from geometrically constrained phosphines.[32]



6 **14**

Scheme 2.14. Synthesis of iminophosphorane **14**.

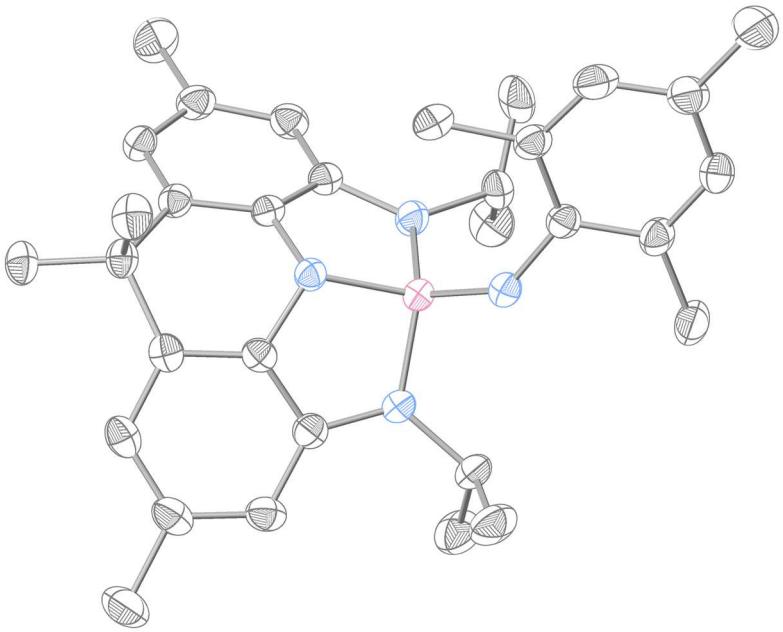
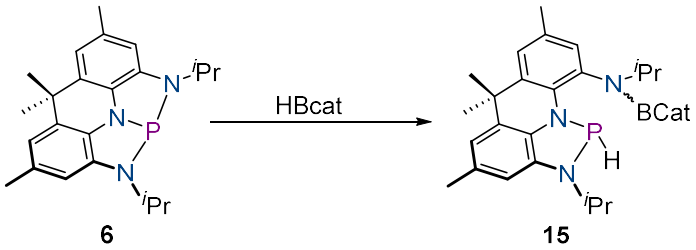


Figure 2.16. Solid-state structure of iminophosphorane **14**. Thermal ellipsoids pictured at 50% probability level. Hydrogen atoms and solvent of crystallisation removed for clarity.

2.3.3 Reactivity towards E–H bonds

To assess the selectivity of E–H bond activation, specifically whether formal oxidative addition or redox-neutral, cooperative substrate activation occurs, **6** was reacted with both hydridic and protic E–H bonds.

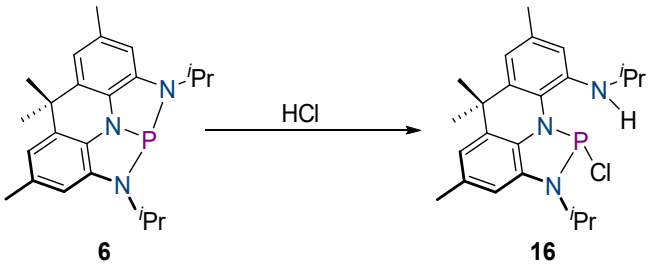
The addition of catecholborane (HBCat) to **6** results in the immediate generation of a colourless solution. $^{31}P\{^{1}H\}$ NMR spectroscopy revealed the full consumption of the starting material, and the clean generation of two new signals at 67.1 and 61.8 ppm (1:0.6 ratio by integration). In the ^{31}P NMR spectrum these signals possess doublet-of-doublet multiplicity, with the larger coupling indicating the formation of a P–H bond; $^{1}J_{P–H}$ (Hz) = 135 (major); 148 (minor). The smaller coupling corresponds to a single ligand-based *iso*-propyl methine proton, with the multiplicity revealing that phosphorus remains bound to only one side-arm nitrogen; $^{3}J_{P–H}$ (Hz) = 11 (major); 12 (minor). Together, these data suggest that redox-neutral cooperative bond activation occurred across a side-arm P–N_{ligand} bond in **6** to give an isomeric mixture of secondary phosphine **15** (Scheme 2.15). This is corroborated in the ^{1}H and $^{1}H\{^{31}P\}$ NMR spectra, with the corresponding P–H protons located at 7.02 (1H, d, $^{1}J_{P–H}$ = 135 Hz) and 7.15 ppm (1H, d, $^{1}J_{P–H}$ = 148 Hz).



Scheme 2.15. Synthesis of an isomeric mixture of secondary phosphine **15**.

To probe whether the product of formal oxidative addition could be accessed, **15** was heated at 80 °C and monitored by $^{31}P\{^{1}H\}$ NMR spectroscopy. This resulted in significant decomposition over several days, predominantly towards phosphine **6** and PH_3, as revealed by a resonance at −242.1 ppm. No signals indicative of a phosphorus(V) species were observed, indicating that formal oxidative addition of HBCat is thermodynamically unfavoured. Despite numerous attempts, single crystals of either isomer could not be grown for structural authentication by X-ray diffraction. To isolate **15** in the solid-state, lyophilisation from a concentrated benzene solution was required as simply removing the reaction/extraction solvent *in vacuo* provided an oily residue. However, subjecting this solid to dynamic vacuum for any extended amount of time (>30 minutes) resulted in significant decomposition to generate phosphine **6** along with several unknown products.

Regarding the reactivity with protic E–H bonds, **6** was reacted with one equivalent of ethereal HCl. This resulted in the immediate generation of a colourless solution, and the clean formation of a single product evidenced by a $^{31}P\{^{1}H\}$ NMR signal at 130.6 ppm. This resonance is within the region expected of a phosphorus(III) compound derived from a geometrically constrained phosphine, with the observed lack of backbone symmetry in the ^{1}H NMR spectrum indicating redox-neutral, cooperative HCl addition across a side-arm P–N_{ligand} bond. A broad signal integrating to one proton was observed at 2.97 ppm in the ^{1}H NMR spectrum, corroborating the formation of a ligand N–H bond. These data confirm the formation of chlorophosphine **16** (74% isolated yield, Scheme 2.16), with SCXRD showing the chloride substituent projecting at an acute angle from the planar acridane unit in the solid-state (Figure 2.17); N2–P–Cl (°) = 97.0(5).



6 16

Scheme 2.16. Synthesis of chlorophosphine **16**.

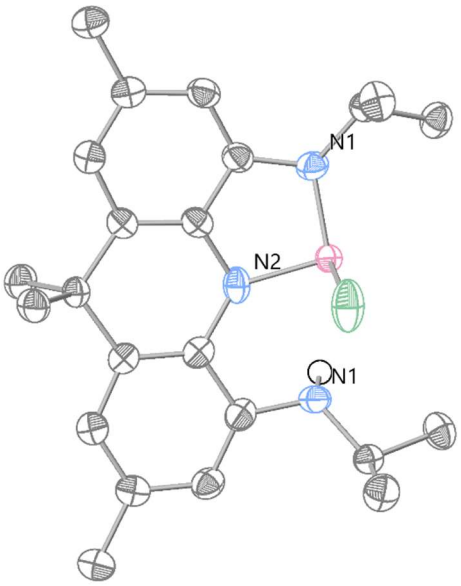
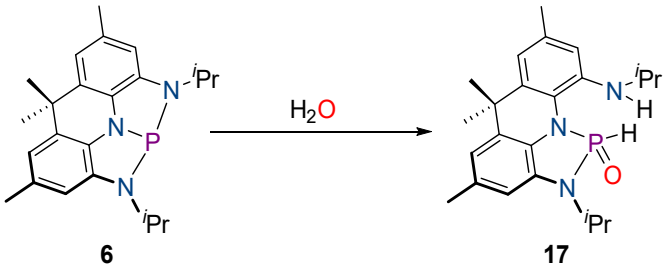


Figure 2.17. Solid-state structure of chlorophosphine **16**. Thermal ellipsoids pictured at 50% probability level. Hydrogen atoms (except for the one in the activated substate) and solvent of crystallisation removed for clarity.

Together, the formation of **15** and **16** from reagents of opposing E–H polarity, whereby the negatively charged fragment associates with the phosphorus centre of **6**, demonstrates the predominantly Lewis acidic character of phosphorus in such a T-shaped geometry. To further study the reactivity between **6** and protic reagents, water was chosen as a substate featuring two O–H bonds to assess whether phosphorus oxidation may enable multiple bond activation reactions. Adding either an excess, or one equivalent of water to **6** results in the immediate generation of a colourless solution and the appearance of a single new species in the $^{31}P\{^{1}H\}$ NMR spectrum at 1.3 ppm. This signal, within the region expected of a phosphorus(V) centre, is split into a doublet of doublets in the ^{31}P spectrum, with coupling constants $^{1}J_{P–H} = 715$ Hz and $^{3}J_{P–H} = 18$ Hz. The larger of these values indicates the formation of a P–H bond, while the smaller reveals that only one P–N bond persists. The ^{1}H NMR spectrum reveals signals

for a fully desymmetrised acridane backbone, along with new proton signals at 9.42 (1H, d, $^{1}J_{P-H}$ = 714 Hz) and 3.85 ppm (1H, s) corresponding to newly formed P–H and N–H bonds, respectively. SCXRD reveals a P=O double bond (1.4827(13) Å), thus confirming the formation of secondary phosphine oxide **17** (79% isolated yield, Scheme 2.17, Figure 2.18).



6 **17**

Figure 2.17. Synthesis of secondary phosphine oxide **17**.

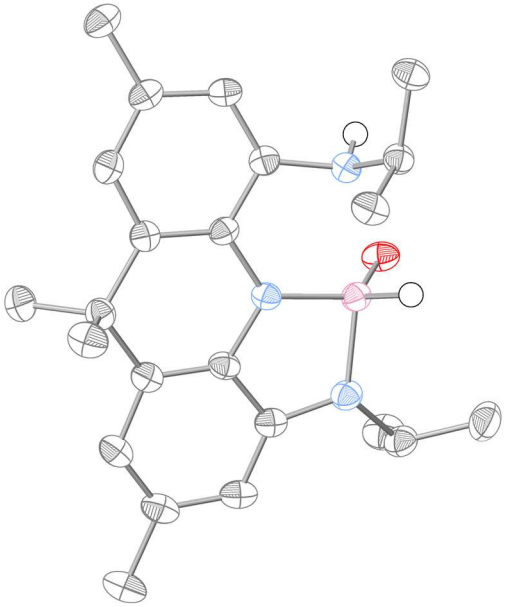
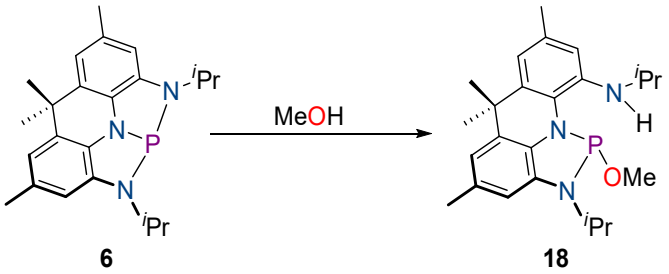


Figure 2.18. Solid-state structure of secondary phosphine oxide **17**. Thermal ellipsoids pictured at 50% probability level. Hydrogen atoms (except for those in the activated substrate) and solvent of crystallisation removed for clarity.

Performing this reaction with D_2O provided a signal in the $^{31}P\{^{1}H\}$ NMR spectrum at the same chemical shift as **17** but with triplet multiplicity ($^{1}J_{P-D}$ = 110 Hz), and led to the disappearance of the signals previously assigned to the product P–H and N–H bonds. Based on the mounting evidence of a predominantly electrophilic phosphorus centre in **6**, it was postulated that initial Lewis adduct formation between the Lewis acidic phosphorus centre and the Lewis basic oxygen atom in water occurred, resulting in an acidified O–H bond which undergoes deprotonation by a flanking side-arm nitrogen.

The resulting phosphinous acid (i.e. the intermediate P^{III}–OH containing species) tautomerises to provide **17**; a process known to occur for electronically unstabilised secondary phosphine oxides.[33–38] To further substantiate this claim, a substate containing only one O–H bond was chosen to assess whether the proposed phosphorus(III) intermediate is isolable if tautomerisation cannot occur. To this end, methanol (one equivalent) was added to **6**, resulting in full conversion to a single product with a $^{31}P\{^{1}H\}$ NMR signal at 97.3 ppm. ^{1}H NMR spectroscopy confirmed that O–H addition occurred across a P–N_{ligand} bond in **6** to yield phosphine alkoxide **18** (74% isolated yield, Scheme 2.18), revealed through desymmetrised acridane backbone signals, and the presence of a methyl signal displaying coupling to phosphorus at 2.81 ppm (d, $^{3}J_{P–H}$ = 7.4 Hz). SCXRD corroborates this assignment and reveals the formation of a new single P–O bond (Figure 2.19); P–O (Å) = 1.629(4).[41]



6 **18**

Scheme 2.18. Synthesis of phosphine alkoxide **18**.

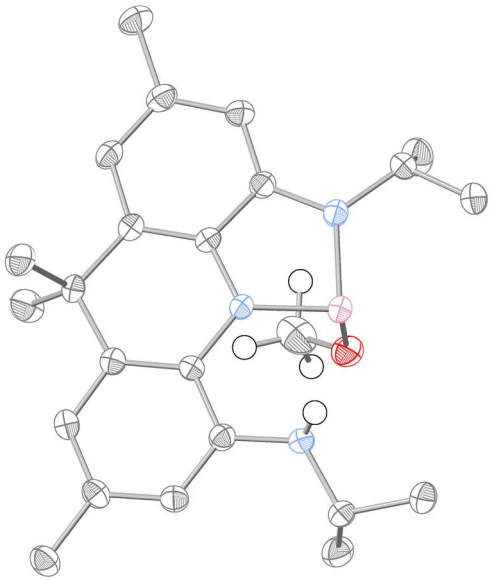


Figure 2.19. Solid-state structure of phosphine alkoxide **18**. Thermal ellipsoids pictured at 50% probability level. Hydrogen atoms (except for those in the activated substate) removed for clarity.

2.4 Conclusions

Through steric tuning of an acridane derived NNN-pincer ligand, a stable T-shaped phosphine (**6**) was synthesised and its reactivity studied. **6** underwent facile reaction with the nucleophilic reagent potassium *tert*-butoxide. By contrast, more forcing conditions were required for reaction with the electrophile methyl triflate. Together these reactions demonstrated the pronounced electron acceptor properties, and diminished nucleophilicity, of such geometrically constrained phosphines. Oxidised derivatives of **6** were synthesised through reaction with chalcogens or azides, and displayed a heavily distorted, or bent, structure to accommodate the phosphorus(V) centre. Finally, the reactivity of **6** towards hydridic and protic E–H bonds was evaluated, proceeding in a redox neutral fashion with the cooperative involvement of a ligand-derived nitrogen atom, and the association of the negatively charged substrate fragment at the phosphorus centre in each case. Sequential O–H bond scission was observed for water, proceeding first *via* cooperative addition, then phosphorus oxidation, towards the full disassembly of the substate into its constituent atoms.

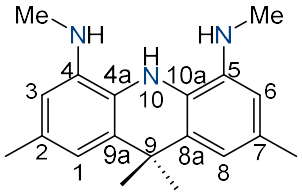
The work in this chapter has been published in *Chemistry – A European Journal*:

A. J. King, J. Abbenseth, J. M. Goicoechea, *Chem. Eur. J.* **2023**, 29, e202300818.[39]

J. Abbenseth contributed experimentally to the work in section 2.2.1.

2.5 Experimental section

2.5.1 Synthesis of 1^{Me}



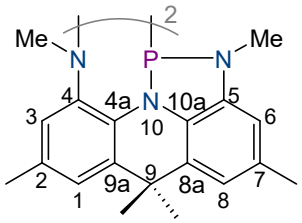
2,7,9,9-Tetramethyl-9,10-dihydro-4,5-dinitroacridine (663 mg, 2.0 mmol, 1.0 eq.) and palladium on carbon (108 mg, 0.10 mmol palladium, 10.0 wt% palladium, 5.0 mol% palladium) were added to a gas-tight ampoule and suspended in ethyl acetate (20 mL). The suspension was freeze-pump-thaw degassed four times, then refilled with dihydrogen gas (1 atm, excess) and stirred at 50 °C for 18 hours. The mixture was cooled to room temperature and the solvent removed *in vacuo*. The residue was extracted into methanol (3 × 10 mL) and filtered. The mixture was cooled to 0 °C then paraformaldehyde (608 mg, 20.6 mmol, 10.0 eq.) added, followed by sodium methoxide (25 w% in methanol, 1.85 mL, 8.1 mmol, 4.0 eq.). The mixture was warmed to reflux and stirred for 1 hour. The mixture was then cooled to 0 °C and sodium borohydride (843 mg, 22.3 mmol, 11 eq.) added in three portions over the course of 15 minutes. The mixture was warmed to reflux and stirred for 2 hours, then cooled to room temperature and the solvent removed *in vacuo*. The residue was extracted into benzene (3 × 10 mL) and filtered. Lyophilisation from a concentrated benzene solution afforded **1^{Me}** (474 mg, 1.61 mmol, 79%) as a white powder.

^{1}H NMR (600 MHz, C_6D_6): δ (ppm) 6.94 (2H, s, $C_{1/8}H$), 6.46 (2H, s, $C_{3/6}H$), 5.69 (1H, br s, $N_{10}H$), 2.55 (2H, br m, $C_{4/5}NH$), 2.46 (6H, d, $^{3}J_{H–H}$ = 5.5 Hz, N–CH_3), 2.36 (6H, s, $C_{2/7}(CH_3)$), 1.73 (6H, s, $C_9(CH_3)_2$).

^{13}C{^{1}H} NMR (151 MHz, C_6D_6): δ (ppm) 136.3 (s, $C_{4/5}$), 129.7 (s, $C_{2/7}$), 129.2 (s, $C_{8a/9a}$), 126.7 (s, $C_{4a/10a}$), 117.5 (s, $C_{1/8}$), 111.3 (s, $C_{3/6}$), 36.2 (s, C_9), 31.9 (s, $C_9(CH_3)_2$), 31.1 (s, $C_{4/5}N(CH_3)$), 21.5 (s, $C_{2/7}(CH_3)$).

HRMS (ESI) *m/z* calcd. for $C_{19}H_{25}N_3$+H^+: 296.2121 $[M+H]^+$; found: 296.2116.

2.5.2 Synthesis of 2



1^{Me} (50 mg, 0.17 mmol, 1.0 eq.) was dissolved in dichloromethane (5 mL) and cooled to −78 °C. Phosphorus trichloride (0.57 M in hexane, 0.30 mL, 0.17 mmol, 1.0 eq.) was added, followed by triethylamine (83 µL, 0.59 mmol, 3.5 eq.). The mixture was gradually warmed to room temperature and stirred for 16 hours, resulting in the generation of a pale-yellow solution and off-white precipitate. The solution was then filtered and the precipitate extracted with dichloromethane (3 × 2 mL). The solvent was removed from the combined extracts *in vacuo* and the resulting residue washed with acetonitrile (3 × 2 mL) at −30 °C. The product was dried under vacuum, providing **2** as a white powder (26 mg, 41 µmol, 49%).

^{1}H NMR (600 MHz, C_6D_6): δ (ppm) 7.19 (1H, s, C_1H), 6.85 (1H, s, C_3H), 6.72 (1H, s, C_8H), 6.26 (1H, s, C_6H), 2.79 (6H, d, $^{3}J_{P–H}$ = 8.0 Hz, $C_5N(CH_3)$), 2.63 (6H, d, $^{3}J_{P–H}$ = 1.3 Hz, $C_4N(CH_3)$), 2.41 (6H, s, $C_7(CH_3)$), 2.24 (6H, s, $C_2(CH_3)$), 1.78 (6H, s, $C_9(CH_3)$), 1.65 (6H, s, $C_9(CH_3)$).

^{1}H{^{31}P} NMR (500 MHz, C_6D_6): as above, except δ (ppm) 2.79 (6H, s, $C_5N(CH_3)$), 2.63 (6H, s, $C_4N(CH_3)$).

^{13}C{^{1}H} NMR (151 MHz, C_6D_6): δ (ppm) 139.2 (d, $^{2}J_{C–P}$ = 7.9 Hz, C_5), 133.8 (dd, $^{2}J_{C–P}$ = 5.2 Hz, $^{3}J_{C–P}$ = 2.7 Hz, C_{4a}), 133.2 (m, C_{Ar})*, 131.0 (s, C_7), 129.9 (d, $^{4}J_{C–P}$ = 2.5 Hz, C_2), 129.2 (d, $^{2}J_{C–P}$ = 8.2 Hz, C_{10a}), 127.5 (d, $^{3}J_{C–P}$ = 7.0 Hz, C_3), 126.3 (d, $^{4}J_{C–P}$ = 2.6 Hz, C_1), 126.2 (s, C_{Ar})*, 115.3 (s, C_8)**, 105.4 (s, C_6)**, 36.8 (s, C_9), 36.6 (s, $C_9(CH_3)$), 34.7 (dd, $^{5TS}J_{C–P}$ = 5.5 Hz, $^{2}J_{C–P}$ = 13.7 Hz, $C_4N(CH_3)$)***, 32.1 (d, $^{2}J_{C–P}$ = 32.2 Hz, $C_5N(CH_3)$), 31.9 (s, $C_9(CH_3)$), 22.1 (s, $C_7(CH_3)$), 21.0 (s, $C_2(CH_3)$).

* C_{8a} and C_{9a} environments could not be distinguished. This is due to the observation of a ^{1}H-^{13}C HMBC cross-peak between each of these and both $C_9(CH_3)$ signals.

** Assigned by comparison to **15**, **16** and **17**.

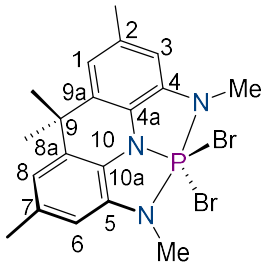
*** TS = through space coupling to phosphorus in close proximity.[40]

^{31}P NMR (243 MHz, C_6D_6): δ (ppm) 112.1 ppm (m, $^{3}J_{P–H}$ = 8.0 Hz).

^{31}P{^{1}H} NMR (162 MHz, C_6D_6): δ (ppm) 112.1 ppm (s).

Elemental analysis calcd. (%) for $C_{38}H_{44}N_6P_2$: C 70.57, H 6.86, N 12.99; found: C 70.63, H 7.01, N 11.45. The value for nitrogen is outside the accepted range – this was a recurring issue for several compounds which may indicate an instrument error.

2.5.3 Synthesis of 3



Phosphorus pentabromide (73 mg, 0.17 mmol, 1.0 eq.) was dissolved in toluene (10 mL) and cooled to −78 °C. Triethylamine (71 µL, 0.51 mmol, 3.0 eq.) was added. A solution of **1^{Me}** (50 mg, 0.17 mmol, 1.0 eq.) in toluene (10 mL) was also cooled to −78 °C and added dropwise to the phosphorus pentabromide solution. The mixture was gradually warmed to room-temperature and stirred for 16 hours, resulting in the generation of an orange solution and off-white precipitate. The solution was then filtered and the precipitate extracted with toluene (3 × 5 mL). The solvent was removed *in vacuo* and the residue dissolved in hexane and cooled to −30 °C for 5 days resulting in the generation of orange solid (an unknown impurity). The solution was then filtered and the solvent removed *in vacuo*. Lyophilisation from a concentrated benzene solution provides **3** as an orange powder (52.0 mg, 0.11 mmol, 64%).

^{1}H NMR (600 MHz, C_6D_6): δ (ppm) 6.67 (2H, s, $C_{1/8}H$), 6.12 (2H, s, $C_{3/6}H$), 2.95 (6H, d, $^{3}J_{P–H}$ = 21.1 Hz, $C_{4/5}N(CH_3)$), 2.26 (6H, s, $C_{2/7}(CH_3)$), 1.51 (6H, s, $C_9(CH_3)_2$).

^{1}H{^{31}P} NMR (500 MHz, C_6D_6): as above, expect δ (ppm) 2.95 (6H, s, $C_{4/5}N(CH_3)$).

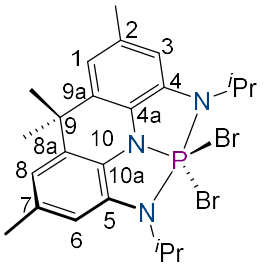
$^{13}C\{^{1}H\}$ NMR (151 MHz, C_6D_6): δ (ppm) 135.1 (d, $^{2}J_{C–P}$ = 12.2 Hz, $C_{4/5}$), 133.6 (s, $C_{2/7}$), 129.7 (d, $^{3}J_{C–P}$ = 9.2 Hz, $C_{8a/9a}$), 116.5 (d, $^{4}J_{C–P}$ = 1.8 Hz, $C_{1/8}$), 116.1 (d, $^{2}J_{C–P}$ = 13.4 Hz, $C_{4a/10a}$), 105.4 (d, $^{3}J_{C–P}$ = 7.6 Hz, $C_{3/6}$), 36.9 (d, $^{4}J_{C–P}$ = 1.7 Hz, C_9), 32.6 (s, $C_9(CH_3)_2$), 31.5 (d, $^{2}J_{C–P}$ = 5.5 Hz, $C_{4/5}N(CH_3)$), 22.6 (s, $C_{2/7}(CH_3)$).

^{31}P NMR (243 MHz, C_6D_6): δ (ppm) −107.5 (sept, $^{3}J_{P–H}$ = 21.1 Hz).

$^{31}P\{^{1}H\}$ NMR (162 MHz, C_6D_6): δ (ppm) −107.6 (s).

Elemental analysis calcd. (%) for $C_{19}H_{22}Br_2N_3P$: C 47.23, H 4.59, N 8.70; found: C 47.32, H 4.94, N 8.03. The value for nitrogen is outside the accepted range – this was a recurring issue for several compounds which may indicate an instrument error.

2.5.4 Synthesis of 5



A solution of phosphorous pentabromide (366 mg, 0.85 mmol, 1.0 eq.) in toluene (10 mL) was cooled to −78 °C. Triethylamine (0.60 mL, 4.27 mmol, 5.0 eq.) was added, followed by the addition of a −78 °C solution of **1**^{iPr} (300 mg, 0.85 mmol, 1.0 eq.) in toluene (10 mL). The resulting bright green solution was gradually warmed to room temperature and stirred for 16 hours, over which the solution turned dark brown along with the precipitation of a light-brown solid. The mixture was filtered and the precipitate extracted with toluene (3 × 5 mL). The solvent was removed *in vacuo* providing an orange-brown residue, which was then washed with diethyl ether (3 × 5 mL) at −78 °C. The resulting bright orange powder was dried *in vacuo* to provide **5** (250 mg, 0.46 mmol, 54%).

^{1}H NMR (500 MHz, C_6D_6): δ (ppm) 6.64 (2H, s, $C_{1/8}H$), 6.62 (2H, s, $C_{3/6}H$), 4.74 (2H, d-sept, $^{3}J_{P–H}$ = 27.3 Hz, $^{3}J_{H–H}$ = 6.9 Hz, $C_{4/5}NCH(CH_3)_2$), 2.26 (6H, s, $C_{2/7}(CH_3)$), 1.53 (12H, d, $^{3}J_{H–H}$ = 6.9 Hz, $C_{4/5}NCH(CH_3)_2$), 1.52 (6H, s, $C_9(CH_3)_2$).

$^{1}H\{^{31}P\}$ NMR (500 MHz, C_6D_6): as above, except δ (ppm) 4.74 (2H, sept, $^{3}J_{H-H}$ = 6.9 Hz, $C_{4/5}NCH(CH_3)_2$).

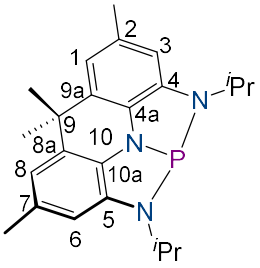
$^{13}C\{^{1}H\}$ NMR (151 MHz, C_6D_6): δ (ppm) 133.0 (d, $^{4}J_{C-P}$ = 1.7 Hz, $C_{2/7}$), 132.7 (d, $^{2}J_{C-P}$ = 13.7 Hz, $C_{4/5}$), 130.4 (d, $^{3}J_{C-P}$ = 9.4 Hz, $C_{8a/9a}$), 116.7 (d, $^{2}J_{C-P}$ = 14.3 Hz, $C_{4a/10a}$), 115.8 (m, $C_{1/8}$), 107.9 (d, $^{3}J_{C-P}$ = 9.9 Hz, $C_{3/6}$), 46.7 (d, $^{2}J_{C-P}$ = 6.0 Hz, $C_{4/5}NCH(CH_3)_2$), 36.7 (d, $^{4}J_{C-P}$ = 1.8 Hz, C_9), 33.0 (s, $C_9(CH_3)_2$), 22.7 (s, $C_{2/7}(CH_3)$), 19.0 (d, $^{3}J_{C-P}$ = 6.5 Hz, $C_{4/5}NCH(CH_3)_2$).

^{31}P NMR (202 MHz, C_6D_6): δ (ppm) −120.1 (t, $^{3}J_{P-H}$ = 27.3 Hz).

$^{31}P\{^{1}H\}$ NMR (162 MHz, C_6D_6): δ (ppm) −120.1 (s).

Elemental analysis calcd. (%) for $C_{23}H_{30}Br_2N_3P$: C 51.22, H 5.61, N 7.79; found: C 51.08, H 5.26, N 7.41.

2.5.5 Synthesis of 6



5 (200 mg, 0.37 mmol, 1.0 eq.) was dissolved in toluene (10 mL). A solution of trimethyl-phosphine (0.19 mL, 1.85 mmol, 5.0 eq.) in toluene (1 mL) was added and the mixture stirred for 15 minutes, resulting in the generation of a bright orange solution and off-white precipitate. The solution was filtered and the precipitate extracted with toluene (3 × 5 mL). The solvent was removed *in vacuo*. Lyophilisation from a concentrated benzene solution provided **6** as an orange powder (127 mg, 0.34 mmol, 90%).

Alternate procedure: **5** (100 mg, 0.19 mmol, 1.0 eq.) and magnesium powder (92 mg, 3.71 mmol, 20.0 eq.) were dissolved in tetrahydrofuran (5 mL) and stirred at room temperature for 15 minutes. The solvent was removed *in vacuo* and the product extracted into pentane (3 × 2 mL) and filtered. The solvent is removed *in vacuo* from the combined extracts. Lyophilisation from a concentrated benzene solution provided **6** as an orange powder (63.0 mg, 0.17 mmol, 90%).

^{1}H NMR (500 MHz, C_6D_6): δ (ppm) 6.86 (2H, s, $C_{1/8}H$), 6.79 (2H, s, $C_{3/6}H$), 4.42 (2H, apparent sept, $^{3}J_{H–H}$ = 6.9 Hz, $C_{4/5}NCH(CH_3)_2$)*, 2.37 (6H, s, $C_{2/7}(CH_3)$), 1.72 (6H, s, $C_9(CH_3)_2$), 1.52 (12H, d, $^{3}J_{H–H}$ = 6.9 Hz, $C_{4/5}NCH(CH_3)_2$).

* Coupling to phosphorus was not observed.

^{1}H{^{31}P} NMR (500 MHz, C_6D_6): as above.

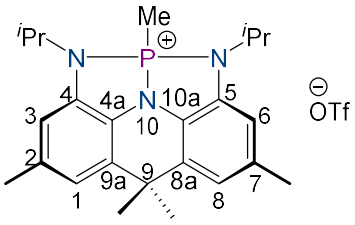
^{13}C{^{1}H} NMR (151 MHz, C_6D_6): δ (ppm) 135.9 (d, $^{2}J_{C–P}$ = 12.6 Hz, $C_{4/5}$), 133.5 (d, $^{3}J_{C–P}$ = 4.6 Hz, $C_{8a/9a}$), 133.4 (s, $C_{2/7}$), 130.5 (d, $^{2}J_{C–P}$ = 11.2 Hz, $C_{4a/10a}$), 115.7 (s, $C_{1/8}$), 109.1 (s, $C_{3/6}$), 45.1 (d, $^{2}J_{C–P}$ = 20.9 Hz, $C_{4/5}NCH(CH_3)_2$), 38.3 (s, C_9), 31.3 (s, $C_9(CH_3)_2$), 23.6 (d, $^{3}J_{C–P}$ = 6.4 Hz, $C_{4/5}NCH(CH_3)_2$), 22.6 (s, $C_{2/7}(CH_3)$).

^{31}P NMR (202 MHz, C_6D_6): δ (ppm) 145.0 (br s).

^{31}P{^{1}H} NMR (162 MHz, C_6D_6): δ (ppm) 145.0 (br s).

Elemental analysis calcd. (%) for $C_{23}H_{30}N_3P$: C 72.80, H 7.97, N 11.07; found: C 72.35, H 7.79, N 10.21. The value for nitrogen is outside the accepted range – this was a recurring issue for several compounds which may indicate an instrument error.

2.5.6 Synthesis of 7[OTf]



6 (10 mg, 26.4 µmol, 1.0 eq.) was dissolved in benzene (0.5 mL). Methyl triflate (2.9 µL, 26.4 µmol, 1.0 eq.) was added and the solution heated to 80 °C for 3 hours. Yellow needle-like crystals formed over the course of the reaction. The mixture was cooled gradually to room temperature and left for 16 hours. The crystals were filtered, washed with benzene (3 × 0.5 mL) and dried *in vacuo* to yield **7**[OTf] (7.5 mg, 13.8 µmol, 52%).

^{1}H NMR (500 MHz, CD_2Cl_2): δ (ppm) 6.88 (2H, s, $C_{1/8}H$), 6.81 (2H, s, $C_{3/6}H$), 4.55 (2H, d-sept, $^{3}J_{P–H}$ = 11.6 Hz, $^{3}J_{H–H}$ = 6.9 Hz, $C_{4/5}NCH(CH_3)_2$), 3.13 (3H, d, $^{2}J_{P–H}$ = 15.6 Hz, P–CH_3), 2.38 (6H, s, $C_{2/7}(CH_3)$), 1.82 (3H, s, $C_9(CH_3)$), 1.70 (6H, d, $^{3}J_{H–H}$ = 7.0 Hz, $C_{4/5}NCH(CH_3)$), 1.64 (3H, s, $C_9(CH_3)$), 1.58 (6H, d, $^{3}J_{H–H}$ = 6.8 Hz, $C_{4/5}NCH(CH_3)$).

^{1}H{^{31}P} NMR (500 MHz, CD_2Cl_2): as above, except δ (ppm) 4.55 (2H, sept, $^{3}J_{H–H}$ = 6.8 Hz, $C_{4/5}NCH(CH_3)_2$), 3.13 (3H, s, P–CH_3).

^{13}C{^{1}H} NMR (151 MHz, CD_2Cl_2): δ (ppm) 137.0 (s, $C_{4a/10a}$), 136.4 (d, $^{3}J_{C–P}$ = 10.4 Hz, $C_{8a/9a}$), 133.0 (d, $^{4}J_{C–P}$ = 3.0 Hz, $C_{2/7}$), 131.4 (d, $^{2}J_{C–P}$ = 15.7 Hz, $C_{4/5}$), 119.4 (d, $^{4}J_{C–P}$ = 1.8 Hz, $C_{1/8}$), 113.0 (d, $^{3}J_{C–P}$ = 9.1 Hz, $C_{3/6}$), 47.9 (d, $^{2}J_{C–P}$ = 4.1 Hz, $C_{4/5}NCH(CH_3)_2$), 40.5 (s, C_9), 26.9 (s, $C_9(CH_3)$), 22.5 (s, $C_9(CH_3)$), 22.2 (s, $C_{2/7}(CH_3)$), 21.6 (s, $C_{4/5}NCH(CH_3)$), 21.1 (d, $^{3}J_{C–P}$ = 5.8 Hz, $C_{4/5}NCH(CH_3)$), 16.0 (d, $^{1}J_{C–P}$ = 125.1 Hz, P–CH_3).

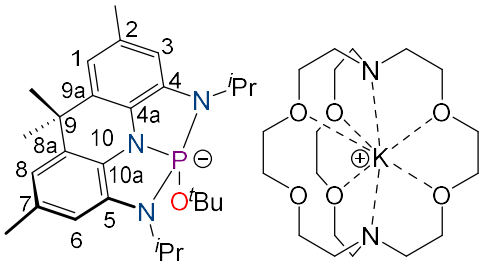
^{31}P NMR (243 MHz, CD_2Cl_2): δ (ppm) 80.5 (qt, $^{2}J_{P–H}$ = 15.4 Hz, $^{3}J_{P–H}$ = 11.6 Hz).

^{31}P{^{1}H} NMR (243 MHz, CD_2Cl_2): δ (ppm) 80.5 (s).

^{19}F{^{1}H} NMR (470 MHz, CD_2Cl_2): δ (ppm) 78.9 (s, $S(O)_3(CF_3)^-$).

Elemental analysis calcd. (%) for $C_{25}H_{33}F_3N_3O_3PS$: C 55.24, H 6.12, N 7.73; found: C 55.81, H 6.07, N 7.59.

2.5.7 Synthesis of [K(2,2,2-crypt)]8



Potassium *tert*-butoxide (3.1 mg, 27.8 µmol, 1.0 eq.) and 4,7,13,16,21,24-hexaoxa-1,10-diazabicyclo[8.8.8]hexacosane (10.5 mg, 27.8 µmol, 1.0 eq.) were dissolved in diethyl ether (0.5 mL). The resulting solution was added to **6** (10.5 mg, 27.8 µmol, 1.0 eq) producing a yellow solution. The

solution was filtered and half of the solvent is removed *in vacuo*. Crystallisation from this concentrated diethyl ether at room temperature yielded [K(2,2,2-crypt)]**8** (11.0 mg, 12.7 µmol, 46%) as yellow crystals.

^{1}H NMR (500 MHz, d_8-THF): δ (ppm) 5.82 (2H, s, $C_{1/8}H$), 5.57 (2H, s, $C_{3/6}H$), 3.70 (2H, apparent sept, $^{3}J_{H–H}$ = 6.6 Hz, $C_{4/5}NCH(CH_3)_2$)*, 3.37 (14H, s, CH^{crypt}), 3.32 (14H, t, $^{3}J_{H–H}$ = 4.6 Hz, CH^{crypt}), 2.36 (14H, t, $^{3}J_{H–H}$ = 4.6 Hz, CH^{crypt}), 2.11 (6H, s, $C_{2/7}(CH_3)$), 1.60 (3H, s, $C_9(CH_3)$), 1.50 (3H, s, $C_9(CH_3)$), 1.41 (6H, d, $^{3}J_{H–H}$ = 6.7 Hz, $C_{4/5}NCH(CH_3)$), 1.35 (6H, d, $^{3}J_{H–H}$ = 6.7 Hz, $C_{4/5}NCH(CH_3)$), 0.90 (9H, s, P–$OC(CH_3)_3$).

* Coupling to phosphorus was not observed

^{1}H{^{31}P} NMR (500 MHz, d_8-THF): as above.

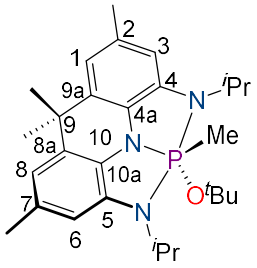
^{13}C{^{1}H} NMR (151 MHz, d_8-THF): δ (ppm) 142.3 (d, $^{2}J_{C–P}$ = 13.2 Hz, C_4), 128.0 (s, $C_{4a/10a}$),127.9 (s, $C_{2/7}$), 125.3 (s, $C_{8a/9a}$), 107.0 (s, $C_{1/8}$H), 100.8 (d, $^{3}J_{C–P}$ = 2.8 Hz, $C_{3/6}$H), 73.0 (d, $^{2}J_{C–P}$ = 21.6 Hz, P–$OC(CH_3)_3$), 71.3 (s, C^{crypt}), 68.5 (s, C^{crypt}), 54.8 (s, C^{crypt}), 46.8 (d, $^{2}J_{C–P}$ = 8.3 Hz, $C_{4/5}NCH(CH_3)_2$), 36.8 (m, C_9), 36.8 (s, $C_9(CH_3)$), 33.7 (m, $C_9(CH_3)$), 32.1 (d, $^{2}J_{C–P}$ = 4.1 Hz, P–$OC(CH_3)_3$), 23.1 (s, $C_{2/7}(CH_3)$), 23.0 (d, $^{3}J_{C–P}$ = 3.3 Hz, $C_{4/5}NCH(CH_3)$), 22.9 (d, $^{3}J_{C–P}$ = 6.1 Hz, $C_{4/5}NCH(CH_3)$).

^{31}P NMR (243 MHz, d_8-THF): δ (ppm) 50.2 (s).

^{31}P{^{1}H} NMR (162 MHz, d_8-THF): δ (ppm) 50.0 (s).

Elemental analysis calcd. (%) for $C_{45}H_{75}K_1N_5O_7P$: C 62.26, H 8.71, N 8.07; found: C 61.81, H 8.77, N 7.52.

2.5.8 Synthesis of 9



Potassium *tert*-butoxide (3.1 mg, 27.8 µmol, 1.0 eq.) was suspended in diethyl ether (0.5 mL) then added to **6** (10.5 mg, 27.8 µmol, 1.0 eq.) resulting in a yellow solution. The solvent was removed *in vacuo* and a solution of methyl triflate (3.0 µL, 27.8 µmol, 1.0 eq.) in benzene (0.5 mL) added, producing a colourless solution. The solvent was removed *in vacuo* and the product extracted into pentane (3 × 0.5 mL). The solvent was removed, then yellow crystals of **9** grown from a concentrated hexane solution at −30 °C (5.0 mg, 10.7 µmol, 38%).

^{1}H NMR (600 MHz, C_6D_6): δ (ppm) 6.64 (2H, s, $C_{1/8}H$), 6.46 (2H, s, $C_{3/6}H$), 3.75 (2H, apparent oct, $^{3}J_{P–H}$ = 6.7 Hz, $^{3}J_{H–H}$ = 6.7 Hz, $C_{4/5}NCH(CH_3)_2$), 2.43 (6H, s, $C_{2/7}(CH_3)$), 1.83 (3H, s, $C_9(CH_3)$), 1.81 (3H, s, $C_9(CH_3)$), 1.63 (3H, d, $^{2}J_{P–H}$ = 16.6 Hz, P–CH_3), 1.46 (6H, d, $^{3}J_{H–H}$ = 6.7 Hz, $C_{4/5}NCH(CH_3)$), 1.35 (6H, d, $^{3}J_{H–H}$ = 6.8 Hz, $C_{4/5}NCH(CH_3)$), 1.04 (9H, s, P–$OC(CH_3)_3$).

^{1}H{^{31}P} NMR (600 MHz, C_6D_6): as above, except δ (ppm) 3.75 (2H, sept, $^{3}J_{H–H}$ = 6.7 Hz, $C_{4/5}NCH(CH_3)_2$), 1.63 (3H, s, P–CH_3).

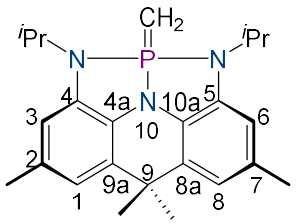
^{13}C{^{1}H} NMR (151 MHz, C_6D_6): δ (ppm) 135.2 (d, $^{2}J_{C–P}$ = 8.7 Hz, $C_{4/5}$), 131.6 (s, $C_{2/7}$), 128.6 (s, $C_{8a/9a}$), 118.9 (d, $^{2}J_{C–P}$ = 12.7 Hz, $C_{4a/10a}$), 112.1 (s, $C_{1/8}$), 105.7 (d, $^{3}J_{C–P}$ = 4.4 Hz, $C_{3/6}$), 80.0 (d, $^{2}J_{C–P}$ = 11.2 Hz, P–$OC(CH_3)_3$), 45.9 (d, $^{2}J_{C–P}$ = 2.6 Hz, $C_{4/5}NCH(CH_3)_2$), 36.4 (m, C_9), 35.2 (s, $C_9(CH_3)$), 32.8 (s, $C_9(CH_3)$), 30.5 (d, $^{3}J_{C–P}$ = 5.9 Hz, P–$OC(CH_3)_3$), 25.8 (d, $^{1}J_{C–P}$ = 179.4 Hz, P–CH_3), 23.0 (s, $C_{2/7}(CH_3)$), 20.6 (d, $^{3}J_{C–P}$ = 2.2 Hz, $C_{4/5}NCH(CH_3)$), 20.5 (s, $C_{4/5}NCH(CH_3)$).

^{31}P NMR (243 MHz, C_6D_6): δ (ppm) −39.4 (m).

^{31}P{^{1}H} NMR (162 MHz, C_6D_6): δ (ppm) −39.4 (s).

Elemental analysis calcd. (%) for $C_{28}H_{42}N_3OP$: C 71.92, H 9.05, N 8.99; found: C 72.20, H 9.46, N 8.47.

2.5.9 Synthesis of 10



6 (10.5 mg, 27.8 µmol, 1.0 eq.) was dissolved in benzene (0.5 mL). Methyl triflate (3.0 µL, 27.8 µmol, 1.0 eq.) was added and the solution heated at 80 °C for 3 hours. The solvent was removed *in vacuo* and the residues dissolved in a solution of potassium *tert*-butoxide (3.1 mg, 27.8 µmol, 1.0 eq.) in tetrahydrofuran (0.5 mL), resulting in a colourless solution. The solvent was removed *in vacuo* and the product extracted into hexane (2 × 0.5 mL). Colourless crystals of **10** (7.6 mg, 19.3 µmol, 69%) were grown from a concentrated hexane solution at −30 °C.

^{1}H NMR (600 MHz, C_6D_6): δ (ppm) 6.63 (2H, s, $C_{1/8}H$), 6.47 (2H, s, $C_{3/6}H$), 4.23 (2H, d-sept, $^3J_{P–H}$ = 11.4 Hz, $^3J_{H–H}$ = 7.0 Hz, $C_{4/5}NCH(CH_3)_2$), 2.26 (6H, s, $C_{2/7}(CH_3)$), 1.65 (3H, s, $C_9(CH_3)$), 1.59 (3H, s, $C_9(CH_3)$), 1.40 (6H, d, $^3J_{H–H}$ = 7.0 Hz, $C_{4/5}NCH(CH_3)$), 1.20 (2H, d, $^2J_{P–H}$ = 18.5 Hz, P–(CH_2)), 1.19 (6H, d, $^3J_{H–H}$ = 7.1 Hz, $C_{4/5}NCH(CH_3)$).

^{1}H{^{31}P} NMR (600 MHz, C_6D_6): as above, except δ (ppm) 4.23 (2H, sept, $^3J_{H–H}$ = 7.0 Hz, $C_{4/5}NCH(CH_3)_2$), 1.20 (2H, s, P–(CH_2)).

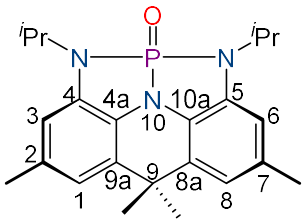
^{13}C{^{1}H} NMR (151 MHz, C_6D_6): δ (ppm) 133.8 (d, $^2J_{C–P}$ = 4.1 Hz, $C_{4a/10a}$), 133.1 (d, $^2J_{C–P}$ = 16.4 Hz, $C_{4/5}$), 132.9 (d, $^3J_{C–P}$ = 10.3 Hz, $C_{8a/9a}$), 132.4 (s, $C_{2/7}$), 115.6 (s, $C_{1/8}$), 109.8 (d, $^3J_{C–P}$ = 8.9 Hz, $C_{3/6}$), 47.1 (d, $^2J_{C–P}$ = 3.9 Hz, $C_{4/5}NCH(CH_3)_2$), 39.4 (s, C_9), 27.4 (s, $C_9(CH_3)$), 22.8 (s, $C_9(CH_3)$), 22.4 (s, $C_{2/7}(CH_3)$), 20.9 (s, $C_{4/5}NCH(CH_3)$), 20.5 (d, $^3J_{C–P}$ = 5.2 Hz, $C_{4/5}NCH(CH_3)$), 16.9 (d, $^1J_{C–P}$ = 240.1 Hz, P–(CH_2)).

^{31}P NMR (243 MHz, C_6D_6): δ (ppm) 61.2 (m).

$^{31}P\{^{1}H\}$ NMR (162 MHz, C_6D_6): δ (ppm) 61.2 (s).

Elemental analysis calcd. (%) for $C_{24}H_{32}N_3P$: C 73.25, H 8.20, N 10.68; found: C 73.63, H 8.40, N 10.16.

2.5.10 Synthesis of 11



6 (7.0 mg, 18.5 µmol, 1.0 eq.) was dissolved in tetrahydrofuran (0.5 mL), then freeze-pump-thaw degassed four times before being placed under an atmosphere of oxygen (1 atm., excess). The resulting dark red solution was heated at 60 °C for 16 hours. The solution was then cooled to room temperature and the solvent removed *in vacuo*. The residues were extracted with pentane (3 × 1 mL). Colourless crystals of **11** (4.0 mg, 10.1 µmol, 55%) were grown from a concentrated pentane solution at −30 °C.

Alternate procedure: **6** (10.5 mg, 27.8 µmol, 1.0 eq.) and pyridine-N-oxide (2.6 mg, 27.8 µmol, 1.0 eq.) were dissolved in benzene (0.5 mL) and stirred at room temperature for 2 hours. The solvent was removed *in vacuo* and the residue extracted into pentane (0.5 mL). Colourless crystals of **11** (6.3 mg, 15.9 µmol, 57%) were grown from a concentrated pentane solution at −30 °C.

^{1}H NMR (500 MHz, C_6D_6): δ (ppm) 6.56 (2H, s, $C_{1/8}H$), 6.32 (2H, s, $C_{3/6}H$), 3.98 (2H, d-sept, $^{3}J_{P-H}$ = 15.4 Hz, $^{3}J_{H-H}$ = 6.9 Hz, $C_{4/5}NCH(CH_3)_2$), 2.19 (6H, s, $C_{2/7}(CH_3)$), 1.59 (3H, s, $C_9(CH_3)$), 1.55 (3H, s, $C_9(CH_3)$), 1.48 (6H, d, $^{3}J_{H-H}$ = 6.8 Hz, $C_{4/5}NCH(CH_3)$), 1.35 (6H, d, $^{3}J_{H-H}$ = 6.8 Hz, $C_{4/5}NCH(CH_3)$).

$^{1}H\{^{31}P\}$ NMR (500 MHz, C_6D_6): as above, except δ (ppm) 3.98 (2H, sept, $^{3}J_{H-H}$ = 6.9 Hz, $C_{4/5}NCH(CH_3)_2$).

$^{13}C\{^{1}H\}$ NMR (151 MHz, C_6D_6): δ (ppm) 135.3 (s, C_{Ar}), 135.2 (d, J_{C-P} = 9.68 Hz, C_{Ar}), 133.9 (s, $C_{2/7}$), 133.2 (d, J_{C-P} = 8.8 Hz, C_{Ar}), 115.8 (s, $C_{1/8}$), 109.9 (d, $^{3}J_{C-P}$ = 10.5 Hz, $C_{3/6}$), 46.6 (d, $^{2}J_{C-P}$ = 3.5 Hz,

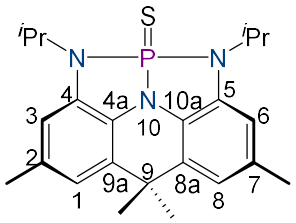
$C_{4/5}NCH(CH_3)_2$), 40.2 (m, C_9), 26.4 (s, $C_9(CH_3)$), 22.6 (s, $C_9(CH_3)$), 22.3 (s, $C_{2/7}(CH_3)$), 21.4 (d, $^3J_{C-P}$ = 1.1 Hz, $C_{4/5}NCH(CH_3)$), 20.8 (d, $^3J_{C-P}$ = 2.0 Hz, $C_{4/5}NCH(CH_3)$.

^{31}P NMR (202 MHz, C_6D_6): δ (ppm) 37.4 (t, $^3J_{P-H}$ = 15.4 Hz).

$^{31}P\{^1H\}$ NMR (162 MHz, C_6D_6): δ (ppm) 37.4 (s).

Elemental analysis calcd. (%) for $C_{23}H_{30}N_3O_1P$: C 69.85, H 7.65, N 10.63; found: C 69.19, H 7.61, N 10.09.

2.5.11 Synthesis of 12



11 (6.0 mg, 15.2 µmol, 1.0 eq.) and 2,4-bis(4-methoxyphenyl)-1,3,2,4-dithiadiphosphetane-2,4-disulfide (3.1 mg, 7.6 µmol, 0.5 eq.) were dissolved in toluene (0.5 mL) and heated at 110 °C for 16 hours. The solvent was removed *in vacuo* and the product extracted into hexane (0.5 mL). **12** was crystallised at −30 °C following concentration of this hexane solution by slow evaporation (6.0 mg, 14.6 µmol, 96%).

^{1}H NMR (500 MHz, C_6D_6): δ (ppm) 6.55 (2H, s, $C_{1/8}H$), 6.34 (2H, s, $C_{3/6}H$), 4.26 (2H, d-sept, $^3J_{P-H}$ = 15.0 Hz, $^3J_{H-H}$ = 7.1 Hz, $C_{4/5}NCH(CH_3)_2$), 2.17 (6H, s, $C_{2/7}CH_3$), 1.58 (3H, s, $C_9(CH_3)$), 1.56 (3H, s, $C_9(CH_3)$), 1.51 (6H, d, $^3J_{H-H}$ = 7.0 Hz, $C_{4/5}NCH(CH_3)$), 1.29 (6H, d, $^3J_{H-H}$ = 7.0 Hz, $C_{4/5}NCH(CH_3)$).

$^1H\{^{31}P\}$ NMR (500 MHz, C_6D_6): as above, except δ (ppm) 4.26 (2H, sept, $^3J_{H-H}$ = 7.0 Hz, $C_{4/5}NCH(CH_3)_2$).

$^{13}C\{^1H\}$ NMR (151 MHz, C_6D_6): δ (ppm) 135.4 (d, $^3J_{C-P}$ = 10.6 Hz, $C_{8a/9a}$), 134.5 (s, C_{Ar}), 134.4 (d, J_{C-P} = 12.6 Hz, C_{Ar}), 133.8 (s, $C_{2/7}$), 116.1 (s, $C_{1/8}$) 109.9 (s, $C_{3/6}$), 48.4 (d, $^2J_{C-P}$ = 5.9 Hz,

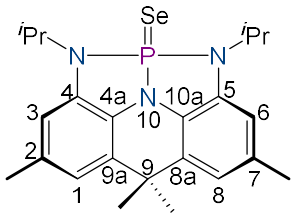
$C_{4/5}NCH(CH_3)_2$), 40.2 (s, C_9), 26.2 (s, $C_9(CH_3)$), 22.7 (s, $C_9(CH_3)$), 22.2 (s, $C_{2/7}(CH_3)$), 20.8 (d, $^3J_{C-P}$ = 1.6 Hz, $C_{4/5}NCH(CH_3)$), 20.1 (d, $^3J_{C-P}$ = 3.5 Hz, $C_{4/5}NCH(CH_3)$).

^{31}P NMR (202 MHz, C_6D_6): δ (ppm) 83.8 (t, $^3J_{P-H}$ = 15.0 Hz).

$^{31}P\{^1H\}$ NMR (162 MHz, C_6D_6): δ (ppm) 83.8 (s).

HRMS (ESI) *m/z* calcd. for $C_{23}H_{30}N_3PS+H^+$: 412.1971 $[M+H]^+$; found: 412.1964.

2.5.12 Synthesis of 13



6 (10.0 mg, 26.4 µmol, 1.0 eq.) and selenium powder (10.4 mg, 0.13 mmol, 5.0 eq.) were suspended in dichloromethane (0.5 mL) and stirred for 2.5 hours at room temperature. The solvent was removed *in vacuo* and the residue washed with hexane (0.5 mL). The product was extracted into tetrahydrofuran (0.3 mL), filtered, and crystals of **13** grown by vapour diffusion of pentane (2 mL) into this solution (6.5 mg, 14.2 µmol, 54%).

^{1}H NMR (500 MHz, C_6D_6): δ (ppm) 6.55 (2H, s, $C_{1/8}H$), 6.36 (2H, s, $C_{3/6}H$), 4.43 (2H, d-sept, $^3J_{P-H}$ = 14.6 Hz, $^3J_{H-H}$ = 6.9 Hz, $C_{4/5}NCH(CH_3)_2$), 2.16 (6H, s, $C_{2/7}CH_3$), 1.58 (3H, s, $C_9(CH_3)$), 1.55 (3H, s, $C_9(CH_3)$), 1.52 (6H, d, $^3J_{H-H}$ = 6.9 Hz, $C_{4/5}NCH(CH_3)$), 1.27 (6H, d, $^3J_{H-H}$ = 7.0 Hz, $C_{4/5}NCH(CH_3)$).

$^1H\{^{31}P\}$ NMR (500 MHz, C_6D_6): as above, except δ (ppm) 4.43 (2H, sept, $^2J_{H-H}$ = 7.0 Hz, $C_{4/5}NCH(CH_3)_2$).

$^{13}C\{^1H\}$ NMR (151 MHz, C_6D_6): δ (ppm) 135.4 (d, $^3J_{C-P}$ = 10.4 Hz, $C_{9a/8a}$), 135.0 (d, $^2J_{C-P}$ = 3.0 Hz, $C_{4a/10a}$), 134.0 (d, $^2J_{C-P}$ = 14.9 Hz, $C_{4/5}$), 133.8 (s, $C_{2/7}$), 116.2 (s, $C_{1/8}$), 110.1 (d, $^3J_{C-P}$ = 8.6 Hz, $C_{3/6}$), 47.1 (d, $^2J_{C-P}$ = 7.4 Hz, $C_{4/5}NCH(CH_3)$), 40.2 (s, C_9), 26.3 (s, $C_9(CH_3)$), 22.6 (s, $C_9(CH_3)$), 22.2 (s, $C_{2/7}(CH_3)$), 20.7 (d, $^3J_{C-P}$ = 1.7 Hz, $C_{4/5}NCH(CH_3)$), 20.0 (d, $^3J_{C-P}$ = 3.9 Hz, $C_{4/5}NCH(CH_3)$).

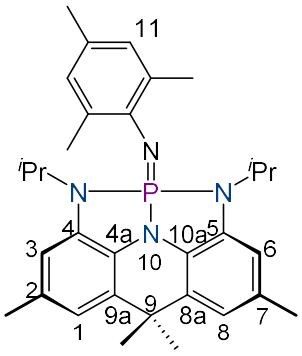
^{31}P NMR (243 MHz, C_6D_6): δ (ppm) 75.7 (dt, $^{1}J_{P–77Se}$ = 919.2 Hz, $^{3}J_{P–H}$ = 14.7 Hz).

^{31}P{^{1}H} NMR (162 MHz, C_6D_6): δ (ppm) 75.6 (dt, $^{1}J_{P–77Se}$ = 918.8 Hz).

^{77}Se NMR (95 MHz, C_6D_6): δ (ppm) −35.4 (d, $^{1}J_{P–77Se}$ = 916.8 Hz).

Elemental analysis calcd. (%) for $C_{23}H_{30}N_3PSe$: C 60.26, H 6.60, N 9.17; found: C 60.05, H 6.61, N 9.05.

2.5.13 Synthesis of 14



6 (10.5 mg, 27.8 µmol, 1.0 eq.) was added to a toluene (0.5 mL) solution of mesityl-azide (4.5 mg, 27.8 µmol, 1.0 eq.) then heated at 110 °C for 2 hours, generating a colourless solution. The solvent was removed *in vacuo* and the residues heated under dynamic vacuum for 30 minutes to remove any unreacted mesityl-azide. The residue was dissolved in hexane (0.5 mL) and crystals of **14** (10.0 mg, 19.5 µmol, 70%) grown by slow evaporation of this hexane solution.

^{1}H NMR (500 MHz, C_6D_6): δ (ppm) 6.92 (2H, s, $C_{11}H$), 6.61 (2H, s, $C_{1/8}H$), 6.44 (2H, s, $C_{3/6}H$), 4.13 (2H, d-sept, $^{3}J_{P–H}$ = 11.7 Hz, $^{3}J_{H–H}$ = 7.0 Hz, $C_{4/5}NCH(CH_3)_2$), 2.50 (6H, br s, $C_{Mes}(CH_3)$), 2.26 (3H, d, $J_{P–H}$ = 2.8 Hz, $C_{Mes}(CH_3)$), 2.21 (6H, s, $C_{2/7}(CH_3)$, 1.66 (3H, s, $C_9(CH_3)$), 1.64 (3H, s, $C_9(CH_3)$), 1.30 (6H, d, $^{3}J_{H–H}$ = 6.9 Hz, $C_{4/5}NCH(CH_3)$), 1.17 (6H, d, $^{3}J_{H–H}$ = 7.0 Hz, $C_{4/5}NCH(CH_3)$).

^{1}H{^{31}P} NMR (500 MHz, C_6D_6): as above, except δ (ppm) 4.13 (2H, sept, $^{3}J_{H–H}$ = 7.0 Hz, $C_{4/5}NCH(CH_3)_2$), 2.26 (3H, s, $C_{Mes}(CH_3)$).

^{13}C{^{1}H} NMR (151 MHz, C_6D_6): δ (ppm) 143.1 (d, $J_{C–P}$ = 3.4 Hz, C_{Mes}), 134.4 (d, $^{3}J_{C–P}$ = 10.0 Hz, $C_{8a/9a}$), 133.8 (d, $^{2}J_{C–P}$ = 19.6 Hz, $C_{4/5}$), 133.5 (d, $^{2}J_{C–P}$ = 7.3 Hz, $C_{4a/10a}$), 133.5 (s, $C_{2/7}$), 131.3 (m, C_{Mes}),

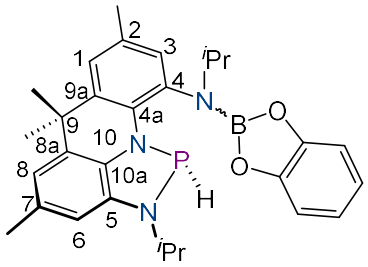
129.5 (m, C_{11}), 129.0 (d, J_{C-P} = 4.1 Hz, C_{Mes}), 115.6 (s, $C_{1/8}$), 110.3 (d, $^{3}J_{C-P}$ = 10.4 Hz, $C_{3/6}$), 47.0 (d, $^{2}J_{C-P}$ = 2.6 Hz, $C_{4/5}NCH(CH_3)_2$), 40.0 (s, C_9), 26.8 (s, $C_9(CH_3)$), 22.5 (s, $C_9(CH_3)$), 22.3 (s, $C_{2/7}(CH_3)$), 20.95 – 20.88 (overlapping signals corresponding to one $C_{Mes}(CH_3)$ environment, and one set of $C_{4/5}NCH(CH_3)$ environments), 20.7 (s, $C_{Mes}(CH_3)$), 20.0 (d, $^{3}J_{C-P}$ = 4.4 Hz, $C_{4/5}NCH(CH_3)$).

^{31}P NMR (243 MHz, C_6D_6): δ (ppm) 18.1 (m).

^{31}P{^{1}H} NMR (243 MHz, C_6D_6): δ (ppm) 18.1 (s).

Elemental analysis calcd. (%) for $C_{32}H_{41}N_4P$: C 74.97, H 8.06, N 10.93; found: C 74.91, H 8.30, N 10.54.

2.5.14 Synthesis of 15



6 (10.0 mg, 26.4 µmol, 1.0 eq.) was dissolved in benzene (0.5 mL) and 2*H*-1,3,2-benzodioxaborole (2.8 µL, 26.4 µmol, 1.0 eq.) added, resulting in the immediate generation of a colourless solution. Full conversion to an isomeric mixture of **15** (1:0.6 ratio) was observed by ^{31}P NMR spectroscopy.

^{1}H NMR (600 MHz, C_6D_6): ***major isomer*** δ (ppm) 7.20 (1H, s, C_1H), 7.02 (1H, d, $^{1}J_{P-H}$ = 135.0 Hz, P–H), 6.91 ($C_{13}H$)*, 6.86 (1H, m, C_3H), 6.70 (1H, s, C_8H), 6.68 ($C_{12}H$)*, 6.27 (1H, s, C_6H), 4.35 (1H, sept, $^{2}J_{H-H}$ = 6.7 Hz, $C_4NCH(CH_3)_2$), 3.54 (1H, d-sept, $^{3}J_{P-H}$ = 11.6 Hz, $^{3}J_{H-H}$ = 6.6 Hz, $C_5NCH(CH_3)_2$), 2.30 (3H, s, $C_7(CH_3)$), 2.18 (3H, s, $C_2(CH_3)$), 1.71 (3H, s, $C_9(CH_3)$), 1.51 (3H, s, $C_9(CH_3)$), 1.43 (3H, d, $^{2}J_{H-H}$ = 6.6 Hz, $C_4NCH(CH_3)$), 1.18 (3H, d, $^{2}J_{H-H}$ = 6.8 Hz, $C_5NCH(CH_3)$), 1.18 (3H, d, $^{2}J_{H-H}$ = 6.6 Hz, $C_4NCH(CH_3)$), 0.94 (3H, d, $^{2}J_{H-H}$ = 6.5 Hz, $C_5NCH(CH_3)$). ***minor isomer*** δ (ppm) 7.16 (C_1H)*, 7.15 (1H, d, $^{1}J_{P-H}$ = 148.0 Hz, P–H), 6.98 (2H, br m, $C_{13}H$), 6.91 (C_3H)*, 6.74 (2H, dd, $^{3}J_{H-H}$ = 5.7 Hz, $^{4}J_{H-H}$ = 3.3 Hz, $C_{12}H$), 6.66 (1H, s, C_8H), 6.25 (s, 1H, C_6H), 4.11 (1H, sept, $^{2}J_{H-H}$ = 6.7 Hz, $C_4NCH(CH_3)_2$), 3.44 (1H, d-sept, $^{3}J_{P-H}$ = 12.7 Hz, $^{2}J_{H-H}$ = 6.3 Hz, $C_5NCH(CH_3)_2$), 2.29 (3H, s,

$C_7(CH_3)$), 2.18 (3H, s, $C_2(CH_3)$), 1.64 (3H, s, $C_9(CH_3)$), 1.59 (3H, s, $C_9(CH_3)$), 1.38 (3H, d, $^2J_{H–H}$ = 6.5 Hz, $C_4NCH(CH_3)$), 1.00 (3H, d, $^2J_{H–H}$ = 6.6 Hz, $C_5NCH(CH_3)$), 0.90 (3H, d, $^2J_{H–H}$ = 6.5 Hz, $C_4NCH(CH_3)$), 0.86 (3H, d, $^2J_{H–H}$ = 6.6 Hz, $C_5NCH(CH_3)$).

* Signal overlap prevents integration and multiplet analysis

$^1H\{^{31}P\}$ NMR (500 MHz, C_6D_6): ***major isomer*** as above, except δ (ppm) 7.02 (1H, s, P–H), 3.54 (1H, sept, $^2J_{H–H}$ = 6.6 Hz, $C_5NCH(CH_3)_2$). ***minor isomer*** as above, except δ (ppm) 7.15 (1H, s, P–H), 3.44 (1H, sept, $^2J_{H–H}$ = 6.3 Hz, $C_5NCH(CH_3)_2$).

$^{13}C\{^1H\}$ NMR (151 MHz, C_6D_6): ***major isomer*** δ (ppm) 149.4 (s, C_{11}), 139.6 (d, $^2J_{C–P}$ = 6.7 Hz, C_5), 135.5 (d, $^2J_{C–P}$ = 3.6 Hz, C_{4a}), 134.5 (d, $^3J_{C–P}$ = 2.1 Hz, C_{8a}), 133.3 (d, $^2J_{C–P}$ = 9.5 Hz, C_{10a}), 131.3 (s, C_7), 130.9 (s, C_3), 130.0 (s, C_2), 128.4 (s, C_{9a}), 127.0 (s, C_1), 122.3 (s, C_{12}), 116.4 (s, C_8), 112.1 (s, C_{13}), 108.5 (s, C_6), 51.9 (d, $^{5TS}J_{C–P}$ = 13.4 Hz, $C_4NCH(CH_3)_2$)**, 47.5 (d, $^2J_{C–P}$ = 17.4 Hz, $C_5NCH(CH_3)_2$), 36.6 (s, C_9), 34.8 (s, $C_9(CH_3)$), 31.5 (s, $C_9(CH_3)$), 24.3 (s, $C_4NCH(CH_3)$), 22.2 (d, $^3J_{C–P}$ = 10.9 Hz, $C_5NCH(CH_3)$), 21.9 (s, $C_7(CH_3)$), 21.4 (s, $C_5NCH(CH_3)$), 20.9 (s, $C_2(CH_3)$), 19.0 (d, $^{6TS}J_{C–P}$ = 6.1 Hz, $C_4NCH(CH_3)$)**. ***minor isomer*** δ (ppm) 149.7 (s, C_{11}), 139.5 (d, $^2J_{C–P}$ = 6.5 Hz, C_5), 134.4 (s, C_{4a}), 133.8 (d, $^3J_{C–P}$ = 2.0 Hz, C_{8a}), 132.8 (d, $^2J_{C–P}$ = 7.8 Hz, C_{10a}), 131.2 (s, C_7), 129.3 (s, C_3), 128.3 (s, C_{9a}), 126.8 (s, C_2), 126.7 (s, C_1), 122.0 (s, C_{12}),116.8 (s, C_8), 112.0 (s, C_{13}), 108.8 (s, C_6), 50.5 (s, $C_4NCH(CH_3)_2$), 47.9 (d, $^2J_{C–P}$ = 18.1 Hz, $C_5NCH(CH_3)_2$), 36.7 (s, C_9), 34.6 (s, $C_9(CH_3)$), 33.0 (s, $C_9(CH_3)$), 25.1 (s, $C_4NCH(CH_3)$), 21.9 (s, $C_7(CH_3)$), 21.6 (d, $^2J_{C–P}$ = 12.2 Hz, $C_5NCH(CH_3)$), 21.3 (s, $C_5NCH(CH_3)$), 20.9 (s, $C_2(CH_3)$), 20.6 (s, $C_4NCH(CH_3)$).

* ^{13}C peak for C_4 could not be identified.

** TS = through space coupling to phosphorus in close proximity.[40]

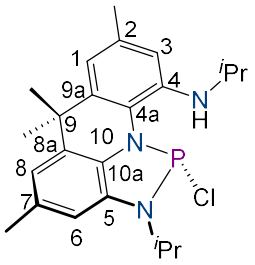
^{31}P NMR (243 MHz, C_6D_6): ***major isomer*** δ (ppm) 67.1 (dd, $^1J_{P–H}$ = 135.0 Hz, $^3J_{P–H}$ = 11.3 Hz). ***minor isomer*** δ (ppm) 61.8 (dd, $^1J_{P–H}$ = 148.4 Hz, $^3J_{P–H}$ = 12.3 Hz).

$^{31}P\{^1H\}$ NMR (202 MHz, C_6D_6): ***major isomer*** δ (ppm) 67.1 (s). ***minor isomer*** δ (ppm) 61.8 (s).

$^{11}B\{^1H\}$ NMR (128 MHz, C_6D_6): δ (ppm) −28.6 (br), −34.0 (br).*

* Assignment of major and minor isomer could not be achieved.

2.5.15 Synthesis of 16



6 (10.5 mg, 27.8 µmol, 1.0 eq.) was dissolved in benzene (0.5 mL). Hydrochloric acid (0.2 M in diethyl ether, 0.14 mL, 27.8 µmol, 1.0 eq.) was added, instantly generating a colourless solution. The solvent was removed *in vacuo* and the product dissolved in pentane (0.5 mL). Pale yellow crystals of **16** (8.5 mg, 20.4 µmol, 74%) were grown from a concentrated pentane solution at −30 °C.

^{1}H NMR (500 MHz, C_6D_6): δ (ppm) 7.06 (1H, s, C_1H), 6.83 (1H, s, C_8H), 6.58 (1H, s, C_3H), 6.55 (1H, s, C_6H), 3.99 (1H, d-sept, $^{3}J_{P–H}$ = 11.5 Hz, $^{3}J_{H–H}$ = 6.7 Hz, $C_5NCH(CH_3)_2$), 3.19 (1H, sept, $^{3}J_{H–H}$ = 6.2 Hz, $C_4NCH(CH_3)_2$), 2.97 (1H, br s, N–H), 2.33 (3H, s, $C_7(CH_3)$), 2.19 (3H, s, $C_2(CH_3)$), 1.57 (6H, br s, $C_9(CH_3)_2$)*, 1.54 (6H, d, $^{3}J_{H–H}$ = 6.6 Hz, $C_5NCH(CH_3)_2$), 1.10 (6H, d, $^{3}J_{H–H}$ = 6.2 Hz, $C_4NCH(CH_3)_2$).

* Broad signal indicating overlap between inequivalent methyl groups.

^{1}H{^{31}P} NMR (500 MHz, C_6D_6): as above, except δ (ppm) 3.99 (1H, sept, $^{3}J_{H–H}$ = 6.7 Hz, $C_5NCH(CH_3)_2$).

^{13}C{^{1}H} NMR (151 MHz, C_6D_6): δ (ppm) 134.9 (d, $^{2}J_{C–P}$ = 9.8 Hz, C_5), 134.7 (d, $^{3}J_{C–P}$ = 3.4 Hz, C_{8a}), 133.6 (s, C_4), 132.4 (s, C^{Ar})*, 132.3 (s, C^{Ar})*, 131.2 (d, $^{2}J_{C–P}$ = 8.0 Hz, C_{4a}), 130.1 (s, C_{9a}), 129.1 (d, $^{2}J_{C–P}$ = 12.1 Hz, C_{10a}), 125.2 (s, C_3), 125.0 (s, C_1), 117.9 (s, C_8), 109.1 (s, C_6), 49.0 (d, $^{5TS}J_{C–P}$ = 6.0 Hz, $C_4NCH(CH_3)_2$)**, 47.5 (d, $^{2}J_{C–P}$ = 15.8 Hz, $C_5NCH(CH_3)_2$), 36.4 (s, C_9), 22.0 (s, $C_7(CH_3)$), 21.1 (s, $C_2(CH_3)$).***

* Due to overlap of 2D spectra, $C_{2/7}$ cannot be distinguished.

** TS = through space coupling to phosphorus in close proximity.[40]

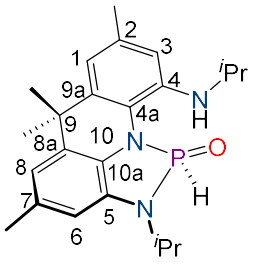
*** Overlap results in a broad signal from 22.3 ppm to 21.4 ppm. 2D spectra indicate resonances corresponding both $C_9(CH_3)_2$ and $C_{4/5}NCH(CH_3)_2$) environments are present within this region.

^{31}P NMR (243 MHz, C_6D_6): δ (ppm) 130.6 (m).

$^{31}P\{^1H\}$ NMR (243 MHz, C_6D_6): δ (ppm) 130.6 (s).

Elemental analysis calcd. (%) for $C_{23}H_{31}ClN_3P$: C 66.42, H 7.51, N 10.10; found: C 67.21, H 8.24, N 9.01. These values are consistent with the presence of 0.5 eq. pentane in the sample: calcd (%) for $C_{25.5}H_{37.5}Cl_1N_3P_1$: C 67.68, H 8.35, N 9.29.

2.5.16 Synthesis of 17



6 (31.0 mg, 81.7 µmol, 1.0 eq.) was dissolved in benzene (0.5 mL). Deionised water (1.5 µL, 81.7 µmol, 1.0 eq.) was added resulting in the immediate generation of a colourless solution. The solvent was removed *in vacuo* and the remaining residue heated under vacuum to remove traces of water. Lyophilisation from a concentrated benzene solution yields **17** as a colourless powder (25.5 mg, 64.2 µmol, 79%).

^1H NMR (400 MHz, C_6D_6): δ (ppm) 9.42 (1H, d, $^1J_{P–H}$ = 714.6 Hz, P–*H*), 6.97 (1H, s, C_1H), 6.69 (1H, s, C_8H), 6.64 (1H, s, C_3H), 6.29 (1H, s, C_6H), 3.85 (1H, s, N–H), 3.72 (1H, d-sept, $^3J_{P–H}$ = 18.0 Hz, $^3J_{H–H}$ = 6.7 Hz, $C_5NCH(CH_3)_2$), 3.31 (1H, sept, $^3J_{H–H}$ = 6.3 Hz, $C_4NCH(CH_3)_2$), 2.31 (3H, s, $C_7(CH_3)$), 2.18 (3H, s,$C_2(CH_3)$), 1.64 (3H, s, $C_9(CH_3)$), 1.54 (3H, s, $C_9(CH_3)$), 1.41 (3H, d, $^3J_{H–H}$ = 6.7 Hz, $C_4NCH(CH_3)$), 1.40 (3H, d, $^3J_{H–H}$ = 6.7 Hz, $C_5NCH(CH_3)$), 1.21 (3H, d, $^3J_{H–H}$ = 6.3 Hz, $C_4NCH(CH_3)$), 0.95 (3H, d, $^3J_{H–H}$ = 6.3 Hz, $C_4NCH(CH_3)$).

$^1H\{^{31}P\}$ NMR (400 MHz, C_6D_6): as above, except δ (ppm) 9.42 (1H, s, P–H), 3.72 (1H, sept, $^3J_{H–H}$ = 6.7 Hz, $C_5NCH(CH_3)_2$).

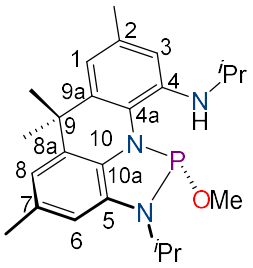
$^{13}C\{^{1}H\}$ NMR (151 MHz, C_6D_6): δ (ppm) 133.6 (s, C_4), 133.0 (d, $^{2}J_{C–P}$ = 8.6 Hz, C_{10a}), 132.9 (d, $^{2}J_{C–P}$ = 5.7 Hz, C_{8a}), 131.9 (s, C_2), 131.5 (s, C_7), 129.9 (s, C_{4a}), 127.3 (d, $^{3}J_{C–P}$ = 5.9 Hz, C_{9a}), 125.1 (d, $^{2}J_{C–P}$ = 10.8 Hz, C_5), 123.9 (s, C_1), 121.8 (s, C_3), 116.3 (s, C_8), 106.6 (d, $^{3}J_{C–P}$ = 6.16 Hz, C_6), 47.0 (s, $C_4NCH(CH_3)_2$)), 46.3 (d, $^{2}J_{C–P}$ = 5.0 Hz, $C_5NCH(CH_3)_2$), 36.2 (s, C_9), 34.5 (s, $C_9(CH_3)$), 34.0 (s, $C_9(CH_3)$), 22.6 (s, $C_4NCH(CH_3)$), 22.1 (s, $C_7(CH_3)$), 21.8 (s, $C_5NCH(CH_3)$), 21.2 (s, $C_2(CH_3)$), 21.0 (s, $C_4NCH(CH_3)$), 20.0 (d, $^{3}J_{C–P}$ = 3.73 Hz, $C_5NCH(CH_3)$).

^{31}P NMR (162 MHz, C_6D_6): δ (ppm) 1.3 (dd, $^{1}J_{P–H}$ = 714.6 Hz, $^{3}J_{P–H}$ = 18.3 Hz).

$^{31}P\{^{1}H\}$ NMR (162 MHz, C_6D_6): δ (ppm) 1.3 (s).

Elemental analysis calcd. (%) for $C_{23}H_{32}N_3OP$: C 69.50, H 8.11, N 10.57; found: C 68.72, H 7.68, N 9.97. These values are consistent with the presence of 0.25 eq. water in the sample: calcd (%) for $C_{23}H_{32.5}N_3O_{1.25}P_1$: C 68.72, H 8.15, N 10.45.

2.5.17 Synthesis of 18



6 (10.5 mg, 27.8 µmol, 1.0 eq.) was dissolved in benzene (0.5 mL). Methanol (2 M in DME, 14 µL, 27.8 µmol, 1.0 eq.) was added resulting in the generation of a pale-yellow solution. The solvent was removed *in vacuo* and the residue extracted with pentane (2 × 0.5 mL). Crystals of **18** (8.5 mg, 20.7 µmol, 74%) were grown from a concentrated pentane solution at −30 °C.

^{1}H NMR (600 MHz, C_6D_6): δ (ppm) 7.02 (1H, s, C_8H), 6.79 (1H, s, C_1H), 6.57 (1H, s, C_6H), 6.43 (1H, s, C_3H), 3.92 (1H, d-sept, $^{3}J_{P–H}$ = 10.2 Hz, $^{3}J_{H–H}$ = 6.7 Hz, $C_5NCH(CH_3)_2$)), 3.47 – 3.39 (2H, overlapping multiplet corresponding to N*H* and $C_4NCH(CH_3)_2$) environments), 2.81 (3H, d, $^{3}J_{P–H}$ = 7.4 Hz, P–OCH_3), 2.39 (3H, s, $C_2(CH_3)$), 2.28 (3H, s, $C_7(CH_3)$), 1.76 (3H, s, $C_9(CH_3)$), 1.72 (3H, s, $C_9(CH_3)$),

1.43 (3H, dd, $^{3}J_{H–H}$ = 6.7 Hz, $^{4}J_{P–H}$ = 1.1 Hz, $C_5NCH(CH_3)$), 1.38 (3H, d, $^{3}J_{H–H}$ = 6.7 Hz, $C_5NCH(CH_3)$), 1.19 – 1.17 (6H, overlapping doublets corresponding to both $C_4NCH(CH_3)$ environments).

$^{1}H\{^{31}P\}$ NMR (600 MHz, C_6D_6): as above, except δ (ppm) 3.92 (1H, sept, $^{3}J_{H–H}$ = 6.7 Hz, $C_5NCH(CH_3)_2$)), 2.81 (3H, s, P–OCH_3), 1.43 (3H, d, $^{3}J_{H–H}$ = 6.7 Hz, $C_5NCH(CH_3)$).

$^{13}C\{^{1}H\}$ NMR (151 MHz, C_6D_6): δ (ppm) 136.4 (d, $^{2}J_{C–P}$ = 7.8 Hz, C_5), 134.4 (d, $^{3}J_{C–P}$ = 1.5 Hz, C_4), 133.4 (d, $^{3}J_{C–P}$ = 2.1 Hz, $C_{8a/9a}$), 130.8 (s, C_7), 130.7 (s, C_2), 130.1 (d, $^{2}J_{C–P}$ = 8.8 Hz, C_{4a}), 128.6 (s, C_{10a}), 127.0 (s, $C_{8a/9a}$), 121.3 (s, C_8), 119.0 (s, C_6), 116.2 (s, C_1), 106.1 (s, C_3), 49.7 (d, $^{2}J_{C–P}$ = 5.4 Hz, P–OCH_3), 46.7 (d, $^{2}J_{C–P}$ = 19.5 Hz, $C_5NCH(CH_3)_2$), 46.5 (d, $^{5TS}J_{C–P}$ = 5.9 Hz, $C_4NCH(CH_3)_2$),* 36.6 (s, C_9), 34.7 (s, $C_9(CH_3)$), 34.6 (s, $C_9(CH_3)$), 22.7 – 22.6 (overlapping multiplets, $C_5NCH(CH_3)_2$), 22.4 (s, $C_4NCH(CH_3)_2$), 22.1 (s, $C_2(CH_3)$), 21.3 (s, $C_7(CH_3)$).

* TS = through space coupling to phosphorus in close proximity.[40]

^{31}P NMR (243 MHz, C_6D_6): δ (ppm) 97.3 (m).

$^{31}P\{^{1}H\}$ NMR (243 MHz, C_6D_6): δ (ppm) 97.3 (s).

Elemental analysis calcd. (%) for $C_{24}H_{34}N_3OP$: C 70.05, H 8.33, N 10.21; found: C 70.15, H 8.44, N 9.80.

2.6 References

[1] A. Brand, W. Uhl, *Chem. Eur. J.* **2019**, *25*, 1391–1404.

[2] S. Kundu, *Chem. Asian J.* **2020**, *15*, 3209–3224.

[3] T. P. Robinson, D. M. De Rosa, S. Aldridge, J. M. Goicoechea, *Angew. Chem., Int. Ed.* **2015**, *54*, 13758–13763.

[4] W. Zhao, S. M. McCarthy, T. Y. Lai, H. P. Yennawar, A. T. Radosevich, *J. Am. Chem. Soc.* **2014**, *136*, 17634–17644.

[5] A. Tanushi, A. T. Radosevich, *J. Am. Chem. Soc.* **2018**, *140*, 8114–8118.

[6] A. J. I. Arduengo, C. A. Stewart, F. Davidson, D. A. Dixon, J. Y. Becker, S. A. Culley, M. B. Mizen, *J. Am. Chem. Soc.* **1987**, *109*, 627–647.

[7] S. A. Culley, A. J. I. Arduengo, *J. Am. Chem. Soc.* **1984**, *106*, 1164–1165.

[8] A. Hentschel, A. Brand, P. Wegener, W. Uhl, *Angew. Chem., Int. Ed.* **2018**, *57*, 832–835.

[9] W. Uhl, D. Kovert, M. Layh, A. Hepp, *Chem. Eur. J.* **2011**, 17, 13553–13561.

[10] J. Cui, Y. Li, R. Ganguly, A. Inthirarajah, H. Hirao, R. Kinjo, *J. Am. Chem. Soc.* **2014**, *136*, 16764–16767.

[11] K. M. Marczenko, J. A. Zurakowski, M. B. Kindervater, S. Jee, T. Hynes, N. Roberts, S. Park, U. Werner-Zwanziger, M. Lumsden, D. N. Langelaan, S. S. Chitnis, *Chem. Eur. J.* **2019**, *25*, 16414–16424.

[12] M. B. Kindervater, K. M. Marczenko, U. Werner-Zwanziger, S. S. Chitnis, *Angew. Chem., Int. Ed.* **2019**, *58*, 7850–7855.

[13] M. K. Mondal, L. Zhang, Z. Feng, S. Tang, R. Feng, Y. Zhao, G. Tan, H. Ruan, X. Wang, *Angew. Chem., Int. Ed.* **2019**, *58*, 15829–15833.

[14] C. Bonningue, D. Houalla, R. Wolf, J. Jaud, *J. Chem. Soc., Perkin Trans. 2* **1983**, 773.

[15] S. E. Frazier, R. P. Nielsen, H. H. Sisler, *Inorg. Chem.* **1964**, *3*, 292–294.

[16] S. F. Spangenberg, H. H. Sisler, *Inorg. Chem.* **1969**, *8*, 1006–1010.

[17] J. C. Summers, H. H. Sisler, *Inorg. Chem.* **1970**, *9*, 862–869.

[18] A. Schumann, F. Reiß, H. Jiao, J. Rabeah, J.-E. Siewert, I. Krummenacher, H. Braunschweig, C. Hering-Junghans, *Chem. Sci.* **2019**, *10*, 7859–7867.

[19] J.-E. Siewert, A. Schumann, C. Hering-Junghans, *Dalton Trans.* **2021**, *50*, 15111–15117.

[20] J. Underhill, E. S. Yang, T. Schmidt-Räntsch, W. K. Myers, J. M. Goicoechea, J. Abbenseth, *Chem. Eur. J.* **2023**, *29*, e202203266.

[21] A. J. King, J. M. Goicoechea, *Chem. Eur. J.* **2024**, *30*, e202400624.

[22] P. Pyykkö, *J. Phys. Chem. A* **2015**, *119*, 2326–2337.

[23] T. P. Robinson, S.-K. Lo, D. De Rosa, S. Aldridge, J. M. Goicoechea, *Chem. Eur. J.* **2016**, *22*, 15712–15724.

[24] J. Cui, Y. Li, R. Ganguly, R. Kinjo, *Chem. Eur. J.* **2016**, *22*, 9976–9985.

[25] T. P. Robinson, D. De Rosa, S. Aldridge, J. M. Goicoechea, *Chem. Eur. J.* **2017**, *23*, 15455–15465.

[26] A. Okuniewski, D. Rosiak, J. Chojnacki, B. Becker, *Polyhedron* **2015**, *90*, 47–57.

[27] H. Khatoon, E. Abdulmalek, *Molecules* **2021**, *26*, 6937.

[28] D. W. Allen, B. F. Taylor, *J. Chem. Soc., Dalton Trans.* **1982**, 51–54.

[29] N. Beims, T. Greven, M. Schmidtmann, J. I. van der Vlugt, *Chem. Eur. J.* **2023**, *29*, e202302463.

[30] Yu. G. Gololobov, I. N. Zhmurova, L. F. Kasukhin, *Tetrahedron* **1981**, *37*, 437–472.

[31] Y. G. Gololobov, L. F. Kasukhin, *Tetrahedron* **1992**, *48*, 1353–1406.

[32] Y.-C. Lin, J. C. Gilhula, A. T. Radosevich, *Chem. Sci.* **2018**, *9*, 4338–4347.

[33] J. E. Griffiths, A. B. Burg, *J. Am. Chem. Soc.* **1960**, *82*, 1507–1508.

[34] W. J. Bailey, R. B. Fox, *J. Org. Chem.* **1963**, *28*, 531–534.

[35] W. J. Bailey, R. B. Fox, *J. Org. Chem.* **1964**, *29*, 1013–1017.

[36] B. Hoge, S. Neufeind, S. Hettel, W. Wiebe, C. Thösen, *J. Organomet. Chem.* **2005**, *690*, 2382–2387.

[37] A. Christiansen, C. Li, M. Garland, D. Selent, R. Ludwig, A. Spannenberg, W. Baumann, R. Franke, A. Börner, *Eur. J. Org. Chem.* **2010**, *2010*, 2733–2741.

[38] B. G. Janesko, H. C. Fisher, M. J. Bridle, J.-L. Montchamp, *J. Org. Chem.* **2015**, *80*, 10025–10032.

[39] A. J. King, J. Abbenseth, J. M. Goicoechea, *Chem. Eur. J.* **2023**, 29, e202300818.

[40] J.-C. Hierso, *Chem. Rev.* **2014**, *114*, 4838–4867.

[41] B. Gamoke, D. Neff, J. Simons, *J. Phys. Chem. A* **2009**, 113, 5677–5684.

Chapter 3

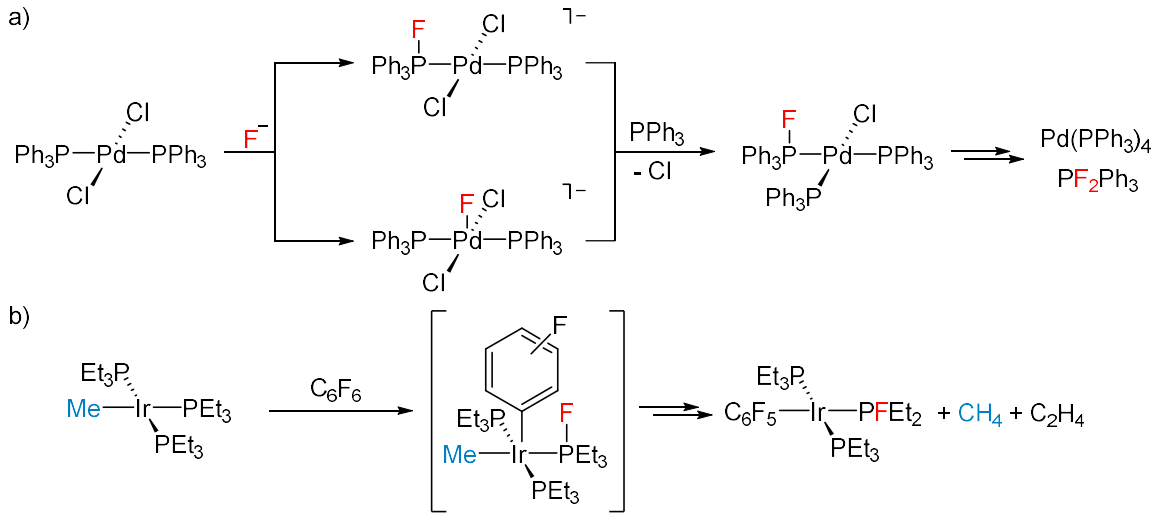
Coordination Chemistry of a T-Shaped Phosphine

Abstract. On complexation to transition metals, T-shaped phosphine **6** adopts a distorted trigonal pyramidal, or "bent", structure. A barrier to inversion of coordinated **6** of 19.3(5) kcal/mol was determined by variable-temperature NMR spectroscopy of gold(I) complex **19**. A combination of heteronuclear NMR spectroscopy, vibrational spectroscopy, SCXRD, and DFT calculations reveal **6** to be a moderate σ-donor with enhanced π-acceptor properties. Following coordination, **6** retains its ability to activate E–H bonds; doing so in a cooperative fashion across a ligand-based P–N bond without involvement of the metal centre. In the case of amine substrates, including ammonia, this process was reversible.

3.1 The reactivity of coordinated phosphines

3.1.1 Phosphine-assisted reaction pathways

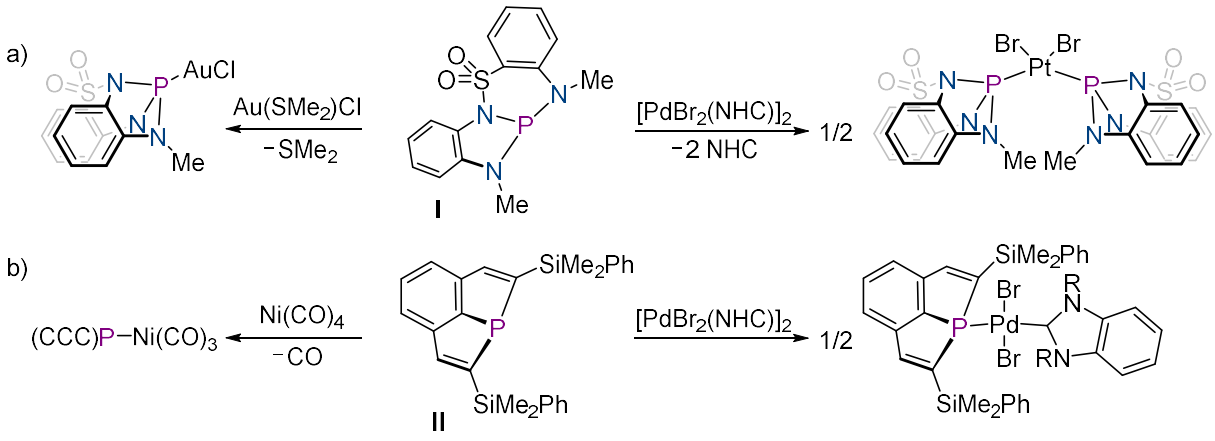
Although phosphines are well-known spectator ligands in transition metal catalysis, several studies suggest that they can play a more active role in the reactivity of organometallic complexes. For instance, the substituents of some transition metal bound phosphines have been shown to be labile, exchanging with other groups bonded to the metal, or exogenous sources of C, N and O based nucleophiles.[1] Additionally, phosphine-based reactivity with fluoride sources has been used in the preparation of active palladium(0) catalysts from more stable palladium(II) precursors (Scheme 3.1a). This process invokes the formation of a metallophosphorane - a class of compound often cited as a key intermediate in catalytic processes, or in catalyst decomposition pathways.[2–5] Iridium and platinum complexes of simple alkyl phosphines can activate aryl C–F bonds *via* a phosphine assisted pathway, again with the supposed generation of an intermediate metallophosphorane (Scheme 3.1b).[6–8] Proposed mechanisms such as these were supported by the recent discovery of C–F activation by simple trialkyl phosphines, enabling solely phosphorus based hydrodefluorination and aminodefluorination catalysis.[9]



Scheme 3.1. Fluoride induced disproportionation of $Pd(Cl)_2(PPh_3)_2$. Phosphine assisted C_{aryl}–F bond activation.

3.1.2 Geometrically constrained phosphines as ligands

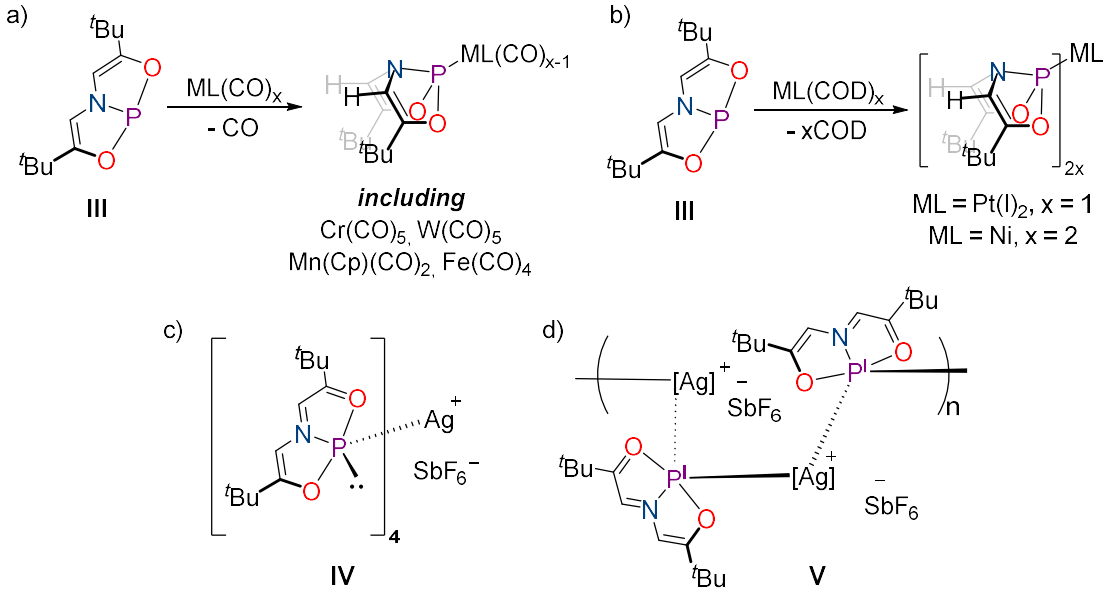
Several research groups have investigated the complexation of geometrically constrained phosphines to transition metals.[10] *Cs* symmetric (bent) phosphines were shown to undergo only a slight structural change upon complexation, which was exemplified by the coordination of **I**, possessing an unsymmetric backbone, to gold(I) and platinum(II) (Scheme 3.2a).[11] When used as a ligand, phosphine **II** was shown to possess similar electronic properties as PPh_3, and readily formed complexes with group 10 metals (Scheme 3.2b).[12]



Scheme 3.2. Select examples of geometrically constrained phosphines being used as ligands to transition metals.

The coordination chemistry of T-shaped phosphine **III** has been explored extensively, with compounds of group 6, 7, 8, 10 and 11 transition metals reported by Arduengo and co-workers (Scheme 3.3).[13] For

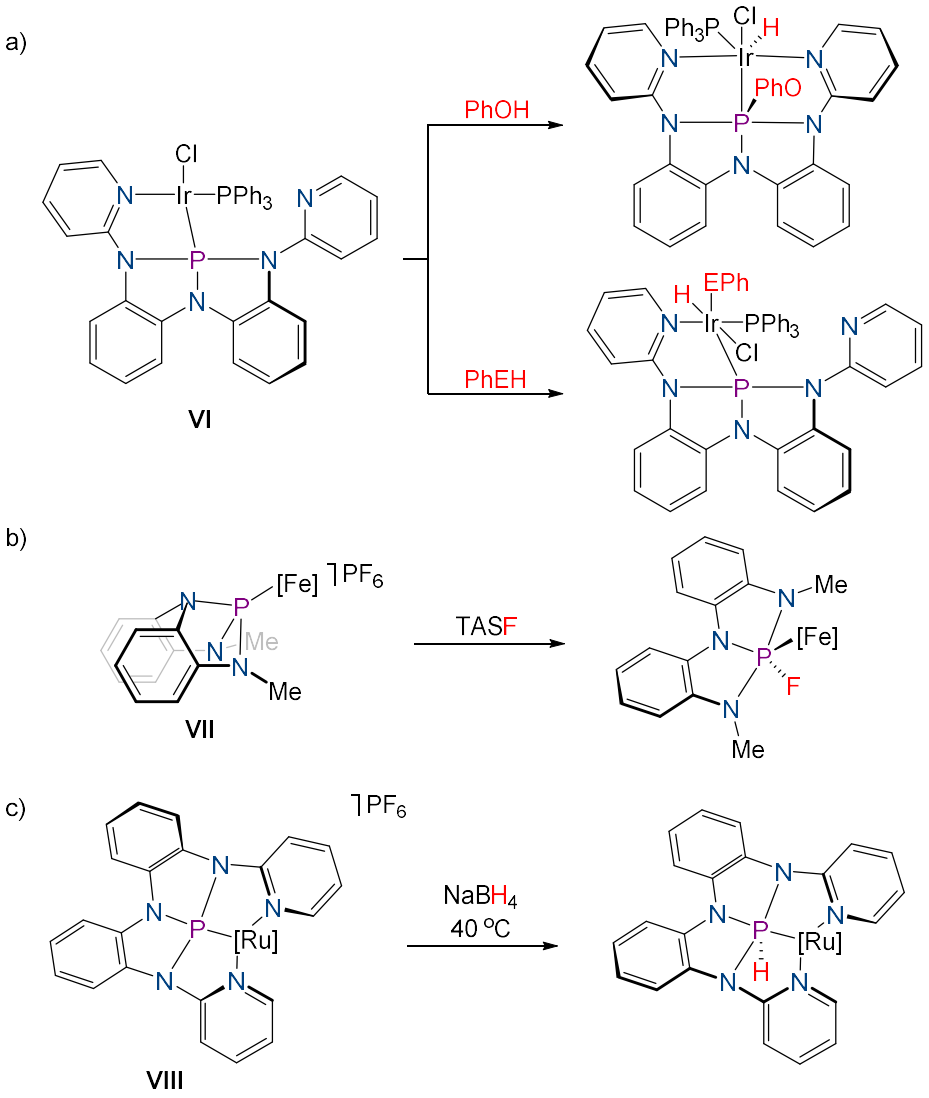
the majority of these systems, **III** behaved as an L-type ligand and adopted a bent geometry, thus increasing the donor capacity of its phosphorus-based lone-pair (on account of its reduced s-orbital character in this geometry). Planar coordination of **III** was also reported for complexes of silver(I), providing either the discrete molecular species **IV**, or polymeric **V**, whereby **III** acts as a bridging 2L, 4e⁻, donor (Scheme 3.3c and 3.3d). This binding mode was attributed to the supposed phosphorus(I) oxidation state of the planar free ligand **III**, affording two stereogenic lone-pairs at the phosphorus centre, both of which capable of donation to a metal centre.



Scheme 3.3. Complexes of T-shaped phosphine **III** with group 6, 7, 8, 10 and 11 transition metals.

The majority of reports describing the coordination chemistry of geometrically constrained phosphines lack any follow up reactivity after complexation, except for those recently disclosed by Radosevich and co-workers. Iridium complex **VI** was shown to activate (Ph)E–H bonds either cooperatively across the Ir–P bond for E = O, or solely at the metal with the phosphine behaving as a spectator ligand for E = S and Se (Scheme 3.4a).[14] Such difference in reactivity was attributed to better orbital overlap between the phosphorus and oxygen centres, while the softer iridium preferentially bound to the heavier chalcogens. Over time, complex **VI** dimerises, demonstrating the retention of phosphorus-based Lewis acidity following coordination to a transition metal. Radosevich also reported cationic group 8 metal complexes **VII** and **VIII**, and demonstrated their ability to associate a fluoride or hydride ion to the

phosphorus centre, respectively (Scheme 3.4b and 3.4c).[15,16] The latter of these underwent further reactivity by delivering the associated hydride to unsaturated substrates, demonstrating fully phosphorus-based hydride transfer catalysis whereby the transition metal (ruthenium) maintains a spectator role.

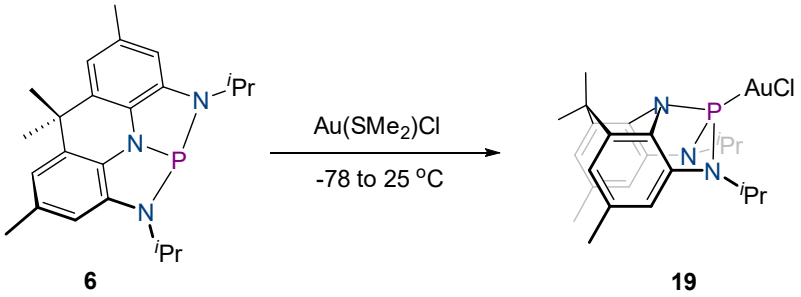


Scheme 3.4. Reported examples of the reactivity of transition metal bound geometrically constrained phosphines.

3.2 Ligand properties of 6

3.2.1 Coordination chemistry

Reaction of **6** with $Au(SMe_2)Cl$ results in L-type ligand exchange to yield complex **19** (59% isolated yield, Scheme 3.5). This complex features a $^{31}P\{^1H\}$ NMR resonance of 126.8 ppm (s); a signal which splits into a triplet in the ^{31}P NMR spectrum ($^3J_{P–H}$ = 12.5 Hz) confirming the retention of each ligand P–N bond. The ^1H NMR spectrum of **19** displays signals corresponding to a bent acridane backbone, a structural motif corroborated through SCXRD (Figure 3.1); N1–P–N3 (°) = 128.0(4).



6 **19**

Scheme 3.5. Synthesis of complex **19**.

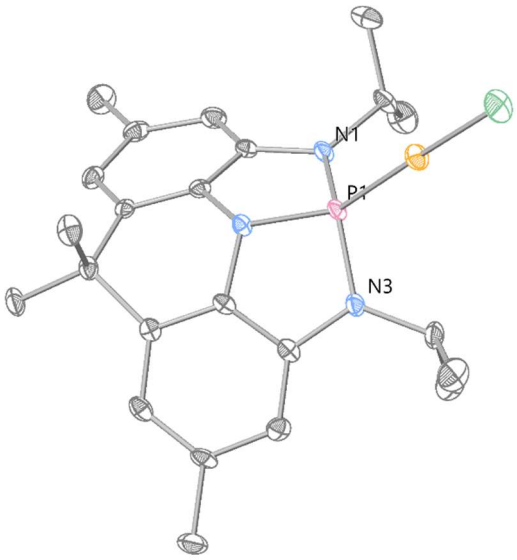


Figure 3.1. Solid-state structure of complex **19**. Thermal ellipsoids pictured at 50% probability level. Hydrogen atoms and solvent of crystallisation removed for clarity.

This distortion away from planarity towards a structure resembling that of the methyl phosphonium ion, **7**, and phosphine chalcogenides, **11**–**13**, relaxes the geometric constraint at phosphorus, resulting in

reduced s-orbital character of the phosphorus lone-pair of electrons (from 74% to 61% by NBO analysis, see Chapter 2).[17] As such, this geometry provides increased Lewis donor capacity at phosphorus, hence being the favoured conformation on complexation to transition metals.[18–20] Calculations at the ZORA-ωB97X-D3/{ZORA-def2-TZVPP, SARC-ZORA-TZVPP(Au)} level of theory confirmed the greater stability of this bent conformation (**19**$_{\mathbf{bent}}$) compared to the planar conformer (**19**$_{\mathbf{planar}}$). The latter was identified as a transition state structure through the presence of a single negative frequency along a bending coordinate relating the two geometries (Figure 3.2). Thus, the difference in energy between these two conformations was calculated as the energy barrier to phosphorus inversion for this complex (Scheme 3.6): $\Delta G^{\ddagger}$ = 22.3 kcal/mol at 298 K ($\Delta H^{\ddagger}$ = 19.76 kcal/mol, $\Delta S^{\ddagger}$ = −2.58 kcal/mol).

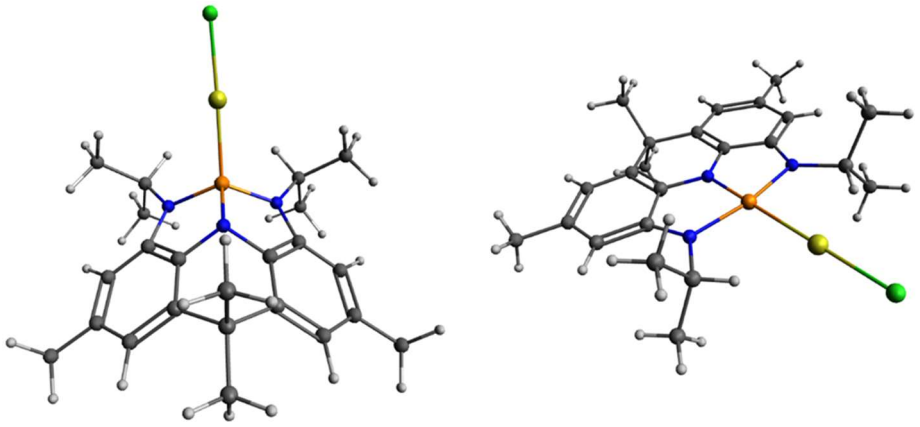
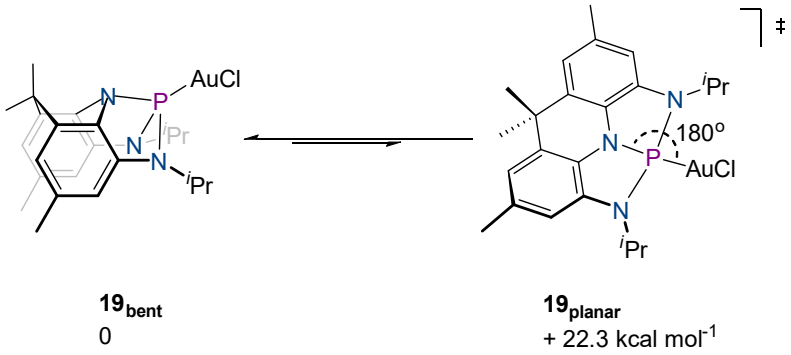


Figure 3.2. Calculated optimised geometries of **19**$_{\mathbf{bent}}$ (left) and **19**$_{\mathbf{planar}}$ (right). For **19**$_{\mathbf{planar}}$ the central N–P–Au angle was constrained to 180° throughout the optimisation.



Scheme 3.6. Phosphorus inversion of **19**$_{\mathbf{bent}}$ *via* **19**$_{\mathbf{planar}}$.

Variable-temperature ^{1}H NMR measurements (at 500 MHz) were conducted on a d_8-toluene solution of **19** to experimentally probe this computed inversion energy barrier (Figure 3.3). The diagnostic signals being monitored were the ^{1}H NMR resonances of the *iso*-propyl methyl groups; in a planar coordination mode these are equivalent, while for a bent acridane backbone, those above or below the acridane ring system are inequivalent, and provide sufficient chemical shift separation for line shape analysis. At low temperature (243 K) signals corresponding to a bent acridane backbone are observed, evidenced by the presence of two doublets each integrating to six protons centred at 1.12 and 0.98 ppm. Increasing the sample temperature results in the coalescence of these doublets at 328 K owing to fast inversion of **19** *via* $\mathbf{19_{planar}}$, until at 373 K a single doublet integrating to twelve protons at 1.29 ppm remained. Overall, the high temperature spectrum corresponds to that of a C_{2v} symmetric (i.e. averaged planar) acridane backbone.

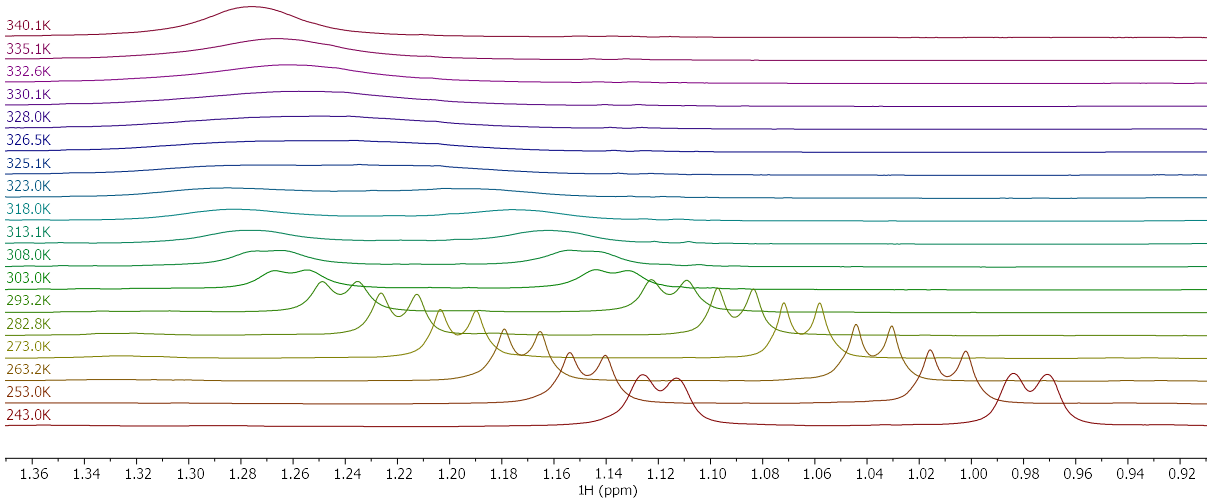


Figure 3.3. Stacked ^{1}H NMR spectra of **19** in d_8-toluene at increasing temperatures. Spectral width limited to the region corresponding to the *iso*-propyl methyl groups. For clarity, only the slow and intermediate exchange regions are displayed.

On increasing temperature, along with signal coalescence corresponding to rapid phosphorus inversion, a temperature-dependence of the chemical shift of the relevant signals was observed. Therefore, prior to line shape analysis, the temperature dependence of these chemical shifts must be determined. It was found that a second-order polynomial function sufficiently describes this phenomenon, identified through tracking the movement of these signals in the slow exchange regime (Figure 3.4).

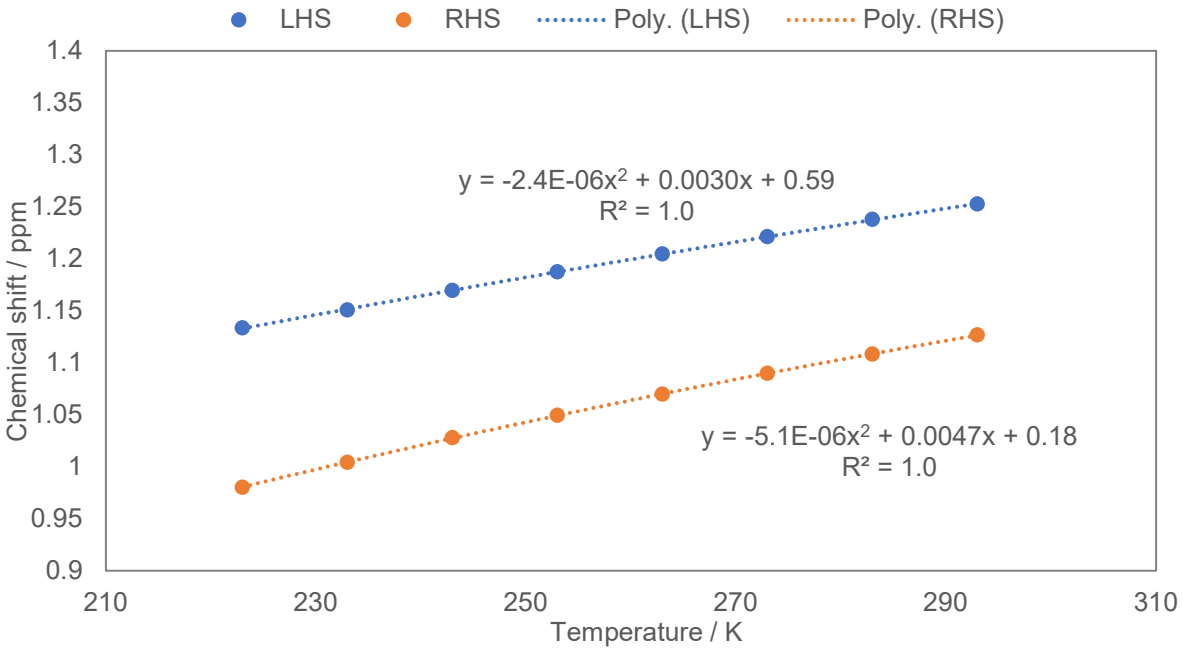


Figure 3.4. A plot of the chemical shifts of the *iso*-propyl C*H*$_3$ environments at different temperatures within the slow-exchanging regime. LHS refers to the left-hand signal, while RHS refers to the right-hand signal.

Exchange line shapes for the intermediate exchange regime using chemical shift values obtained from the equations in Figure 3.4, were fitted using Dynamic NMR (D NMR) such that exchange rate constants, *k*, for each temperature could be calculated (Figure 3.5).

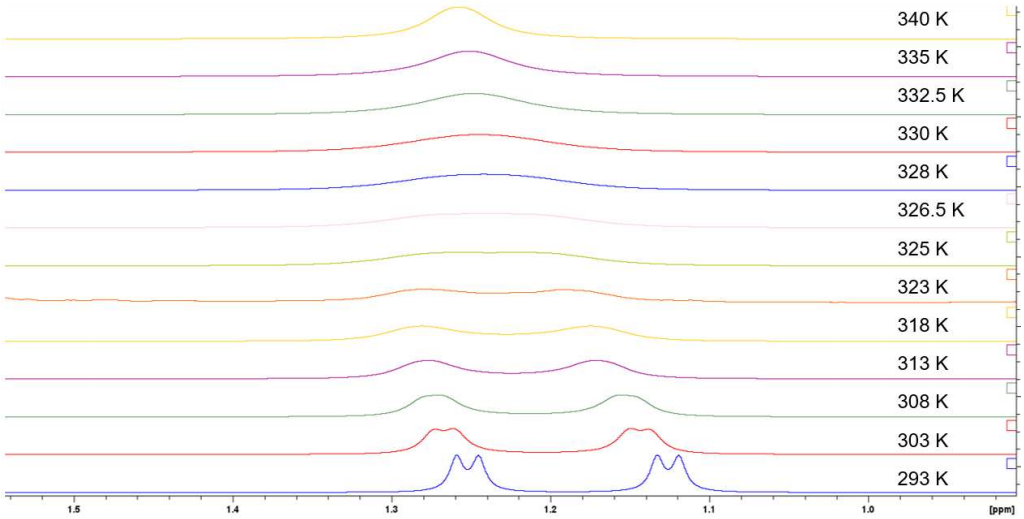


Figure 3.5. Stacked simulated ^{1}H NMR spectra within the intermediate exchange regime of **19**.

An energy barrier to inversion of 19.3(5) kcal/mol was calculated through Arrhenius analysis of these data (Figure 3.6). This value, independent of entropy, aligns closely with the enthalpy of activation obtained through DFT calculations (cf. 19.76 kcal/mol).

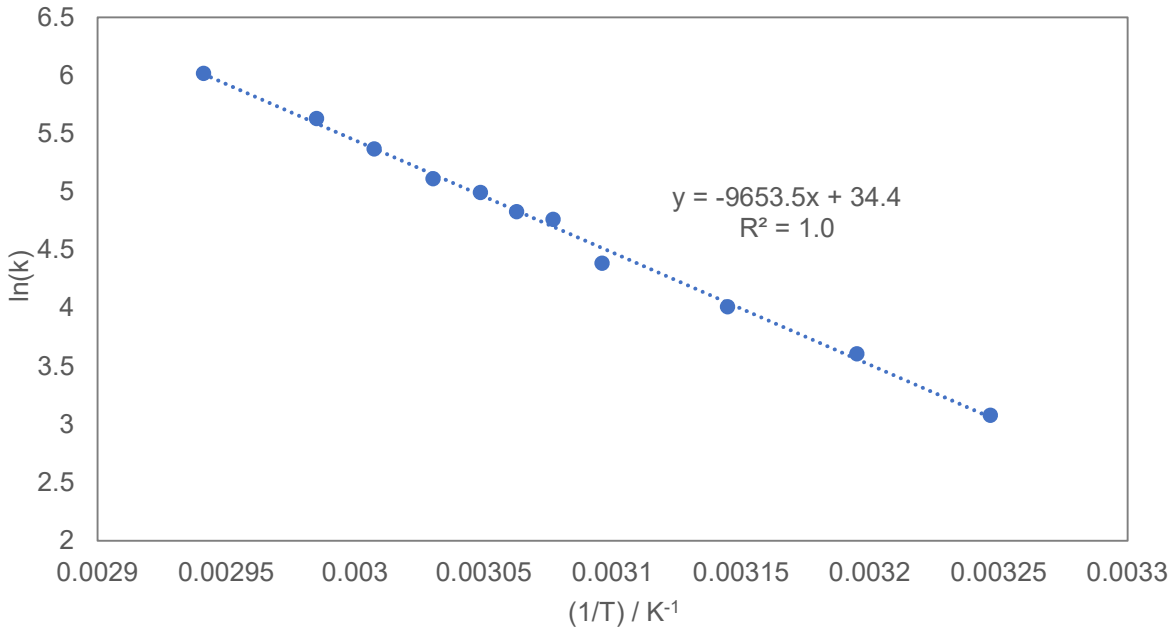
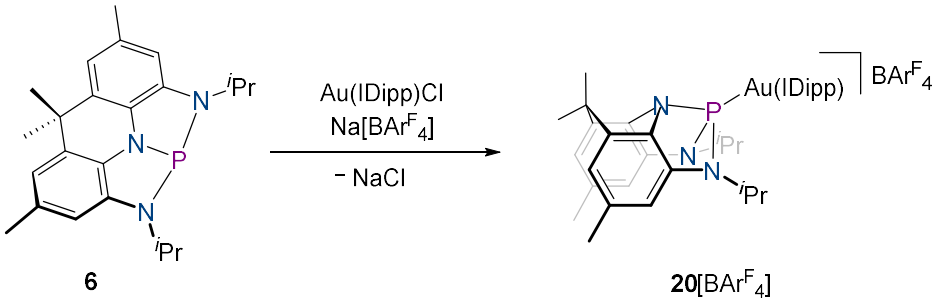


Figure 3.6. A plot of ln(*k*) versus 1/T (Arrhenius plot) using the values for k obtained through line-fitting analysis.

3.2.2 σ-Donor ability of 6

The $^{13}C\{^{1}H\}$ NMR chemical shift of the carbenic carbon of complexes of the type [Au(NHC)L][X] is highly sensitive to the σ-donor strength of the ligand located in a *trans* position relative to the carbene.[21–23] Such a complex, featuring **6** as the L-type ligand, was targeted through the reaction of **6** with NHC complex Au(IDipp)Cl (IDipp = 1,3-bis(2,6-diisopropylphenyl)imidazole-2-ylidene) in the presence of Na[BAr^F_4]. This reaction proceeded with the precipitation of NaCl, and afforded salt **20**[BAr^F_4] in 31% isolated yield (Scheme 3.7).



Scheme 3.7. Synthesis of complex **20**[BAr^F_4].

20[BAr$^{F}_{4}$] is characterised by a singlet $^{31}P\{^{1}H\}$ NMR signal at 145.7 ppm which, as with compound **19**, splits into a triplet ($^{3}J_{P–H}$ = 11.7 Hz) in the ^{31}P NMR spectrum. The $^{13}C\{^{1}H\}$ NMR spectrum of **20**[BAr$^{F}_{4}$] features a doublet at 186.1 ppm ($^{2}J_{P–C}$ = 196.1 Hz) corresponding to the carbenic carbon of the IDipp ligand (Figure 3.7). This value is slightly lower than that of the respective PPh_3 complex (188.2 ppm), and significantly lower than the P^{n}Bu$_3$ and P^{t}Bu$_3$ complexes (191.6 and 191.9 ppm, respectively), suggesting **6** to be only a moderate σ-donor, relatively weak compared to most phosphines.[24]

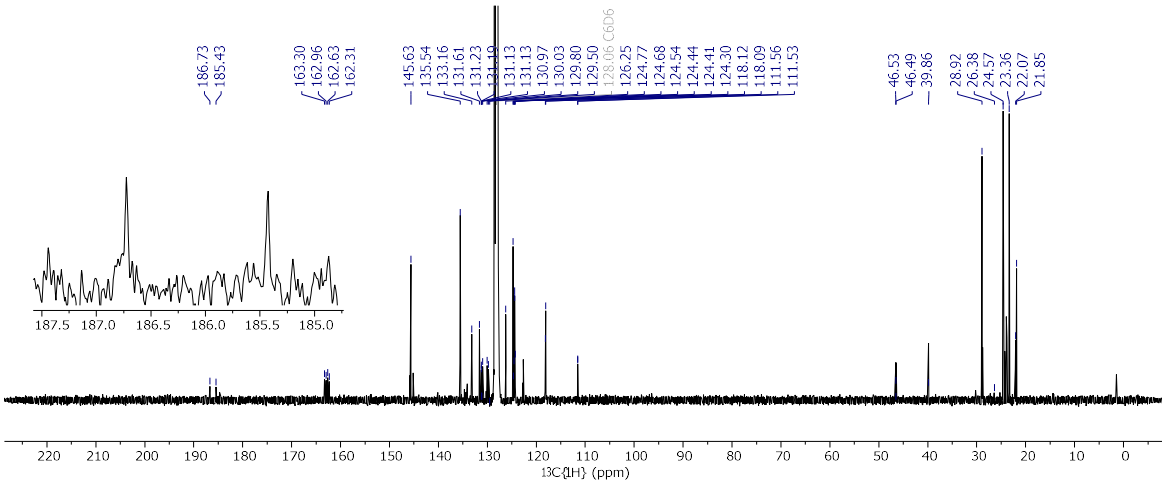


Figure 3.7. $^{13}C\{^{1}H\}$ NMR spectrum of **20**[BAr$^{F}_{4}$] in C_6D_6. Inset: spectrum enhanced at the IDipp carbenic carbon resonance.

SCXRD analysis of **20**[BAr$^{F}_{4}$] revealed a bent acridane backbone at the phosphine ligand (Figure 3.8), a structure corroborated through ^{1}H NMR spectroscopy. The P–Au–C bond angle of 167.61(10)° is significantly distorted from linearity, more so than the respective PPh_3 complex (174.61(12)°), a facet of the unsymmetrical distribution of steric bulk about the bent phosphine in **20**.

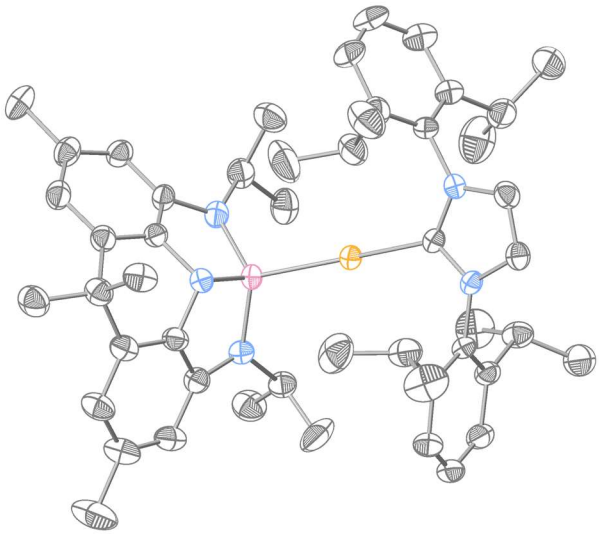
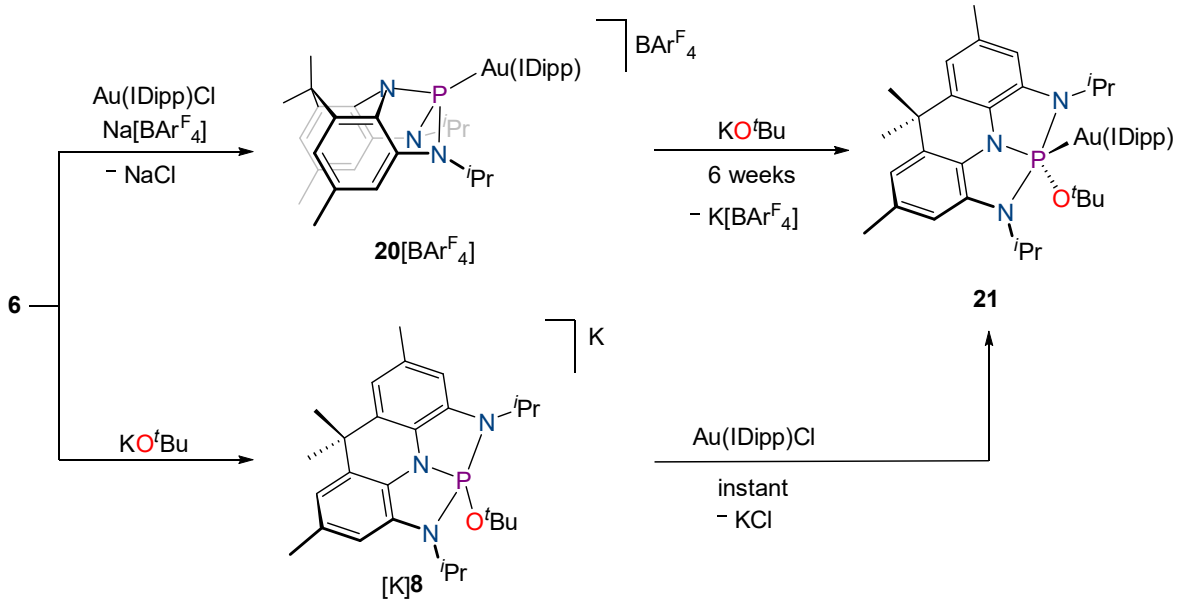


Figure 3.8. Solid-state structure of complex **20**[BAr^F_4]. Thermal ellipsoids pictured at 50% probability level. Hydrogen atoms, solvent of crystallisation and the counterion removed for clarity.

Exchange of the weakly coordinating borate anion of **20**[BAr^F_4] to a more strongly coordinating counterion was targeted. Reaction of **20**[BAr^F_4] with potassium *tert*-butoxide resulted in the appearance of a new resonance at 46.3 ppm in the $^{31}P\{^1H\}$ NMR spectrum after stirring for several days. This reaction was slow, with full conversion to the anion exchanged product (**21**) achieved after six weeks (Scheme 3.8). Therefore, an alternative route, *via* the initial synthesis of phosphine alkoxide [K]**8** by reaction of **6** with potassium *tert*-butoxide (see Chapter 2), followed by reaction with Au(IDipp)Cl, was used for the isolation and characterisation of **21** (33% isolated yield, Scheme 3.8).



Scheme 3.8. Synthesis of complex **21**.

SCXRD of **21** revealed that, upon close association of the alkoxide anion to the phosphorus centre (P–O bond length; 1.628(2)Å), planarisation of the acridane backbone occurred to provide a five-coordinate (at phosphorus) structure between square pyramidal and pentagonal bipyramidal geometry (τ_5 = 0.38, Figure 3.9); N2–P1–O1 (°) = 114.9(4); N2–P1–Au1 (°) = 140.9(4).[25] In this structure, the gold centre and *tert*-butoxide unit reside in the trigonal plane, with the meridionally coordinating acridane ligand occupying one equatorial and two axial positions. The P–Au bond length is shortened with respect to that of **20** — suspected to be a result of increased steric crowding about the phosphorus centre due to both the planarised acridane fragment, and the additional alkoxide ligand; P1–Au1 (Å) = 2.351(3) (**21**), 2.257(1) (**20**).

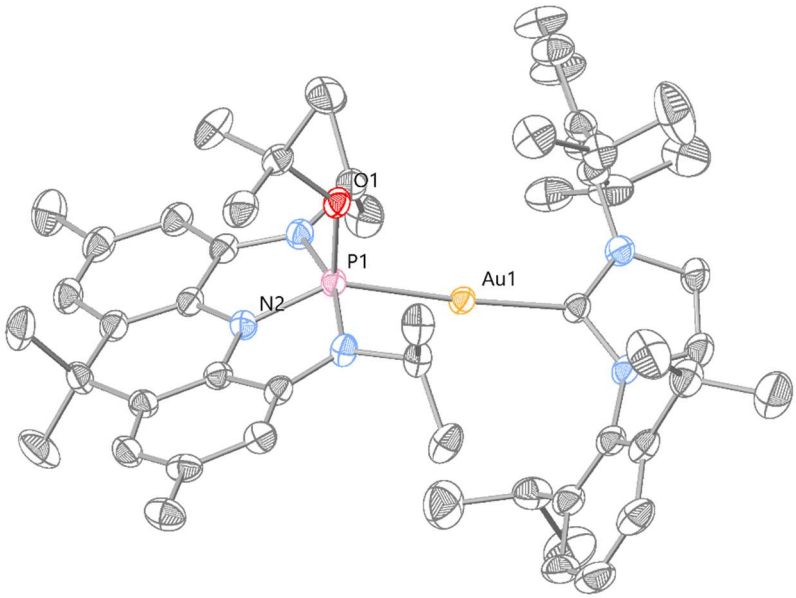


Figure 3.9. Solid-state structure of **21**. Thermal ellipsoids pictured at 50% probability level. Hydrogen atoms and solvent of crystallisation removed for clarity.

The $^{13}C\{^1H\}$ NMR spectrum of **21** reveals a carbenic carbon chemical shift of 192.7 ppm (d, $^2J_{P-C}$ = 256.3 Hz), representing a downfield shift with respect to that of **20**[BAr^F_4] (Figure 3.10). This value suggests an increased σ-donor strength of the phosphorus lone-pair; a result of increased Lewis basicity at phosphorus afforded through anion association. Previously, this process was termed "L/X-switching" with regard to the coordination mode of the phosphine.[15,16] Together these data confirm that, in cationic complexes such as **20**, the positive charge is localised at the phosphorus centre, with exchange of the weakly coordinating anion a possible route of tuning the σ-donor strength of the P–M interaction.

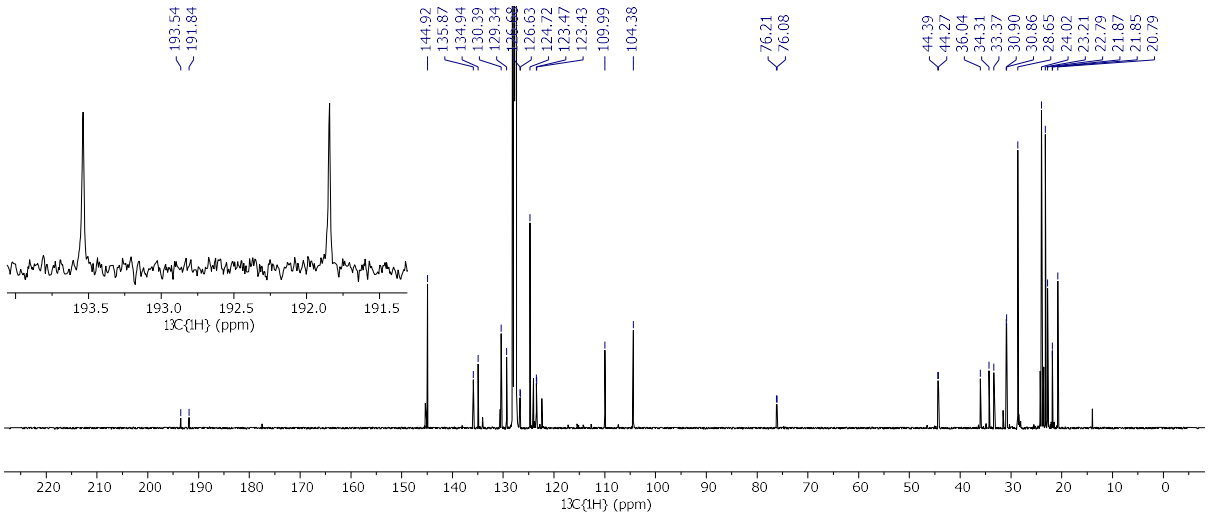
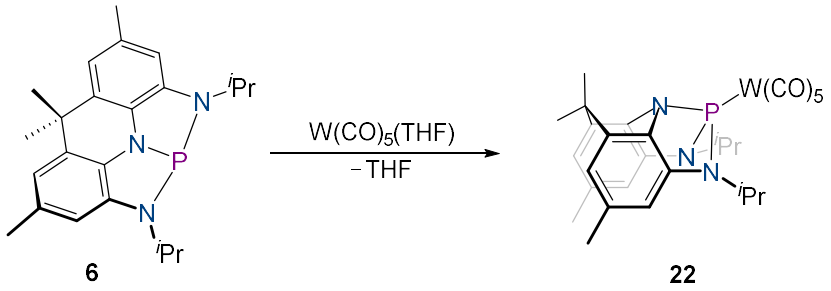


Figure 3.10. $^{13}C\{^{1}H\}$ NMR spectrum of **21** in C_6D_6. Inset: enhanced at the IDipp carbenic carbon resonance.

3.2.3 π-Acceptor ability of 6

As discussed previously, geometric constraint results in an energetically accessible, p-type LUMO at phosphorus (see Chapter 2). This has a significant impact on the reactivity of **6**, resulting in predominantly Lewis acidic, or electrophilic, reaction pathways. Therefore, it was likely that this orbital perturbation would have a stark impact on the bonding of **6** to a transition metal. To investigate this, **6** was reacted with *in situ* generated $W(CO)_5(THF)$, formed through the UV-irradiation of the respective hexacarbonyl complex in THF, to provide tungsten phosphine complex **22** (Scheme 3.9).



Scheme 3.9. Synthesis of tungsten phosphine complex **22**.

SCXRD analysis of **22** revealed a bent acridane backbone, as is common amongst the gold complexes of **6** discussed previously, and a pseudo-octahedral geometry about the tungsten centre (Figure 3.11). The P–W–C_{axial} bond angle of 165.88(7)° is significantly distorted form linearity; a structural motif generally ascribed to the steric clash between the equatorial carbonyl ligands at tungsten, and the phosphene-based substituents for such compounds.[26]

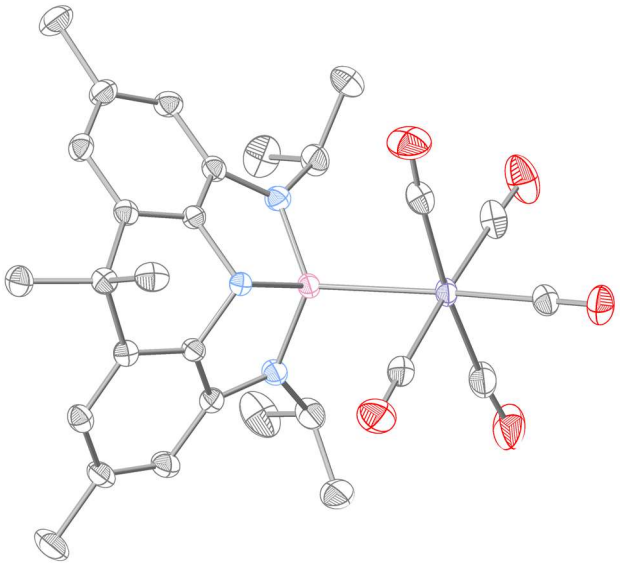


Figure 3.11. Solid-state structure of complex **22**. Thermal ellipsoids pictured at 50% probability level. Hydrogen atoms removed for clarity

A comparison with reported complexes of the type $W(PR_3)(CO)_5$ offers further insight into the extent of this distortion. For the respective PMe_3 complex, the P–W–C_{axial} bond angle of 179.3(3)° approaches linearity, providing an overall octahedral tungsten centre.[26] The W–P bond length of this complex is 2.516(2) Å — a benchmark for complexes of this type with minimal steric clash between the phosphine and carbonyl substituents. Meanwhile, the respective P^tBu_3 complex which has more sterically imposing substituents, features a more acute P–W–C_{axial} bond angle of 175.6(6) Å and an extended P–W bond length of 2.686(4) Å.[27] Both of these metrics were attributed to the increased steric bulk at the phosphine ligand. In the case of the **22**, the significant distortion of the P–W–C_{axial} bond angle initially suggests a large degree of steric crowding, more so than for P^tBu_3, however, the W–P bond length of 2.498(1) Å is shorter than that observed for the PMe_3 complex, indicating a significantly stronger bond.

It was postulated that the W–P bond strengthening arose through significant π-back-donation from the tungsten centre to the LUMO of the phosphine in **22**. To probe this, IR spectroscopy measurements were conducted for complex **22** (Figure 3.12). The $A_1^{(1)}$ stretching frequency of the carbonyl ligands in complexes of the type $ML(CO)_x$ has been used as an indicator of the π-acceptor abilities of the ligand L, providing an alternative to the Tolman Electronic Parameter.[28] Strong π-accepting ligands result in

less back-donation to the carbonyl ligands, thus strengthening the C–O bonds which results in a blue-shift of the $A_1^{(1)}$ band. Complex **22** displays a series of IR stretching frequencies in the region 2070–1850 cm^{-1} corresponding to the carbonyl co-ligands. However, one of these bands was significantly broadened and hampered assignment of these stretches. This band was assigned (*vide infra*) as the degenerate E set of vibrations, presumed to be broadened on account of the unsymmetrical nature of the substituents of ligand **6** (i.e. the bent acridane backbone) thus reducing overall molecular symmetry and lifting the degeneracy of this stretch. Instead, the dispersive Raman spectrum of **22** was collected, whereby the degenerate E set of stetches are symmetry forbidden. As a result, the intensity of this band was drastically reduced, enabling the assignment of the four expected carbonyl stretching frequencies (Figure 3.12).

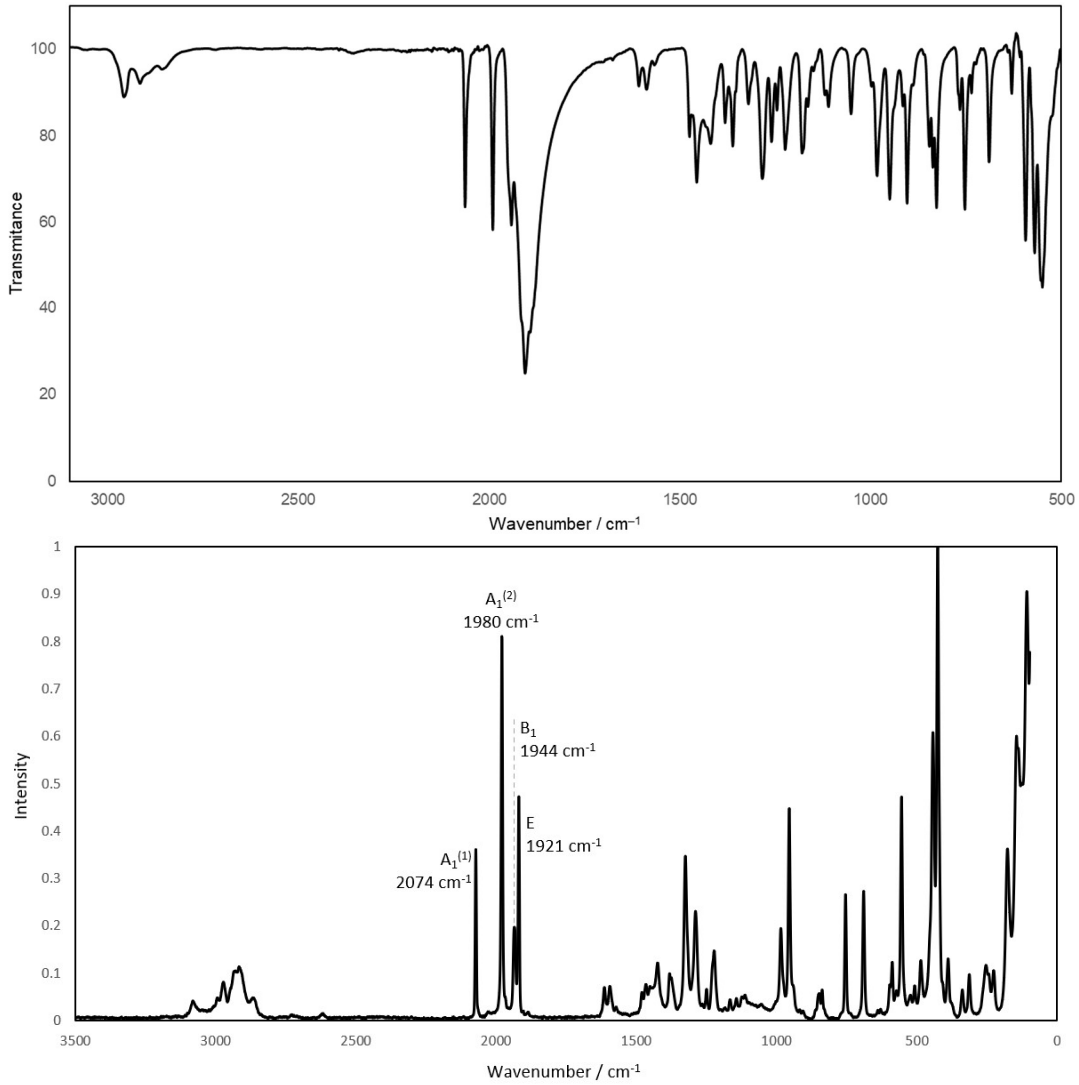


Figure 3.12. ATR-FTIR spectrum (top) and the dispersive Raman spectrum (bottom) of **22**, with the latter featuring assignments of the stretching bands.

The $A_1^{(1)}$ stretching frequency of **22** was observed at 2074 cm^{-1}. Relative to other complexes of the type $W(PR_3)(CO)_5$, this stretching frequency is observed at high wavenumbers, implying that **6** is a poor σ-donor and that a significant degree of π-back-donation from the metal centre to the phosphine is likely. As this method of measuring π-interaction is susceptible to synergistic effects, further methods, based on heteronuclear NMR measurements, were employed. For context, the following data is given relative to that of PPh_3 — a phosphine of similar σ-donor strength, providing good grounds for comparison of π-effects.

In its $^{31}P\{^1H\}$ NMR spectrum, complex **22** exhibits a singlet resonance at 129.2 ppm bearing two, low intensity, satellite doublet peaks corresponding to coupling to the 14.3% abundant, spin ½, ^{183}W nucleus ($^1J_{P–W}$ = 369 Hz, Figure 3.13).

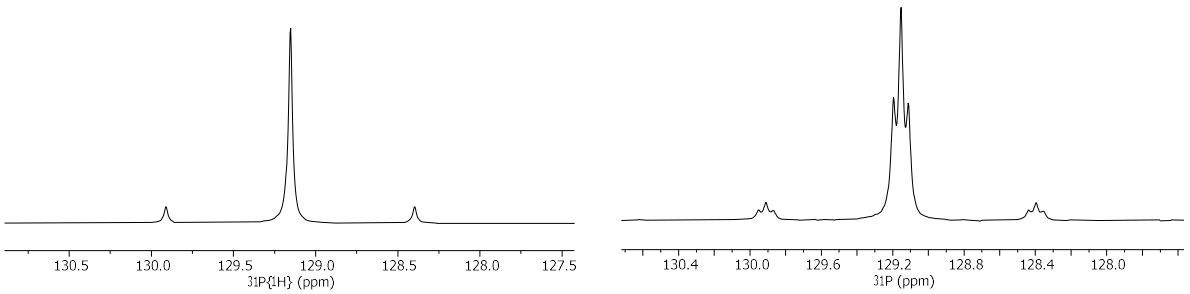


Figure 3.13. $^{31}P\{^1H\}$ (left) and ^{31}P (right) NMR spectra of **22** in C_6D_6.

The magnitude of $^1J_{M–P}$ coupling in phosphine-metal complexes is influenced by the s-character of the phosphorus lone-pair.[29] This was previously demonstrated to be high in the case of **6**, both through NBO analysis and the observation of a large $^1J_{P–Se}$ coupling in the respective selenophosphorane.[17] Another factor influencing the magnitude of $^1J_{M–P}$ coupling is the π-acceptor capacity of the transition metal bound phosphine; with strong π-acceptors showing a greater coupling constant.[30,31] The coupling constant measured for **22** is comparatively large with respect to other phosphine complexes of the type $WL(CO)_5$ (Table 3.1), for instance the moderate π-accepting ligand PPh_3 ($^1J_{W–P}$ = 280 Hz).[32] Generally, a plot of $^1J_{W–P}$ versus $\nu(A_1^{(1)})$ for such complexes yields a positive linear correlation as each increase with stronger ligand π-acceptance — a trend observed in the case of **22**, albeit with a relatively weaker fit compared to the literature data (Figure 3.14).

Table 3.1. Values of $A_1^{(1)}$ and $^1J_{W-P}$ for previously reported complexes of the type $WL(CO)_5$.

L	$A_1^{(1)}$ / cm^{-1}	$^1J_{W-P}$ / Hz	Ref.
PF_3	2101	485	[33]
$P(CF_3)_3$	2101		[34]
PCl_3	2094	426	[35]
PBr_3	2092	398	[35]
$PMe(CF_3)_2$	2091		[34]
$P(OPh)_3$	2083	415	[32]
$PMe_2(CF_3)$	2081		[34]
$P(OMe)_3$	2079	387	[36]
PPh_3	2072	280	[32]
PPh_2Me	2073	245	[30]
PPh_2Et	2073	240	[30]
$PPh_2{}^iPr$	2074	240	[30]
$PPh_2{}^nBu$	2073	250	[30]
$PPh_2{}^tBu$	2072	240	[30]
PPh^nBu_2	2071	235	[30]
$PPh(NEt_2)_2$	2070	290	[36]
PMe_3	2069	227	[32]
$P(NMe_2)_3$	2067	313	[32,37]
22	2074	369	–

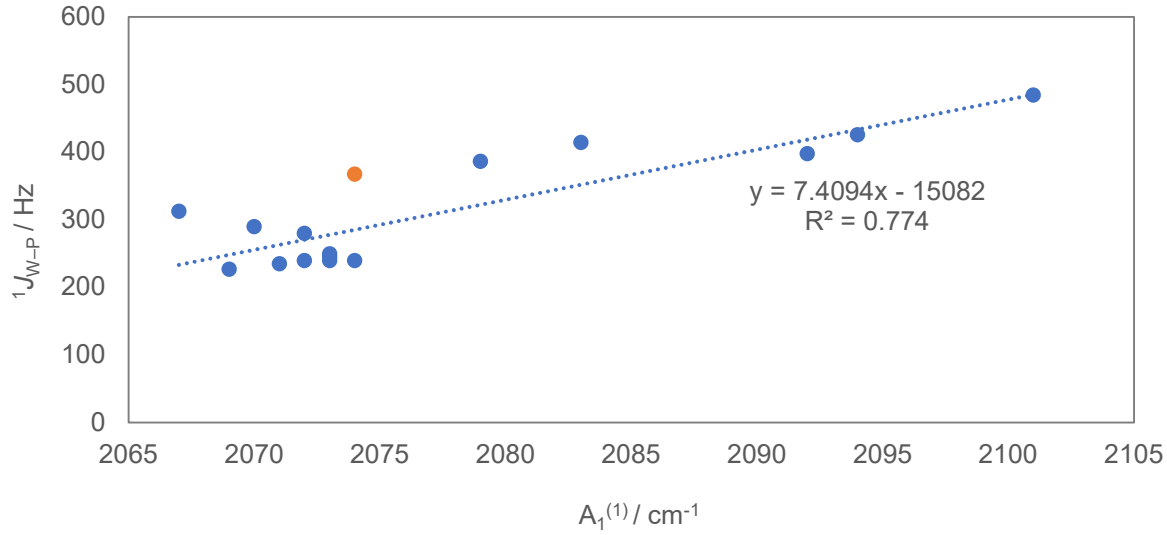


Figure 3.14. A plot of $^1J_{W-P}$ versus $\nu(A_1^{(1)})$ for a series of $WL(CO)_5$ complexes. The data point in orange is the value corresponding to **22**, while those in blue are literature reported values.

Another indicator of π-acceptor strength is the $^{2}J_{P–C}$ coupling between a phosphine and the carbonyl co-ligands, with increased electron withdrawal by the phosphine giving rise to a larger coupling constant.[32,38] In the case of **22**, signals at 199.8 and 196.4 ppm in the $^{13}C\{^{1}H\}$ NMR spectrum correspond to the *trans* and *cis* carbonyl ligands relative to **6**, with $^{2}J_{P–C}$ = 37 and 10 Hz, respectively (Figure 3.15). These coupling constants are larger than those observed for PPh_3 ($^{2}J_{P–C}$ = 22 and 7 Hz, *trans* and *cis*, respectively), again highlighting the stronger π-acceptor capacity of **6** compared to a phosphine of comparable σ-donor strength.

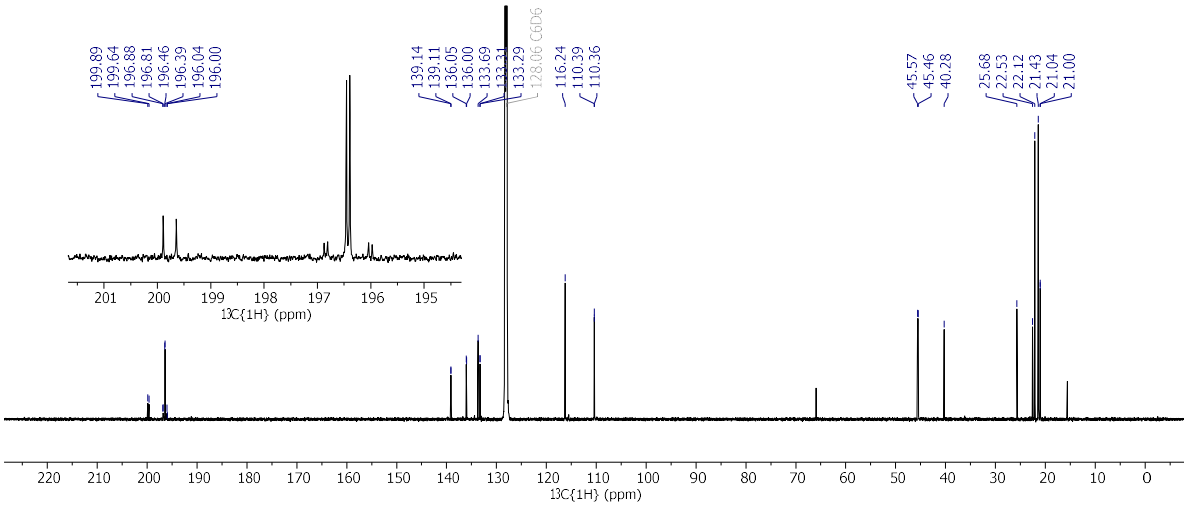


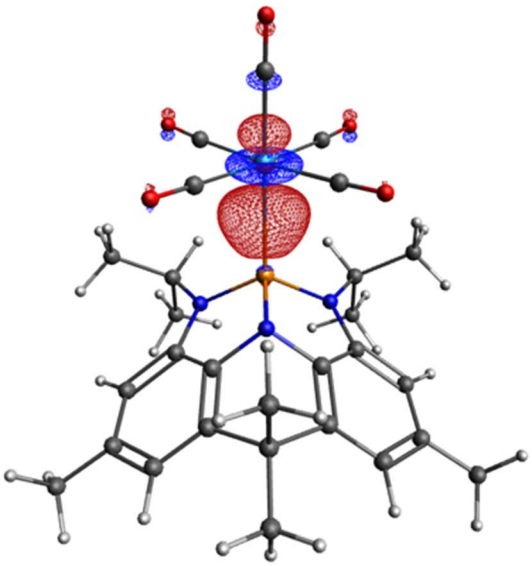
Figure 3.15. $^{13}C\{^{1}H\}$ NMR spectrum of **22** in C_6D_6. Inset: spectrum enhanced at the signals corresponding to the carbonyl co-ligands.

To gain insight into the electronics of the W–P bond in **22**, Energy Decomposition Analysis (EDA) was undertaken at the ZORA-ωB97X-D3/{ZORA-def2-TZVPP, SARC-ZORA-TZVPP(W)} level of theory (Table 3.2). The major contribution to bonding (φ_1), accounting for 59% of overall electron density movement, corresponds to the donation of the phosphorus lone-pair to tungsten in a σ-bonding fashion. The second largest contribution is π-backdonation from the metal to the phosphine, providing 33% of the bonding electron transfer. This π-contribution is significantly larger than that of PPh_3, which, at the same level of theory, accounted for 26% of overall bonding electron transfer. Typically, π-bonding in metal-phosphine complexes comprises two bonding modes corresponding to electron donation from the metal into two degenerate $\sigma^*_{P–R}$ antibonding orbitals (R = phosphine substituent). However, in the case of **22** the phosphorus-based acceptor orbitals are not

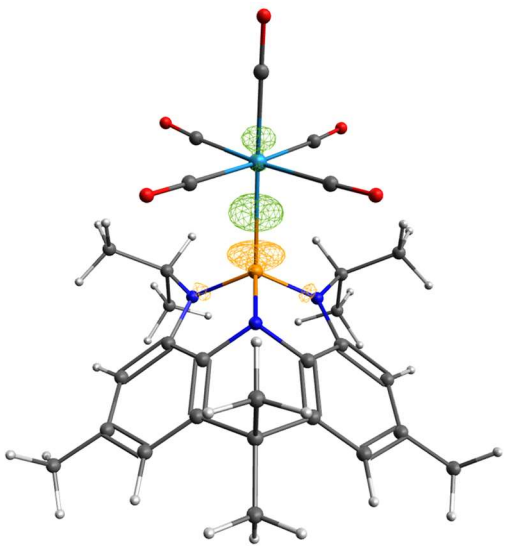
degenerate, and so do not contribute equally to overall bonding (Figure 3.16). The major π-component (φ_2, 62%) involves electron movement from the metal into a vacant p-type orbital at phosphorus — this orbital evolved from the LUMO of **6**, which is proposed to be energetically accessible by geometric constraint. The minor π-component (φ_3, 38%) consists of the typical electron donation into a σ^*_{P-R} orbital at the phosphine.

Table 3.2. Summary of EDA-NOCV analysis of the W–P bond in some representative $WL(CO)_5$ complexes, calculated at the aforementioned level of theory. Energies in kcal mol^{-1}. $\Delta E_{tot} = \Delta E_{steric} + \Delta E_{disp} + \Delta E_{oi}$.

	ΔE_{tot}	ΔE_{steric}	ΔE_{disp}	ΔE_{oi}	%σ	%π
22	–51.2	32.9	–33.0	–51.0	58.6	32.6
$W(P^tBu_3)(CO)_5$	–40.1	25.8	–25.8	–40.0	62.8	20.9
$W(PMe_3)(CO)_5$	–48.8	8.7	–25.8	–40.0	68.2	25.4
$W(PPh_3)(CO)_5$	–46.0	20.4	–20.5	–45.9	64.2	26.1
$W(P(C_6F_5)_3)(CO)_5$	–45.9	23.5	–23.7	–45.7	55.6	35.1
$W(PF_3)(CO)_5$	–63.1	4.4	–4.6	–62.8	48.5	48.0



φ_1



$\Delta\rho_1$

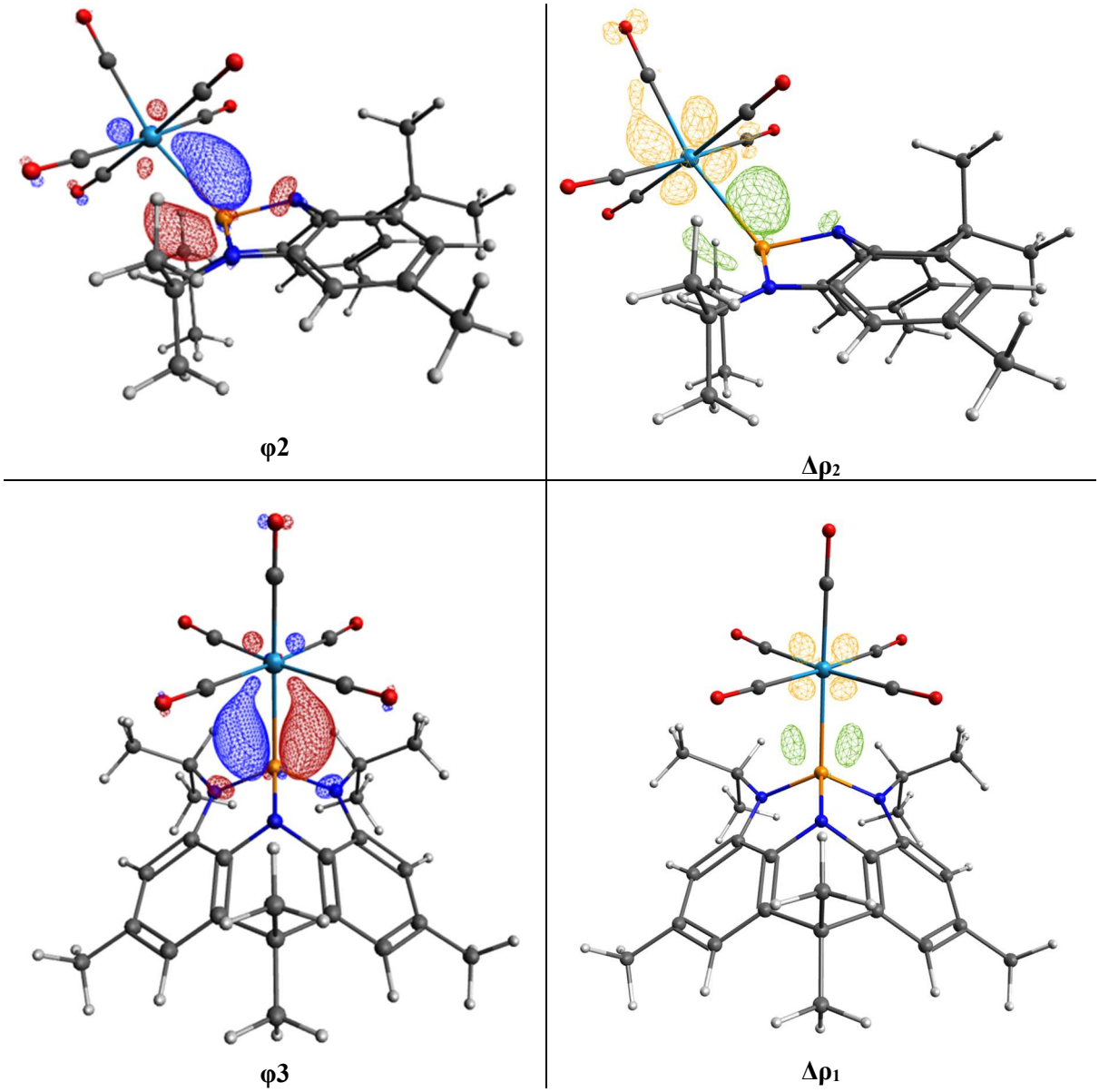
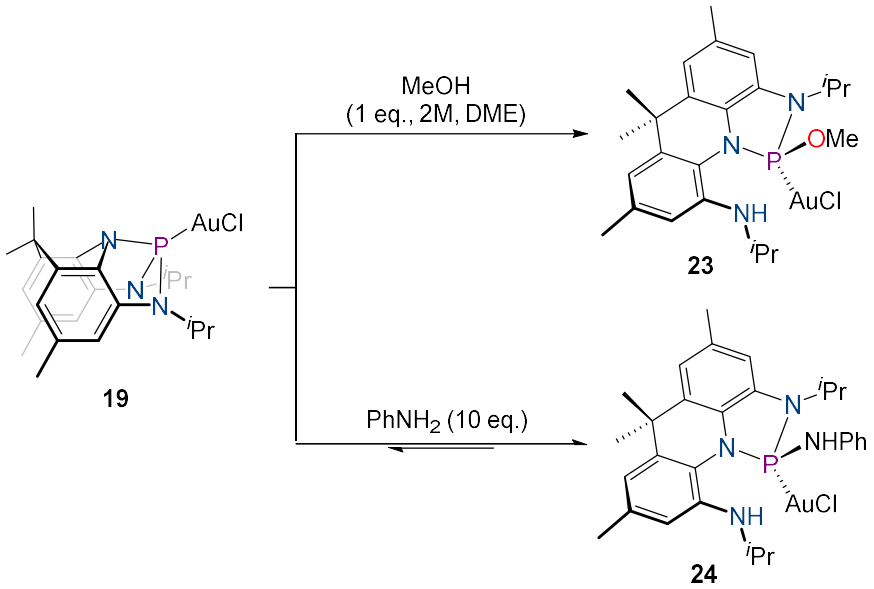


Figure 3.16. Contours of NOCVs (Natural Orbitals for Chemical Valence) φ_1, φ_2, and φ_3, ($V > 0$), and their contributions to the deformation density, $\Delta\rho_1$, $\Delta\rho_2$ and $\Delta\rho_3$ (green: $\Delta\rho > 0$, orange: $\Delta\rho < 0$) for the W–P interaction in **22**. φ_1 corresponds to σ-donation, whereas φ_2 and φ_3 correspond to π-back-donation.

3.2.4 Ligand centred reactivity of 19

As described in Chapter 2, the reaction of **6** with substrates containing E–H bonds resulted in redox-neutral cooperative bond activation proceeding with involvement of the pendant nitrogen side-arm of the acridane ligand.[17] The resulting phosphorus(III) products retained their Lewis basic lone-pair of electrons at phosphorus, and thus maintained their ability to behave as ligands to transition metals. Therefore, the reactivity of transition metal bound derivatives of **6** with protic E–H bonds was targeted to assess whether donation to a transition metal influences this reactivity.

Addition of methanol to gold complex **19** at room temperature results in the immediate appearance of a new singlet in the $^{31}P\{^{1}H\}$ NMR spectrum at 107.1 ppm. In the ^{31}P NMR spectrum this signal split into an apparent quintet ($^{3}J_{P-H}$ = 13.8 Hz), with the corresponding signals in the ^{1}H NMR spectrum at 4.07 and 2.58 ppm. The origin of this multiplet is due to coupling to a single *iso*-propyl methine proton and a methoxy group, each of comparable coupling constant. This confirms cooperative addition of the methanol O–H bond across a phosphine-based P–N bond in **19** to provide complex **23** (59% isolated yield, Scheme 3.10). Reaction with N–H bonds proceeded analogously, as revealed by reaction of **19** with aniline to give complex **24** (Scheme 3.10); characterised by a $^{31}P\{^{1}H\}$ NMR resonance at 88.8 ppm and a ^{1}H NMR spectrum featuring desymmetrised acridane backbone signals.



Scheme 3.10. Synthesis of complexes **23** and **24**.

N–H bond activation was found to be reversible, with an excess of 10 equivalents of aniline required for full conversion to **24**. Such reversibility prevented bulk isolation of **24**, as exposure to vacuum, or allowing crystals to dry under ambient conditions, resulted in significant re-formation of complex **19**. Despite this, crystals of **24** suitable for SCXRD analysis could be grown, confirming ligand centred reactivity to provide a structure akin to complex **23** (Figure 3.17). Regarding the latter, the P–O bond length is shortened with respect to that of **18**, the product of methanol addition to "free" **6**; P–O (Å) = 1.597(4) (**23**), 1.629(4) (**18**). It is suspected that this is on account of reduced electron-pair repulsion; the phosphorus lone-pair in **23** is engaged in bonding to gold, therefore interacting less strongly with those on oxygen. Both **23** and **24** contain a slightly lengthened P–Au bond with respect to **19**; P–Au (Å) = 2.206(3) (**19**), 2.220(3) (**23**), 2.255(1) (**24**). These differences were attributed to an increased steric congestion about the phosphorus centre due the substituent on the activated alcohol/amine.

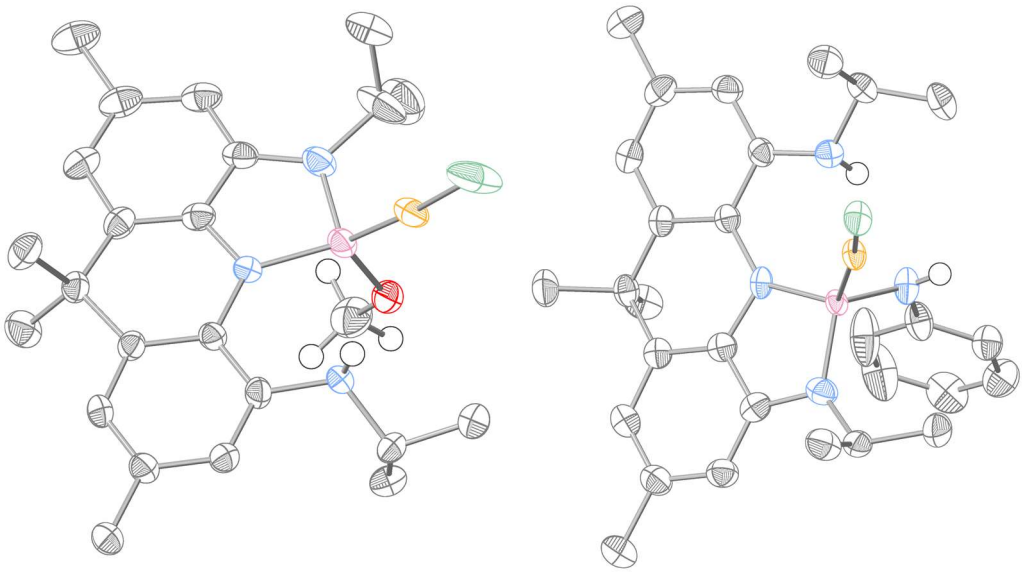
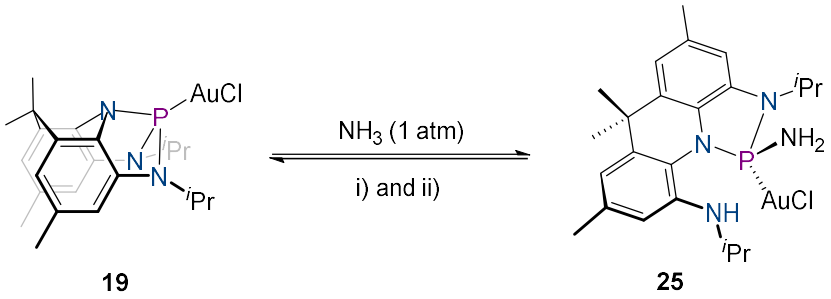


Figure 3.17. Solid-state structures of complexes **23** (left) and **24** (right). Thermal ellipsoids pictured at 50% probability level. Hydrogen atoms, except for those in the activated substrate, removed for clarity.

Having established the phosphine centred reactivity of ligated **6** with E–H bonds, a more challenging substrate was sought to assess the scope of this reaction. Ammonia, on account of strong N–H bonds and tendency to form Lewis adducts with transition metal (and main-group) compounds, is a difficult substate to harness in catalysis, and a useful benchmark for highly reactive systems.[39,40] Charging a

J. Young NMR tube containing a solution of **19** with 1 atmosphere of ammonia results in the full conversion to a new product exhibiting a $^{31}P\{^{1}H\}$ NMR resonance at 95.9 ppm. The ^{1}H NMR spectrum features a desymmetrised acridane backbone analogous to **23** and **24**, with an additional signal at 2.33 ppm corresponding to a newly formed P–NH_2 group. Together, these data confirm the formation of complex **25**, the product of phosphine-based N–H bond activation (Scheme 3.11).



19 **25**

Scheme 3.11. Synthesis of complex **25**. The reverse process was observed under the following conditions; i) N_2 (1 atm.), T > 328 K, d_8- toluene; ii) static vacuum (10^{-2} mbar), T > 308 K, d_8-toluene.

The formation of complex **25** is reversible, precluding crystallisation (with only crystals of **19** forming instead). This reversibility was further investigated through variable temperature NMR measurements on a sample of **25**. Regarding sample preparation; excess ammonia was removed *in vacuo* carefully from the reaction mixture (so as to minimise the reverse reaction). Following this, the residue was re-dissolved in d_8-toluene and sealed under a N_2 atmosphere. Heating this solution of **25** in steps of 10 K from room temperature results in the gradual formation of **19** through the loss of ammonia at temperatures above 328 K (Figure 3.18). Upon reaching the solvent limit (373 K), complexes **19** and **25** were present in a ratio of approximately 2:1 by integration of their respective $^{31}P\{^{1}H\}$ NMR signals. Following the collection of the high temperature spectra, the sample was cooled and shaken to promote the *forward* reaction; a process resulting in the consumption all generated **19** (and ammonia) to provide **25**. However, sample decomposition at these elevated temperatures was evidenced by the presence of several low intensity signals in the $^{31}P\{^{1}H\}$ NMR spectrum of the final (cooled) sample, and the deposition of colloidal gold.

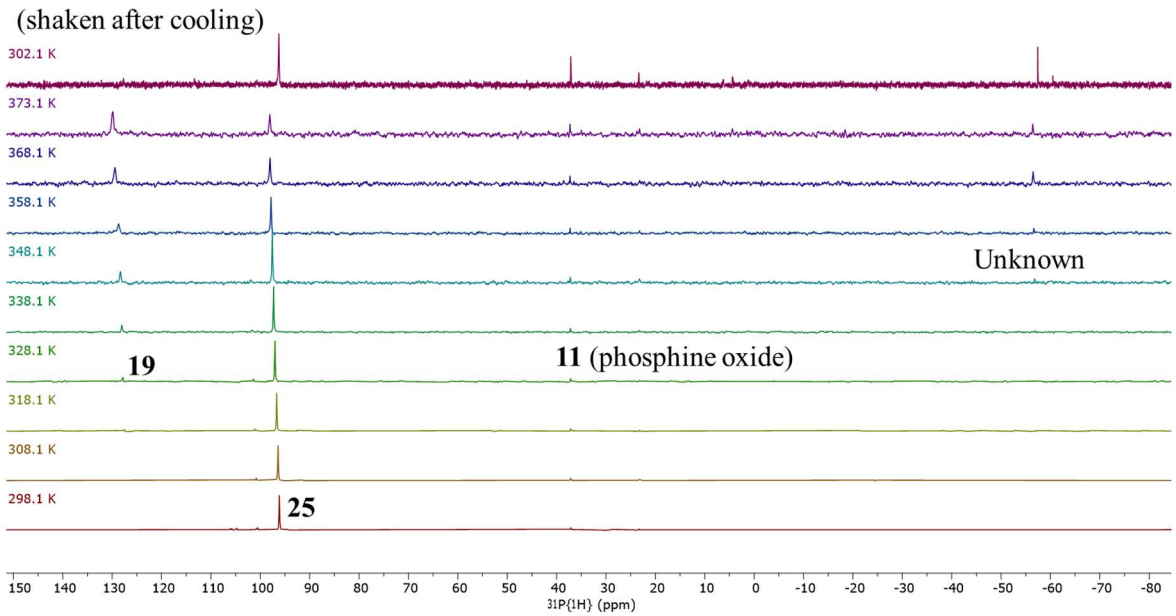


Figure 3.18. Variable temperature $^{31}P\{^{1}H\}$ NMR spectra of **25** under an N_2 atmosphere in d_8-toluene.

Sample decomposition was avoided by performing variable temperature NMR with a solution of **25** under a static vacuum of approximately 10^{-2} mbar. Under these conditions, the reverse reaction occurred at temperatures above 308 K, evidenced by the formation of **19** through $^{31}P\{^{1}H\}$ NMR spectroscopy (Figure 3.19). A product ratio of 2:1, as achieved above (Figure 3.18), was reached at 358 K; a significantly lower temperature than under ambient pressure and below the threshold of sample decomposition, such that a pure sample of **25** was returned upon cooling a shaking (Figure 3.19).

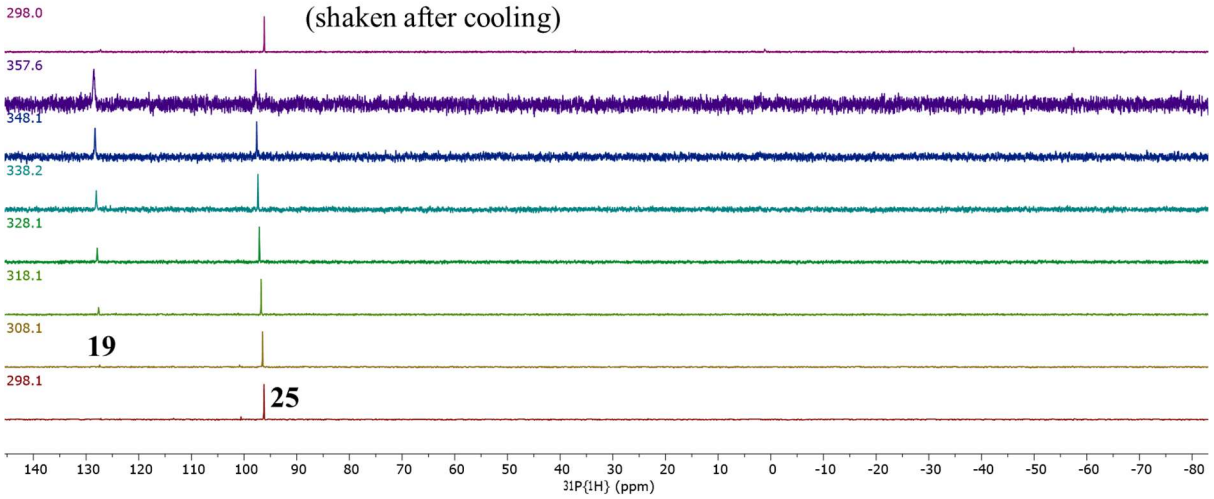


Figure 3.19. Variable temperature $^{31}P\{^{1}H\}$ NMR spectra of **25** under a static vacuum (10^{-2} mbar) in d_8-toluene.

Reversible ammonia activation, with heating as the only external stimulus, is known for ambiphilic carbenes, and only recently reported by Goicoechea and Abbenseth for a phosphorus-based compound.[41,42] Positioning the centre of reversible ammonia activation within the vicinity of a transition metal (as shown above for **19**/**25**) hints towards opportunities for metal-ligand cooperativity, ideally towards the hydroamination of unsaturated substrates.

3.3 Conclusions

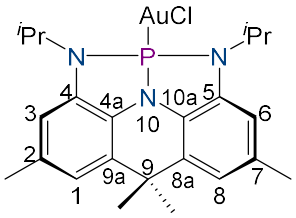
Upon complexation to transition metals, **6** adopts a bent geometry. In the case of gold(I)-chloride complex **19**, variable-temperature NMR spectroscopy revealed the structure of the phosphine to be fluxional, with a thermally accessible energy barrier to phosphorus inversion of 19.3(5) kcal/mol. **6** was shown to possess similar σ-donor properties to PPh_3 though comparison of the carbenic chemical shift for gold(I)-carbene complexes of each. Conversely, **6** is a potent π-acceptor as revealed through a combination of SCXRD, heteronuclear NMR spectroscopy, and IR/Raman spectroscopy of its respective tungsten(O)-pentacarbonyl complex **22**, in addition to Energy Decomposition Analysis calculations. While acting as a ligand, phosphorus centred O–H and N–H activation of alcohols and amines was maintained for complex **19**; occurring cooperatively across an acridane derived P–N bond as observed for free **6**, with no involvement of the metal fragment. Furthermore, the reversible activation of an ammonia N–H bond was observed for complex **19**, a key reaction towards to sustainable hydroamination processes.

The work in this chapter has been published in *Chemistry – A European Journal*:

A. J. King, J. M. Goicoechea, *Chem. Eur. J.* **2024**, 30, e202400624.[43]

3.4 Experimental section

3.4.1 Synthesis of 19



Phosphine **6** (10 mg, 26.4 µmol, 1.0 eq.) was dissolved in toluene (2 mL) and cooled to −78 °C. In a separate flask, $Au(SMe_2)Cl$ (7.8 mg, 26.4 µmol, 1.0 eq.) was dissolved in toluene (2 mL) and cooled to −78 °C. The solution of **6** was added dropwise to the solution of the gold complex at −78 °C, and stirred at this temperature for 2 minutes. In the dark, the reaction mixture was then warmed to room temperature over the course of 20 minutes. The solvent was removed *in vacuo* then the product extracted into hexane (3 × 1 mL) and filtered. Slow evaporation of the solvent to a final volume of 0.5 mL followed by storage at −35 °C for 48 hours resulted in the growth of yellow crystals of **19** (9.5 mg, 15.5 µmol, 59% yield) which were dried *in vacuo* for 4 hours.

^{1}H NMR (600 MHz, C_6D_6): δ (ppm) 6.57 (2H, s, $C_{1/8}H$), 6.27 (2H, s, $C_{3/6}H$), 4.00 (2H, d-sept, $^{3}J_{P-H}$ = 12.9 Hz, $^{3}J_{H-H}$ = 6.8 Hz, $C_{4/5}NCH(CH_3)_2$), 2.13 (6H, s, $C_{2/7}(CH_3)$), 1.58 (6H, br s, $C_9(CH_3)_2$), 1.23 (6H, d, $^{3}J_{H-H}$ = 6.7 Hz, $C_{4/5}NCH(CH_3)$), 1.10 (6H, d, $^{3}J_{H-H}$ = 6.7 Hz, $C_{4/5}NCH(CH_3)$).

^{1}H{^{31}P} NMR (600 MHz, C_6D_6): δ (ppm) as above, except 4.00 (2H, sept, $^{3}J_{H-H}$ = 6.8 Hz, $C_{4/5}NCH(CH_3)_2$).

^{13}C{^{1}H} NMR (151 MHz, C_6D_6): δ (ppm) 136.6 (d, $^{2}J_{P-C}$ = 1.9 Hz, $C_{4a/10}$), 135.6 (d, $^{3}J_{P-C}$ = 9.7 Hz, $C_{8a/9a}$), 134.3 (s, $C_{2/7}$), 132.4 (d, $^{2}J_{P-C}$ = 8.1 Hz, $C_{4/5}$), 117.1 (d, $^{4}J_{P-C}$ = 1.0 Hz, $C_{1/8}$), 111.2 (d, $^{3}J_{P-C}$ = 5.4 Hz, $C_{3/6}$), 46.5 (d, $^{2}J_{P-C}$ = 17.2 Hz, $C_{4/5}NCH(CH_3)_2$), 40.0 (s, C_9), 26.5 (s, $C_9(CH_3)$), 22.6 (s, $C_9(CH_3)$), 22.0 (s, $C_{2/7}(CH_3)$), 21.5 (br s, $C_{4/5}NCH(CH_3)$), 21.4 (br s, $C_{4/5}NCH(CH_3)$).

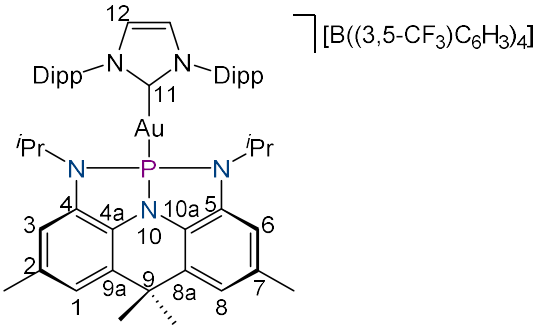
^{31}P{^{1}H} NMR (243 MHz, C_6D_6): δ (ppm) 126.8 (s).

^{31}P NMR (243 MHz, C_6D_6): δ (ppm) 126.8 (t, $^{3}J_{P-H}$ = 12.5 Hz).

Elemental analysis calcd. (%) for $C_{23}H_{30}Au_1Cl_1N_3P_1$: C 45.15, H 4.94, N 6.87; Found: C 47.91, H 5.26, N 6.51. These values are consistent with the presence of 0.5 eq. hexane in the sample: calcd. (%) for $C_{26}H_{38}Au_1Cl_1N_3P_1$: C 47.60, H 5.84, N 6.41.

HRMS (ESI) *m/z* calcd. for $C_{23}H_{30}Au_1Cl_1N_3P_1$+$Na^+$: 635.1496 [*M*+Na]$^+$; Found: 635.2203.

3.4.2 Synthesis of 20[BAr$^F_4$]



Phosphine **6** (10 mg, 26.4 µmol, 1.0 eq.), Au(IDipp)Cl (16.4 mg, 26.4 µmol, 1.0 eq.) and sodium BAr^F (23.4 mg, 26.4 µmol, 1.0 eq.) were combined and dissolved in benzene (2 mL). The mixture was stirred for 5 minutes, then the solvent was removed *in vacuo*. The product was extracted into benzene (3 × 0.5 mL) and filtered. The solution was concentrated *in vacuo* to a volume of 0.5 mL, then layered with hexane (5 mL). Storage of this layered solution at −35 °C yielded yellow needle-like crystals of **20**[BAr$^F_4$] (15 mg, 8.2 µmol, 31% yield) which were dried *in vacuo* for 4 hours.

^{1}H NMR (400 MHz, C_6D_6): δ (ppm) 8.42 (8H, br s, BArF^{Ar}*H*), 7.72 (4H, s, BArF^{Ar}*H*), 7.10 (2H, t, $^3J_{H–H}$ = 7.6 Hz, IDipp^{Ar}), 6.88 (4H, d, $^3J_{H–H}$ = 7.6 Hz, IDipp^{Ar}), 6.57 (2H, s, $C_{1/8}$*H*), 6.26 ($C_{3/6}$*H*),* 6.26 (C_{12}*H*),* 3.57 (2H, d-sept, $^3J_{P–H}$ = 11.8 Hz, $^3J_{H–H}$ = 6.7 Hz, $C_{4/5}$NC*H*(CH_3)$_2$), 2.25 (4H, sept, IDipp^{iPr}), 2.08 (6H, s, $C_{2/7}$(C*H*$_3$)), 1.59 (C_9(C*H*$_3$)),* 1.56 (C_9(C*H*$_3$)),* 1.07 (12H, d, $^3J_{H–H}$ = 6.8 Hz, IDipp^{iPr}) 0.98 (12H, d, $^3J_{H–H}$ = 6.8 Hz, IDipp^{iPr}), 0.84 (12H, br, $C_{4/5}$NCH(C*H*$_3$)$_2$).

* overlapping signals prevented integration and multiplet analysis.

^{1}H{^{31}P} NMR (600 MHz, C_6D_6): δ (ppm) above except 3.57 (2H, sept, $^3J_{H–H}$ = 6.9 Hz, $C_{4/5}$NC*H*(CH_3)$_2$).

^{13}C{^{1}H} NMR (151 MHz, C_6D_6): δ = 186.1 (d, $^2J_{P–C}$ = 196.1 Hz, *C*$_{11}$), 162.8 (q, $^1J_{B–C}$ = 50.0 Hz, BAr$^F_4$^{Ar}), 145.6 (s, IDipp^{Ar}), 135.5 (*C*$_{2/7}$),* 135.5 (BAr$^F_4$^{Ar}),* 133.2 (s, IDipp^{Ar}), 131.7 (s, IDipp^{Ar}),

131.3 – 131.0 ($C_{4/5}$ and $C_{4a/10a}$),* 129.9 (q, $^{2}J_{C–F}$ = 31.7 Hz, $BAr^{F}{}_{4}{}^{Ar}$), 126.3 (s, $BAr^{F}{}_{4}{}^{Ar}$), 124.5 ($BAr^{F}{}_{4}{}^{CF3}$),* 124.8 (s, $IDipp^{Ar}$), 124.4 (d, $^{4}J_{P–C}$ = 4.5 Hz, C_{12}), 118.1 (m, $BAr^{F}{}_{4}{}^{Ar}$), 118.1 (s, $C_{1/8}$), 111.5 (d, $^{3}J_{P–C}$ = 4.5 Hz, $C_{3/6}$), 46.5 (d, $^{2}J_{P–C}$ = 16.4 Hz, $C_{4/5}NCH(CH_3)_2$), 39.9 (s, C_9), 28.9 (s, $IDipp^{iPr}$), 26.4 (br, $C_9(CH_3)$) 24.6 (s, $IDipp^{iPr}$), 23.4 (s, $IDipp^{iPr}$), 22.1 $C_{4/5}NCH(CH_3)_2$),* 22.1 ($C_9(CH_3)$),* 21.8 (s, $C_{2/7}(CH_3)$).

* Overlapping signals prevented multiplet analysis.

** The peak corresponding to $C_{9a/8a}$ could not be located.

$^{31}P\{^{1}H\}$ NMR (162 MHz, C_6D_6): δ (ppm) 145.7 (s).

$^{31}P\{^{1}H\}$ NMR (243 MHz, C_6D_6): δ (ppm) 145.7 (t, $^{3}J_{P–H}$ = 11.7 Hz).

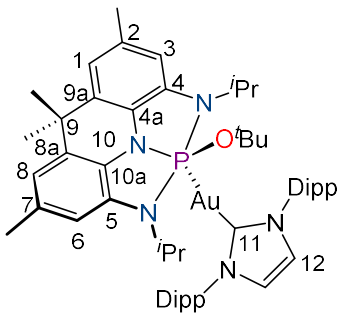
^{11}B NMR (193 MHz, C_6D_6): δ (ppm) 5.9 (s).

^{19}F NMR (471 MHz, C_6D_6): δ (ppm) –62.1 (s).

Elemental analysis calcd. (%) for $C_{82}H_{78}Au_1B_1F_{24}N_5P_1$: C 53.87, H 4.30, N 3.83; Found: C 53.57, H 3.73, N 3.65.

HRMS (ESI) *m/z* calcd. for $C_{50}H_{66}Au_1N_5P_1^{+}$: 964.4716 $[M]^{+}$; Found: 964.4720.

3.4.3 Synthesis of 21



Phosphine **6** (10 mg, 26.4 µmol, 1.0 eq.) and potassium *tert*-butoxide (3.0 mg, 26.4 µmol, 1.0 eq.) were dissolved in tetrahydrofuran and stirred for 5 minutes. The solvent was then removed *in vacuo*. Au(IDipp)Cl (16.4 mg, 26.4 µmol, 1.0 eq.) and toluene (1 mL) were subsequently added and the mixture stirred for 5 minutes. The solvent was then removed *in vacuo* and the product extracted into

benzene (3 × 0.5 mL) and filtered. The solvent was then removed *in vacuo* and the resulting residue washed with pentane (3 × 1 mL). The residue was dissolved in benzene (0.5 mL) then layered with pentane (5 mL). Storage of this layered solution at room temperature for 5 days resulted in the growth of yellow needle-like crystals of **21** (9 mg, 8.7 μmol, 33% yield) which were dried *in vacuo* for 4 hours.

^{1}H NMR (600 MHz, C_6D_6): δ (ppm) 7.16 (IDipp^{Ar}),* 7.01 (4H, d, $^{3}J_{H–H}$ = 7.9 Hz, IDipp^{Ar}), 6.55 (2H, s, $C_{1/8}H$), 6.37 (2H, s, $C_{3/6}H$), 6.25 (2H, d, $^{5}J_{P–H}$ = 1.5 Hz, $C_{12}H$), 4.34 (2H, d-sept, $^{3}J_{P–H}$ = 20.6 Hz, $^{3}J_{H–H}$ = 6.8 Hz, $C_{4/5}NCH(CH_3)_2$), 2.73 (4H, sept, $^{3}J_{H–H}$ = 6.9 Hz, IDipp^{iPr}), 2.45 (6H, s, $C_{2/7}(CH_3)$), 1.95 (3H, s, $C_9(CH_3)$), 1.82 (3H, s, $C_9(CH_3)$), 1.40 (6H, d, $^{3}J_{H–H}$ = 6.8 Hz, $C_{4/5}NCH(CH_3)$), 1.25 (12H, d, $^{3}J_{H–H}$ = 6.9 Hz, IDipp^{iPr}), 1.07 (9H, s, O^{t}Bu), 1.06 (6H, d, $^{3}J_{H–H}$ = 6.8 Hz, $C_{4/5}NCH(CH_3)$), 0.97 (12H, d, $^{3}J_{H–H}$ = 6.9 Hz, IDipp^{iPr}).

* overlap with solvent peak prevented multiplet analysis and integration

^{1}H{^{31}P} NMR (600 MHz, C_6D_6): δ (ppm) as above, except 6.25 (2H, s, $C_{12}H$), 4.34 ppm (2H, sept, $^{3}J_{H–H}$ = 6.8 Hz, $C_{4/5}NCH(CH_3)_2$).

^{13}C{^{1}H} NMR (151 MHz, C_6D_6): δ (ppm) 192.7 (d, $^{2}J_{P–C}$ = 256.3 Hz, C_{11}), 144.9 (s, IDipp^{Ar}), 135.9 (s, $C_{4/5}$), 134.9 (s, IDipp^{Ar}), 130.4 (s, IDipp^{Ar}), 129.3 (s, $C_{2/7}$), 126.7 (d, $^{3}J_{P–C}$ = 6.8 Hz, $C_{9a/8a}$), 124.7 (s, IDipp^{Ar}), 123.5 (d, $^{4}J_{P–C}$ = 6.7 Hz, C_{12}), 110.0 (s, $C_{1/8}$), 104.4 (s, $C_{3/6}$), 76.1 (d, $^{2}J_{P–C}$ = 20.2 Hz, –O^{t}Bu), 44.3 (d, $^{2}J_{P–C}$ = 18.2 Hz, $C_{4/5}NCH(CH_3)_2$), 36.0 (s, C_9), 34.3 (s, $C_9(CH_3)$), 33.4 (s, $C_9(CH_3)$), 30.9 (d, $^{3}J_{P–C}$ = 6.2 Hz, –O^{t}Bu), 28.6 (s, IDipp^{iPr}), 24.0 (s, IDipp^{iPr}), 23.2 (s, IDipp^{iPr}), 22.8 (s, $C_{2/7}(CH_3)$), 21.8 (d, $^{3}J_{P–C}$ = 3.2 Hz, $C_{4/5}NCH(CH_3)$), 20.8 (s, $C_{4/5}NCH(CH_3)$).

*The peak corresponding to $C_{10a/4a}$ could not be located.

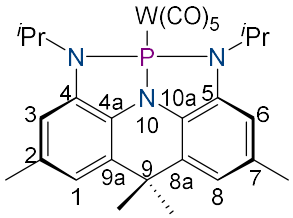
^{31}P{^{1}H} NMR (162 MHz, C_6D_6): δ (ppm) 46.3 ppm (s).

^{31}P NMR (243 MHz, C_6D_6): δ = 46.3 (br m).

Elemental analysis calcd. (%) for $C_{54}H_{75}Au_1N_5O_1P_1$: C 62.47, H 7.28, N 6.75; Found: C 62.26, H 7.02, N 6.00. The value for nitrogen is outside the accepted range – this was a recurring issue for several compounds which may indicate an instrument error.

HRMS (ESI) *m/z* calcd. for $C_{54}H_{75}Au_1N_5O_1P_1+H^+$: 1038.5448 $[M+H]^+$; Found: 1038.5426.

3.4.4 Synthesis of 22



Tungsten hexacarbonyl (9.3 mg, 26.4 µmol, 1.0 eq.) was added to a quartz J. Young NMR tube and dissolved in tetrahydrofuran (0.5 mL). The solution was freeze-pump-thaw degassed 4 times then placed under a static vacuum. The solution was subjected to UV irradiation for 4 hours. The resulting bright yellow solution was freeze-pump-thaw degassed a further 4 times, after which phosphine **6** (10 mg, 26.4 µmol, 1.0 eq.) was added and the solution stirred for 16 hours. The solvent was removed *in* vacuo and the resulting residue dissolved in benzene (0.5 mL), lyophilisation from which provided **22** as a yellow powder (5 mg, 7.1 µmol, 27% yield). Single crystals suitable for SCXRD analysis were grown from a concentrated diethyl ether solution of **22** at room temperature.

^{1}H NMR (600 MHz, C_6D_6): δ (ppm) 6.55 (2H, s, $C_{1/8}H$), 6.41 (2H, s, $C_{3/6}H$), 4.14 (2H, d-sept, $^3J_{P-H}$ = 10.4 Hz, $^3J_{H-H}$ = 6.7 Hz, $C_{4/5}NCH(CH_3)_2$), 2.15 (6H, s, $C_{2/7}(CH_3)$), 1.80 (3H, s, $C_9(CH_3)$), 1.60 (3H, s, $C_9(CH_3)$), 1.47 (6H, d, $^3J_{H-H}$ = 6.8 Hz, $C_{4/5}NCH(CH_3)$), 1.06 (6H, d, $^3J_{H-H}$ = 6.8 Hz, $C_{4/5}NCH(CH_3)$).

^{1}H{^{31}P} NMR (600 MHz, C_6D_6): δ (ppm) as above, except 4.14 (2H, sept, $^3J_{H-H}$ = 6.7 Hz, $C_{4/5}NCH(CH_3)_2$).

^{13}C{^{1}H} NMR (151 MHz, C_6D_6): δ (ppm) 199.8 (d, $^2J_{P-C}$ = 37 Hz, CO_{trans}), 196.4 (dd, $^1J_{W-C}$ = 126 Hz, $^2J_{P-C}$ = 10 Hz, CO_{cis}), 139.1 (d, $^2J_{P-C}$ = 5.2 Hz, $C_{4a/10a}$), 136.0 (d, $^3J_{P-C}$ = 8.8 Hz, $C_{8a/9a}$), 133.7 (s, $C_{2/7}$), 133.3 (d, $^2J_{P-C}$ = 2.4 Hz, $C_{4/5}$), 116.2 (s, $C_{1/8}$), 110.4 (d, $^3J_{P-C}$ = 3.9 Hz, $C_{3/6}$), 45.5 (d, $^2J_{P-C}$ = 16.7 Hz, $C_{4/5}NCH(CH_3)_2$), 40.3 (s, C_9), 25.7 (s, $C_9(CH_3)$), 22.5 (s, $C_9(CH_3)$), 22.1 (s, $C_{2/7}(CH_3)$), 21.4 (s, $C_{4/5}NCH(CH_3)$), 21.0 (d, $^3J_{P-C}$ = 6.6 Hz, $C_{4/5}NCH(CH_3)$).

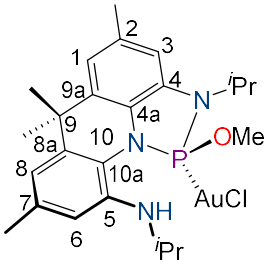
^{31}P{^{1}H} NMR (243 MHz, C_6D_6): δ (ppm) 129.2 (d, $^1J_{P-W}$ = 369 Hz).

^{31}P NMR (243 MHz, C_6D_6): δ (ppm) 129.2 (dt, $^{1}J_{P\text{-}W}$ = 369 Hz, $^{3}J_{P\text{-}H}$ = 10.4 Hz).

Elemental analysis calcd. (%) for $C_{28}H_{30}N_3O_5P_1W_1$: C 47.81, H 4.30, N 5.97; found: C 50.98, H 4.93, N 5.60. These values are consistent with the presence of 0.5 eq. benzene in the sample: calcd. (%) for $C_{31.5}H_{34}N_3O_5P_1W_1$ C 50.48, H 4.57, N 5.61.

HRMS (ESI) *m/z* calcd. for $C_{28}H_{30}N_3O_5P_1W_1$+H^+: 704.1505 $[M+H]^+$; Found: 704.1510.

3.4.5 Synthesis of 23



Gold complex **19** (13.2 µmol, 1.0 eq.) was dissolved in toluene (0.5 mL). To this solution, methanol (2 M in DME, 13 µL, 1.0 eq.) was added and the reaction mixture stirred for 5 minutes. The volatiles were removed *in vacuo* and the resulting residue dissolved in benzene (0.5 mL), lyophilisation from which provided **23** as an off-white powder (10 mg, 15.5 µmol, 59% yield). Single crystals suitable for SCXRD analysis were grown from a diethyl ether solution of **23** concentrated to an oil and stored at room temperature for two weeks.

^{1}H NMR (600 MHz, C_6D_6): δ (ppm) 6.97 (1H, s, C_1H), 6.69 (1H, s, C_8H), 6.56 (1H, s, C_3H), 6.38 (1H, s, C_6H), 4.07 (1H, d-sept, $^{3}J_{P\text{–}H}$ = 13.8 Hz, $^{3}J_{H\text{–}H}$ = 7.0 Hz, $C_4NCH(CH_3)_2$), 3.49 (1H, sept, $^{3}J_{H\text{–}H}$ = 6.3 Hz, $C_5NCH(CH_3)_2$), 2.94 (1H, br s, N*H*), 2.58 (3H, d, $^{3}J_{P\text{-}H}$ = 14.0 Hz, PO(CH_3)), 2.24 (3H, s, $C_7(CH_3)$), 2.17 (3H, s, $C_2(CH_3)$), 1.62 (3H, s, $C_9(CH_3)$), 1.58 (3H, d, $^{3}J_{H\text{–}H}$ = 6.3 Hz, $C_5NCH(CH_3)$), 1.54 (3H, s, $C_9(CH_3)$), 1.28 (3H, d, $^{3}J_{H\text{–}H}$ = 7.0 Hz, $C_4NCH(CH_3)$), 1.20 (3H, d, $^{3}J_{H\text{–}H}$ = 6.9 Hz, $C_4NCH(CH_3)$), 1.13 (3H, d, $^{3}J_{H\text{–}H}$ = 6.3 Hz, $C_5NCH(CH_3)$).

^{1}H{^{31}P} NMR (600 MHz, C_6D_6): δ (ppm) as above, except 4.07 (1H, sept, $^{3}J_{H\text{–}H}$ = 7.0 Hz, $C_4NCH(CH_3)$), 2.58 (3H, s, PO(CH_3)).

$^{13}C\{^{1}H\}$ NMR (151 MHz, C_6D_6): δ (ppm) 134.9 (s, C_5), 133.3 (d, $^{2}J_{P\text{-}C}$ = 5.7 Hz, C_{4a}), 132.8 (s, C_2), 132.3 (d, $^{2}J_{P\text{-}C}$ = 3.0 Hz, C_4), 132.2 (s, C_7), 129.0 (s, C_{9a}), 127.7 (s, C_{8a}), 123.3 (s, C_1), 121.1 (s, C_3), 116.9 (s, C_8), 108.1 (s, C_6), 50.4 (d, $^{2}J_{P\text{-}C}$ = 11.8 Hz, PO(CH_3)), 47.2 (d, $^{2}J_{P\text{-}C}$ = 18.9 Hz, $C_4NCH(CH_3)_2$), 46.8 (s, $C_5NCH(CH_3)_2$), 36.1 (s, C_9), 34.9 (s, $C_9(CH_3)$), 33.4 (s, $C_9(CH_3)$), 23.5 (s, $C_5NCH(CH_3)$), 21.5 (s, $C_7(CH_3)$), 21.1 (s, $C_2(CH_3)$), 21.1 (s, $C_5NCH(CH_3)$), 21.0 (d, $^{3}J_{P\text{-}C}$ = 1.7 Hz, $C_4NCH(CH_3)$), 20.3 (d, $^{3}J_{P\text{-}C}$ = 5.7 Hz, $C_4NCH(CH_3)$).

The peak corresponding to C_{10a} could not be located

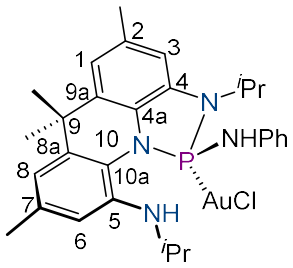
$^{31}P\{^{1}H\}$ NMR (243 MHz, C_6D_6): δ (ppm) 107.1 (s).

^{31}P NMR (243 MHz, C_6D_6): δ (ppm) 107.1 (apparent quartet, $^{3}J_{P\text{–}H}$ = 13.8 Hz).

Elemental analysis calcd. (%) for $C_{24}H_{34}Au_1Cl_1N_3O_1P_1$: C 44.77, H 5.32, N 6.53; Found: C 46.20, H 5.26, N 6.31. These values are consistent with the presence of 0.25 eq. benzene in the sample: calcd. (%) for $C_{25.5}H_{35.5}Au_1Cl_1N_3P_1$: C 46.16, H 5.39, N 6.33.

HRMS (ESI) *m/z* calcd. for $C_{24}H_{34}Au_1Cl_1N_3O_1P_1+H^+$: 644.1866 $[M+H]^+$; Found: 644.1861.

3.4.6 Synthesis of 24



Gold complex **19** (13.2 µmol, 1.0 eq.) was dissolved in benzene (0.5 mL). To this solution, aniline (1.2 mg, 13.2 µmol, 1.0 eq.) was added and the reaction stirred for 5 minutes. $^{31}P\{^{1}H\}$ NMR revealed *ca*. 40% conversion to complex **24** for this 1:1 ratio of reagents, with 10 eq. of aniline required to achieve full conversion. To achieve single crystals suitable for SCXRD analysis; the volatiles were removed *in vacuo* and the product extracted into pentane (0.5 mL), slow evaporation to half the volume and storage at room temperature for 10 minutes yielded colourless, large block-like crystals. Isolation of **24** as a bulk solid was precluded by the reverse reaction generating a significant amount of complex

19 – this was observed when re-dissolving crystals of **24** grown at −35 °C (*ca*. 50% conversion to **19** by $^{31}P\{^{1}H\}$ NMR of the dissolved crystals).

*The following ^{1}H, $^{31}P\{^{1}H\}$ and ^{13}C NMR assignments are for a sample of **24** containing ca. 30% **19**.*

^{1}H NMR (600 MHz, C_6D_6): δ (ppm) 6.91 (1H, s, C_8H), 6.74 – 6.72 (2H, m, $ArH_{aniline}$), 6.71 (1H, s, C_1H), 6.52 – 6.47 (3H, m, $ArH_{aniline}$), 6.45 (1H, s, C_6H), 6.43 (1H, s, C_3H), 5.90 (1H, br d, $^{2}J_{P\text{-}H}$ = 20.3 Hz, PN*H*(Ph)), 4.19 (1H, d-sept, $^{3}J_{P–H}$ = 14.3 Hz, $^{3}J_{H–H}$ = 7.0 Hz, $C_4NCH(CH_3)_2$), 3.45 (1H, sept, $^{3}J_{H–H}$ = 6.3 Hz, $C_5NCH(CH_3)_2$), 3.40 (1H, s, C_5NH), 2.24 (3H, s, $C_2(CH_3)$), 2.08 (3H, s, $C_7(CH_3)$), 1.60 (3H, s, $C_9(CH_3)$), 1.59 (3H, s, $C_9(CH_3)$), 1.46 (3H, d, $^{3}J_{H–H}$ = 6.3 Hz, $C_5NCH(CH_3)$), 1.38 (3H, d, $^{3}J_{H–H}$ = 7.0 Hz, $C_4NCH(CH_3)$), 1.14 (3H, d, $^{3}J_{H–H}$ = 7.0 Hz, $C_4NCH(CH_3)$), 1.13 (3H, d, $C_5NCH(CH_3)$)*.

*Overlap prevented measurement of coupling constant.

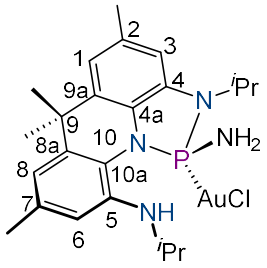
$^{1}H\{^{31}P\}$ NMR (600 MHz, C_6D_6): δ (ppm) as above, except 5.90 (1H, br s, PN*H*(Ph)), 4.19 (1H, sept, $^{3}J_{H–H}$ = 7.0 Hz, $C_4NCH(CH_3)$).

$^{13}C\{^{1}H\}$ NMR (151 MHz, C_6D_6): δ (ppm) 139.9 (d, $^{2}J_{P\text{-}C}$ = 11.5 Hz, $ArC_{aniline}$), 134.1 (s, C_5), 133.4 (d, $^{3}J_{P\text{-}C}$ = 5.1 Hz, C_{9a}), 132.7 (s, C_2), 132.3 (s, C_7), 132.2 (d, $^{2}J_{P\text{-}C}$ = 6.4 Hz, C_4), 128.7 (d, $^{2}J_{P\text{-}C}$ = 4.8 Hz, C_{10a}), 128.5 (s, C_{8a}), 127.4 (d, $^{2}J_{P\text{-}C}$ = 3.9 Hz, C_{4a}), 123.0 (s, C_8), 122.6 (s, $ArC_{aniline}$), 121.3 (s, C_6), 118.7 (d, $^{3}J_{P\text{-}C}$ = 6.8 Hz, $ArC_{aniline}$), 118.4 (s, C_1), 116.6 (s, $ArC_{aniline}$), 108.5 (d, $^{3}J_{P\text{-}C}$ = 6.0 Hz, C_3), 47.4 (s, $C_5NCH(CH_3)_2$), 46.9 (d, $^{2}J_{P\text{-}C}$ = 17.0 Hz, $C_4NCH(CH_3)_2$), 36.1 (s, C_9), 34.4 (s, $C_9(CH_3)$), 33.4 (s, $C_9(CH_3)$), 23.3 (s, $C_5NCH(CH_3)$), 22.2 (s, $C_5NCH(CH_3)$), 22.0 (s, $C_2(CH_3)$), 21.0 (s, $C_7(CH_3)$), 20.1 (d, $^{3}J_{P\text{-}C}$ = 2.2 Hz, $C_4NCH(CH_3)$), 19.9 (d, $^{3}J_{P\text{-}C}$ = 4.0 Hz, $C_4NCH(CH_3)$).

$^{31}P\{^{1}H\}$ NMR (243 MHz, C_6D_6): δ (ppm) 88.8 (s).

^{31}P NMR (243 MHz, C_6D_6): δ (ppm) 88.8 (t, $^{3}J_{P\text{-}H}$ = 16.6 Hz).

3.4.7 Synthesis of 25



Gold complex **19** (13.2 µmol, 1.0 eq.) was dissolved in benzene (0.5 mL). The solution was freeze-pump-thaw degassed 4 times in a J Young NMR tube, after which ammonia (1 atm) was added to the reaction vessel. The reaction was stirred for 2 minutes. $^{31}P\{^{1}H\}$ revealed the full conversion to complex **25**. The solvent was removed *in vacuo*, with care taken to not subject the resulting oily residue to dynamic vacuum for longer than 1 minute before re-dissolving in d_6-benzene for NMR characterisation. Attempts to crystalise **25** for SCXRD analysis were unsuccessful as **19** was regenerated on loss of ammonia.

^{1}H NMR (600 MHz, C_6D_6): δ (ppm) 7.00 (1H, s, C_8H), 6.72 (1H, s, C_1H), 6.52 (1H, s, C_6H), 6.41 (1H, s, C_3H), 4.04 (1H, d-sept, $^{3}J_{P-H}$ = 14.3 Hz, $^{3}J_{H-H}$ = 6.9 Hz, $C_4NCH(CH_3)_2$), 3.43 (1H, br s, C_5NH), 3.40 (1H, sept, $^{3}J_{H-H}$ = 6.2 Hz, $C_4NCH(CH_3)_2$), 2.33 (2H, br s, $P(NH_2)$), 2.29 (3H, s, $C_2(CH_3)$), 2.21 (3H, s, $C_7(CH_3)$), 1.71 (3H, s, $C_9(CH_3)$), 1.50 (3H, s, $C_9(CH_3)$), 1.39 (3H, d, $^{3}J_{H-H}$ = 6.3 Hz, $C_5NCH(CH_3)$), 1.28 (3H, d, $^{3}J_{H-H}$ = 6.9 Hz, $C_4NCH(CH_3)$), 1.27 (3H, d, $^{3}J_{H-H}$ = 6.9 Hz, $C_4NCH(CH_3)$), 1.00 (3H, d, $^{3}J_{H-H}$ = 6.3 Hz, $C_5NCH(CH_3)$).

$^{1}H\{^{31}P\}$ NMR (600 MHz, C_6D_6): δ (ppm) as above, except 4.04 (1H, sept, $^{3}J_{H-H}$ = 6.9 Hz, $C_4NCH(CH_3)_2$).

$^{13}C\{^{1}H\}$ NMR (151 MHz, C_6D_6): δ (ppm) 133.4 (m, C_{8a}), 132.4 (s, C_7), 131.8 (s, C_2), 131.6 (d, $^{2}J_{P-C}$ = 6.6 Hz, C_4), 128.8 (s, C_{10a}), 128.5 (s, C_5), 122.4 (s, C_8), 120.0 (s, C_6), 116.0 (s, C_1), 108.4 (d, $^{3}J_{P-C}$ = 6.0 Hz, C_3), 46.8 (d, $^{2}J_{P-C}$ = 6.0 Hz, $C_4NCH(CH_3)_2$), 46.5 (s, $C_5NCH(CH_3)_2$), 36.1 (s, C_9), 35.1 (s, $C_9(CH_3)$), 31.7 (s, $C_9(CH_3)$), 23.6 (s, $C_5NCH(CH_3)$), 21.9 (s, $C_2(CH_3)$), 21.7 (s, $C_5NCH(CH_3)$), 21.2 (s, $C_7(CH_3)$), 20.8 (d, $^{3}J_{P-C}$ = 2.7 Hz, $C_4NCH(CH_3)$), 20.0 (d, $^{3}J_{P-C}$ = 3.9 Hz, $C_4NCH(CH_3)$).

Peaks for C_{4a} and C_{9a} could not be located due to overlap with the solvent signal.

$^{31}P\{^{1}H\}$ NMR (162 MHz, C_6D_6): δ (ppm) 95.9 (s).

^{31}P NMR (243 MHz, C_6D_6): δ (ppm) 95.9 (d, $^{3}J_{P\text{-}H}$ = 14.3 Hz).

3.5 References

[1] S. A. Macgregor, *Chem. Soc. Rev.* **2006**, *36*, 67–76.

[2] M. L. H. Green, M. J. Smith, H. Felkin, G. Swierczewski, *J. Chem. Soc. D* **1971**, 158b–159.

[3] M. R. Mason, J. G. Verkade, *Organometallics* **1990**, *9*, 864–865.

[4] M. R. Mason, J. G. Verkade, *Organometallics* **1992**, *11*, 2212–2220.

[5] J. Goodman, S. A. Macgregor, *Coord. Chem. Rev.* **2010**, *254*, 1295–1306.

[6] O. Blum, F. Frolow, D. Milstein, *J. Chem. Soc., Chem. Commun.* **1991**, 258–259.

[7] S. Erhardt, S. A. Macgregor, *J. Am. Chem. Soc.* **2008**, *130*, 15490–15498.

[8] A. Nova, S. Erhardt, N. A. Jasim, R. N. Perutz, S. A. Macgregor, J. E. McGrady, A. C. Whitwood, *J. Am. Chem. Soc.* **2008**, *130*, 15499–15511.

[9] S. Bonfante, C. Lorber, J. M. Lynam, A. Simonneau, J. M. Slattery, *J. Am. Chem. Soc.* **2024**, 146, 2005–2014.

[10] A. Brand, W. Uhl, *Chem. Eur. J.* **2019**, *25*, 1391–1404.

[11] N. Beims, T. Greven, M. Schmidtmann, J. I. van der Vlugt, *Chem. Eur. J.* **2023**, *29*, e202302463.

[12] A. Hentschel, A. Brand, P. Wegener, W. Uhl, *Angew. Chem., Int. Ed.* **2018**, *57*, 832–835.

[13] A. J. Arduengo, C. A. Stewart, *Chem. Rev.* **1994**, *94*, 1215–1237.

[14] M. J. Drance, A. Tanushi, A. T. Radosevich, *J. Am. Chem. Soc.* **2022**, *144*, 20243–20248.

[15] G. T. Cleveland, A. T. Radosevich, *Angew. Chem., Int. Ed.* **2019**, *58*, 15005–15009.

[16] Q. J. Bruch, A. Tanushi, P. Müller, A. T. Radosevich, *J. Am. Chem. Soc.* **2022**, *144*, 21443–21447.

[17] A. J. King, J. Abbenseth, J. M. Goicoechea, *Chem. Eur. J.* **2023**, *29*, e202300818.

[18] A. J. Arduengo III, M. Lattman, J. C. Calabrese, P. J. Fagan, *Heteroat. Chem.* **1990**, *1*, 407–417.

[19] A. J. Arduengo III, M. Lattman, D. A. Dixon, J. C. Calabrese, *Heteroat. Chem.* **1991**, *2*, 395–407.

[20] A. J. I. Arduengo, M. Lattman, H. V. R. Dias, J. C. Calabrese, M. Kline, *J. Am. Chem. Soc.* **1991**, *113*, 1799–1805.

[21] H. V. Huynh, Y. Han, R. Jothibasu, J. A. Yang, *Organometallics* **2009**, *28*, 5395–5404.

[22] M. V. Baker, P. J. Barnard, S. K. Brayshaw, J. L. Hickey, B. W. Skelton, A. H. White, *Dalton Trans.* **2005**, 37–43.

[23] E. S. Yang, E. Combey, J. M. Goicoechea, *Chem. Sci.* **2023**, *14*, 4627–4632.

[24] S. Gaillard, P. Nun, A. M. Z. Slawin, S. P. Nolan, *Organometallics* **2010**, *29*, 5402–5408.

[25] A. W. Addison, T. N. Rao, J. Reedijk, J. van Rijn, G. C. Verschoor, *J. Chem. Soc., Dalton Trans.* **1984**, 1349–1356.

[26] F. A. Cotton, D. J. Darensbourg, B. W. S. Kolthammer, *Inorg. Chem.* **1981**, *20*, 4440–4442.

[27] J. Pickardt, L. Rösch, H. Schumann, *Z. Anorg. Allg. Chem.* **1976**, *426*, 66–76.

[28] C. A. Tolman, *J. Am. Chem. Soc.* **1970**, *92*, 2953–2956.

[29] R. L. Keiter, J. G. Verkade, *Inorg. Chem.* **1969**, *8*, 2115–2120.

[30] S. O. Grim, D. A. Wheatland, William. McFarlane, *J. Am. Chem. Soc.* **1967**, *89*, 5573–5577.

[31] S. O. Grim, R. L. Keiter, W. McFarlane, *Inorg. Chem.* **1967**, *6*, 1133–1137.

[32] W. Buchner, W. A. Schenk, *Inorg. Chem.* **1984**, *23*, 132–137.

[33] S. H. Strauss, K. D. Abney, *Inorg. Chem.* **1984**, *23*, 515–516.

[34] J. Apel, R. Bacher, J. Grobe, D. Le Van, *Z. Anorg. Allg. Chem.* **1979**, *453*, 39–52.

[35] M. S. Davies, R. K. Pierens, M. J. Aroney, *J. Organomet. Chem.* **1993**, *458*, 141–146.

[36] W. H. Hersh, P. Xu, B. Wang, J. W. Yom, C. K. Simpson, *Inorg. Chem.* **1996**, *35*, 5453–5459.

[37] W. A. Schenk, W. Buchner, *Inorg. Chim. Acta* **1983**, *70*, 189–196.

[38] G. M. Bodner, M. P. May, L. E. McKinney, *Inorg. Chem.* **1980**, *19*, 1951–1958.

[39] S. Streiff, F. Jérôme, *Chem. Soc. Rev.* **2021**, *50*, 1512–1521.

[40] V. Lavallo, G. D. Frey, B. Donnadieu, M. Soleilhavoup, G. Bertrand, *Angew. Chem., Int. Ed.* **2008**, *47*, 5224–5228.

[41] J. P. Moerdyk, G. A. Blake, D. T. Chase, C. W. Bielawski, *J. Am. Chem. Soc.* **2013**, *135*, 18798–18801.

[42] J. Abbenseth, O. P. E. Townrow, J. M. Goicoechea, *Angew. Chem., Int. Ed.* **2021**, *60*, 23625–23629.

[43] A. J. King, J. M. Goicoechea, *Chem. Eur. J.* **2024**, 30, e202400624.

Chapter 4

Ammonia Activation at a T-Shaped Phosphine and its Less Constrained Derivatives

Abstract. The T-shaped phosphine **6** was shown to activate an ammonia N–H bond *via* redox-neutral cooperative addition, ultimately equilibrating in favour of the oxidative-addition product. This compound underwent reductive elimination upon heating, demonstrating the reversibility of ammonia activation at **6**. Methyl-phosphonium ion **7**, phosphine oxide **11**, and iminophosphorane **30**, each a derivative of **6** bearing reduced geometric constraint, were also shown to activate an ammonia N–H bond, in some cases more rapidly than **6**. DFT calculations and experimental observations support a mechanism involving the initial Lewis adduct formation between ammonia and the phosphorus centre in these compounds, followed by inter-/intra-molecular deprotonation of the now acidified N–H bond. These results highlight some alternative methodologies beyond geometric constraint for accessing phosphorus-based Lewis acidic reactivity which may be exploited towards desirable bond activation reactions.

4.1 The reaction of 6 with ammonia

N–H bond activation is regarded as a useful benchmark for reactivity, particularly in the case of ammonia, which poses a challenge for transition metal-based systems.[1–3] A C_6D_6 solution of T-shaped phosphine **6** was degassed and stirred under an ammonia atmosphere (1 bar). The $^{31}P\{^1H\}$ NMR spectrum acquired immediately after ammonia addition revealed the partial conversion to a compound with a signal at 84.7 ppm (Figure 4.1). In the ^1H NMR spectrum, signals corresponding to an unsymmetrical acridane backbone were observed, indicating that cooperative addition of an ammonia N–H bond across a P–N bond of **6** occurred to provide **26a** (Scheme 4.1). Continued stirring of this solution resulted in the gradual formation of a resonance at −60.0 ppm in the $^{31}P\{^1H\}$ NMR spectrum, in the region expected of a phosphorus(V) compound. This signal split into a doublet-of-triplets in the

^{31}P NMR spectrum. A large coupling constant, $^{1}J_{P–H}$ = 711.4 Hz, revealed the presence of a new P–H bond, while the triplet splitting ($^{3}J_{P–H}$ = 14.8 Hz) confirms P–N bonding to all three acridane derived nitrogen atoms. The ^{1}H NMR spectrum corroborates the formation of a P–H bond (8.36 ppm), and displays inequivalent signals above/below the acridane plane. These data are consistent with the formation of N–H oxidative addition product **26b** (Scheme 4.1), however full conversion to this species could not be achieved. Under the above conditions, **26a** and **26b** equilibrated at a ratio of 1:2.5 respectively (by integration of their ^{31}P{^{1}H} NMR resonances) after 2 days (Figure 4.1).

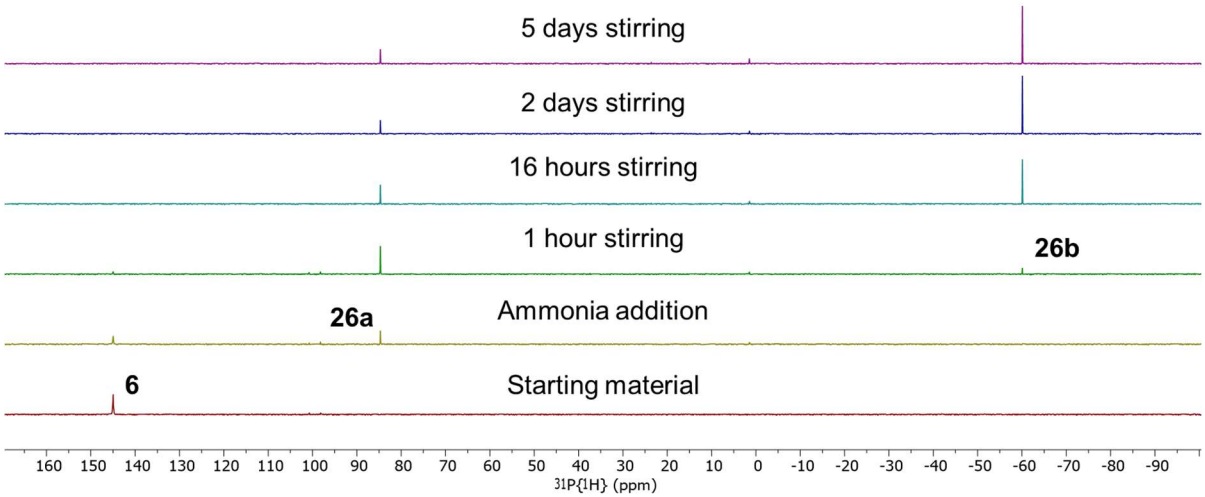
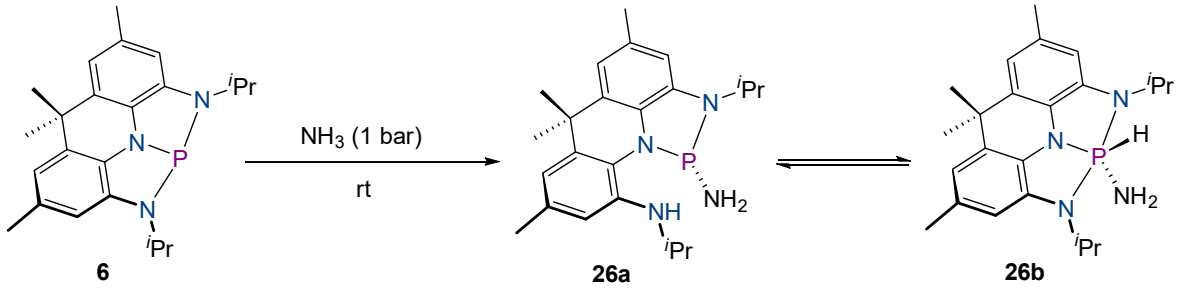


Figure 4.1. Stacked ^{31}P{^{1}H} NMR spectra monitoring the reaction between **6** and ammonia in C_6D_6. Note the presence of hydrolysis product **17** forming after extended stirring, attributed to the presence of trace amounts of water in the ammonia.



Scheme 4.1. Synthesis of **26a** and **26b**.

Calculations at the PBE0/DEF2-TZVP level of theory confirm the preferential formation of **26b** over **26a**, with both products being thermodynamically downhill with respect to **6**: ΔG_{DFT} (kcal mol^{-1}): 0.0 (**6** + NH_3); −10.1 (**26a**); −14.3 (**26b**). Following equilibration, solvent and excess ammonia were

removed from a sample of **26a** and **26b** *in vacuo*, which resulted in the generation of a small amount of **6**; 7% by integration of $^{31}P\{^{1}H\}$ NMR signals relative to an internal standard (triphenylphosphine oxide). This apparent reversibility of ammonia N–H bond activation was probed through variable temperature $^{31}P\{^{1}H\}$ NMR spectroscopy (Figure 4.2). The above sample, in toluene under an N_2 atmosphere, was heated in 20 K increments from room temperature to 85 °C, with the sample held at each temperature for 10 minutes prior to acquisition. It was found that the concentration of cooperative addition product **26a** remained constant throughout this temperature range (Figure 4.3). Conversely, the concentration of oxidative addition product **26b** was found to steadily decrease, accompanied by a proportional increase in the concentration of **6**. Conversion to **6** increased on holding the sample at elevated temperatures for extended periods of time.

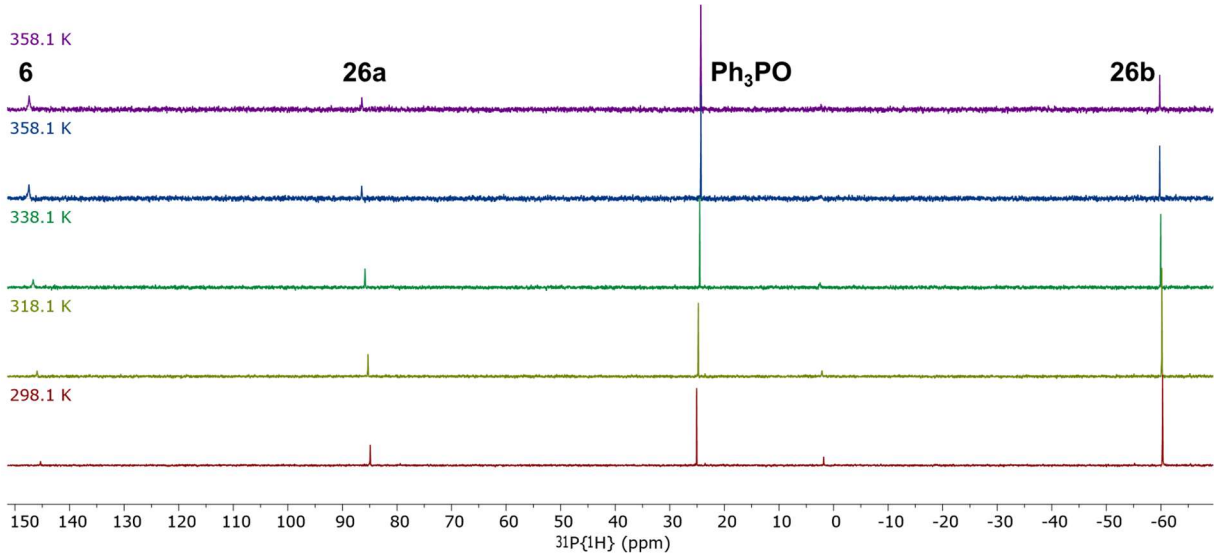


Figure 4.2. Stacked $^{31}P\{^{1}H\}$ NMR spectra of a mixture of **26a** and **26b** in toluene at the temperature indicated on the left-hand side of each stacked spectrum. Top spectrum was acquired after holding the sample at 358 K for 1 hour.

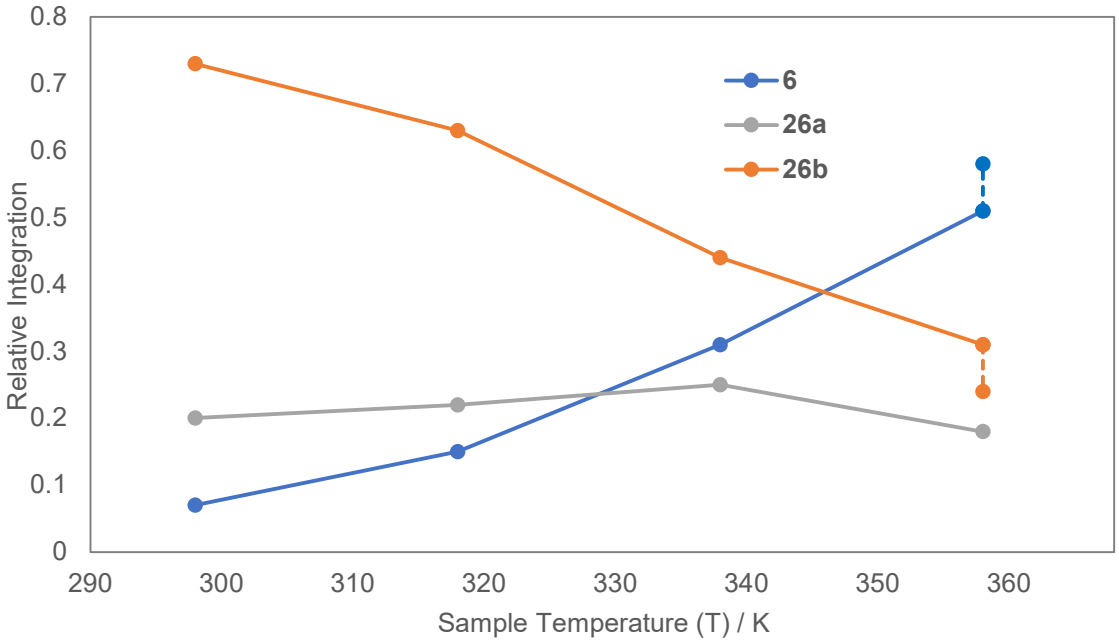
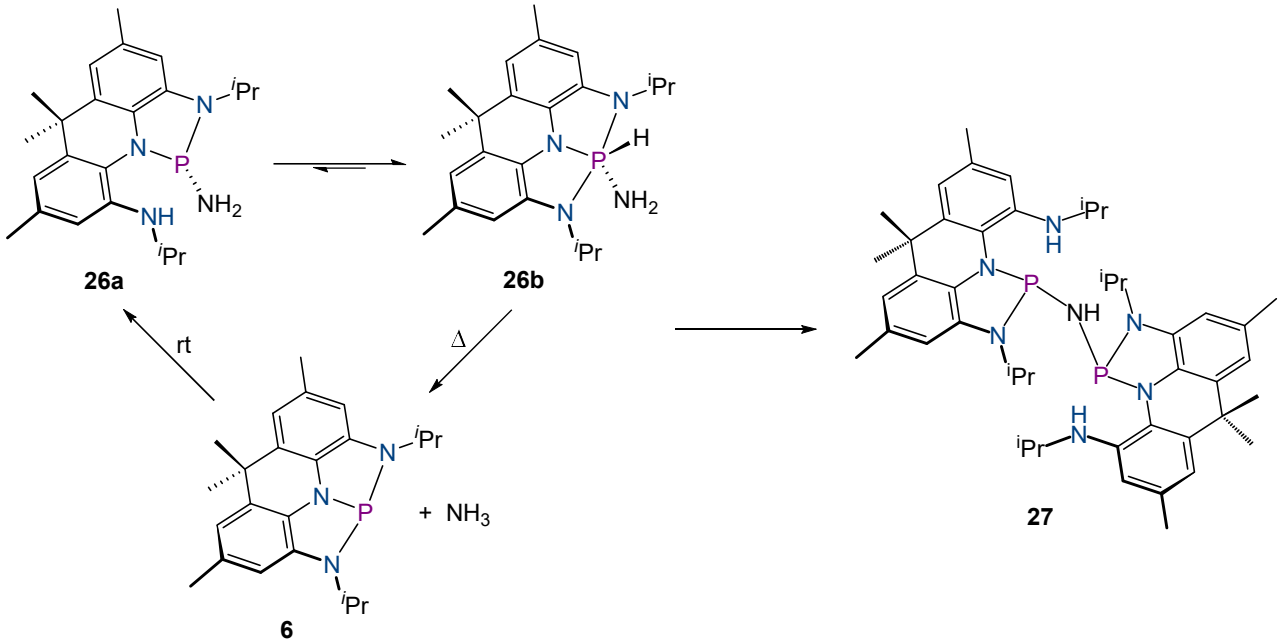


Figure 4.3. A plot of sample composition versus temperature for the above variable temperature NMR spectra.

Following the collection of these spectra at elevated temperatures, the sample was cooled to 298 K, and a $^{31}P\{^{1}H\}$ NMR spectrum acquired after 10 minutes. At this time, the forward reaction between **6** and ammonia was evidenced by a decrease in concentration of **6** with a proportional increase in that of **26a**. Together, these data suggest that **6** reacts with ammonia *via* initial cooperative addition to provide **26a**, which converts to the more thermodynamically favoured isomer **26b**, itself capable of reductively eliminating ammonia upon heating (Scheme 4.2).



Scheme 4.2. Relationship between **6**, **26a**, **26b** and **27** *via* reversable ammonia activation.

On leaving a mixture of **26a** and **26b** under a nitrogen atmosphere at room temperature, a new signal at 79.0 ppm could be observed, becoming a significant component of the mixture after one month. SCXRD enabled its identification as bisphosphine **27**, formed through the subsequent activation of two N–H bonds of a single ammonia molecule (Figure 4.4). It was suspected that **27** formed through the reaction of **6** and **26a**, both of which would be present in solution following ammonia reductive elimination from **26b**. An analogous structure bearing a central oxygen atom was previously observed by Goicoechea and Aldridge following the dual oxidative addition of water to an ONO-ligated C_s symmetric phosphine.[4]

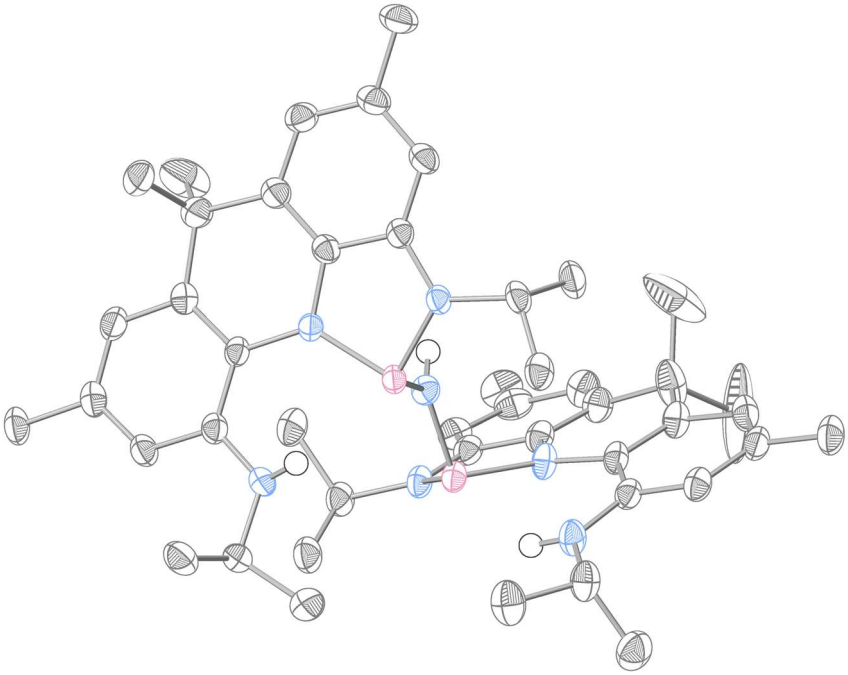


Figure 4.4. Solid-state structure of **27**. Thermal ellipsoids pictured at 50% probability level. Hydrogen atoms, except for those derived from ammonia, and solvent of crystallisation removed for clarity.

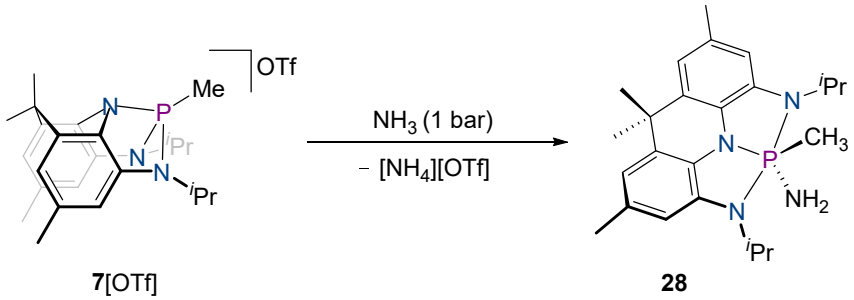
4.2 The reactions of less constrained derivatives of 6 with ammonia

In Chapter 3, phosphine centred N–H bond activation of ammonia was described for **19** — the gold(I)chloride complex of **6**.[5] SCXRD of complex **19** revealed a bent acridane backbone, and a geometry about phosphorus approaching tetrahedral ($\tau'_4 = 0.73$).[6] Geometric constraint at phosphorus was substantially reduced with respect to the free phosphine, therefore the observed reactivity towards N–H bonds was attributed to enhanced Lewis acidity through electron donation to the transition metal.

This prompted further investigation into alternative methods of phosphorus Lewis acidification, and to challenge the notion that substantial geometric constraint is needed to promote such bond activation chemistry. This was further fuelled by a recent study by Bonfante *et al.*, where C_{aryl}–F bond activation was demonstrated with simple non-constrained phosphines.[7]

4.2.1 Phosphonium salt 7[OTf]

Reaction of **6** with methyl triflate resulted in phosphorus centred methylation to generate phosphonium salt **7**[OTf] (Chapter 2, Section 2.3.1).[8] Despite its reduced geometric constraint with respect to **6** (τ'_4 = 0.73), **7**[OTf] was postulated to possess a highly Lewis acidic phosphorus centre on account of its localised positive charge and weakly coordinating (triflate) counterion.[6] To assess whether phosphorus methylation is sufficient to facilitate Lewis acidic reactivity, **7**[OTf] was placed under an atmosphere of ammonia (1 bar). This immediately resulted in the formation of a colourless solution and the precipitation of a colourless solid. $^{31}P\{^1H\}$ NMR spectroscopy revealed the complete conversion of **7**[OTf] to a compound exhibiting a broad signal at −50.5 ppm. In the ^1H NMR spectrum, a broad singlet at 2.61 ppm corresponding to an $–NH_2$ group, and a doublet signal at 1.97 ppm ($^2J_{P–H}$ = 15.3 Hz) corresponding to a phosphorus bound methyl group (and which collapsed to a singlet upon ^{31}P-decoupling) were present. This, together with SCXRD confirmed the formation of aminophosphorane **28** (92% isolated yield, Scheme 4.3, Figure 4.5).



7[OTf] **28**

Scheme 4.3. Synthesis of aminophosphorane **28**.

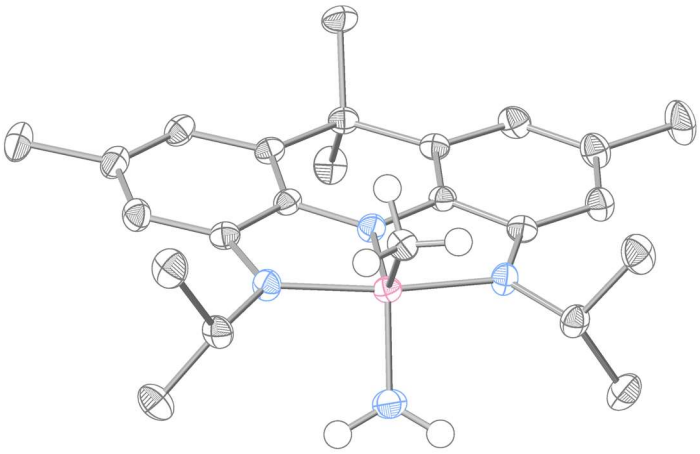
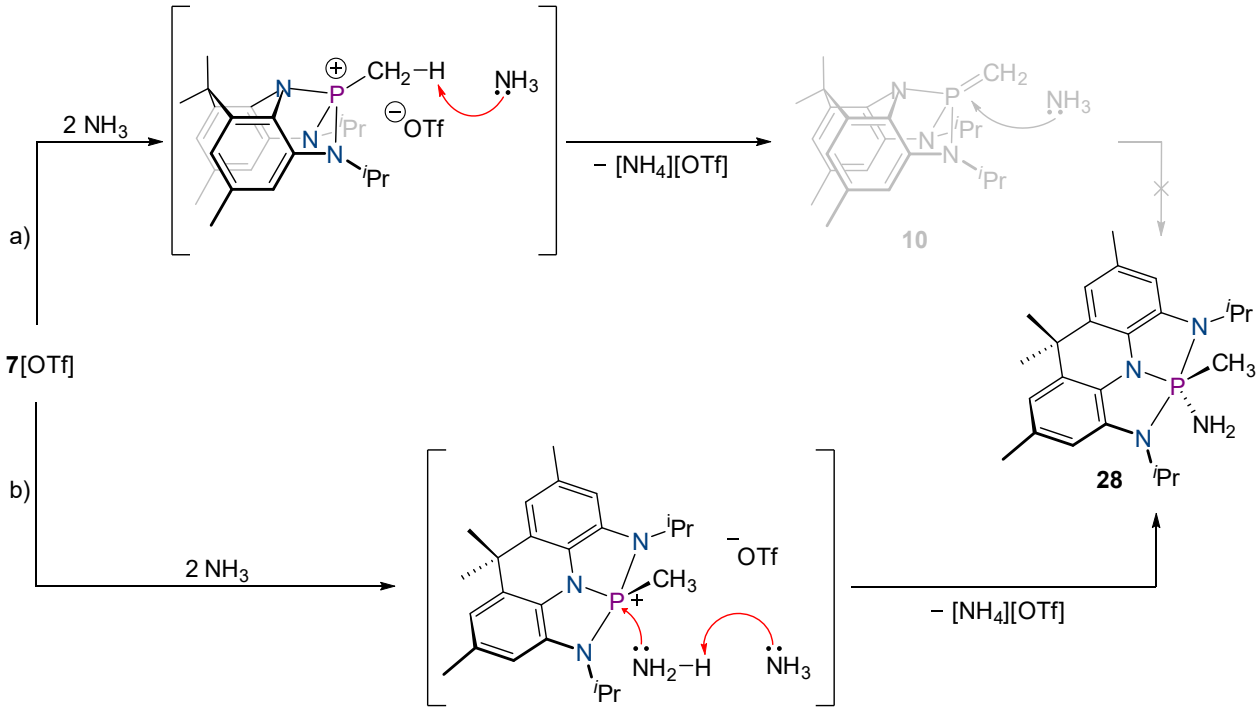


Figure 4.5. Solid-state structure of **28**. Thermal ellipsoids pictured at 50% probability level. Hydrogen atoms, except for those on the phosphorus substituents, and solvent of crystallisation removed for clarity.

Two mechanisms were proposed for the synthesis of **28** (Scheme 4.4). In the first case, C–H deprotonation of cation **7** by a molecule of ammonia provides the previously described ylide **10**, which then undergoes further reaction with an additional molecule of ammonia across the P=C bond. Alternatively, adduct formation between a Lewis basic ammonia nitrogen atom and the Lewis acidic phosphorus can take place, followed by N–H deprotonation by an additional ammonia molecule.

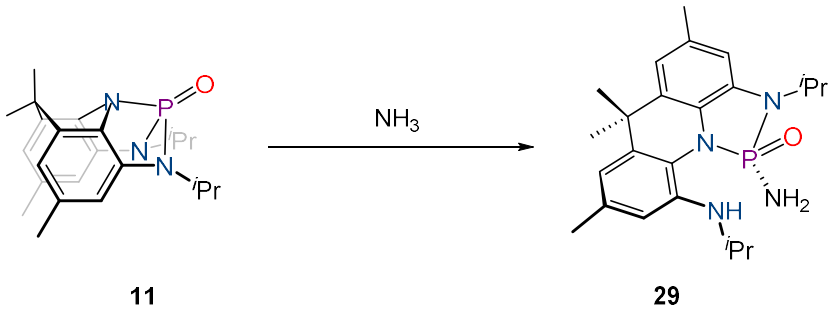


Scheme 4.4. Proposed mechanisms for the synthesis of **28** by the reaction of **7**[OTf] and ammonia.

Route a) (Scheme 4.4) is unlikely as **10** fails to react with ammonia under equivalent conditions. Conversely, route b) is supported by previous computational studies of reactions between geometrically constrained phosphines and N–H bonds; namely *base-assisted* bond activation employing multiple molecules of the Lewis basic substrate.[9] In a deviation from the reactivity observed for **6**, the acridane-based nitrogen side-arm did not participate in N–H bond activation. This was suspected to result from the reduced electron density on the ligand nitrogen atoms. Additionally, the significantly faster rate of reaction of **7** with ammonia compared to that of **6** implies a greater Lewis acidification at phosphorus, achieved instead through chemical engagement of the phosphine lone-pair rather than geometric constraint.

4.2.2 Phosphine oxide 11 and iminophosphorane 30

Phosphine **6** underwent oxidation with elemental chalcogens to yield the respective phosphine chalcogenides possessing a bent acridane backbone (see Chapter 2).[8] Phosphine oxide **11** was amongst these, and chosen as a model compound to assess whether oxidation to phosphorus(V) provides a sufficiently Lewis acidic phosphorus centre to promote N–H bond activation. Phosphine oxide **11** possesses a neutral phosphorus centre, providing more basic ligand nitrogen atoms compared to phosphonium ion **7**, thus potentially promoting cooperative N–H bond activation akin to **6**. Charging a benzene solution of **11** with an ammonia atmosphere (1 bar) resulted in its immediate consumption, and the generation of a new species with a $^{31}P\{^{1}H\}$ NMR signal at 23.5 ppm (s). In the proton coupled ^{31}P NMR spectrum, this signal split into an apparent doublet ($^{3}J_{P–H}$ = 16.8 Hz), which, along with ^{1}H NMR signals corresponding to an unsymmetrical acridane backbone, implied cooperative N–H addition across a side-arm P–N bond to generate **29** (94% isolated yield, Scheme 4.5).



Scheme 4.5. Synthesis of **29**.

Calculations at the PBE0/DEF2-TZVP level of theory revealed the formation of a Lewis adduct between ammonia and **11** along the reaction path to towards thermodynamically favoured **29**. From this adduct, featuring a planarised acridane fragment, a transition state to cooperative addition of the ammonia N–H bond could be located *via* a relaxed surface scan of the distance between this proton and a side-arm nitrogen (Figures 4.6 and 4.7): ΔG_{DFT} (kcal mol^{-1}) = 0.0 (**11**), +13.3 (**11**$_{\mathbf{Adduct,1°}}$), +20.3 (**11**$_{\mathbf{TS}}$), −13.6 (**28**).

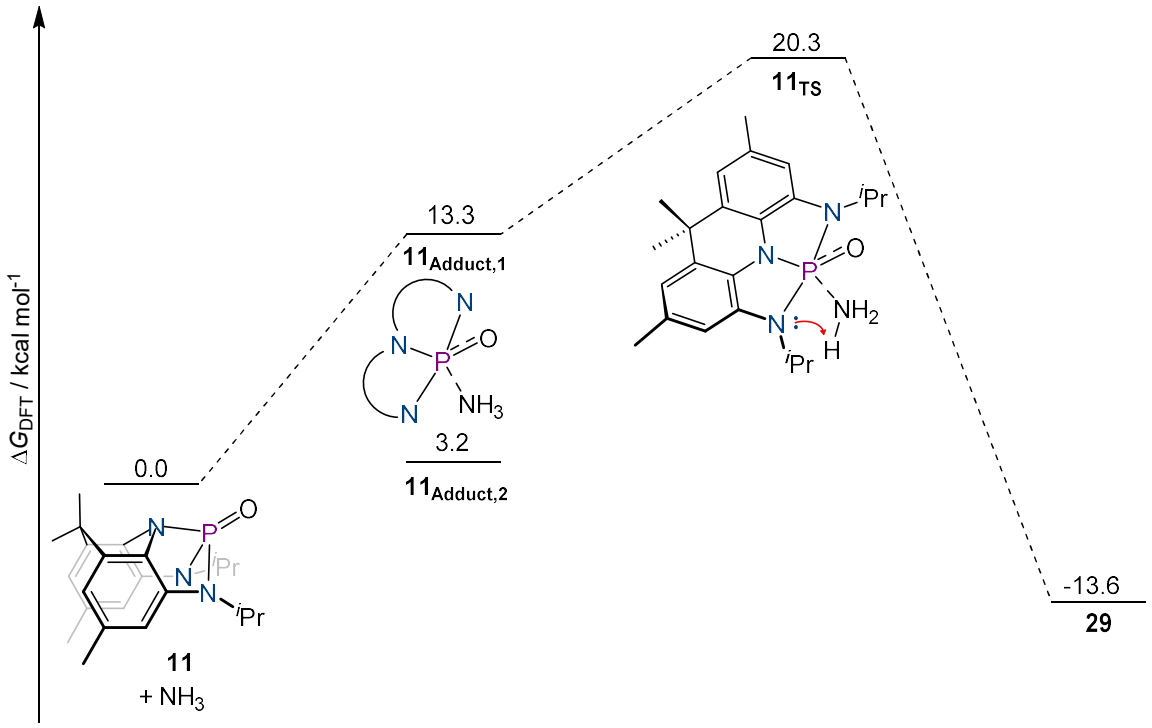


Figure 4.6. Calculated energy landscape for the reaction of **11** with ammonia. Energies are relative to **11** + NH_3 (or + $2NH_3$ in the case of **11**$_{\mathbf{Adduct,2°}}$).

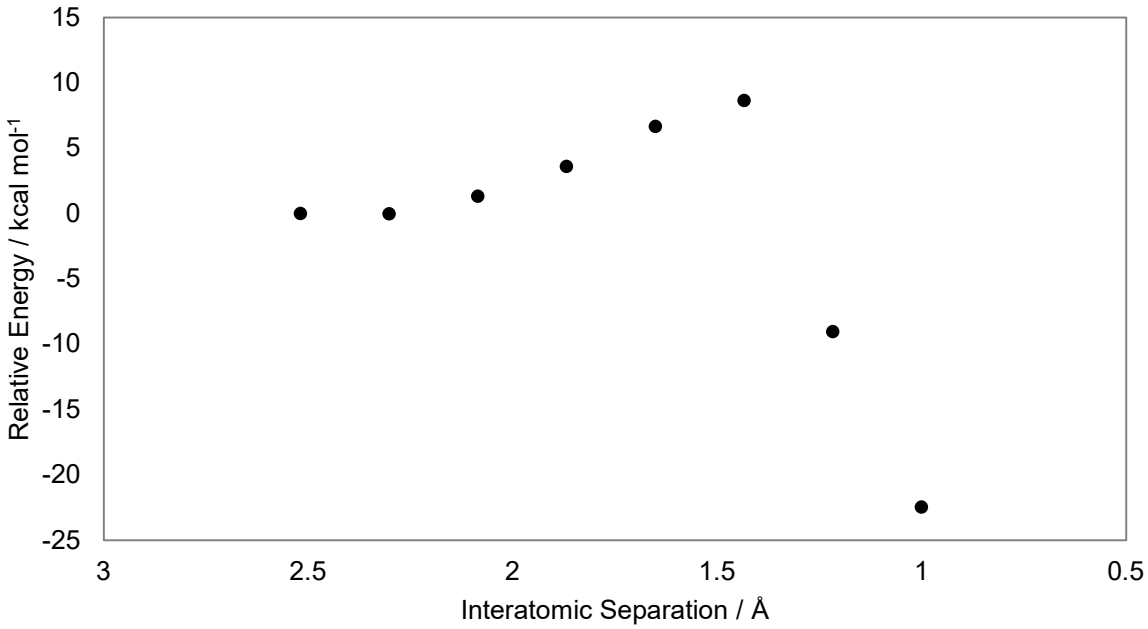


Figure 4.7. A graph of the relative energies obtained through a relaxed surface scan of the interatomic separation between an ammonia proton and a side-arm acridane-based nitrogen, from an initial separation of 2.519 Å to 1.000 Å, using the optimised geometry of $\mathbf{11}_{\mathbf{Adduct,1°}}$ as the starting coordinates. Energies are relative to that of $\mathbf{11}_{\mathbf{Adduct,1°}}$.

As highlighted in Figure 4.6, the calculated adduct between ammonia and **11** was further stabilised on inclusion of a second molecule of ammonia within a hydrogen bonding network involving the coordinated ammonia molecule and the phosphine oxide moiety (Figure 4.8): ΔG_{DFT} (kcal mol^{-1}) = +3.2 ($\mathbf{11}_{\mathbf{Adduct,2°}}$). Therefore, the energy barrier calculated using $\mathbf{11}^{\mathbf{TS}}$ is the upper limit for this reaction, with a *base-assisted* mechanism more likely to occur.[9] However, without experimental thermochemical data, an accurate assessment of ammonia molecularity could not be made, and so only a qualitative understanding of energy barriers was gleamed from these calculations.

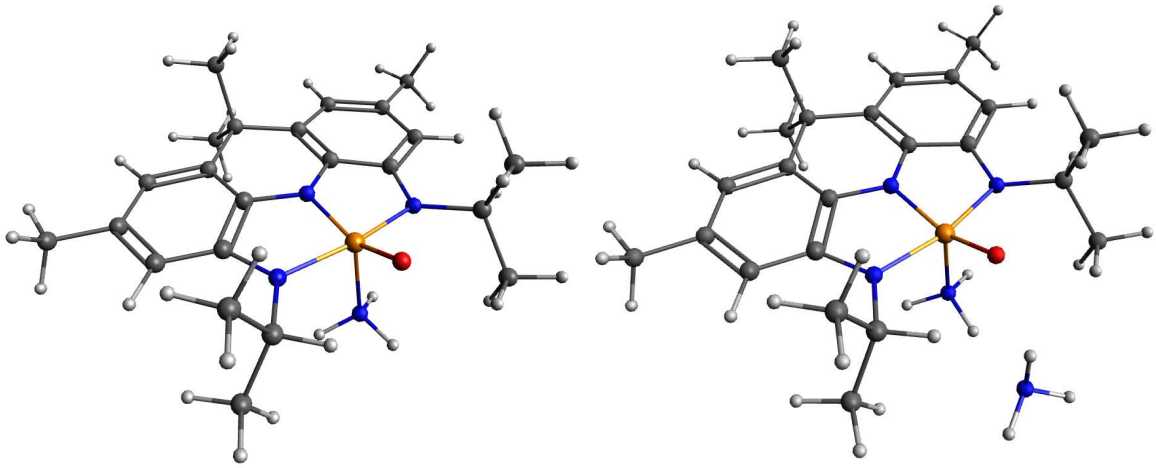


Figure 4.8. Optimised calculated geometries of phosphine oxide-ammonia adducts $\mathbf{11}_{\mathbf{Adduct,1°}}$ (left) and $\mathbf{11}_{\mathbf{Adduct,2°}}$ (right) containing one and two molecules of ammonia, respectively.

Regarding the planarisation of the acridane backbone, **11** was unable to access this conformation on account of it being thermodynamically disfavoured: ΔG_{DFT} (kcal mol^{-1}) = +27.3 ($\mathbf{11}_{\mathbf{Planar}}$; Figure 4.9). Therefore, the planarisation observed upon formation of $\mathbf{11}_{\mathbf{Adduct,1°}}$ was determined to be induced by Lewis adduct formation such that the now five-coordinate phosphorus centre is accommodated (τ_5^{DFT} = 0.24).[10] The Lewis acidity of the phosphorus centre in **11** was attributed to its +5 oxidation-state, whereby the oxygen centre essentially withdraws electron density from phosphorus. This rationale is supported by the calculated P=O bond length becoming elongated upon formation of $\mathbf{11}_{\mathbf{Adduct,1°}}$ and $\mathbf{11}_{\mathbf{Adduct,2°}}$ (P–O (Å) = 1.467 ($\mathbf{7}_{\mathbf{DFT}}$); 1.485 ($\mathbf{7}_{\mathbf{Adduct,1°}}$); 1.495 ($\mathbf{7}_{\mathbf{Adduct,2°}}$)), consistent with the movement of electron density towards the oxygen centre throughout the course of the reaction.

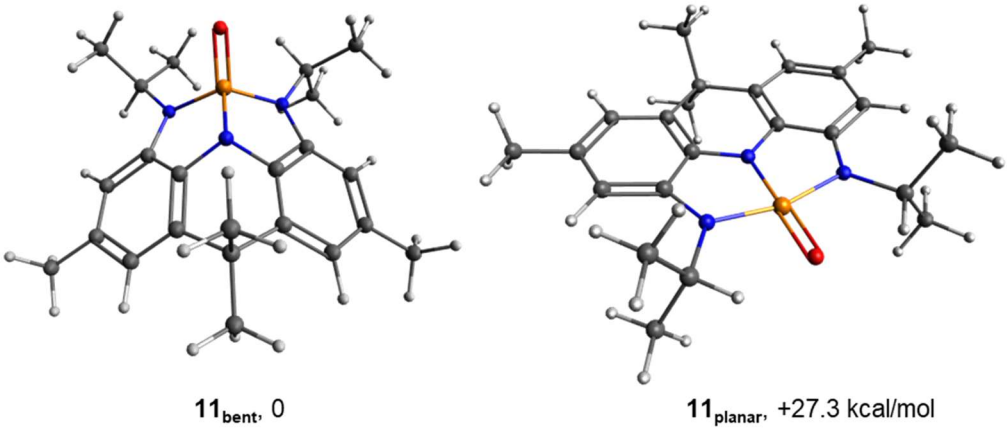


Figure 4.9. Relative energies of bent and planar conformations of **11**. Optimised structures depicted.

In the ^{1}H NMR spectrum of **29**, the newly formed N–H bond located on the acridane side-arm is characterised by a doublet at 6.75 ppm ($^{3}J_{H–H}$ = 4.0 Hz). By comparison with previously synthesised *cooperative* addition products, this chemical shift is unusually high for this environment.[5,8] It was suspected that this results due to hydrogen bonding of this proton with the phosphine oxide moiety. This was corroborated through SCXRD of **29**, which reveals that the N–H bond is directed towards the oxygen atom, and their interatomic separation of 1.946(24) Å (and 2.807(7) Å between the oxygen atom and parent nitrogen) is a suitable distance for hydrogen bonding to occur (Figure 4.10). Furthermore, a P–O bond length of 1.476(9) Å confirms the retention of a P=O double bond.

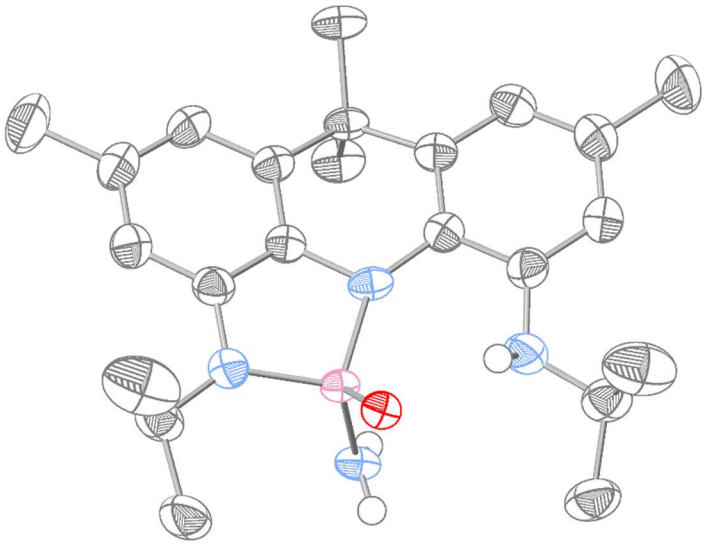
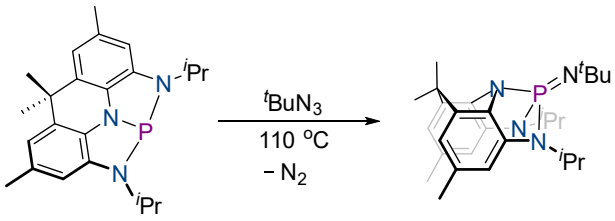


Figure 4.10. Solid-state structure of **29**. Thermal ellipsoids pictured at 50% probability level. Hydrogen atoms, except for those derived from ammonia, and solvent of crystallisation removed for clarity.

The aforementioned hydrogen bond suggests that, for systems possessing a more basic P=E (E = hydrogen-bond-acceptor) unit, intramolecular proton transfer would be possible, potentially enabling further transformations at phosphorus. Therefore, replacement of the phosphine oxide functionality present in **11** with a more basic iminophosphorane P=N moiety was explored. To this end, the Staudinger reaction between **6** and *tert*-butyl azide proceeded at 110 °C to give iminophosphorane **30** (86% yield, Scheme 4.6).



6 **30**

Scheme 4.6. Synthesis of iminophosphorane **30**.

In its $^{31}P\{^{1}H\}$ NMR spectrum, **30** exhibits a singlet resonance at 6.8 ppm which splits into a triplet in the proton-coupled spectrum ($^{3}J_{P-H}$ = 13.2 Hz). The ^{1}H NMR spectrum of **30** exhibits signals corresponding to a bent acridane backbone, consistent with previously synthesised iminophosphoranes bearing an NNN-pincer ligand, and corroborated through SCXRD (Figure 4.11).[8,11]

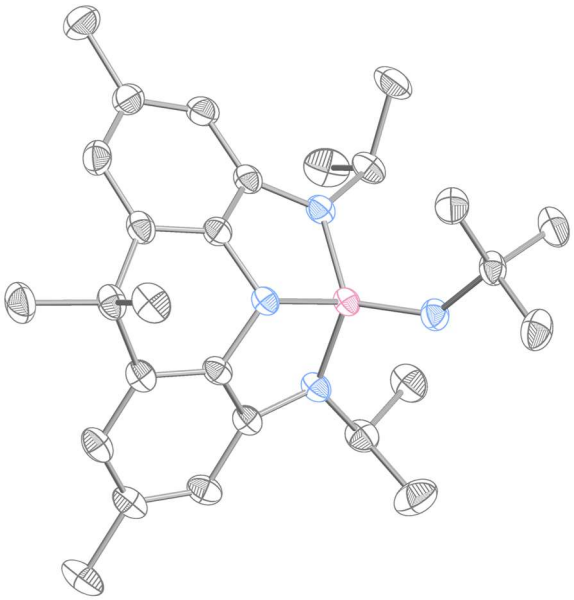


Figure 4.11. Solid-state structure of **30**. Thermal ellipsoids pictured at 50% probability level. Hydrogen atoms and solvent of crystallisation removed for clarity.

In contrast to phosphonium salt **7**[OTf] and phosphine oxide **11**, placing **30** under an ammonia atmosphere (1 bar) did not result in immediate reaction, as evidenced by a lack of change in the $^{31}P\{^{1}H\}$ NMR spectrum of the mixture. Instead, heating to 110 °C overnight was required for a reaction to occur, resulting in the generation of several new phosphorus containing species (Figure 4.12). It is suspected that such forcing conditions are required on account of the lower electronegativity of the nitrogen atom

in the P=N unit of **30**, providing a less Lewis acidic phosphorus centre in comparison to that of **7** and **11**.

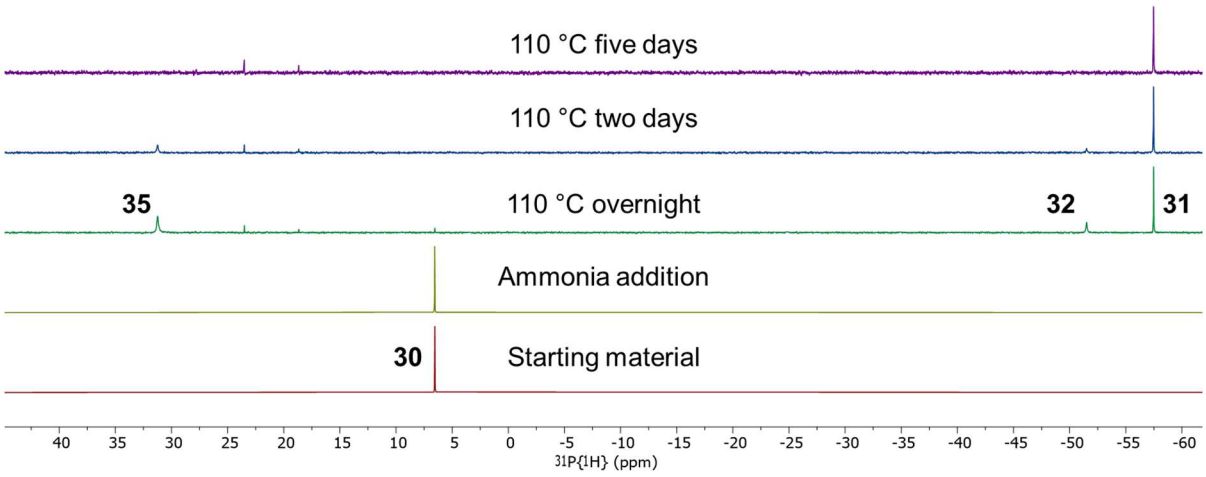
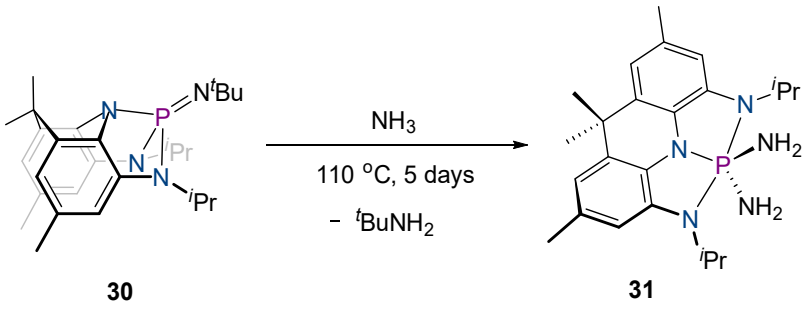


Figure 4.12. Stacked $^{31}P\{^{1}H\}$ NMR spectra (acquired at room temperature) of the reaction between **30** and ammonia at 110 °C in d_8-toluene. Trace amounts of oxidised impurities are present in the final spectrum.

The initial product mixture revealed $^{31}P\{^{1}H\}$ NMR signals at 31.2 ppm, −51.5 ppm and −57.5 ppm, with the latter being the sole product after heating at 110 °C for several days. Regarding this final reaction mixture, cooling the solution to room temperature resulted in the formation of colourless needle-like crystals of the final product. Whilst the $^{31}P\{^{1}H\}$ NMR spectrum of this final product contained a singlet resonance at −57.5 ppm, the ^{31}P NMR spectrum sees this signal split into an apparent septet ($^{2}J_{P–H} = {}^{3}J_{P–H} = 7.2$ Hz), implying the coupling between phosphorus and six protons. The ^{1}H NMR spectrum revealed a C_{2v} symmetric, planar acridane backbone, and the retention of each P–N bond to the acridane ligand. A doublet resonance displaying coupling to phosphorus was observed at 2.70 ppm ($^{2}J_{P–H} = 7.2$ Hz) which integrated to four protons, overall suggesting the formation of two phosphorus bound –NH_2 groups (Scheme 4.7). These data, together with SCXRD, confirm the formation of **31** (64% isolated yield, Figure 4.13) — an aminophosphorane containing a pentagonal bipyramidal phosphorus centre singly bonded to five amino fragments; P–N (Å) = 1.820(2) (N1/3), 1.674(2) (N2), 1.661(2) (N4/5).



30 **31**

Scheme 4.7. Synthesis of aminophosphorane **31**.

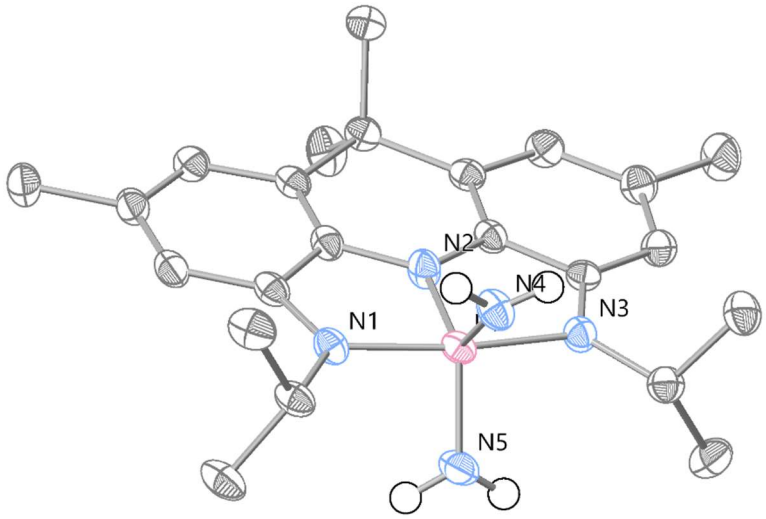


Figure 4.13. Solid-state structure of **31**. Thermal ellipsoids pictured at 50% probability level. Hydrogen atoms, except for those derived from ammonia, and solvent of crystallisation removed for clarity.

Monitoring the mixture using ^{1}H NMR spectroscopy reveals that *tert*-butyl amine is formed over the course of this reaction (Figure 4.14). It could also be isolated by vacuum transfer of the volatiles present in the final reaction mixture (Figure 4.15). The formation of *tert*-butyl amine, originating from the iminophosphorane –N^{t}Bu fragment, suggests that following initial ammonia activation by **30**, several proton-transfer steps take place.

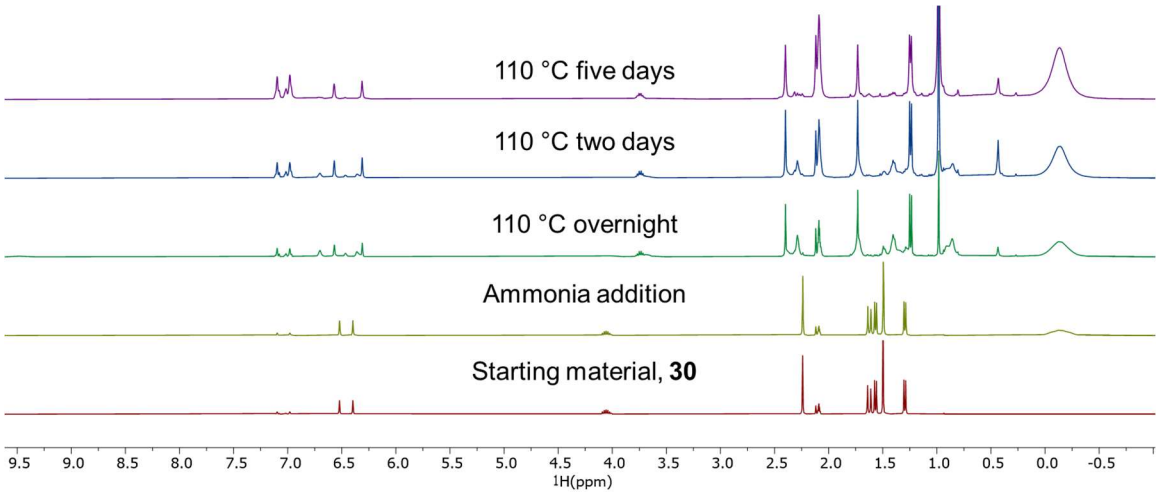


Figure 4.14. Stacked $^{31}P\{^{1}H\}$ NMR spectra of the reaction between **30** and ammonia at 110 °C in d_8-toluene.

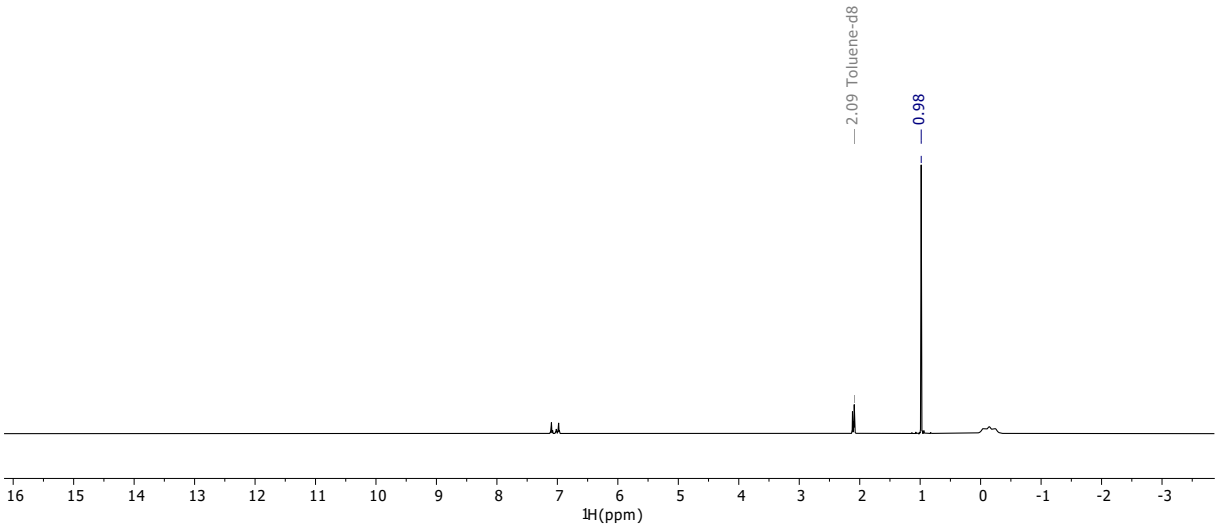


Figure 4.15. ^{1}H NMR spectrum of the volatiles from the reaction between **30** and ammonia following vacuum transfer. The signal at 0.98 ppm corresponds to *tert*-butyl amine, while the peak at −0.14 ppm corresponds to unreacted ammonia.

Identification of the other phosphorus containing initial products may provide further insight into the mechanism of this reaction. A sample of **30** was heated under an ammonia atmosphere (1 bar) for 16 hours, then cooled and concentrated to a residue *in vacuo*. The phosphorus-containing products (cf. $^{31}P\{^{1}H\}$ δ (ppm): 31.2; −51.5; −57.5 (**31**)) were extracted with pentane, slow evaporation of which yielded a mixture of crystals suitable for SCXRD consisting of **31** and the new mixed aminophosphorane **32** (Figure 4.16). The latter of these features a phosphorus centre bonded to five amino-fragments in a slightly distorted trigonal bipyramidal overall geometry. The –N^{t}Bu fragments in

32 is tilted under the acridane ring system, suspected to be a result of steric clash between its large *tert*-butyl group and the *iso*-propyl side-arm substituents; N2–P1–N (°) = 121.8(5) (N4), 128.3(5) (N5). This is also reflected in the P–N4 bond length being noticeably longer than both the P1–N5 bond length, and the respective distance in **31**; P1–N (Å) = 1.684(4) (N4, **32**), 1.652 (N5, **32**), 1.661(2) (N4/5, **31**).

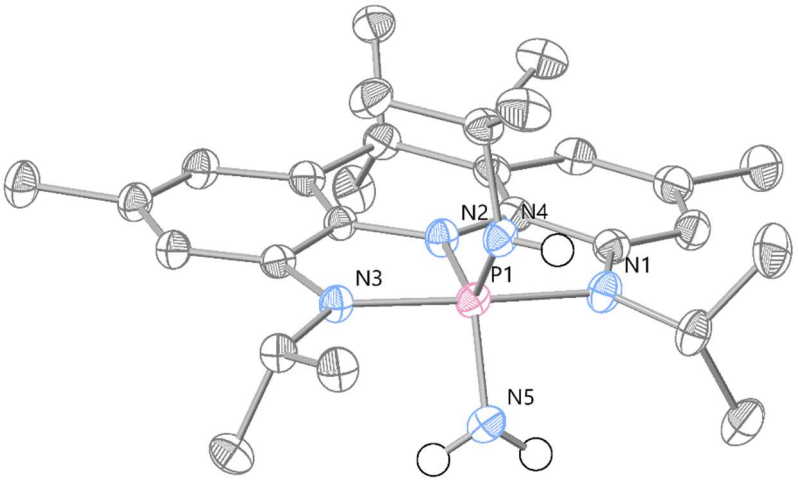
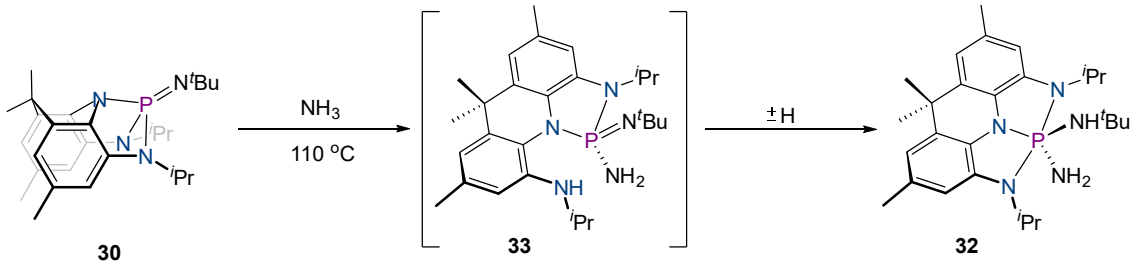


Figure 4.16. Solid-state structure of **32**. Thermal ellipsoids pictured at 50% probability level. Hydrogen atoms, except for those derived from ammonia, and solvent of crystallisation removed for clarity.

Aminophosphorane **32**, containing –NH^{t}Bu and –NH$_2$ fragments, is the product of formal 1,2-addition of ammonia across the P=N bond of iminophosphorane **30**. It was suspected that, *en route* to **32**, initial cooperative addition of ammonia occurred across an acridane derived P–N bond of **30** to provide intermediate **33**, analogous to the reaction between ammonia and phosphine oxide **11**. Following this, proton transfer from the side-arm nitrogen to the P=N^{t}Bu fragment yields **32** (Scheme 4.8). Such proton transfer was alluded to by the apparent intramolecular hydrogen bond present in **29**, with the more basic P=N^{t}Bu nitrogen facilitating side-arm deprotonation.



Scheme 4.8. Proposed mechanism for the formation of **32**.

Based on its similar phosphorus environment to **31**, the resonance at −51.5 ppm in $^{31}P\{^{1}H\}$ NMR spectrum of the product mixture was tentatively assigned to **32**. DFT calculations were performed to help elucidate the mechanism for the reaction between **30** and ammonia (Figure 4.17). Supporting the postulated mechanism above (Scheme 4.8), initial cooperative addition of an ammonia N–H bond across a side-arm P–N bond of **30** was found to be thermodynamically downhill to provide intermediate **33**. Intramolecular proton transfer from this species then generates **32**. The latter of these represents a local minimum on the potential energy landscape, consistent with the fact it can be isolated and characterised by SCXRD analysis (Figure 4.16). The subsequent release of *tert*-butyl amine from **32** towards protio-iminophosphorane **34** was found to be endergonic. However, follow-up reactivity of **34** with ammonia (in excess during this reaction) was exergonic, proceeding *via* cooperative N–H addition (**35**) and proton transfer to yield final product **31**, which is a thermodynamic sink for the reaction.

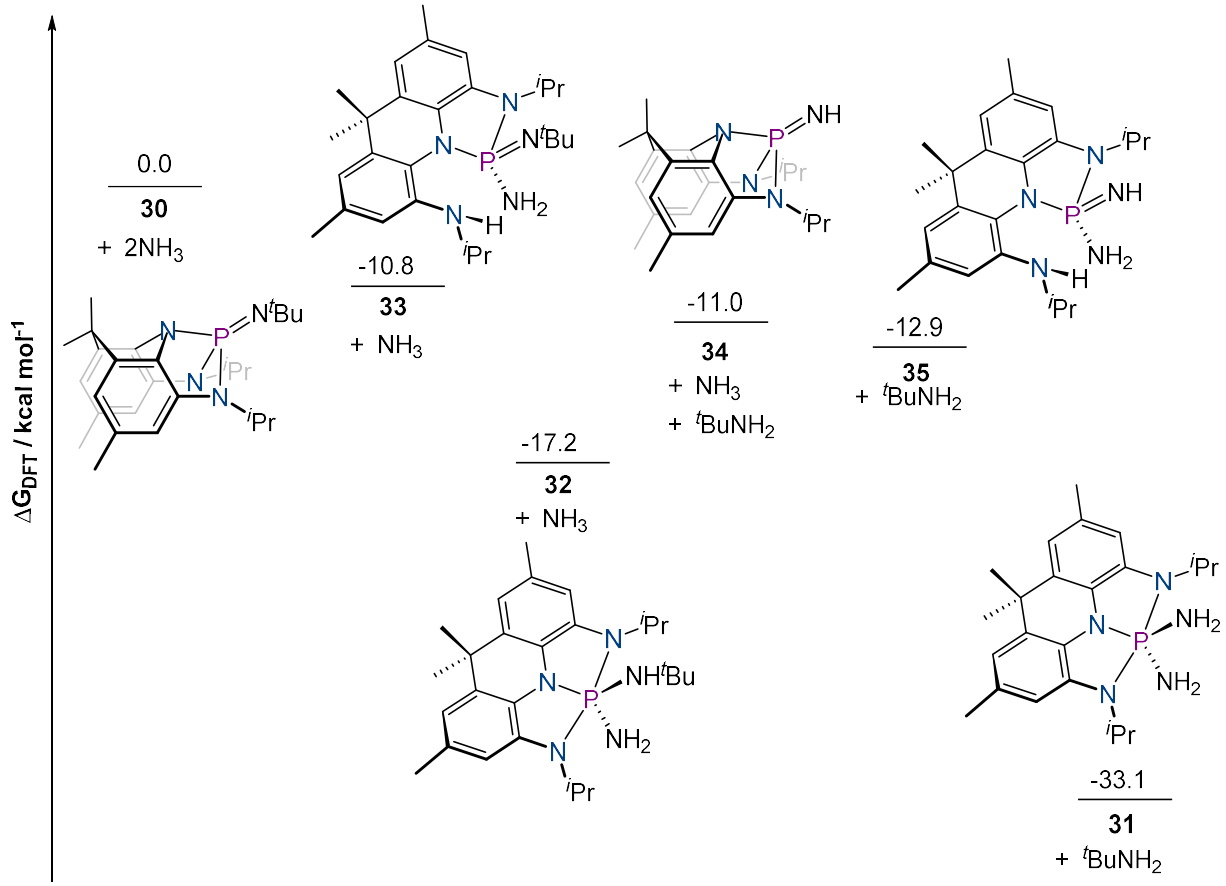


Figure 4.17. Proposed intermediates for the reaction to **30** and ammonia to yield **31**.

Regarding the unaccounted initial product with a $^{31}P\{^{1}H\}$ NMR chemical shift at 31.2 ppm, this was attributed to either cooperative addition products **33** or **35** based on this resonance being in a similar region of the spectrum to **29** (cf. 23.5 ppm). Of these, **35** was favoured due to the observation of a broad, significantly deshielded resonance in the ^{1}H NMR spectrum at 9.47 ppm during the relevant time intervals (Figure 4.18).

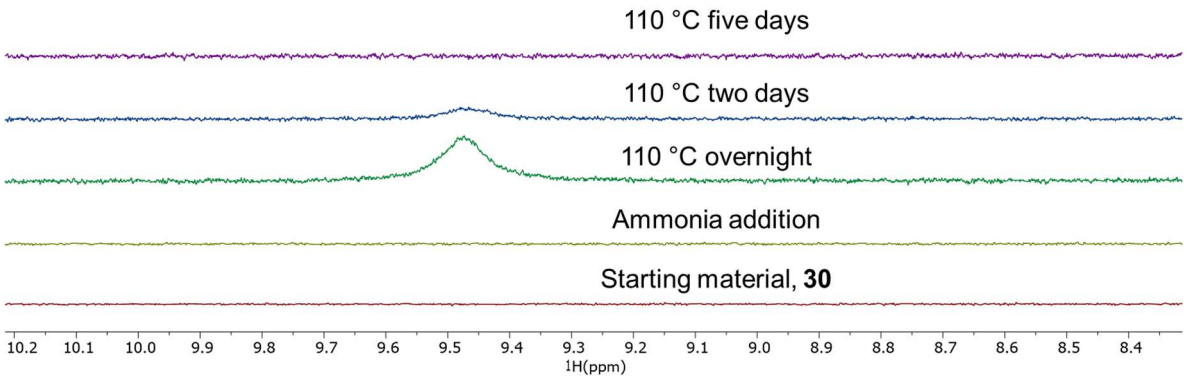


Figure 4.18. Stacked ^{1}H NMR of the reaction between **30** and ammonia.

This ^{1}H NMR resonance was attributed to the P=NH moiety in **35**. Because only limited reports of N–H containing, imine-type structures were available for comparison (and in alternate, polar solvents), this was only a tentative assignment.[12,13]

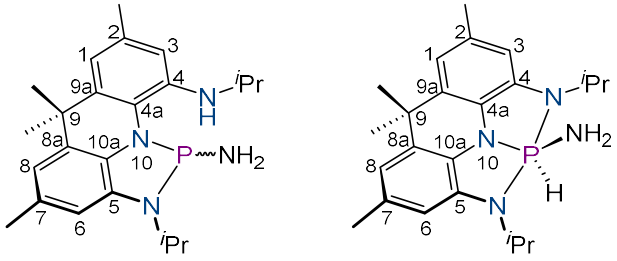
4.3 Conclusions

In conclusion, it was shown that N–H bond activation of ammonia was possible from a range of geometrically unconstrained derivatives of T-shaped phosphine **6**. The latter was shown to undergo N–H bond activation *via* initial cooperative addition product **26a** which eventually converts to formal oxidative addition product **26b**. From this phosphorus(V) species, the release of ammonia *via* reductive elimination regenerates **6** at elevated temperatures, showing that, overall, ammonia activation is reversable for this system. Phosphonium ion **7** and phosphine oxide **11** undergo N–H bond activation with ammonia more rapidly than **6**, despite their lack of geometric constraint about the phosphorus centre. This enhanced reactivity originates through engagement of the phosphorus atom lone pair in a bond, which serves to increase the Lewis acidity at phosphorus, similar to what was observed for transition metal complex **19**. Finally, iminophosphorane **30** was shown to also undergo N–H bond

activation, followed by subsequent intramolecular proton transfer resulting in amine release by formal hydroamination, or aminolysis, of the P=N bond. Together, these results highlight an alternative route toward species capable of ammonia activation, utilising simple phosphorus-derivatisation in place of enforced geometric constraint.

4.4 Experimental Section

4.4.1 Synthesis of 26a and 26b



26a **26b**

6 (5.0 mg, 13.2 μmol, 1.0 eq.) was dissolved in benzene (0.5 mL). This solution was freeze-pump-thaw degassed three times, then charged with an atmosphere of ammonia (1 bar). Initially, cooperative addition product, **26a**, formed exclusively, however on continued stirring (>1 hour), oxidative addition product **26b** was the predominant product. It should be noted that full consumption of **1** required stirring for at least 16 hours. A final **26a**:**26b** ratio of 2:5 was established after stirring for 2 days under these conditions.

Data for **26a**:

^{1}H NMR (600 MHz, C_6D_6): δ (ppm) 7.01 (1H, s, Ar*H*), 6.82 (1H, s, Ar*H*), 6.49 (1H, s, Ar*H*), 6.46 (1H, s, Ar*H*), 3.90 (1H, d-sept, $^{3}J_{P–H}$ = 12.2 Hz, $^{3}J_{H–H}$ = 6.8 Hz, $C_5NCH(CH_3)_2$), 3.69 (1H, dd, $^{TS}J_{P–H}$ = 10.2 Hz, $^{3}J_{H–H}$ = 7.0 Hz, C_4NH), 3.41 (1H, d-sept, $^{3}J_{H–H}$ = 7.3 Hz, $^{3}J_{H–H}$ = 6.3 Hz, $C_4NCH(CH_3)_2$), 2.42 (3H, s, $ArCH_3$), 2.32 (3H, s, $ArCH_3$), 1.84 (3H, s, $C_9(CH_3)$), 1.68 (3H, s, $C_9(CH_3)$), 1.47 (3H, d, $^{3}J_{H–H}$ = 6.8 Hz, $C_5NCH(CH_3)_2$), 1.40 (3H, d, $^{3}J_{H–H}$ = 6.8 Hz, $C_5NCH(CH_3)_2$), 1.11 (3H, d, $^{3}J_{H–H}$ = 6.3 Hz, $C_4NCH(CH_3)_2$), 1.07 (3H, d, $^{3}J_{H–H}$ = 6.3 Hz, $C_4NCH(CH_3)_2$).

$^{1}H\{^{31}P\}$ NMR (600 MHz, C_6D_6): δ (ppm) as above, except 3.90 (1H, sept, $^{3}J_{H–H}$ = 6.8 Hz, $C_5NCH(CH_3)_2$), 3.69 (1H, d, $^{3}J_{H–H}$ = 7.0 Hz, C_4NH).

$^{31}P\{^{1}H\}$ NMR (162 MHz, C_6D_6): δ (ppm) 84.7 (s).

^{31}P NMR (162 MHz, C_6D_6): δ (ppm) 84.7 (m).

$^{13}C\{^{1}H\}$ NMR (151 MHz, C_6D_6): δ (ppm) 135.7 (d, $^{2}J_{P–C}$ = 7.9 Hz, C_5), 134.0 (d, $^{3}J_{P–C}$ = 2.1 Hz, Ar), 130.6 (s, $C^{Ar}(CH_3)$), 130.4 (s, $C^{Ar}(CH_3)$), 128.9 (d, $^{2}J_{P–C}$ = 8.5 Hz, Ar), 127.6 (d, $^{2}J_{P–C}$ = 4.9 Hz, Ar), 127.1 (s, C_4), 119.9 (s, Ar), 117.00 (s, Ar), 115.5 (s, Ar), 107.3 (s, Ar), 46.9 (d, $^{2}J_{P–C}$ = 18.1 Hz, $C_5NCH(CH_3)_2$), 45.1 (d, $^{TS}J_{P–C}$ = 20.8 Hz, $C_4NCH(CH_3)_2$), 36.6 (s, C_9), 34.8 (s, $C_9(CH_3)$), 33.11 (s, $C_9(CH_3)$), 22.8 (s, $C_4NCH(CH_3)$), 22.7 (s, $C_4NCH(CH_3)$), 22.6 (s, $C_5NCH(CH_3)$), 22.5 (s, $C_5NCH(CH_3)$), 21.4 (s, C_2), 21.2 (d, $^{4}J_{P–C}$ = 4.6 Hz, C_7).

* the peak corresponding to either C_{8a} or C_{9a} was obscured by the solvent signal, therefore could not be located accurately.

Data for **26b**:

^{1}H NMR (600 MHz, C_6D_6): δ (ppm) 8.36 (1H, d, $^{1}J_{P–H}$ = 711.0 Hz, P–*H*), 6.70 (2H, s, Ar*H*), 6.50 (2H, s, Ar*H*), 3.51 (2H, d-sept, $^{3}J_{P–H}$ = 12.2 Hz, $^{3}J_{H–H}$ = 7.0 Hz, $C_{4/5}NCH(CH_3)_2$), 2.41 (6H, s, $C_{2/7}(CH_3)$), 1.79 (3H, s, $C_9(CH_3)$), 1.75 (3H, s, $C_9(CH_3)$), 1.28 (6H, d, $^{3}J_{H–H}$ = 7.0 Hz, $C_{4/5}NCH(CH_3)$), 1.20 (6H, d, $^{3}J_{H–H}$ = 7.0 Hz, $C_{4/5}NCH(CH_3)$).

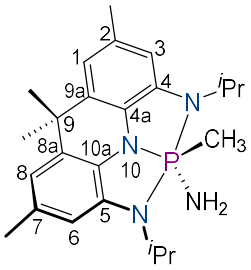
$^{1}H\{^{31}P\}$ NMR (600 MHz, C_6D_6): δ (ppm) as above, except 3.51 (2H, sept, $^{3}J_{H–H}$ = 7.0 Hz, $C_{4/5}NCH(CH_3)_2$).

The resonance at 8.36 ppm could not be decoupled due to the instrument used (decoupling was centred at a significantly different section of the ^{31}P NMR spectra).

$^{31}P\{^{1}H\}$ NMR (162 MHz, C_6D_6): δ (ppm) −60.1 (s).

^{31}P NMR (162 MHz, C_6D_6): δ (ppm) −60.1 (dt, $^{1}J_{P–H}$ = 710.9 Hz, $^{3}J_{P–H}$ = 16.4 Hz).

$^{13}C\{^{1}H\}$ NMR (151 MHz, C_6D_6): δ (ppm) 133.7 (d, $^{2}J_{P–C}$ = 10.9 Hz, $C_{4/5}$), 130.8 (s, $C_{2/7}$), 127.5 (d, $^{3}J_{P–C}$ = 9.2 Hz, $C_{8a/9a}$), 120.9 (d, $^{2}J_{P–C}$ = 12.2 Hz, $C_{4a/10a}$), 113.8 (s, $C_{1/8}H$), 107.2 (d, $^{3}J_{P–C}$ = 4.8 Hz, $C_{3/6}H$), 43.7 (d, $^{2}J_{P–C}$ = 11.3 Hz, $C_{4/5}NCH(CH_3)_2$), 37.2 (s, C_9), 33.7 (s, $C_9(CH_3)$), 32.1 (s, $C_9(CH_3)$), 22.9 (s, $C_{2/7}(CH_3)$), 21.2 (d, $^{3}J_{P–C}$ = 4.8 Hz, $C_{4/5}NCH(CH_3)$), 20.3 (d, $^{3}J_{P–C}$ = 1.5 Hz, $C_{4/5}NCH(CH_3)$).**4.4.2 Synthesis of 28**



6 (5.0 mg, 13.2 µmol, 1.0 eq.) was dissolved in benzene (0.5 mL). To this solution, methyl triflate (1.9 µl, 13.2 µmol, 1.0 eq.) was added, and the mixture heated to 80 °C for 1 hour. The volatiles were removed *in vacuo* and the resulting crystalline solid washed with benzene (0.5 mL), then dissolved in dichloromethane (0.5 mL). This yellow solution was freeze-pump-thaw degassed three times, then charged with an atmosphere of ammonia (1 bar). Instantly, the solution changed from yellow to colourless, and a white precipitate generated. The volatiles were removed *in vacuo*, and the product extracted into dichloromethane (0.5 mL) and filtered. Slow evaporation of this solution yielded **28** as colourless crystals (5.0 mg, 12.2 µmol, 92%). Crystals suitable for SCXRD were grown from a layered dichloromethane:pentane (1:5) solution of **28**.

^{1}H NMR (600 MHz, CD_2Cl_2): δ (ppm) 6.35 (2H, s, $C_{1/8}H$), 6.24 (2H, s, $C_{3/6}H$), 3.85 (2H, d-sept, $^{3}J_{P–H}$ = $^{3}J_{H–H}$ = 6.7 Hz, $C_{4/5}NCH(CH_3)_2$), 2.61 (2H, br s, P–NH_2), 2.27 (6H, s, $C_{2/7}(CH_3)$), 1.97 (3H, d, $^{2}J_{P–H}$ = 15.3 Hz, P–CH_3), 1.60 (3H, s, $C_9(CH_3)$), 1.53 (3H, s, $C_9(CH_3)$), 1.46 (12H, d, $^{3}J_{H–H}$ = 6.7 Hz, $C_{4/5}NCH(CH_3)_2$).

$^{1}H\{^{31}P\}$ NMR (600 MHz, CD_2Cl_2): δ (ppm) as above, except 3.85 (2H, sept, $^{3}J_{H–H}$ = 6.7 Hz, $C_{4/5}NCH(CH_3)_2$), 1.97 (3H, s, P–CH_3).

$^{13}C\{^{1}H\}$ NMR (151 MHz, CD_2Cl_2): δ (ppm) 134.5 (s, $C_{4/5}$), 130.8 (s, $C_{2/7}$), 126.8 (s, $C_{8a/9a}$), 120.3 (s, $C_{4a/10a}$), 111.8 (s, $C_{1/8}$), 105.8 (s, $C_{3/6}$), 45.9 (s, $C_{4/5}NCH(CH_3)_2$), 36.4 (s, C_9), 34.3 (s, $C_9(CH_3)$), 32.0 (s, $C_9(CH_3)$), 22.5 (s, $C_{2/7}(CH_3)$), 22.2 (d, $^{1}J_{P-C}$ = 168 Hz, P–CH_3), 20.1 (s, $C_{4/5}NCH(CH_3)_2$).

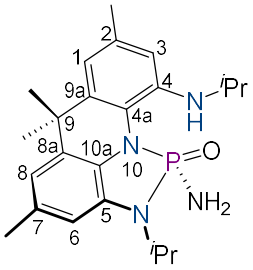
$^{31}P\{^{1}H\}$ NMR (243 MHz, CD_2Cl_2): δ (ppm) −50.5 (br s).

^{31}P NMR (243 MHz, CD_2Cl_2): δ (ppm) −50.5 (br m).

Elemental analysis calcd. (%) for $C_{24}H_{35}N_4P_1$: C 70.21, H 8.59, N 13.65; Found: C 70.42, H 8.65, N 13.36.

HRMS (ESI) *m/z* calcd. for $C_{24}H_{35}N_4P_1+H^+$: 411.2672 $[M+H]^+$; Found: 411.2697.

4.4.3 Synthesis of 29



6 (5.0 mg, 13.2 µmol, 1.0 eq.) and pyridine N-oxide (1.3 mg, 13.2 µmol, 1.0 eq.) were dissolved in benzene and heated to 80 °C for 1 hour to generate phosphine oxide **11**. The volatiles were removed *in vacuo*, and the resulting residue dissolved in benzene. This colourless solution was freeze-pump-thaw degassed three times, then charged with an atmosphere of ammonia (1 bar). Volatiles were removed *in vacuo* and the residue extracted into benzene (0.5 mL) and filtered. Lyophilisation of this solution yielded **29** as a colourless powder (5.1 mg, 12.4 µmol, 94%). Crystals suitable for SCXRD were grown by slow evaporation of a pentane solution of **29** at room temperature.

^{1}H NMR (600 MHz, C_6D_6): δ (ppm) 6.86 (1H, s, C_3H), 6.76 (1H, s, C_8H), 6.75 (1H, d, $^{3}J_{H-H}$ = 4.0 Hz, C_4NH), 6.51 (1H, s, C_1H), 6.33 (1H, s, C_6H), 3.88 (1H, d-sept, $^{3}J_{P-H}$ = 16.8 Hz, $^{3}J_{H-H}$ = 6.8 Hz, $C_5NCH(CH_3)_2$), 3.45 (1H, d-sept, $^{3}J_{H-H}$ = 6.8 Hz, $^{3}J_{H-H}$ = 4.0 Hz, $C_4NCH(CH_3)_2$), 2.34 (2H, br s, P–NH_2), 2.30 (3H, s, $C_7(CH_3)$), 2.28 (3H, s, $C_2(CH_3)$), 1.82 (3H, s, $C_9(CH_3)$), 1.57 (3H, s, $C_9(CH_3)$),

1.44 (3H, d, $^{3}J_{H–H}$ = 6.8 Hz, $C_5NCH(CH_3)$), 1.39 (3H, d, $^{3}J_{H–H}$ = 6.8 Hz, $C_5NCH(CH_3)$), 1.21 (3H, d, $^{3}J_{H–H}$ = 6.3 Hz, $C_4NCH(CH_3)$), 1.14 (3H, d, $^{3}J_{H–H}$ = 6.3 Hz, $C_4NCH(CH_3)$).

$^{1}H\{^{31}P\}$ NMR (600 MHz, C_6D_6): δ (ppm) as above, except 3.88 (1H, d-sept, $^{3}J_{P–H}$ = 16.8 Hz, $^{3}J_{H–H}$ = 6.8 Hz, $C_5NCH(CH_3)_2$).

$^{13}C\{^{1}H\}$ NMR (151 MHz, C_6D_6): δ (ppm) 136.3 (s, C_4), 132.8 (d, $^{3}J_{P–C}$ = 6.7 Hz)*, 132. 1 (s, C_2), 130.5 (d, $^{2}J_{P–C}$ = 15.4 Hz, C_5), 130.2 (s, C_7), 126.7 (d, $^{3}J_{P–C}$ = 6.7 Hz)*, 124.3 (d, $^{2}J_{P–C}$ = 14.1 Hz, C_{10a}), 123.1 (d, $^{2}J_{P–C}$ = 3.4 Hz, C_{4a}), 117.9 (s, C_3), 116.3 (s, C_8), 113.2 (s, C_1), 106.6 (s, $^{3}J_{P–C}$ = 9.1 Hz, C_6), 45.9 (d, $^{2}J_{P–C}$ = 4.8 Hz, $C_5NCH(CH_3)_2$), 43.8 (s, $C_4NCH(CH_3)_2$), 36.0 (s, C_9), 35.7 (s, $C_9(CH_3)$), 32.7 (s, $C_9(CH_3)$), 22.4 (s, $C_5NCH(CH_3)_2$), 22.1 (s, $C_5NCH(CH_3)_2$), 21.6 (s, $C_7(CH_3)$), 21.1 (s, $C_2(CH_3)$), 20.6 (d, $^{4}J_{P–H}$ = 1.6 Hz, $C_4NCH(CH_3)_2$), 20.1 (m, $C_4NCH(CH_3)_2$).

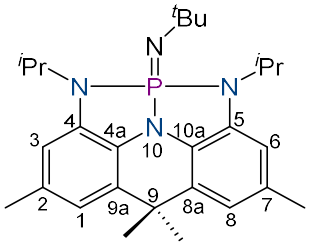
* Signals for $C_{8a/9a}$ could not be distinguished from one another.

$^{31}P\{^{1}H\}$ NMR (243 MHz, C_6D_6): δ (ppm) 23.5 (s).

^{31}P NMR (243 MHz, C_6D_6): δ (ppm) 23.5 (d, $^{3}J_{P–H}$ = 16.8 Hz).

HRMS (ESI) *m/z* calcd. for $C_{23}H_{33}N_4O_1P_1+H^+$: 413.2465 $[M+H]^+$; Found: 413.2502.

4.4.4 Synthesis of 30



6 (10.0 mg, 26.4 µmol, 1.0 eq.) was dissolved in toluene (0.5 mL). *Tert*-butyl azide (1 drop, excess) was added and the solution heated to 110 °C for two hours. The volatiles were removed *in vacuo* and the residue extracted into pentane (2 × 0.5 mL). Slow evaporation of this solution yielded **30** as colourless crystals suitable for SCXRD (10.2 mg, 22.6 µmol, 86%).

^{1}H NMR (600 MHz, C_6D_6): δ (ppm) 6.56 (2H, s, $C_{1/8}H$), 6.43 (2H, s, $C_{3/6}H$), 4.06 (d-sept, $^{3}J_{P–H}$ = 13.3 Hz, $^{3}J_{H–H}$ = 6.7 Hz, $C_{4/5}NCH(CH_3)_2$), 2.23 (6H, s, $C_{2/7}(CH_3)$), 1.68 (3H, s, $C_9(CH_3)$), 1.62 (3H, s, $C_9(CH_3)$), 1.56 (6H, d, $^{3}J_{H–H}$ = 6.7 Hz, $C_{4/5}NCH(CH_3)$), 1.53 (9H, d, $^{4}J_{P–H}$ = 1.1 Hz, P–N^{t}Bu), 1.29 (6H, d, $^{3}J_{H–H}$ = 6.7 Hz, $C_{4/5}NCH(CH_3)$).

^{1}H{^{31}P} NMR (600 MHz, C_6D_6): δ (ppm) as above, except 4.06 (sept, $^{3}J_{H–H}$ = 6.7 Hz, $C_{4/5}NCH(CH_3)_2$), 1.53 (9H, s, P–N^{t}Bu).

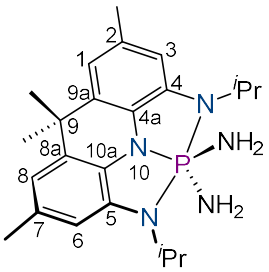
^{13}C{^{1}H} NMR (151 MHz, C_6D_6): δ (ppm) 135.1 (d, $^{2}J_{P–C}$ = 19.3 Hz, $C_{4/5}$), 134.8 (d, $^{3}J_{P–C}$ = 9.9 Hz, $C_{8a/9a}$), 134.2 (d, $^{2}J_{P–C}$ = 6.6 Hz, $C_{4a/10a}$), 132.7 (s, $C_{2/7}$), 114.8 (s, $C_{1/8}$), 109.3 (d, $^{2}J_{P–C}$ = 10.5 Hz, $C_{3/6}$), 51.7 (d, $^{2}J_{P–C}$ = 4.3 Hz, P–N^{t}Bu), 45.9 (d, $^{2}J_{P–C}$ = 2.2 Hz, $C_{4/5}NCH(CH_3)_2$), 40.0 (s, C_9), 34.5 (d, $^{3}J_{P–C}$ = 13.0 Hz, P–N^{t}Bu), 25.6 (s, $C_9(CH_3)$), 22.3 (s, $C_9(CH_3)$), 22.0 (s, $C_{2/7}(CH_3)$), 20.5 (d, $^{3}J_{P–C}$ = 3.3 Hz, $C_{4/5}NCH(CH_3)$), 20.4 (s, $C_{4/5}NCH(CH_3)$).

^{31}P{^{1}H} NMR (243 MHz, C_6D_6): δ (ppm) 6.8 (s).

^{31}P NMR (243 MHz, C_6D_6): δ (ppm) 6.8 (t, $^{3}J_{P–H}$ = 13.2 Hz).

Elemental analysis calcd. (%) for $C_{27}H_{39}N_4P_1$: C 71.97, H 8.72, N 12.43; Found: C 72.18, H 8.70, N 11.65.

4.4.5 Synthesis of 31



6 (5.0 mg, 13.2 µmol, 1.0 eq.) was dissolved in toluene (0.5 mL). *Tert*-butyl azide (1 drop, excess) was added and the solution heated to 110 °C for two hours. The solvent and volatiles were removed *in vacuo* then the residue dissolved in toluene (0.5 mL). The solution was freeze-pump-thaw degassed four times, then charged with an atmosphere of ammonia (1 bar). The solution was heated to 110 °C for 5 days. The solvent and volatiles were removed *in vacuo* then the resulting crystalline solid washed with hexane

(2 × 0.5 mL). The crystalline material was dissolved in dichloromethane (0.5 mL). Slow evaporation of this solution yielded **31** as colourless crystals (3.5 mg, 8.5 μmol, 64%). Crystals suitable for SCXRD were obtained by slowly cooling a benzene solution of **31** from 80 °C to room temperature.

^{1}H NMR (600 MHz, CD_2Cl_2): δ (ppm) 6.37 (2H, s, $C_{1/8}H$), 6.24 (2H, s, $C_{3/6}H$), 4.01 (2H, d-sept, $^{3}J_{P–H} = {}^{3}J_{H–H}$ = 7.0 Hz, $C_{4/5}NCH(CH_3)_2$), 2.70 (4H, d, $^{2}J_{P–H}$ = 7.2 Hz, P–NH_2), 2.27 (6H, s, $C_{2/7}(CH_3)$), 1.56 (6H, s, $C_9(CH_3)_2$), 1.47 (12H, d, $^{3}J_{P–H}$ = 7.0 Hz, $C_{4/5}NCH(CH_3)_2$).

^{1}H{^{31}P} NMR (600 MHz, CD_2Cl_2): δ (ppm) as above, except 4.01 (2H, sept, $^{3}J_{H–H}$ = 7.0 Hz, $C_{4/5}NCH(CH_3)_2$), 2.70 (4H, s, P–NH_2).

^{13}C{^{1}H} NMR (151 MHz, CD_2Cl_2): δ (ppm) 133.9 (d, $^{2}J_{P–C}$ = 13.5 Hz, $C_{4/5}$), 130.4 (s, $C_{2/7}$), 126.2 (d, $^{3}J_{P–C}$ = 9.7 Hz, $C_{8a/9a}$), 120.3 (d, $^{2}J_{P–C}$ = 14.7 Hz, $C_{4a/10a}$), 112.3 (s, $C_{1/8}$), 106.0 (d, $^{3}J_{P–C}$ = 6.5 Hz, $C_{3/6}$), 46.1 (d, $^{2}J_{P–C}$ = 2.6 Hz, $C_{4/5}NCH(CH_3)_2$), 36.6 (d, $^{4}J_{P–C}$ = 1.3 Hz, C_9), 33.1 (s, $C_9(CH_3)$), 22.5 (s, $C_{2/7}(CH_3)$), 20.0 (d, $^{3}J_{P–C}$ = 2.4 Hz, $C_{4/5}NCH(CH_3)_2$).

^{31}P{^{1}H} NMR (243 MHz, CD_2Cl_2): δ (ppm) −57.8 (s).

^{31}P NMR (243 MHz, CD_2Cl_2): δ (ppm) −57.8 (sept, $^{2}J_{P–H} = {}^{3}J_{P–H}$ = 7.2 Hz).

HRMS (ESI) *m/z* calcd. for $C_{23}H_{34}N_5P_1$+H^+: 412.2625 [*M*+H]$^+$; Found: 412.2678.

4.5 References

[1] S. Ghavam, M. Vahdati, I. A. G. Wilson, P. Styring, *Front. Energy Res.* **2021**, *9*.

[2] V. Lavallo, G. D. Frey, B. Donnadieu, M. Soleilhavoup, G. Bertrand, *Angew. Chem., Int. Ed.* **2008**, *47*, 5224–5228.

[3] S. Streiff, F. Jérôme, *Chem. Soc. Rev.* **2021**, *50*, 1512–1521.

[4] T. P. Robinson, D. M. De Rosa, S. Aldridge, J. M. Goicoechea, *Angew. Chem., Int. Ed.* **2015**, *54*, 13758–13763.

[5] A. J. King, J. M. Goicoechea, *Chem. Eur. J.* **2024**, *30*, e202400624.

[6] A. Okuniewski, D. Rosiak, J. Chojnacki, B. Becker, *Polyhedron* **2015**, *90*, 47–57.

[7] S. Bonfante, C. Lorber, J. M. Lynam, A. Simonneau, J. M. Slattery, *J. Am. Chem. Soc.* **2024**, 146, 2005–2014.

[8] A. J. King, J. Abbenseth, J. M. Goicoechea, *Chem. Eur. J.* **2023**, *29*, e202300818.

[9] S. M. McCarthy, Y.-C. Lin, D. Devarajan, J. W. Chang, H. P. Yennawar, R. M. Rioux, D. H. Ess, A. T. Radosevich, *J. Am. Chem. Soc.* **2014**, *136*, 4640–4650.

[10] A. W. Addison, T. N. Rao, J. Reedijk, J. van Rijn, G. C. Verschoor, *J. Chem. Soc., Dalton Trans.* **1984**, 1349–1356.

[11] Y.-C. Lin, J. C. Gilhula, A. T. Radosevich, *Chem. Sci.* **2018**, *9*, 4338–4347.

[12] G. Pawelke, R. Dammei, W. Poll, *Z. Naturforsch. B* **1992**, *47*, 351–357.

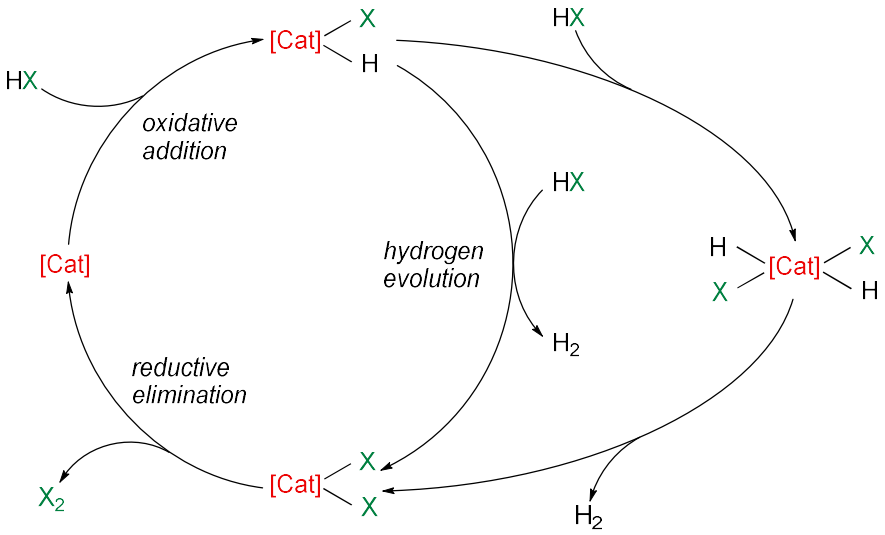
[13] J. L. Ripoll, H. Lebrun, A. Thuillier, *Tetrahedron* **1980**, *36*, 2497–2503.

Chapter 5

Reductive Elimination from Phosphoranes Derived from a T-Shaped Phosphine

Abstract. The synthesis of dihalophosphoranes derived from **6** was attempted. In the case of the difluoro- and diiodophosphoranes, these efforts provided only the respective HX-cooperative addition product. Conversely, the dichloro- and dibromophosphoranes were accessible. Photo-reduction of these phosphorus(V) species was achieved through LED irradiation targeting the Soret band in their UV-Vis spectra. The electronic transition responsible for this spectroscopic feature involved populating a σ^*_{P-X} antibonding orbital, resulting in photo-elimination of halogen radicals from the phosphorus centre. This is supported by TD-DFT calculations and evidenced by heteronuclear NMR spectroscopy and SCXRD analysis. In support of this mechanism, radical elimination was observed upon heating **46** — a phosphorus(V) species bearing substituents at phosphorus which themselves are stable as free-radicals.

5.1 HX-Splitting



Scheme 5.1. General mechanism of catalytic HX-splitting.

HX-splitting is the process of converting a molecule of HX, where X is a halogen, into half an equivalent each of H_2 and X_2. HX-splitting is often considered a simplification of the water-splitting reaction, making it a useful proxy for studying the latter.[1] There are two proposed mechanisms for HX-splitting, each of which are initiated by the oxidative addition of a molecule of HX to a catalyst, followed by hydrogen evolution through either intra- or intermolecular reaction with another molecule of HX, then finally the reductive elimination of X_2 (Scheme 5.1).

5.2 Halogen photoelimination

The final reductive elimination step is the most common bottleneck for developments towards catalysts for HX-splitting, analogous to the limiting oxygen-evolution reaction in electrocatalytic water-splitting.[2,3] The difficulty in X_2 elimination originates from the strong bonds between halogens and transition-metals, resulting in a steep thermodynamic barrier to completing this catalytic cycle. An energy input, often in the form of light, is required to overcome this thermodynamic barrier and regenerate the catalyst. Therefore, the oxidised catalyst must contain the appropriate orbitals to direct this energy towards bond cleavage, namely photo-accessible $\sigma^*_{M–X}$ antibonding orbitals. Promotion into such orbitals labilises the M–X bond for dissociation either through the release of an X_2 molecule or by sequential release of X· radials.[4] To prevent the eliminated halogen from back-reacting with the reduced catalyst, a halogen trapping reagent is often included in these reactions, typically in the form of an alkene.

5.2.1 Transition metal-based systems

Early developments in systems capable of halogen photoelimination employed 2nd and 3rd row transition metals, in particular bimetallic complexes of these metals. The bimetallic core of such complexes features a low-lying, photo-accessible $\sigma^*_{M–M}$ orbital which is simultaneously antibonding with respect to substituents *trans* to the M–M bond.[3] If an M–X bond is situated in this *trans* position, cleavage of this bond may ensue upon irradiation, resulting in halogen elimination. Rhodium complex **I** exemplifies this approach towards a functioning HCl-splitting photocatalyst (Figure 5.1).[5,6] Chlorine radical photoelimination occurs from the mixed valence $LRh^0–Rh^{II}Cl_2$ intermediate, with the sterically

controlling bridging bisphosphine ligands forcing a chloride ligand into the photo-labile *trans* position opposite the Rh–Rh bond.

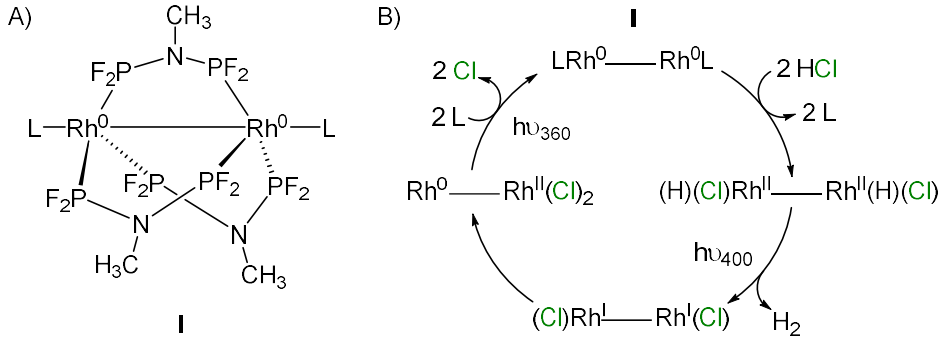


Figure 5.1. A) Structure of HCl-splitting catalyst **I**. B) Proposed catalytic cycle of HCl-splitting by **I**. L = THF.

Efforts to improve the efficiency of halogen photoelimination from complexes such as **I** include the incorporation of Lewis acidic metals into the bimetallic core, such that reduction of the complex is promoted. Towards this, complex **II** (Figure 5.2) featuring a Rh^{II}–Au^{II} heterobimetallic core was synthesised , but proved to be thermally unstable to disproportionation through rupture of the metal–metal bond.[7] As such, metals exhibiting better d-orbital overlap were chosen to stabilise the bimetallic core through increased covalency, exemplified by Pt^{II}–Au^{II} complex **III**.[8] With respect to the parent rhodium homobimetallic **I**, complex **III** boasts approximately a 10-fold increase in chlorine radical photoelimination quantum yield.

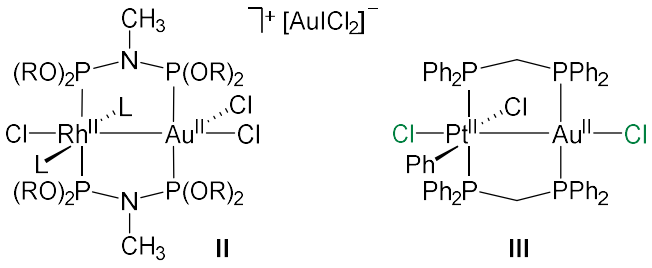


Figure 5.2. Structures of bimetallics **II** and **III**. In green are the chloride atoms which undergo photoelimination. R = CH_2CF_3

Further developments saw trap-free photoelimination of chlorine through solid-state photolysis of **IV**, containing a Pt^{III}–Pt^{III} bimetallic core, proceeding *via* the concerted elimination of a Cl_2 *molecule* rather than sequential radical release (Figure 5.3).[9] Similarly, Au^{III} complexes **V** underwent trap-free

photoelimination of Cl_2 or Br_2.[10] This reaction was initiated by ligand-to-metal charge-transfer (LMCT) upon irradiation, rather than metal-to-metal charge-transfer (MMCT) as for **I**–**III**, hence related monometallic complexes of the type **VI** were also capable of this reactivity. Exploiting LMCT transitions has enabled the development of other monomeric complexes which undergo photoelimination, such as **VII** featuring simple phosphines and alkyl/aryl ligands.[11]

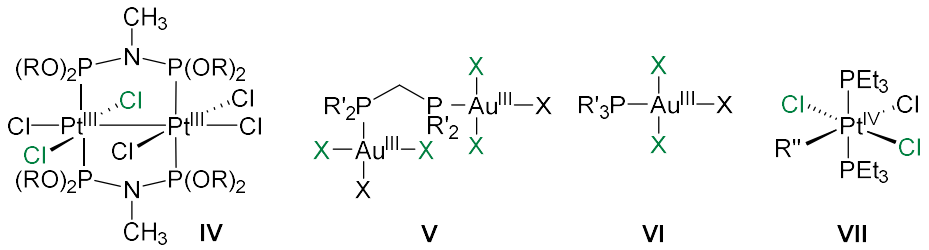
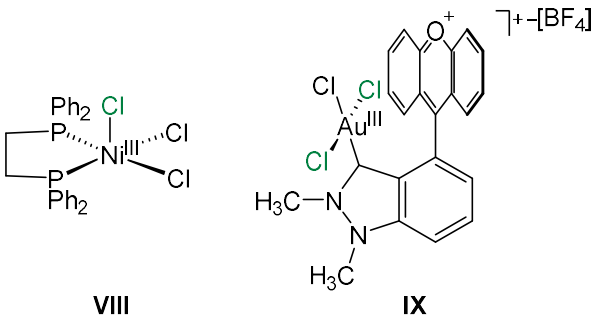


Figure 5.3. Structures of complexes **IV**–**VII**. In green are the halide atoms which undergo photoelimination. R = CH_2CF_3. X = Cl or Br. R′ = Ph or Cy. R″ = Cl, Ph, 9-phenanthryl, 2-trifluoromethylphenyl, 4-trifluoromethylphenyl, 3-perylenyl.

Further work sought to assess the possibility of 3d transition metals enacting this reactivity; attractive on account of their higher crustal abundance than precious metals, as previously investigated. Nickel(II) complex **VIII** (Figure 5.4) undergoes chlorine radical elimination on irradiation (λ>430 nm).[12,13] A related complex, featuring a bipyridyl ligand in place of the bisphosphine, found further application of this reactivity in cascade C(sp^3)–H cross-coupling reactions which utilise the eliminated chlorine radicals in the crucial C–H cleavage step.[14,15] Ligand cooperativity was observed in the photoelimination of chlorine from nickel complex **VIII**; whereby the released chlorine radical was stabilised through radical–π interaction, facilitated by the flanking aryl substituents on the bisphosphine ligand.[12,13] Further ligand cooperativity was observed in chloride radical elimination from gold complex **IX**, whereby the centre of photoexcitation was solely ligand based.[16] Irradiation of **IX** results in the formation of an indazolylidene-xanthylium biradical excited state, which is reductively quenched by a chloride ligand. This reaction was facilitated by an anion–π^+ interaction between the chloride ligand and the pendant xanthylium unit; an interaction observed crystalographically in the ground state of **IX**.

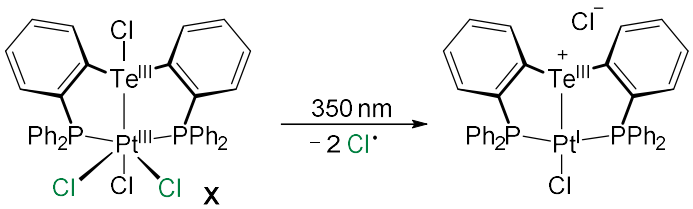


VIII IX

Figure 5.4. Structures of complexes **VIII** and **IX**. In green are the chlorine atoms which undergo photoelimination.

5.2.2 Transition metal-main-group cooperative systems

Motivated by replacing expensive transition metals with main-group elements, Gabbaï and co-workers synthesised a range of compounds featuring a heavy main-group element in the binuclear core of complexes resembling **I**–**IV**. One such complex, **X**, featuring a bond between platinum(III) and a ligand-based tellurium(III) centre, was found to eliminate chlorine radicals upon irradiation with 350 nm light (Scheme 5.2). TD-DFT revealed that this reaction results from photo-induced electronic transitions into the LUMO and LUMO+1 orbitals, each of which bear significant Te–Cl and Pt–Cl antibonding character.[17] The tellurium centre played a spectator role in this redox-cycle, though crucial was its ability to modulate the electronics at platinum. The higher platinum oxidation state was stabilised through increased σ-donation from the tellurium centre, bolstered through close association of a chloride anion to the tellurium atom (making it more electron rich). Conversely, reductive elimination at platinum was facilitated by chloride ion dissociation into the outer sphere – a process promoted through irradiation, resulting in a less electron rich, and thus less strongly donating, tellurium centre.



Scheme 5.2. Chlorine radical photo-elimination of **X** bearing a Pt^{III}–Te^{III} binuclear core. In green are the chlorine atoms which undergo photoelimination.

Platinum complex **XI**, the antimony analogue of **X**, similarly contains strong bands in the UV-Vis spectrum corresponding to excitations into its LUMO and LUMO+1 orbitals bearing significant Pt–Cl antibonding character (Figure 5.5).[18] Thus, irradiation of **XI** resulted in the elimination of two chlorine radicals, and occurred notably more efficiently than for **X**; an observation attributed to the increased number of electron withdrawing chloride substituents at the antimony centre, enabled by the higher-valence of Sb^{V} compared to Te^{IV}. A related complex, **XII**, was synthesised through replacement of platinum with palladium. Reaction of **XII** with $PhICl_2$ results in oxidation at both the main-group and transition-metal centres through "Cl_2" addition across the Sb–Pd bond, yielding **XIII**.[19] Chlorine photoelimination upon irradiation of **XIII** occurred predominantly at the main-group fragment, representing a role-reversal compared to **X** and **XI**.

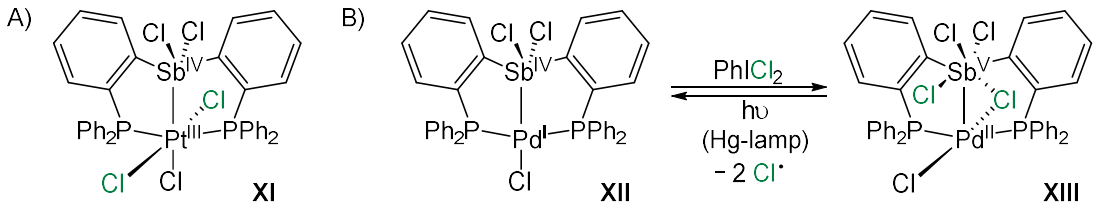


Figure 5.5. A) structure of complex **XI** bearing a Pt^{III}–Sb^{IV} binuclear core. B) Chlorination of **XII** and subsequent reductive elimination of **XIII**. In green are the chlorine atoms which undergo photoelimination.

Moving to the third row of the p-block, the germanium analogue of **XI** was shown to also undergo photoreduction through the release of two metal-based chloride ligands as chlorine radicals.[20] A derivative of this system, **XV**, employing a phenyl substituent at the germanium centre similarly undergoes chlorine photoelimination.[21] However, if an insufficient concentration of halogen trap is used, the eliminated chlorine radicals are partially quenched at the germanium-based phenyl group resulting in the elimination of chlorobenzene (Figure 5.6). Phenyl-groups flanking the position of halogen elimination have been cited to promote photoreduction through stabilising radical–π interactions, as was observed for **VIII**. It is evident, therefore, that aromatic groups flanking the site of radical elimination must not be labile, else ligand disassembly through Ar–Cl elimination occurs.

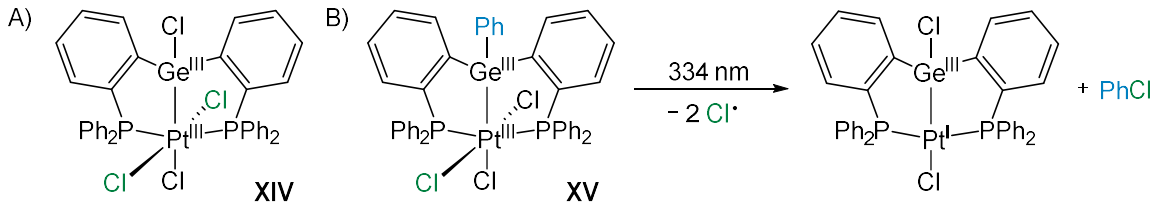


Figure 5.6. A) Photo-reductive elimination of chlorine radicals from **XIV**. B) Phenyl-substituted complex **XV**. In green are the chlorine atoms which undergo photoelimination.

5.2.3 Single-centre main-group systems

Seferos reported the reductive elimination of both chlorine and bromine radicals from a series of 2,5-disubstituted five membered heterocycles containing a Te^{II}/Te^{IV} centre. This was initially observed for **XVI** featuring *iso*-indigo substituents and extended π-conjugation across the whole molecule.[22] The LUMO+2 of **XVI** had partial Te–X antibonding character, and the HOMO–LUMO+2 excitation was accessible using visible (505 nm) light. This was on account of the chromophore effect of the *iso*-indigo substituents, red-shifting the absorption properties of **XVI**. However, photo-reduction was inefficient due to relaxation mechanisms of the targeted photo-excited-state into lower energy states that do not have Te–X antibonding character. This issue was addressed with **XVII** which possess smaller and more simple aryl substituents at the 2,5-positions of the tellurophene (Figure 5.7).[23–25] The LUMO of these compounds was shown to possess significant Te–X antibonding character, and as excitation from the HOMO–LUMO provides the lowest energy excited state, the aforementioned unproductive decay was avoided.

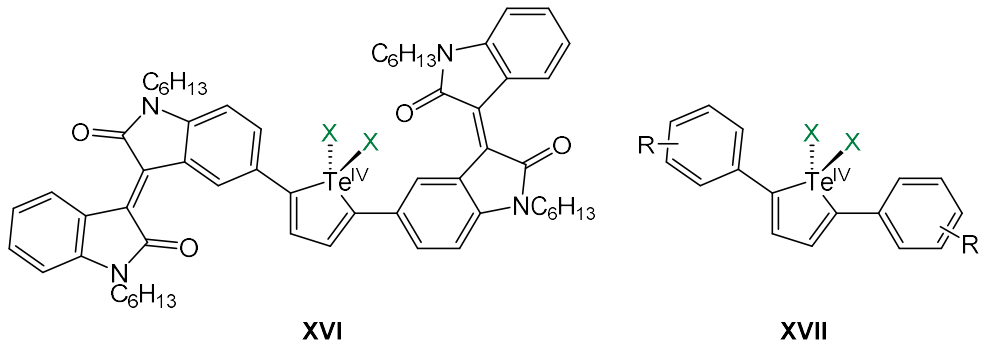
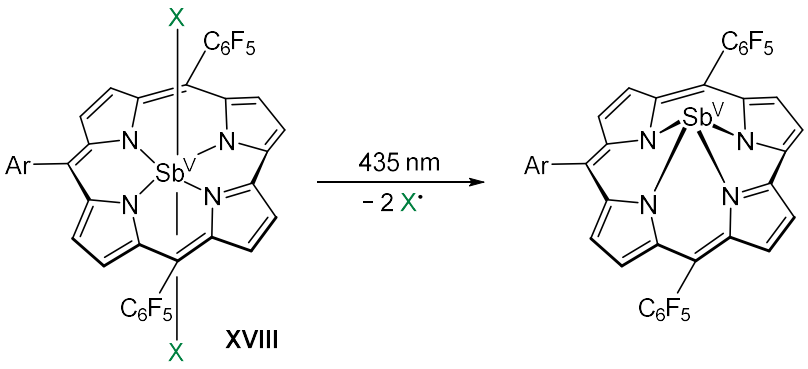


Figure 5.7. Structures of 2,5-disubstituted tellurophenes **XVI** and **XVII**. R = H, *p*-CF_3, *p*-CN, *p*-^{t}Bu etc. See reference for full list of tellurophene derivatives.[24]

Antimony(V) dihalide corrole **XVIII** was shown to undergo photo-reductive elimination of bromine and chlorine radicals upon irradiation with 435 nm light (Scheme 5.3).[26] Irradiation targeted transitions into the LUMO+2 orbital, with the corrole ligand chosen on account of its large absorption cross-section. Despite a multitude of possible derivatives and alternative macrocyclic frameworks, this system was not investigated any further.



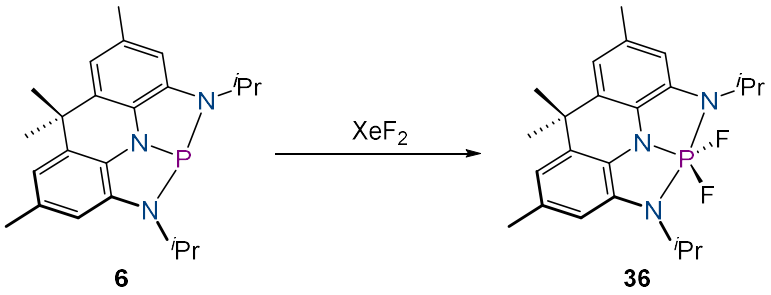
Scheme 5.3. Photo-reductive elimination of halogen radicals from antimony corrole **XVII** X = Cl, Br. Ar = *p*-(COOMe)C_6H_4.

5.3 Synthesis of 6-derived dihalophosphoranes

To assess whether dihalophosphoranes derived from T-shaped phosphine **6** are suitable candidates for halogen photoelimination, the full series of compounds bearing PX_2 (with X = F–I) subunits were targeted. The synthesis of the respective dibromophosphorane, **5**, was described in Chapter 2, therefore the following details the attempted synthesis of the remaining compounds in the series.

5.3.1 Difluorophosphorane, 36

Xenon difluoride was added to a dichloromethane solution of **6**, resulting in a dark purple solution and the generation of a single new product exhibiting a triplet in the $^{31}P\{^1H\}$ NMR spectrum at −40.0 ppm ($^1J_{P–F}$ = 877 Hz). The multiplicity and large coupling constant indicate the formation of two P–F bonds, with the significantly negative $^{31}P\{^1H\}$ NMR chemical shift typical of phosphorus(V) derivatives of geometrically constrained phosphines.[27] The ^1H NMR spectrum of this compound contained resonances describing a C_{2v} symmetric acridane ligand, overall confirming the formation of difluorophosphorane **36** (Scheme 5.4).

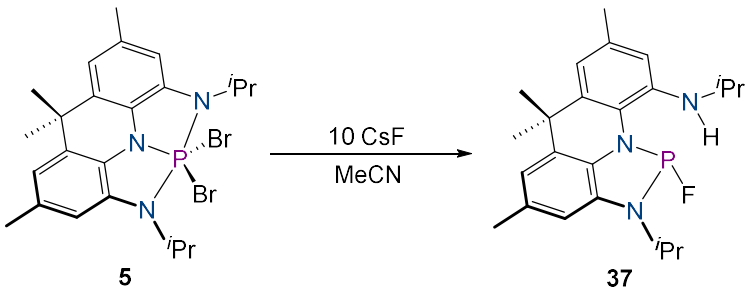


6 36

Scheme 5.4. Synthesis of difluorophosphorane **36**.

However, compositionally pure samples of **36** could not be obtained on account of difficulty in removing unreacted xenon difluoride. Further, the presence of this starting material prevented crystallisation of **36** for diffraction analysis, with only crystals of xenon difluoride forming instead. UV-Vis spectroscopy of **36** was not possible on account of the characteristic dark purple colour of solutions containing xenon difluoride, therefore further photochemistry of **36** was not pursued.

An alternative method of synthesis avoiding the use of xenon difluoride was targeted. Halide exchange of **5** with excess caesium fluoride in acetonitrile proceeded immediately with the generation of a colourless solution The appearance of a doublet in the $^{31}P\{^{1}H\}$ NMR spectrum at 8.9 ppm ($^{1}J_{P–F}$ = 1042 Hz) suggests the formation of a single P–F bond. ^{1}H NMR spectroscopy revealed a desymmetrised acridane backbone formed through the cleavage of a side-arm P–N_{ligand} bond, with the concomitant formation of a new N–H bond revealed by a ^{1}H NMR resonance at 4.56 ppm. These data suggest the formation of fluorophosphine **37** (Scheme 5.5), with the comparatively high ^{1}H NMR chemical shift of its N–H bond indicative of hydrogen bonding to a P–F unit (cf. N–H ^{1}H NMR: δ (ppm) 2.97 (**16**, chloride analogue)).



5 37

Scheme 5.5. Synthesis of fluorophosphine **37**.

It is suspected that protonation results from impurities in the caesium fluoride reagent. This may also explain the significant formation of phosphine oxide **11** on leaving solutions of **37** at room temperature, thus precluding full characterisation and isolation of **37** as a compositionally pure material. Single crystals of **37** could, however, be grown, with SCXRD revealing that in the solid-state **37** is isostructural to the analogous chlorophosphine **16** (Figure 5.8).

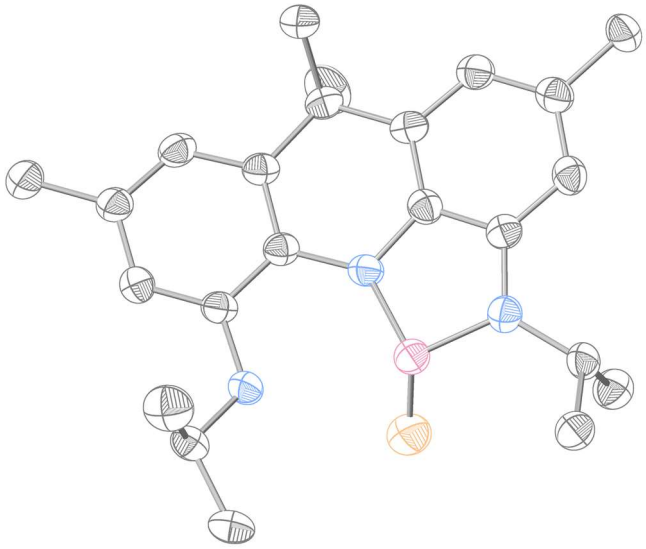
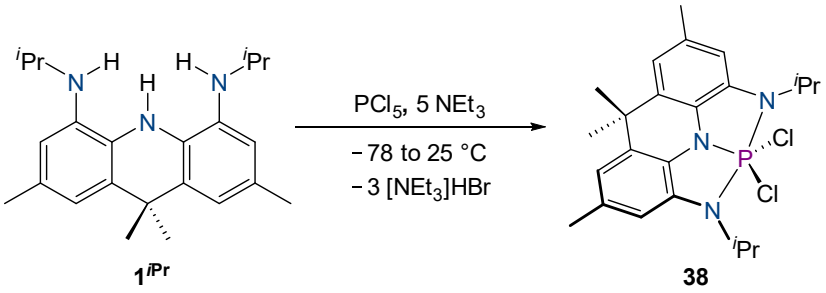


Figure 5.8. Solid-state structure of **37**. Thermal ellipsoids pictured at 50% probability level. Hydrogen atoms removed for clarity.

5.3.2 Dichlorophosphorane, 38

The reaction between PCl_5 the protio ligand $\mathbf{1}^{i\mathbf{Pr}}$ in the presence of NEt_3 provides dichlorophosphorane **38** in 39% isolated yield (Scheme 5.6). **38** is characterised by a peak at −49.7 ppm in its $^{31}P\{^{1}H\}$ NMR spectrum, downfield shifted with respect to that of **5**, but upfield shifted compared to **36**; a trend observed previously for difluoro/chloro/bromo phosphoranes.[27]



Scheme 5.6. Synthesis of dichlorophosphorane **38**.

In the ^{1}H NMR spectrum of **38**, C_{2v} symmetry is observed for the acridane backbone signals, suggesting a flat conformation. This is confirmed in the solid-state through SCXRD (Figure 5.9), which reveals a five-coordinate phosphorus centre of pentagonal-bipyramidal geometry. Two chloride substituents reside in the equatorial plane, as does the central ligand nitrogen atom, while the flanking nitrogen donor atoms are positioned axially. Dichloride **38** is isostructural in the solid-state to dibromide **5**, with the exception of the P–X bond lengths; P–X (Å) = 2.092(9) (X = Cl, **38**), 2.286(6) (X = Br, **5**).

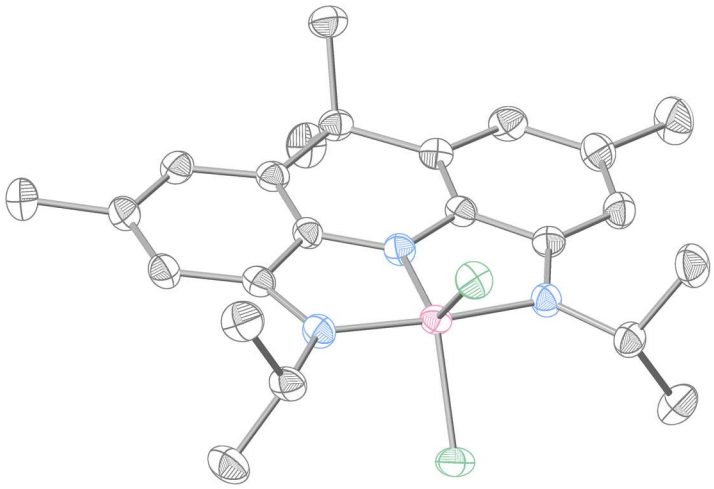
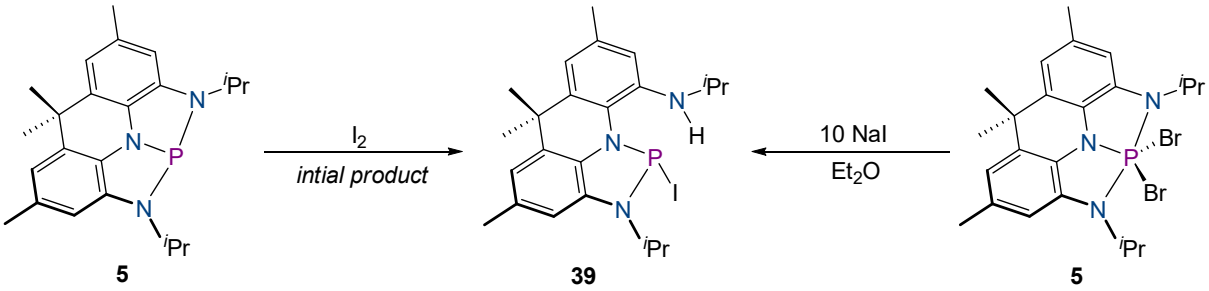


Figure 5.9. Solid-state structure of **38**. Thermal ellipsoids pictured at 50% probability level. Hydrogen atoms removed for clarity.

5.3.3 Diiodophosphorane

Diiodophosphoranes are comparatively rare compared to their lighter counterparts. Reactions between phosphines and elemental iodine typically results in the formation of charged species *via* initial nucleophilic attack of the $\sigma^*_{I\text{–}I}$ orbital of iodine by the phosphorus lone-pair, yielding either "spoke complexes" of the type [R_3P–I–I] or fully ionised iodophosphonium iodides.[28–30] Reaction of **6** with elemental iodine (Scheme 5.7) proceeds with the generation of a new signal in the ^{31}P{^{1}H} NMR spectrum of the reaction mixture at 173.8 ppm, a chemical shift indicative of a phosphorus(III) oxidation state for this class of compound. Continued stirring of this reaction mixture resulted in the formation of several unknown phosphorus-containing compounds evidenced by additional signals growing in the ^{31}P{^{1}H} NMR spectrum over time. This also occurs upon solvent removal from the reaction mixture *in vacuo*, thus precluding isolation of the initial product. However, redissolving this

residue followed by slow evaporation enabled the growth of diffraction quality crystals, permitting the identification of iodophosphine **39** as a reaction product by SCXRD (Figure 5.10). Synthesis of the target diiodophosphorane was also attempted through halide exchange of **5** with NaI in diethyl ether, however this similarly resulted in the formation of **39**.



Scheme 5.7. Synthesis of iodophosphine **39**.

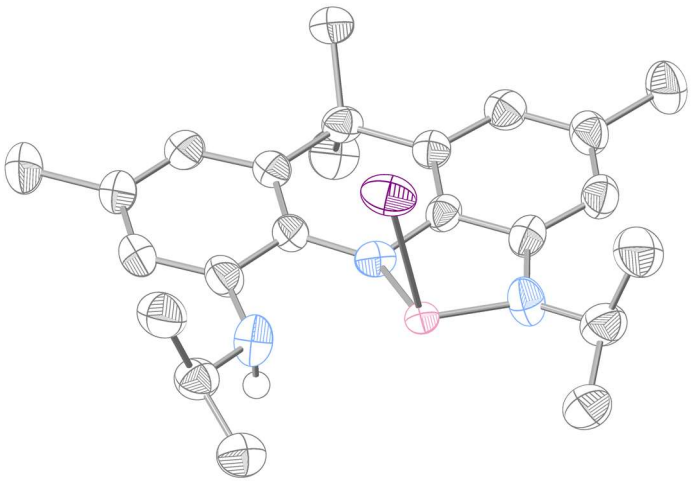
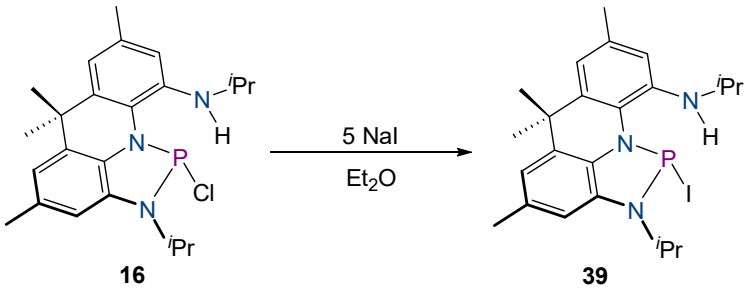


Figure 5.10. Solid-state structure of **39**. Thermal ellipsoids pictured at 50% probability level. Hydrogen atoms, except for the NH unit, removed for clarity.

Independent synthesis of **39** was achieved through halide exchange of chloride analogue **16** using excess NaI in diethyl ether (67% isolated yield, Scheme 5.8). This enabled full heteronuclear NMR characterisation of **39**, and provided further confirmation that it was the initial product observed in the aformentioned reactions. These results suggest the synthetic inaccessibility of a diiodophosphorane derived from **6**, either on account of reaction intermediates abstracting a solvent proton, or by the spontaneous reduction of the target compound (*vide infra*).



Scheme 5.8. Alternative synthesis of iodophosphine **39** for the purpose of bulk isolation.

Iodophosphine **39** has a dynamic structure on the NMR time scale. At room temperature, the ^{1}H NMR signals corresponding to one set of *iso*-propyl methyl groups located at a ligand side-arm appeared to be a broad singlet rather than displaying its usual doublet multiplicity. A similar observation was made for gold complex **19**, which was determined to be a result of rapid phosphorus inversion at high temperature. As such, variable temperature ^{1}H NMR spectroscopy measurements were collected for a d_8-toluene solution of **39** (Figure 5.11).

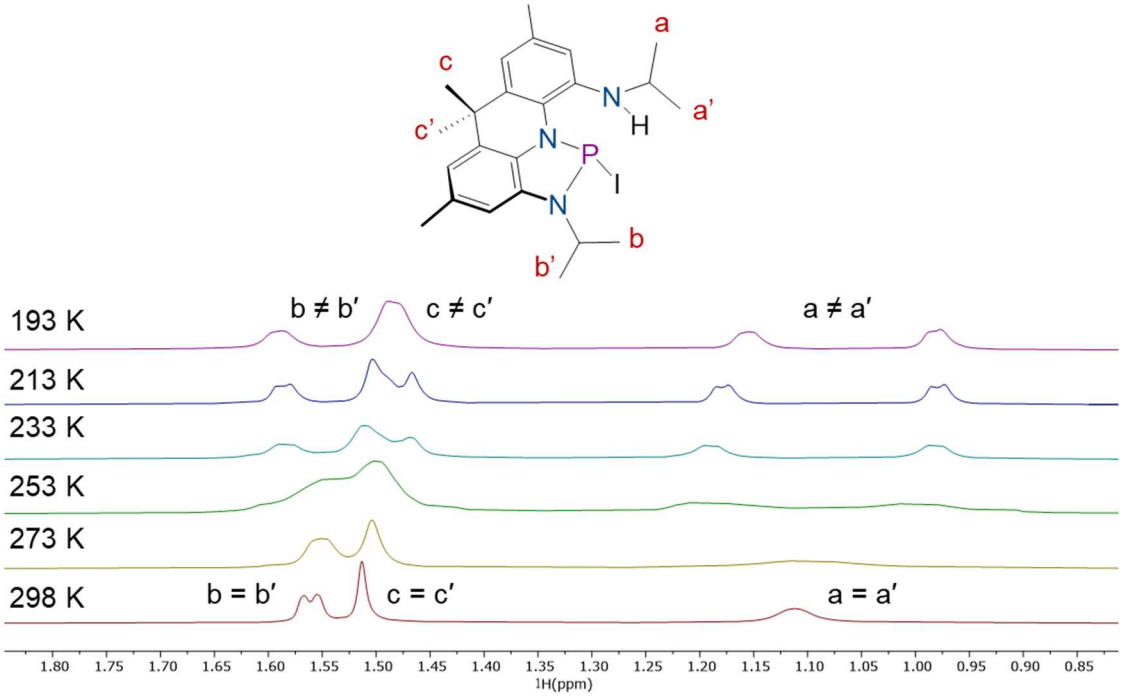


Figure 5.11. Stacked variable temperature ^{1}H NMR spectra of **39** in d_8-toluene enhanced at the aliphatic region. Temperature of each measurement displayed on the left. A depiction of **39** with labelled methyl environments is provided.

On decreasing sample temperature, the aforementioned signal (labelled "a/a′", Figure 5.11) split into two broadened doublets, corresponding to two inequivalent methyl groups. The *iso*-propyl methyl

groups on the other ligand side-arm, and the backbone methyl signals (labelled “b/b′” and “c/c′”, respectively) were more difficult to discern on account of overlap. Though, signals b/b′ appear to undergo the same change as that of a/a′. These data suggest that rapid pyramidal inversion of phosphorus occurs at high temperature, corresponding to the iodide substituent transitioning above/bellow the planar acridane ring network *via* a planar C_{3v} intermediate.

5.4 Photoreduction of dihalophosphoranes

5.4.1 Dichlorophosphorane, 38

In the solid-state and in solution **38** exhibits a pale yellow-green colour. The UV-Vis spectrum of **38** was obtained (Figure 5.12), displaying a broad low intensity “Soret” band beginning at around 400 nm and overlapping with a high intensity signal at 308 nm (within the UV-region). The signal in question resembles a rising baseline, however, it remained present even after four-fold dilution, bolstering confidence that this is a genuine band originating from **38**. The slight colour observed for **38** was attributed to this low intensity Soret band.

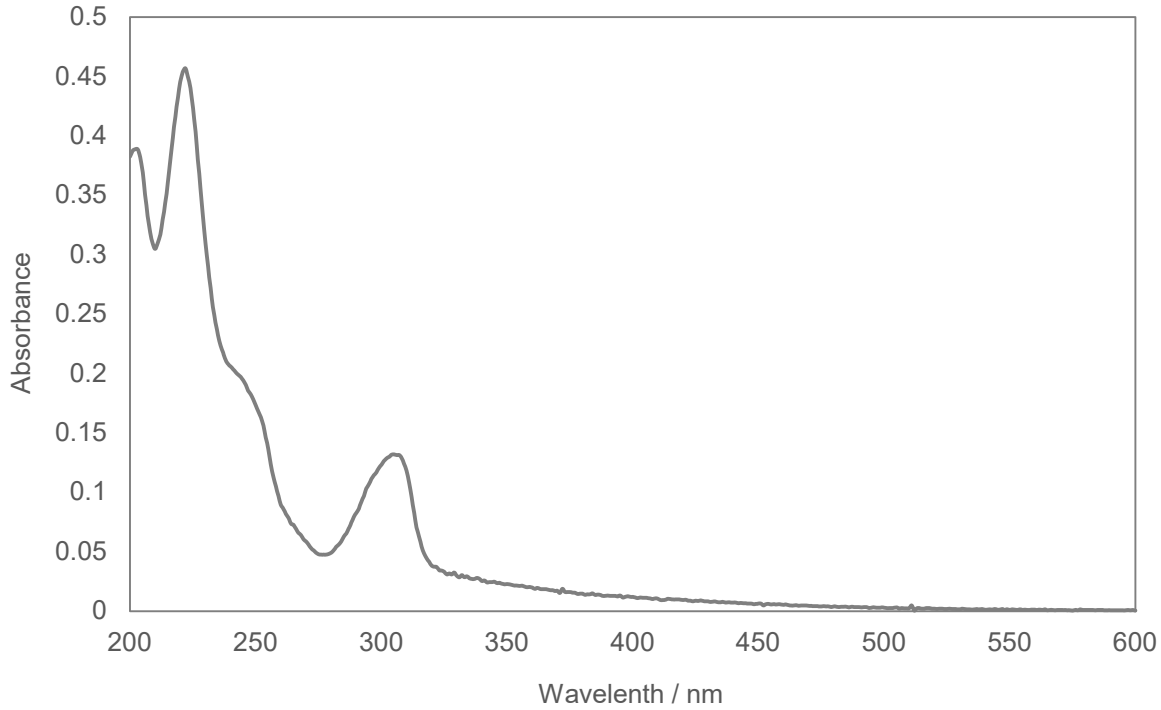


Figure 5.12. UV-Vis spectrum of dichlorophosphorane **38** in pentane.

To establish the orbitals involved in transitions giving rise to this band, TD-DFT calculations were performed on **38**. Such calculations were benchmarked by qualitative comparison of the observed and

calculated UV-Vis spectrum following Gaussian line broadening of the latter to more closely resemble the experimentally obtained spectrum (Figure 5.13 and 5.14). The ωB97X-D3 functional provided the most accurate model, with the aforementioned overlapping Soret peak present as the highest wavenumber transition.

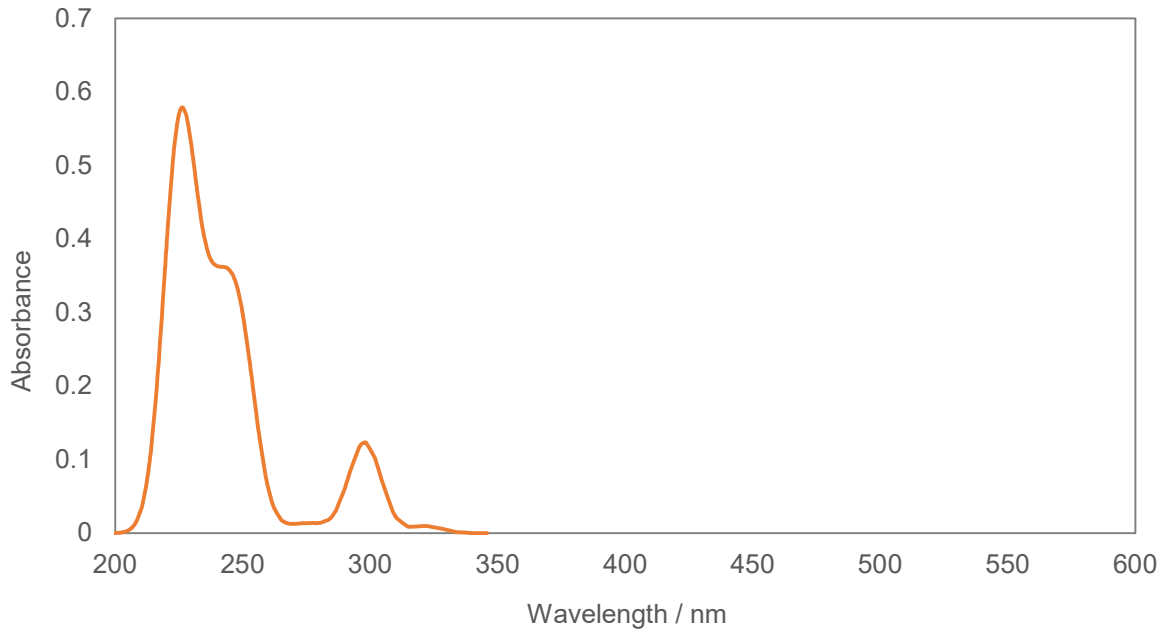


Figure 5.13. TD-DFT theoretical UV-Vis spectrum of **38** calculated at the ωB97X-D3 level of theory. Signals were broadened using a Gaussian function to allow a qualitative comparison with the measured spectrum.

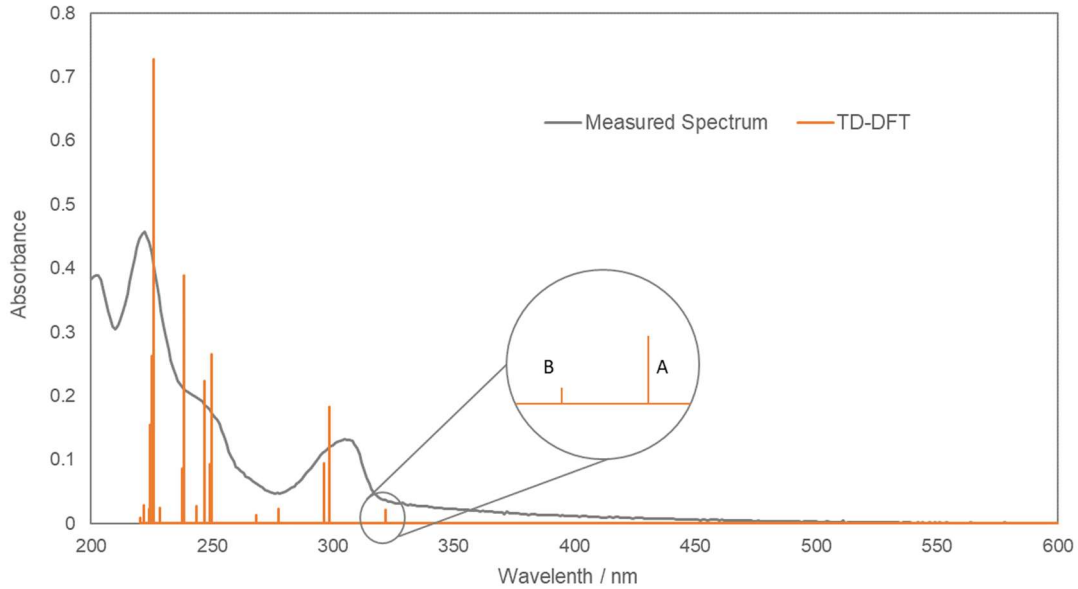


Figure 5.14. Overlayed calculated and measured UV-Vis spectra of **38**. The calculated spectrum is plotted as lines with no Gaussian broadening.

The Soret band was found to originate from electronic transitions originating from the acridane ligand aromatic system, specifically the HOMO and HOMO−1, into the σ^*_{P-Cl} antibonding orbital, which corresponds to the LUMO of **38** (Figure 5.15). A transition from the HOMO to the LUMO of **38** contributes 89% of calculated electron density movement giving rise to band A in the TD-DFT calculated spectrum, with band B corresponding to the equivalent tranition from the HOMO−1. This is the crucial transition required for photoreduction to occur as this provides a weakened P–Cl bond for either homolytic cleavage or direct reaction with a halogen trapping reagent.

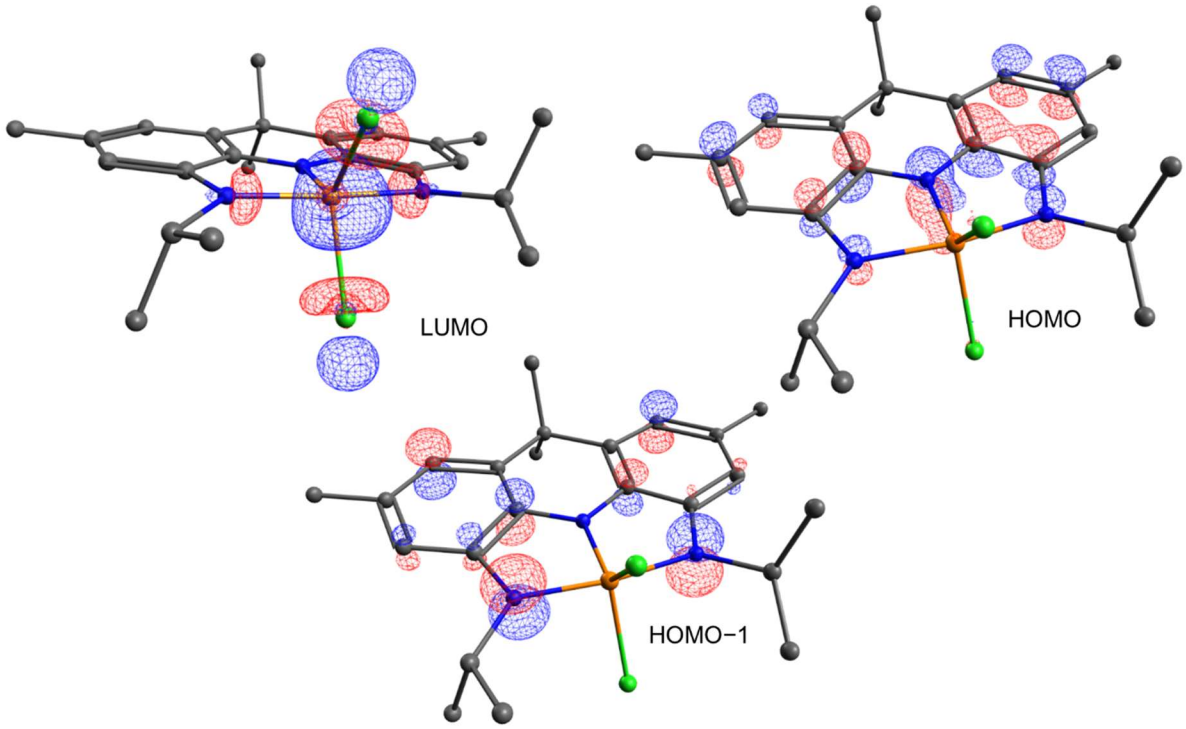


Figure 5.15. Kohn-Sham molecular orbitals involved in transitions giving rise to the Soret band in the UV-Vis spectrum of **38**, calculated at the ωB97X-D3 level of theory. Isosurface value set to 0.07 for each.

As an initial probe for photoreduction, THF solutions of **38** containing varying concentrations of the halogen trapping reagent tetramethylethylene (TME) were irradiated using a medium pressure mercury UV lamp. 5 mg of **38** was dissolved in a mixture of 1.7 M or 3.4 M TME in THF. Irradiation for 45 minutes for either of these trap concentrations, however, did not result in photoreduction of **38**, as evidenced by $^{31}P\{^{1}H\}$ NMR spectroscopy.

As broad-spectrum irradiation proved unsuccessful for the photoreduction of **38**, targeted irradiation was instead performed using 390 nm LEDs. This wavelength was chosen as it is encompassed within the broad Soret band in the UV-Vis spectrum of **38**; the region of the spectrum attributed to transitions populating the σ^*_{P-Cl} antibonding orbital. For solutions of **38** in 1.7 M or 3.4 M TME in THF, partial photoreduction was observed after LED irradiation for 20 minutes, evidenced by a new signal growing at 130.6 ppm in the $^{31}P\{^1H\}$ NMR spectrum of the reaction mixture (Figure 5.16). This signal corresponds to chlorophosphine **16**, previously synthesised by reaction of **6** with HCl (see Chapter 2), containing a phosphorus(III) centre thus confirming that formal photoreduction has occurred. This mixture was irradiated for 200-minutes, after which full consumption of **38** was achieved, providing **16** as the major product along with several low intensity $^{31}P\{^1H\}$ NMR resonances of unknown origin.

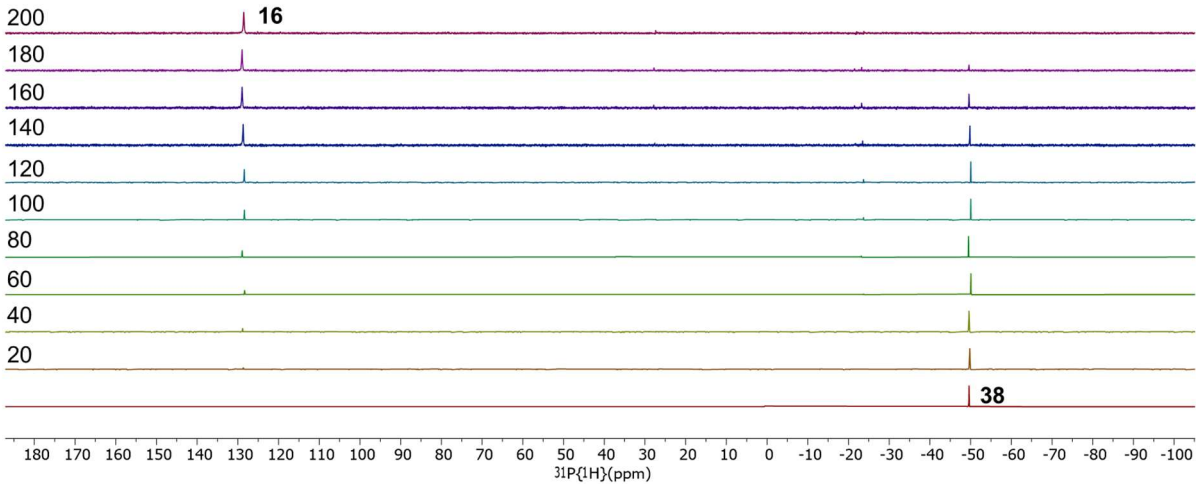
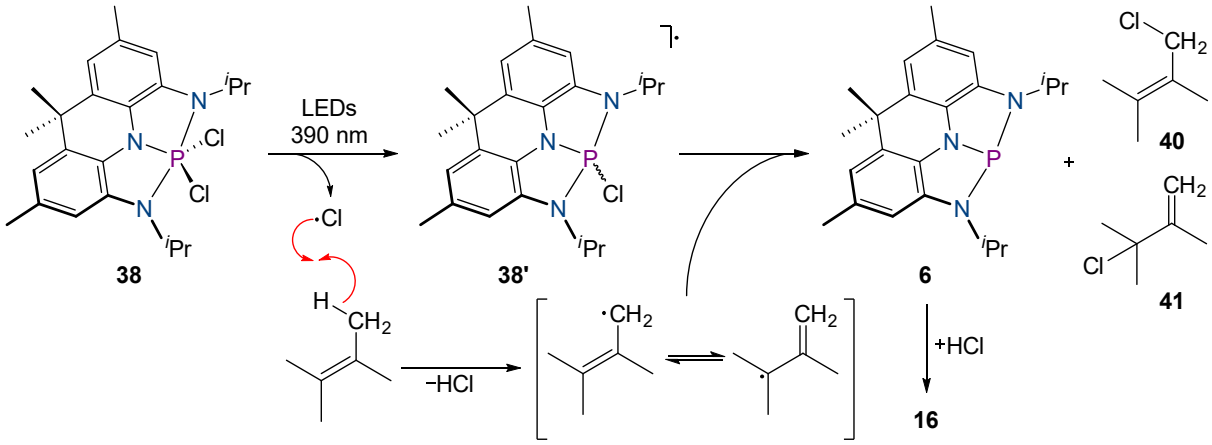


Figure 5.16. Exemplar stacked $^{31}P\{^1H\}$ NMR spectra of **38** after successive 20-minute irradiation periods using 390 nm LEDs with a TME concentration of 3.4 M. Time in minutes displayed on the left of each spectrum.

It is suspected that photoreduction of **38** occurs by successive chlorine radical elimination, with the first of these radicals abstracting a hydrogen atom from TME (Scheme 5.9).[4,11] After this initial halogen-trapping an equivalent of HCl is produced, which is known to react rapidly with **6** to generate **16**.

Regarding the second chloride substituent, conducting this reaction in d_6-benzene enabled monitoring by ^1H NMR spectroscopy. Characteristic signals of halogen trapping products in the region 5.10 – 3.70 ppm were observed, corresponding to chlorinated organics **40** and **41** (Figure 5.17). As

these compounds are volatile, they were separated from the final reaction mixture by vacuum transfer and trapped using a liquid nitrogen cool bath. **40** and **41** result from the reaction between the organic radical generated by hydrogen atom abstraction from TME, and the intermediate radical species **38′** containing one P–Cl bond. **40** forms through direct recombination between the two radicals, whereas **41** results from initial reorganisation of the organic radical species to a more stable tertiary-carbon based radical prior to recombination.



Scheme 5.9. Proposed mechanism of photoreduction of **38** using 390 nm LEDs. Mechanism derived from heteronuclear NMR spectroscopy.

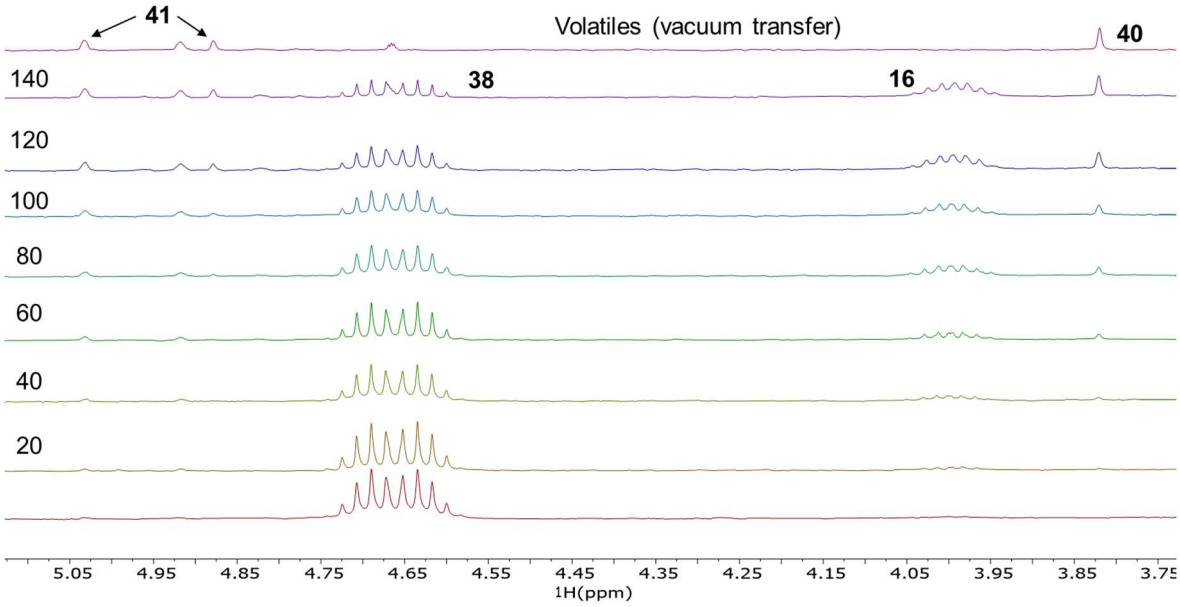


Figure 5.17. Stacked ^{1}H NMR spectra monitoring the photolysis of **38** using 390 nm LEDs enhanced at the region displaying characteristic halogen-trapping product resonances. A TME concentration of 1.7 M in d_6-benzene was used. Irradiation time in minutes displayed on the left of each spectrum.

The formation of product **16** was tracked by integration of its respective $^{31}P\{^{1}H\}$ NMR resonance after successive 20-minute irradiation periods (Figure 5.18). This was performed in triplicate for TME concentrations of 1.7 M and 3.4 M, with minimal variation in degree of product formation observed between the 1st, 2nd and 3rd repeats.

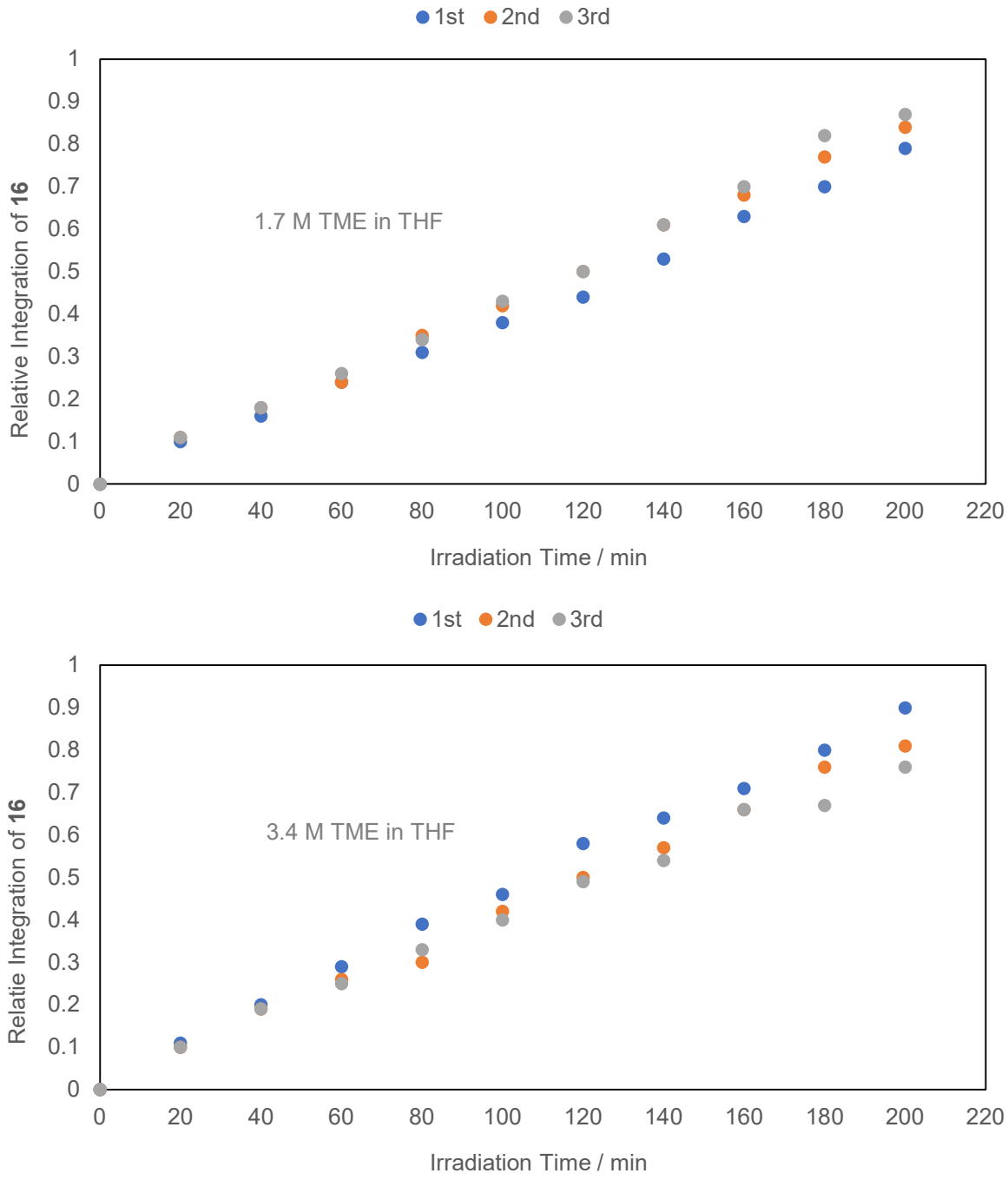


Figure 5.18. A plot of irradiation time versus the relative integration of **16** with respect to all phosphorus containing species, obtained through $^{31}P\{^{1}H\}$ NMR spectroscopy. Top plot is the reaction with 1.7 M TME in THF, and the bottom is with 3.4 M TME in THF

Averaging the results at each time interval over each photolysis run provides a strongly linear relationship, confirming that a constant rate of photoreduction is maintained throughout irradiation (Figure 5.19). The efficiency of photoelimination has been reported to be strongly dependant on the concentration of the halogen-trapping reagent. However, in the present case, a TME concentration of 1.7 M and 3.4 M provided comparable reaction profiles, indicating that TME is most likely not involved in the rate limiting step of this reaction.

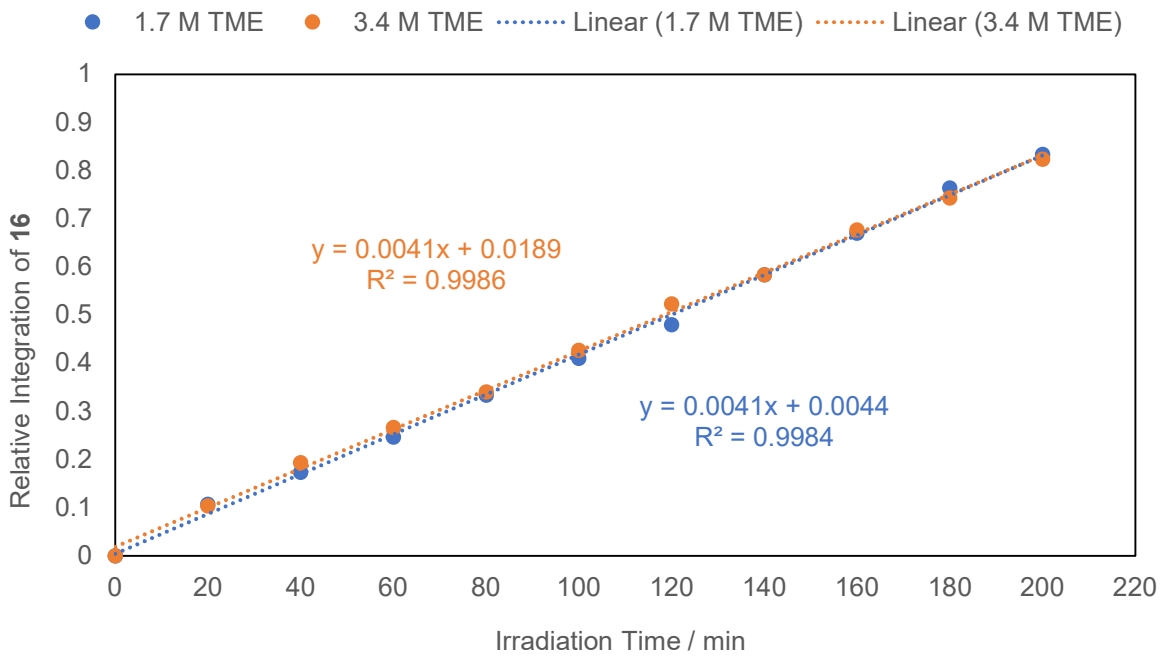


Figure 5.19. A plot of irradiation time versus the averaged relative integration of **16** with respect to all phosphorus containing species, obtained through $^{31}P\{^{1}H\}$ NMR spectroscopy. Data for TME concentrations of 1.7 and 3.4 M are presented.

5.4.2 Dibromophosphorane, 5

In the solid-state and in solution, **5** exhibits a bright orange colour. Its UV-Vis spectrum was obtained, displaying a broad Soret band (as observed for **38**) centred at 404 nm (Figure 5.20). This band was significantly red-shifted with respect to that of **38**, such that overlap with the nearest band in the UV-region of the spectrum was minimal, and a greater range of visible wavelengths encompassed. As such, the colour of **5** was attributed to this peak.

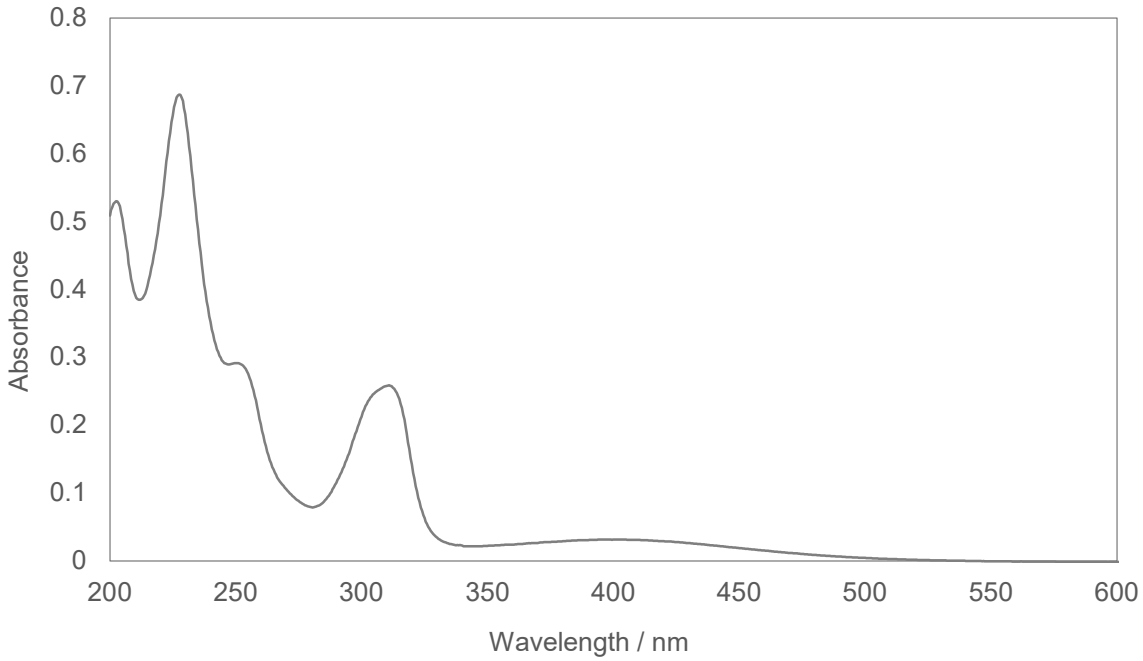


Figure 5.20. UV-Vis spectrum of **5** in pentane.

To establish the orbitals involved in the transitions giving rise to this band, TD-DFT calculations were performed on **5**. Such calculations were benchmarked by qualitative comparison of the observed and calculated UV-Vis spectrum following Gaussian line broadening of the latter to more closely resemble an experimentally obtained spectrum (Figure 5.21 and 5.22). As for the chloride analogue **38**, the ωB97X-D3 functional provided the most accurate model, with the aforementioned Soret peak present as the highest wavenumber transition, and red-shifted with respect to that of **38**.

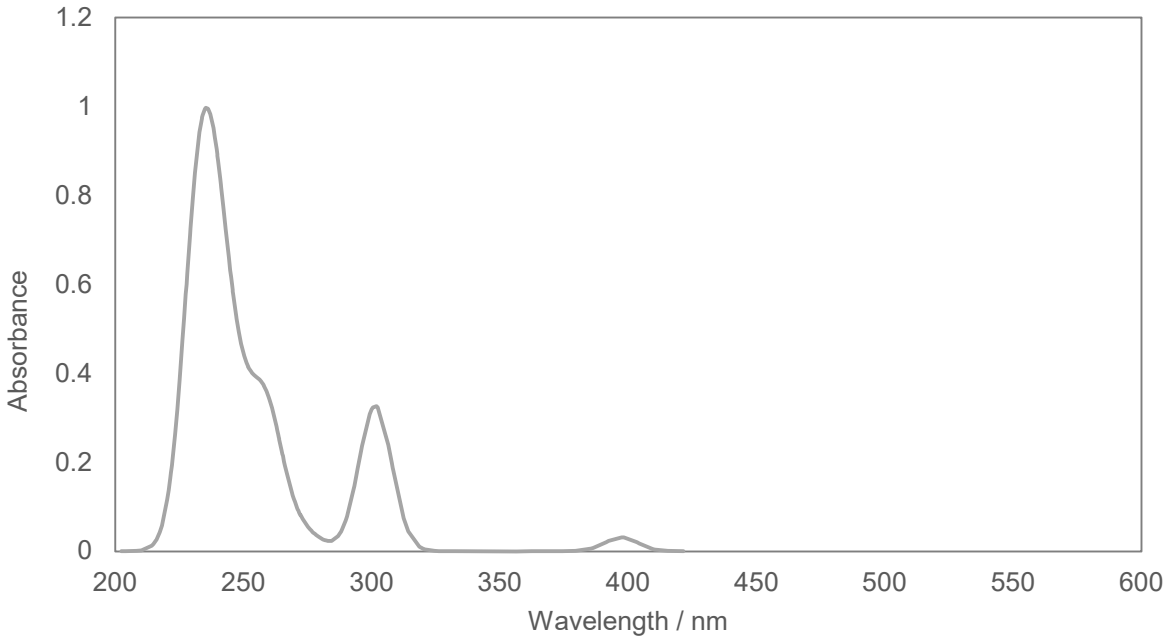


Figure 5.21. TD-DFT theoretical UV-Vis spectrum of **5** calculated at the ωB97X-D3 level of theory. Signals were broadened using a gaussian function to allow a qualitative comparison with the measured spectrum.

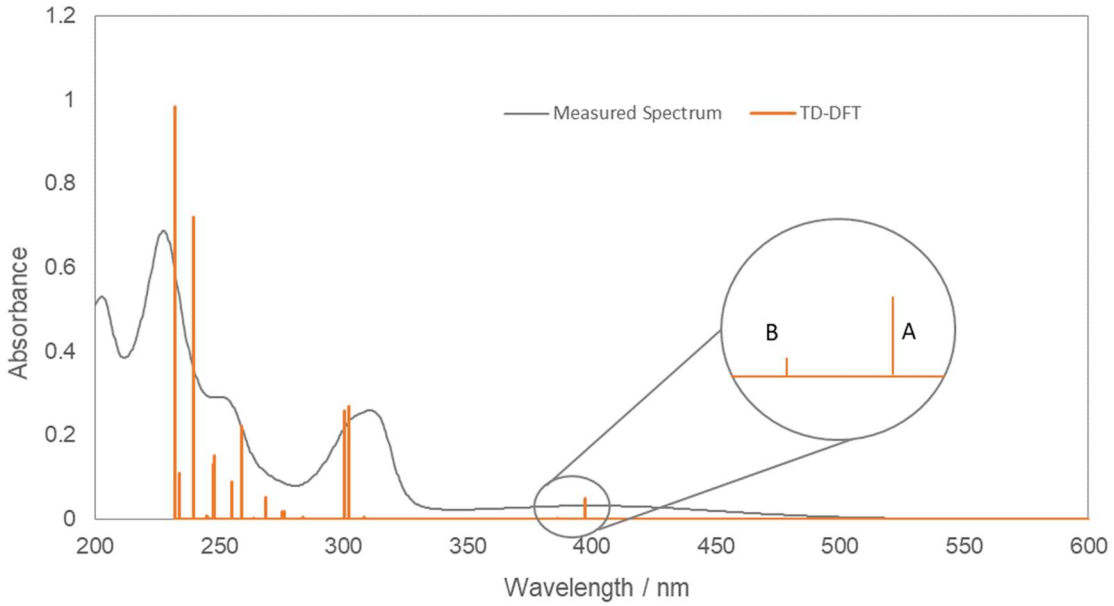


Figure 5.22. Overlayed calculated and measured UV-Vis spectra of **5**. The calculated spectrum plotted as lines with no Gaussian broadening.

The Soret band in the UV-Vis spectrum of **5** was found to originate from electronic transitions originating from the acridane ligand aromatic system, corresponding to the HOMO and HOMO−1, into the $\sigma^*_{P–Br}$ antibonding orbital, corresponding to the LUMO, of **5** (Figure 5.23). A transition from the HOMO in the LUMO of **5** contributes 91% of calculated electron density movement giving rise to band

A in the TD-DFT calculated spectrum, with band B corresponding to 89% electron movement from the HOMO−1.

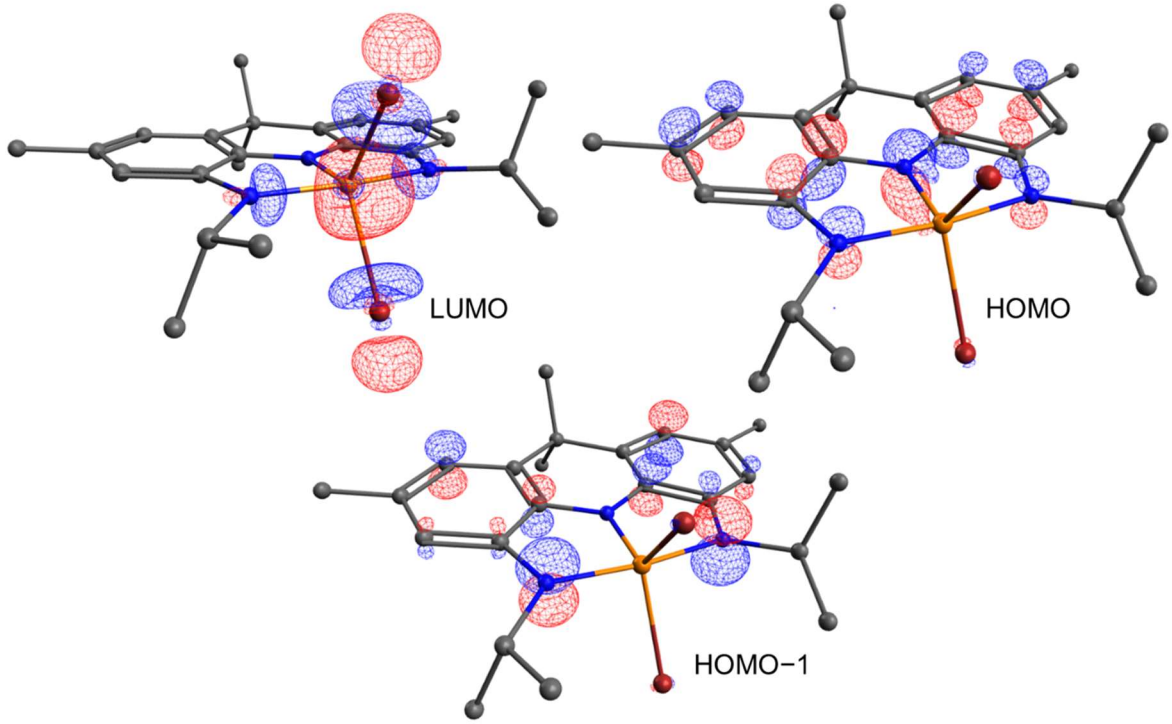


Figure 5.23. Kohn-Sham molecular orbitals involved in transitions giving rise to the Soret band in the UV-Vis spectrum of **5**, calculated at the ωB97X-D3 level of theory. Isosurface value set to 0.07 for each.

As performed for **38**, irradiation of **5** with a medium-pressure mercury UV lamp was used as an initial test for photoreduction. Solutions of **5** (5 mg) in THF with a TME concentration of 1.7 M or 3.4 M were irradiated for 45-minutes, after which a $^{31}P\{^{1}H\}$ NMR spectrum was obtained revealing the formation of a new phosphorus-containing compound with a resonance at 150.6 ppm. This photoproduct resides within the phosphorus(III) region of the NMR spectrum, indicating that photoreduction has occurred. Through crystallisation of the reaction mixture, this photoproduct was identified as bromophosphine **42** by SCXRD analysis (Figure 5.24); the product of HBr addition to **6**.

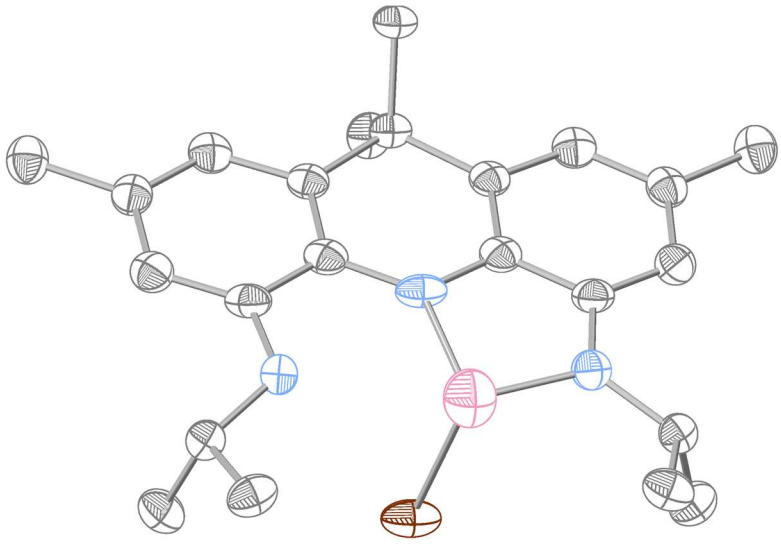


Figure 5.24. Solid-state structure of bromophosphine **42**. Thermal ellipsoids pictured at 50% probability level. Hydrogen atoms and solvent of crystallisation removed for clarity.

On account of the long irradiation times required for appreciable photoreduction, higher TME concentrations of 5.0 and 6.7 M were employed in an attempt to speed up the rate of reaction. Overall, it was found that the concentration of TME had only a small effect on the rate of photoreduction, with a slight increase in initial product formation observed over these concentrations (Figure 5.25).

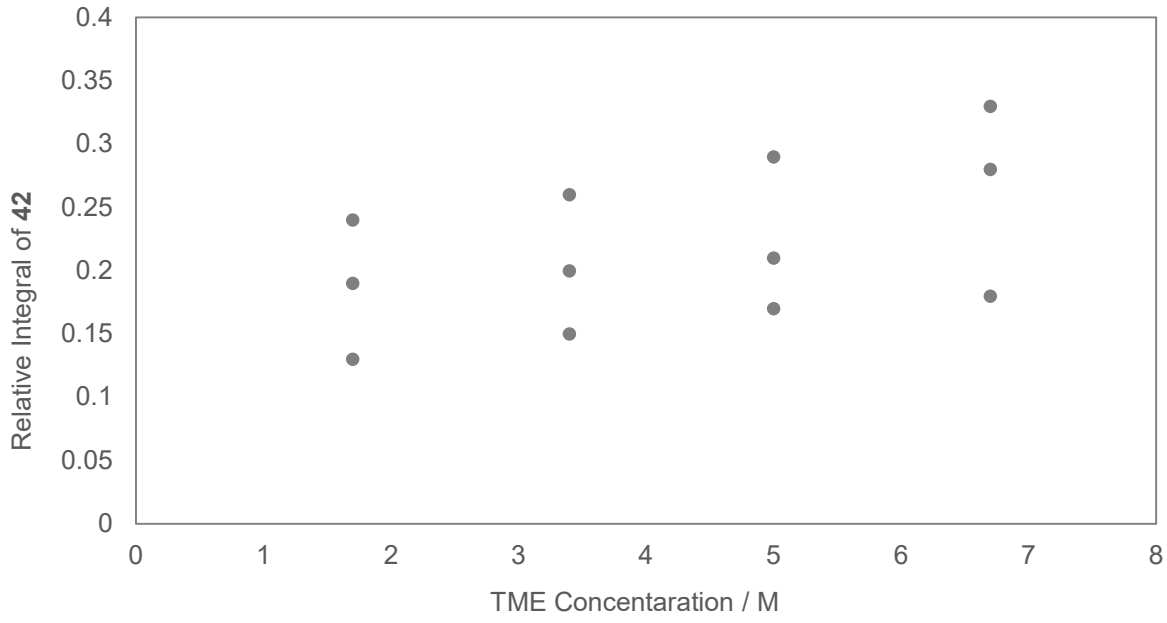
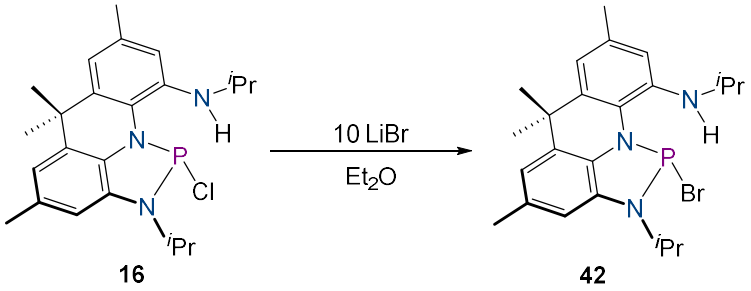


Figure 5.25. A plot of TME concentration verses the relative $^{31}P\{^{1}H\}$ integral of photoproduct **42** after 45-minutes irradiation with a medium-pressure mercury lamp.

Due to the significant spread of the results displayed in Figure 5.25 (obtained in triplicate for each concentration), quantitative assertions cannot be made for this system. It should be noted that when using TME concentrations of 5.0 and 6.7 M, the starting material was partially insoluble in the reaction mixture, therefore these high trap concentrations were not used moving forward.

Assignment of **42** as the photoproduct was confirmed through its independent synthesis by reaction of **16** with an excess of lithium bromide in diethyl ether (92% isolated yield, Scheme 5.10).



Scheme 5.10. Alternative synthesis of bromophosphine **42** for the purpose of bulk isolation.

In the ^{1}H NMR spectrum of **42**, signals corresponding to a dynamic structure were observed, similar to those of iodide analogue **39**. Variable temperature ^{1}H NMR spectroscopy was conducted on a sample of **42** in d_8-toluene (Figure 5.26). The signals displaying significant temperature dependence were those corresponding to the *iso*-propyl methyl environments, a/a′ and b/b′, and the backbone methyl groups, c/c′. At high temperature, these signals are magnetically equivalent on account fast phosphorus inversion, while at low temperature they are inequivalent corresponding to “frozen-out” conformers.

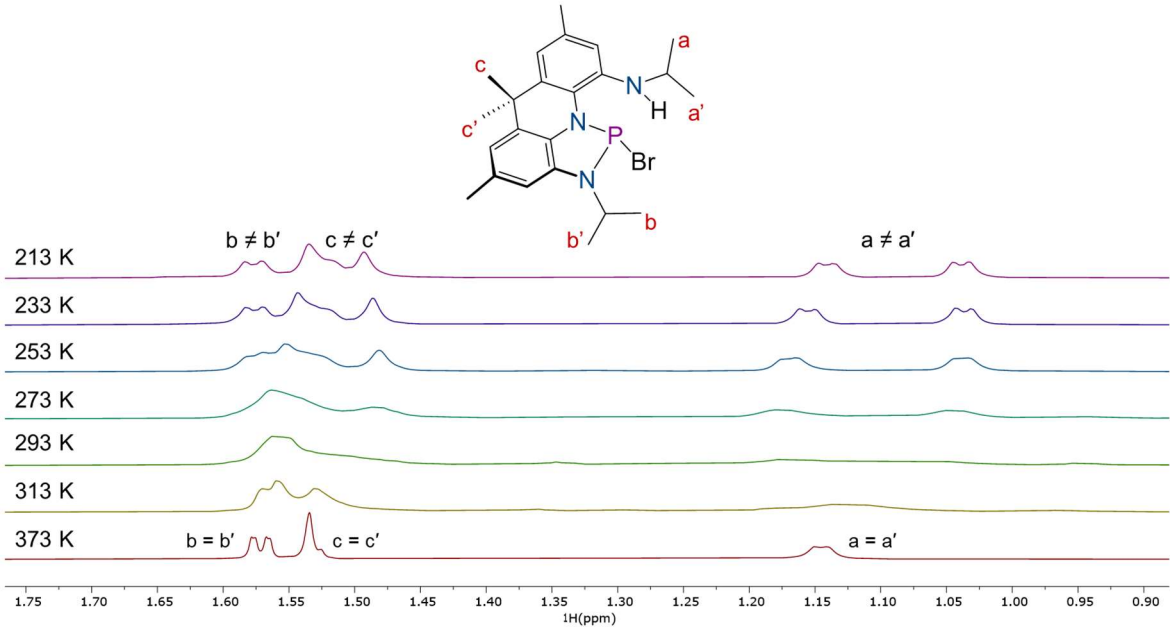


Figure 5.26. Stacked variable temperature ^{1}H NMR spectra of **42** in d_8-toluene enhanced at the aliphatic region. Temperature of each measurement displayed on the left. A depiction of **42** with labelled methyl environments is provided.

Irradiation with 456 nm LEDs was performed to assess whether irradiation targeting the Soret band in the UV-Vis spectrum of **5** improves the efficiency of its photoreduction. This is a visible (blue) light wavelength – a facet often targeted during photoreduction studies on account of improved energy efficiency. For solutions of **5** in 1.7 M or 3.4 M TME in THF, photoreduction towards **42** was observed after 10 minutes of LED irradiation (Figure 5.27). In comparison to irradiation with a medium-pressure mercury UV-lamp, this represents a significant enhancement of the rate of photoreduction of **5**. Additionally, full starting material consumption was observed after only 50-minutes; a far shorter irradiation time than for 390 nm LED irradiation of **38** (cf. 200 minutes required). A small amount of phosphine oxide **11** is generated during this reaction. **11** represents *ca*. 4% of the reaction mixture during photolysis, then significantly increases upon full starting material consumption to *ca.* 10%, as calculated by integration of its respective ^{31}P{^{1}H} NMR resonance. As **11** was not observed during photolysis of **38**, it is suspected to originate from an impurity in starting material **5**.

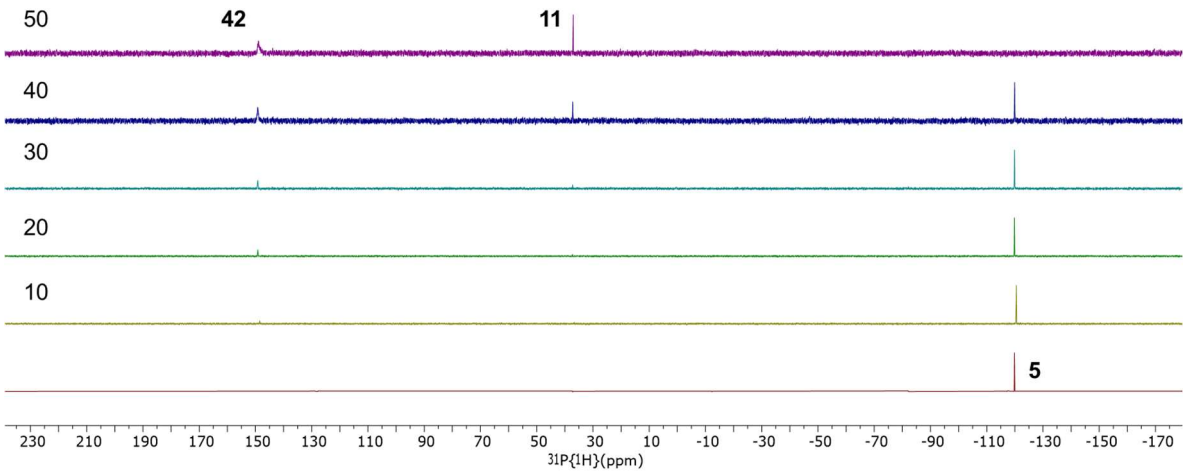


Figure 5.27. Exemplar stacked $^{31}P\{^{1}H\}$ NMR spectra of **5** after successive 10-minute irradiation periods using 456 nm LEDs with a TME concentration of 1.7 M. Time in minutes displayed on the left of each spectrum.

This reaction was monitored using ^{1}H NMR spectroscopy using a TME concentration of 1.7 M TME in d_6-benzene (Figure 5.28). The generation of organic bromides **43** and **44** was observed over the course of the reaction (Scheme 5.11), and were separated from the final reaction mixture by vacuum transfer then trapped using a liquid nitrogen cool bath. This, along with the formation of **42** (suggestive of HBr generation), supports an analogous mechanism to the photoreduction of **38**.

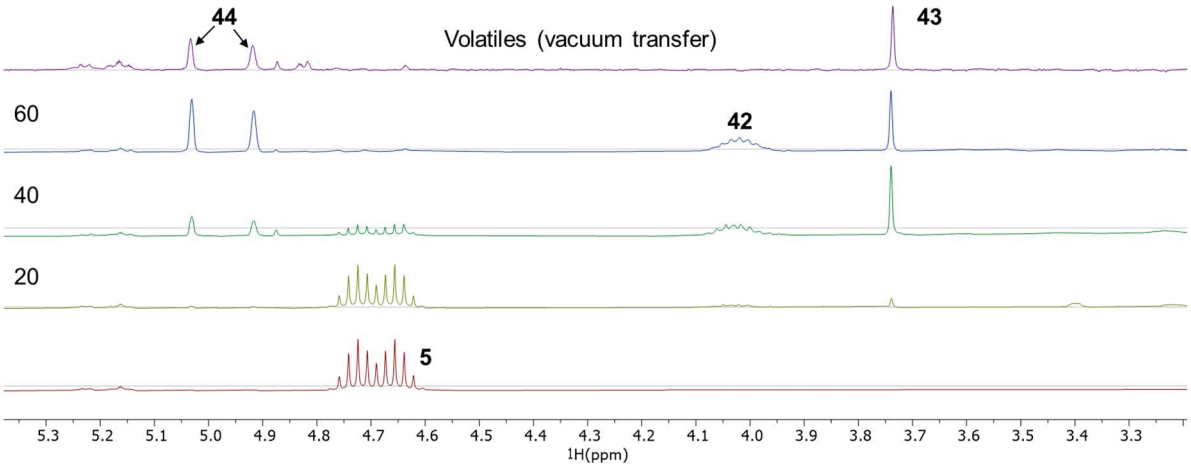
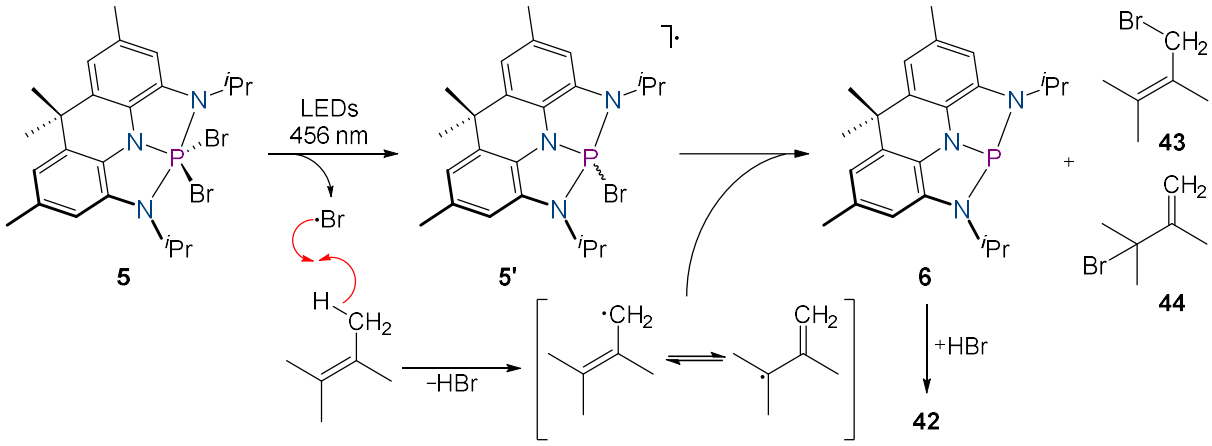


Figure 5.28. Stacked ^{1}H NMR spectra monitoring the photolysis of **5** using 456 nm LEDs enhanced at the region displaying product resonances. A TME concentration of 1.7 M in d_6-benzene was used. Irradiation time in minutes displayed on the left of each spectrum.



Scheme 5.11. Proposed mechanism of photoreduction of **5** using 456 nm LEDs. Mechanism derived from heteronuclear NMR spectroscopy.

The generation of **42** was monitored over the course of the reaction by integration of its $^{31}P\{^{1}H\}$ NMR resonance at 10-minute intervals (Figure 5.29). This was performed in triplicate for each TME concentration, enabling the calculation of an averaged reaction profile under these conditions (Figure 5.30). It was found that photoreduction of **5** exhibits a significant dependence on trap (TME) concentration, particularly in comparison to that of **38**, with 3.4 M TME resulting in full starting material consumption 10-minutes (or 20%) quicker than achieved for reactions with 1.7 M TME. This trap dependence is also reflected in the observation that product formation followed a non-linear trend, and accelerated as irradiation continued. This corresponds to an increasing relative excess of TME upon consumption of starting material.

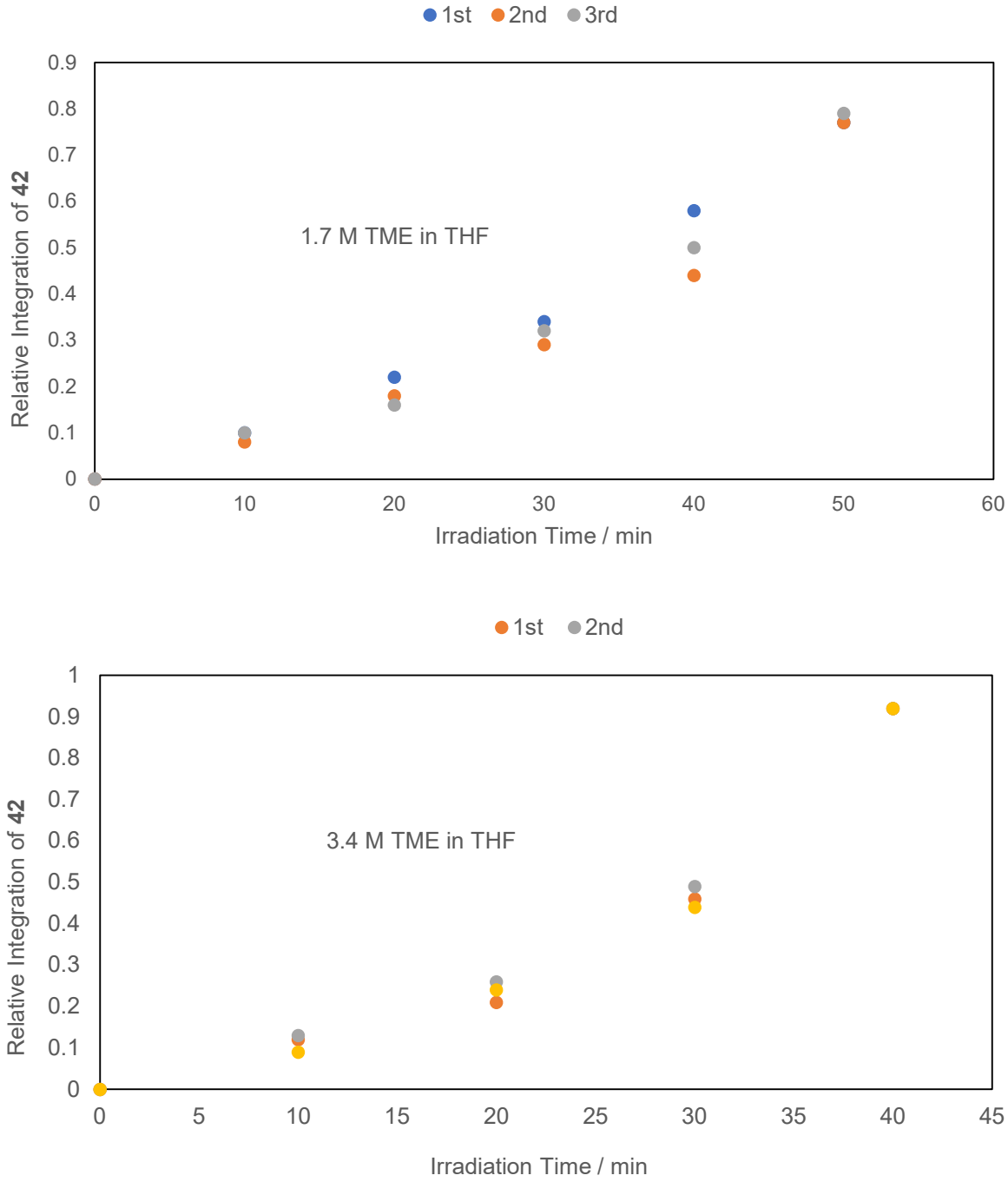


Figure 5.29. A plot of irradiation time versus the relative integration of **42** with respect to all phosphorus containing species, obtained through $^{31}P\{^{1}H\}$ NMR spectroscopy. Top plot is the reaction with 1.7 M TME in THF, and the bottom is with 3.4 M TME in THF.

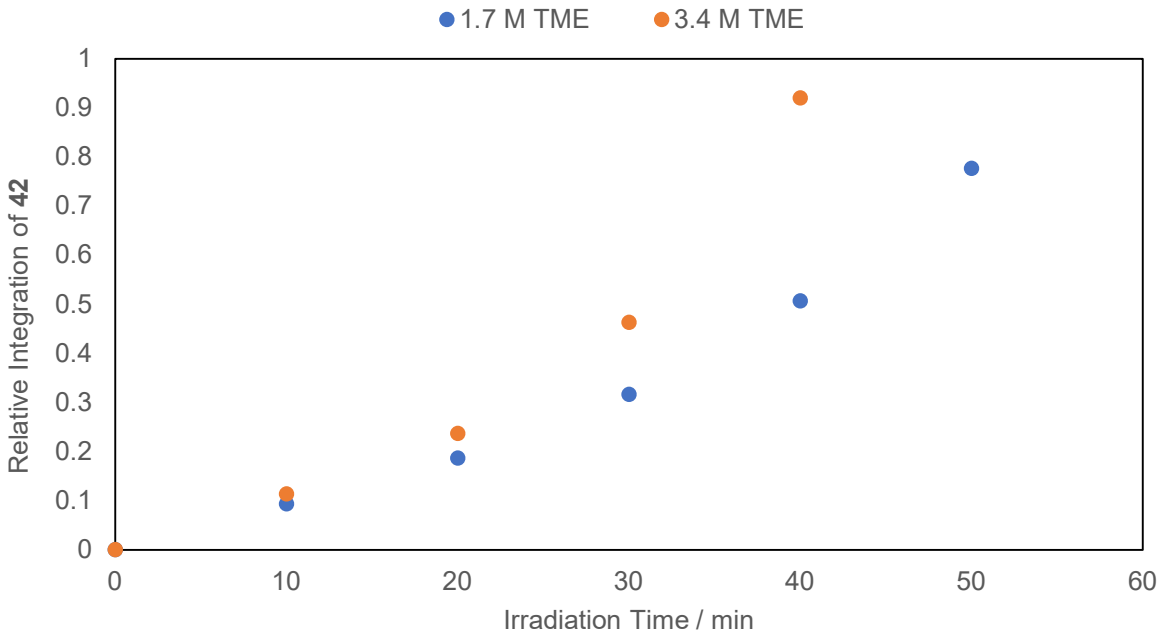


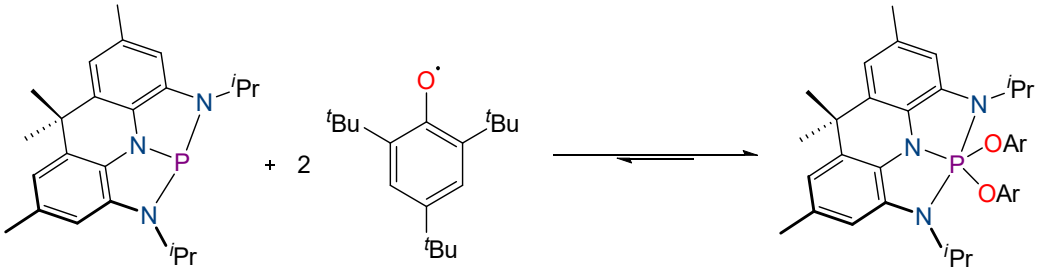
Figure 5.30. A plot of irradiation time versus the averaged relative integration of **42** with respect to all phosphorus containing species, obtained through $^{31}P\{^{1}H\}$ NMR spectroscopy. Data for both 1.7 and 3.4 M TME are presented.

5.5 Thermal reduction of bisaryloxyphosphorane, 46

It was established in Section 5.4 that a likely mechanism for the photoreduction of dihalophosphoranes **5** and **39** involves the sequential release of halogen radicals from the phosphorus centre by homolytic bond cleavage. Therefore, a phosphorus(V) species derived from **6** bearing two substituents at phosphorus, which themselves are stable as free radicals was targeted. It was postulated that for such a system photoreduction would be more efficient on account of the stability of the released radicals, and may provide further evidence for the above proposed mechanism.

The 2,4,6-tri-*tert*-butylphenoxyl radical (**45**) is stable and can be readily synthesised on a large scale from the respective alcohol in accordance with the literature procedure.[31] Reaction of **6** with two equivalents of **45** resulted in 90% conversion (*vide infra*) to a compound bearing a $^{31}P\{^{1}H\}$ NMR resonance at −45.5 ppm, revealed through signal integration. In the ^{1}H NMR spectrum, this product exhibited signals corresponding to a flat acridane backbone with overall C_{2v} symmetry, and additional signals originating from two 2,4,6-tri-*tert*-butylphenyl units. This, along with the $^{31}P\{^{1}H\}$ NMR

resonance indicative of a phosphorus(V) species derived from a geometrically constrained phosphine confirm the formation of bisaryloxyphosphorane **46** (Scheme 5.12), which was isolated as yellow crystals in 73% yield by slow evaporation of a pentane solution.



5 **45** **46**

Scheme 5.12. Synthesis of bisaryloxyphosphorane **46**. Ar = 2,4,6-tri-*tert*-butylphenoxy

The aforementioned crystals of **46** were of diffraction quality, allowing a solid-state structure to be obtained (Figure 5.31). **46** contains a five-coordinate phosphorus centre displaying pentagonal bipyramidal geometry, with the two aryloxy substituents residing in the equatorial plane along with the central acridane nitrogen atom. Interestingly, the 2,4,6-tri-*tert*-butylphenoxy units reside over the acridane ligand plane in the solid-state. This is also reflected in solution as heteronuclear NMR spectroscopy reveals through-space coupling between a $C_{Ar}H$ proton and phosphorus ($^{TS}J_{P-H}$ = 2.9 Hz).

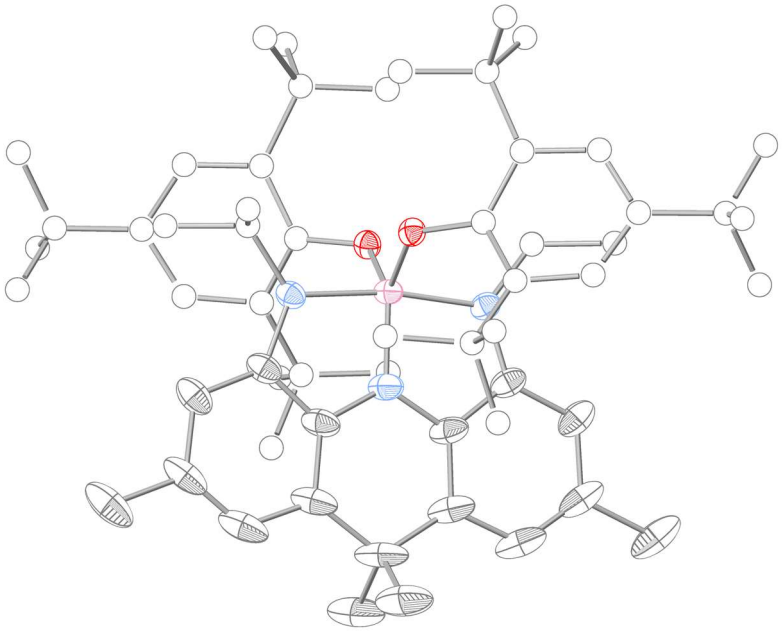


Figure 5.31. Solid-state structure of bromophosphine **42**. Thermal ellipsoids pictured at 50% probability level. Hydrogen atoms and solvent of crystallisation removed for clarity. Carbon atoms corresponding to the *iso*-propyl ligand substituents and 2,4,6-tri-*tert*-butylphenoxy units depicted as spheres of arbitrary radius to aid in visualisation.

In the above reaction, 10% of unreacted starting material **6** remained and could only be removed on addition of 10-equivalents of **45** (a five-fold excess), suggesting that the formation of **46** is an equilibrium process. This redox-equilibrium was probed by variable temperature $^{31}P\{^{1}H\}$ NMR spectroscopy of crystals of **46** dissolved in d_6-benzene (Figure 5.32).

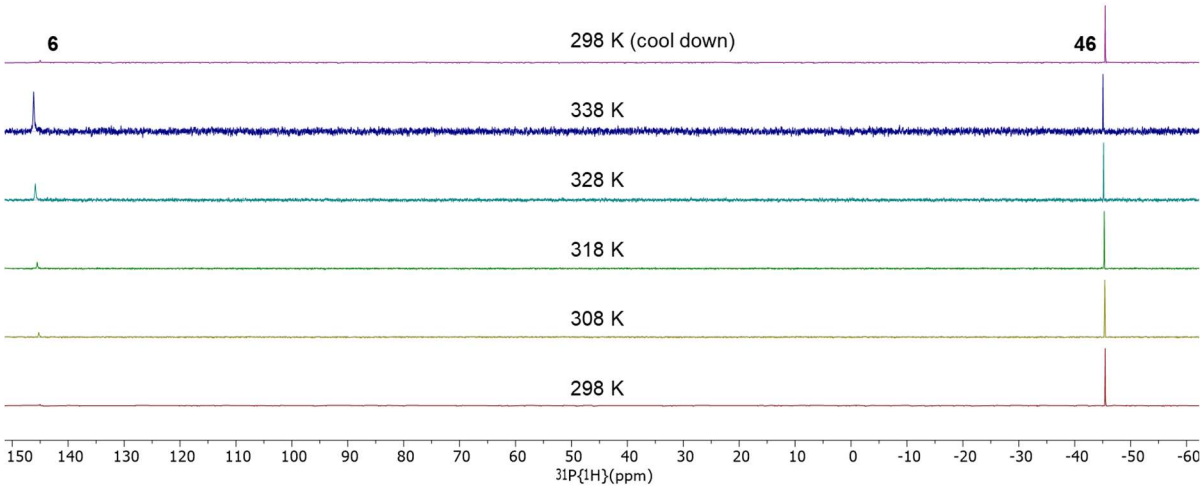


Figure 5.32. Stacked variable temperature $^{31}P\{^{1}H\}$ NMR spectra monitoring the redox equilibrium between **46** and **6** (+**45**) in d_6-benzene. Temperature is displayed in the centre of each spectrum.

At room temperature, **6** represents 10% of phosphorus-containing material by $^{31}P\{^{1}H\}$ NMR resonance integration (as observed in the initial synthesis of **46**). Upon increasing the sample temperature, the proportion of **6** increases in a linear fashion, with a proportional linear decrease in the concentration of **46** (Figure 5.33). Qualitatively, these data are in accordance with the higher entropy system of **6** and two molecules of **45** being favoured at high temperatures, while **46** is enthalpically favoured and persists at low temperature.

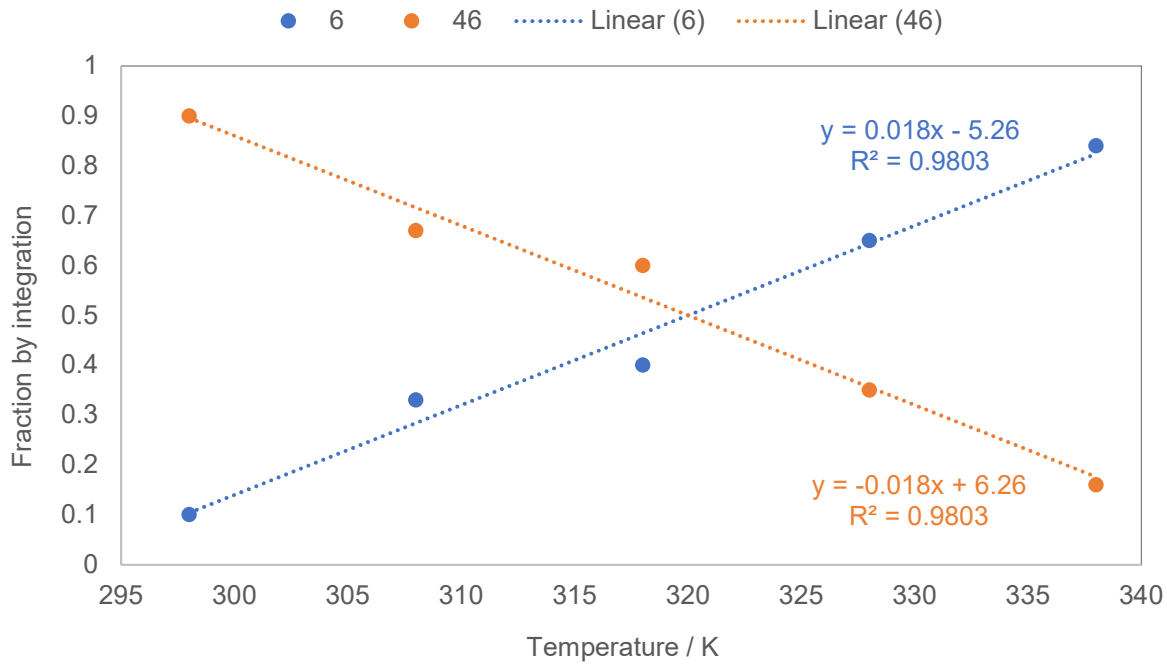


Figure 5.33. A plot of sample temperature verses the relative integrals of **6** and **46** calculated by integration of their respective $^{31}P\{^{1}H\}$ NMR resonances.

Dissolving crystals of **46** in organic solvents results initially in a colourless solution. However, in less than one minute the solution turns bright green; a result of **6** (orange) and **45** (blue) being generated in solution in accordance with the equilibrium depicted in Scheme 5.12. This prevented the measurement of a UV-Vis spectrum of **46**, thus precluding meaningful benchmarking of TD-DFT calculations. Therefore, only broad-spectrum irradiation of **46** was performed using a medium-pressure mercury UV-lamp, rather than targeted LED irradiation. Irradiation for 45-minutes resulted in the formation of phosphine oxide **11**, with full conversion to this product complete after an additional 1.5 hours as monitored by $^{31}P\{^{1}H\}$ NMR spectroscopy (Figure 5.34).

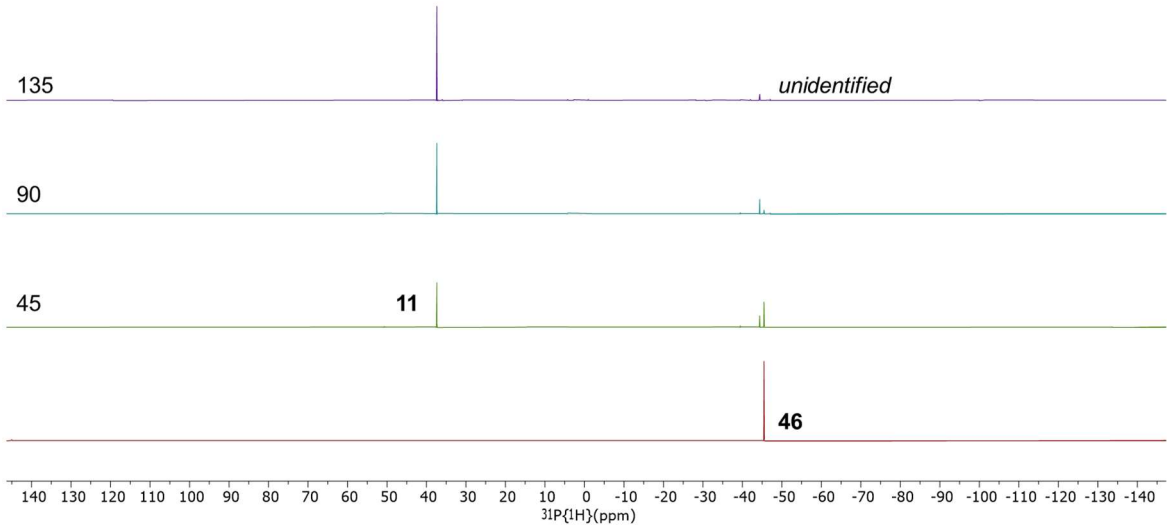
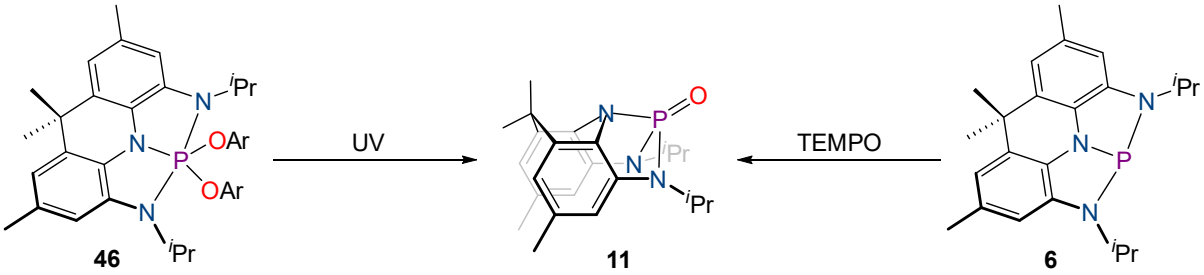


Figure 5.34. Stacked $^{31}P\{^{1}H\}$ NMR spectra of **46** after successive 45-minute irradiation periods using a medium-pressure mercury UV lamp. Time in minutes displayed on the left of each spectrum.

The formation of **11** is suspected to be a result of oxygen-atom transfer from free radical **45** to the phosphorus centre; a reaction pathway observed upon addition of TEMPO to **6** (Scheme 5.13) and similarly observed by Kinjo for a NPN-ligated phosphine.[32]



Scheme 5.13. The generation of phosphine oxide **11** through UV irradiation of **46**, or by reaction of **6** with TEMPO. Ar = 2,4,6-tri-*tert*-butylphenoxy

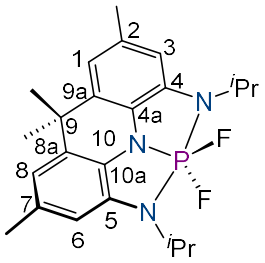
It should be noted that by ^{1}H NMR spectroscopy both 2,4,6-tri-*tert*-butylphenyl, the respective alcohol derived from hydrogen atom transfer (HAT) to eliminated **45**, and *iso*-butene, generated by hydrogen-atom abstraction from a *tert*-butyl group, were observed. These hint toward a mechanism of formation of **11** by initial elimination of an equivalent of **45** from **46**, followed by HAT with the remaining bound –OAr group, generating *iso*–butene with disintegration of the resulting aryl fragment thermodynamically driven by P=O bond formation.

5.6 Conclusions

Dichlorophosphorane **38** and dibromophosphorane **5** were shown to undergo photo-reduction under irradiation with LEDs targeting the Soret band in their UV-Vis spectra. The electronic transition giving rise to this band involves the movement of electron density from the ligand-based acridane π-system into orbitals with $\sigma^*_{P–X}$ antibonding character, and was accessible using 390 nm and 456 nm LEDs for **38** and **5**, respectively. This targeted irradiation proved more efficient than broad-spectrum irradiation using a medium-pressure mercury UV lamp, which did not induce any reduction for **38**. The mechanism of photo-reduction involved elimination of the respective halogen radicals from **38** and **5** as shown by heteronuclear NMR spectroscopy and analysis of halogen-trapping products. This mechanism was supported by the observation of facile thermal radical elimination from **46** — a phosphorus(V) compound bearing two substituents derived from stable free-radicals. Synthesis of the respective diiodo- and difluorophosphorane were targeted. This however proved unsuccessful for the former, while the latter could be synthesised but precluded purification for further reactivity studies.

5.7 Experimental Section

5.7.1 Synthesis of 36



Xenon difluoride (4.5 mg, 26.4 μmol, 1.0 eq.) and phosphine **6** (10 mg, 26.4 μmol, 1.0 eq.) were dissolved in dichloromethane (0.5 mL), immediately resulting in a dark purple solution. The solvent was removed *in vacuo* and the residue extracted with pentane (3 × 0.5 mL) and filtered. The solvent was removed from these extracts *in vacuo* and the residues dissolved in d_6-benzene for NMR spectroscopy. Note the dark purple colour persists through these manipulations

^{1}H NMR (600 MHz, C_6D_6): δ (ppm) 6.79 (2H, s, $C_{1/8}H$), 6.55 (2H, s, $C_{3/6}H$), 4.25 (2H, d-sept, $^{3}J_{P–H}$ = 25.7 Hz, $^{3}J_{H–H}$ = 6.9 Hz, $C_{4/5}NCH(CH_3)_2$), 2.36 (6H, s, $C_{2/7}(CH_3)$), 1.60 (6H, s, $C_9(CH_3)_2$), 1.38 (12H, d, $^{3}J_{H–H}$ = 6.9 Hz, $C_{4/5}NCH(CH_3)_2$).

^{1}H{^{31}P} NMR (600 MHz, C_6D_6): as above, except δ (ppm) 4.25 (2H, sept, $^{3}J_{H–H}$ = 6.9 Hz, $C_{4/5}NCH(CH_3)_2$).

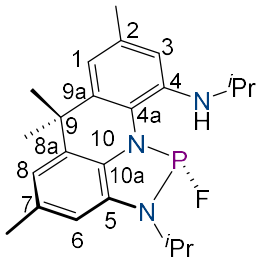
^{13}C{^{1}H} NMR (151 MHz, C_6D_6): δ (ppm) 131.9 (s, $C_{2/7}$), 131.9 (d, $^{2}J_{P–H}$ = 27.5 Hz, $C_{4/5}$), 128.9 (d, $^{3}J_{P–C}$ = 11.0 Hz, $C_{8a/9a}$), 123.6 (d, $^{2}J_{P–C}$ = 13.0 Hz, $C_{4a/10a}$), 115.4 (s, $C_{1/8}$), 109.3 (d, $^{3}J_{P–C}$ = 11.3 Hz, $C_{3/6}$), 48.6 (s, $C_{4/5}NCH(CH_3)_2$), 37.7 (d, $^{4}J_{P–C}$ = 1.7 Hz, C_9), 29.1 (s, $C_9(CH_3)_2$), 22.7 (s, $C_{2/7}(CH_3)$), 21.5 (s, $C_{4/5}NCH(CH_3)_2$).

^{31}P NMR (243 MHz, C_6D_6): δ (ppm) −40.0 (br t, $^{1}J_{P–F}$ = 877 Hz).

^{31}P{^{1}H} NMR (243 MHz, C_6D_6): as above.

The ^{19}F NMR resonance corresponding to **36** could not be located.

5.7.2 Synthesis of 37



Caesium fluoride (14.0 mg, 92.7 μmol, 10 eq.) and dibromophosphorane **5** (5.0 mg, 9.3 μmol, 1.0 eq.) were dissolved in acetonitrile (0.5 mL) and sonicated for 5 minutes to produce a yellow solution. The solvent was removed *in vacuo*, and the residues extracted with pentane (3 × 0.5 mL) and filtered. Slow evaporation of the solvent to 0.5 mL then storage of this concentrated solution at −35 °C overnight resulted in the formation of colourless crystals. ^{1}H and ^{31}P NMR spectroscopy was obtained for a d_6-benzene solution of these crystals (*ca.* 1 mg).

^{1}H NMR (400 MHz, C_6D_6): δ (ppm) 6.89 (s, 1H,), 6.69 (s, 1H), 6.66 (s, 1H), 6.25 (s, 1H), 4.56 (s, 1H, N*H*), 3.78 (1H, d-sept, $^{3}J_{P–H}$ = 18.7 Hz, $^{3}J_{H–H}$ = 7.0 Hz, $C_5NCH(CH_3)_2$), 3.51 (1H, d-sept, $^{3}J_{H–H}$ = 6.2 Hz, $^{3}J_{H–H}$ = 2.1 Hz, $C_4NCH(CH_3)_2$), 2.24 (s, 3H, $C_{2/7}(CH_3)$), 2.18 (s, 3H, $C_{2/7}(CH_3)$), 1.59 (s, 3H, $C_9(CH_3)$), 1.51 (s, 3H, $C_9(CH_3)$), 1.45 (3H, d, $^{3}J_{H–H}$ = 7.0 Hz), 1.38 (3H, d, $^{3}J_{H–H}$ = 6.5 Hz), 1.34 (3H, d, $^{3}J_{H–H}$ = 6.8 Hz), 1.14 (3H, d, $^{3}J_{H–H}$ = 6.1 Hz).

Note that several assignments could not be made due not collecting ^{13}C and 2D NMR spectra.

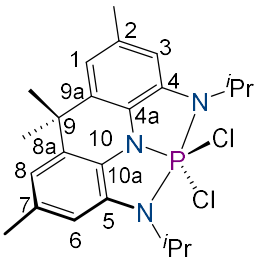
^{1}H{^{31}P} NMR (400 MHz, C_6D_6): as above, except δ (ppm) 3.78 (1H, sept, $^{3}J_{H–H}$ = 7.0 Hz, $C_5NCH(CH_3)_2$).

^{31}P NMR (162 MHz, C_6D_6): δ (ppm) 10.1 (dd, $^{1}J_{P–F}$ = 1046 Hz, $^{3}J_{P–H}$ = 18.7 Hz).

^{31}P{^{1}H} NMR (162 MHz, C_6D_6): δ (ppm) 10.1 (d, $^{1}J_{P–F}$ = 1046 Hz).

The ^{19}F NMR peak corresponding to **37** could not be located.

5.7.3 Synthesis of 38



A solution of phosphorus pentachloride (59 mg, 0.28 mmol, 1.0 eq.) in toluene (10 mL) was cooled to −78 °C. Triethylamine (0.20 mL, 1.42 mmol, 5.0 eq.) was added, followed by the addition of a −78 °C solution of **1^{iPr}** (100 mg, 0.28 mmol, 1.0 eq.) in toluene (10 mL). The resulting bright green solution was gradually warmed to room temperature and stirred for 16 hours, over which the solution turned light brown along with the precipitation of a light-brown solid. The mixture was filtered and the precipitate extracted with toluene (3 × 5 mL). The solvent was removed *in vacuo* providing a light-brown residue, which was then washed with pentane (3 × 2 mL) to provide a light-yellow solid (50 mg, 0.11 mmol, 40%).

^{1}H NMR (600 MHz, C_6D_6): δ (ppm) 6.65 (2H, s, $C_{1/8}H$), 6.64 (2H, s, $C_{3/6}H$), 4.69 (2H, d-sept, $^{3}J_{P–H}$ = 22.5 Hz, $^{3}J_{H–H}$ = 7.0 Hz, $C_{4/5}NCH(CH_3)_2$), 2.28 (6H, s, $C_{2/7}(CH_3)$), 1.55 (6H, s, $C_9(CH_3)_2$), 1.46 (12H, d, $^{3}J_{H–H}$ = 7.0 Hz, $C_{4/5}NCH(CH_3)_2$).

^{1}H{^{31}P} NMR (600 MHz, C_6D_6): as above, except δ (ppm) 4.69 (2H, sept, $^{3}J_{H–H}$ = 7.0 Hz, $C_{4/5}NCH(CH_3)_2$).

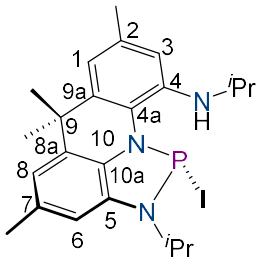
^{13}C{^{1}H} NMR (151 MHz, C_6D_6): δ (ppm) 132.9 (d, $^{4}J_{C–P}$ = 2.1 Hz, $C_{2/7}$), 132.6 (d, $^{2}J_{C–P}$ = 17.8 Hz, $C_{4/5}$), 129.9 (d, $^{2}J_{C–P}$ = 10.4 Hz, $C_{4a/10a}$), 129.3 (s, $C_{8a/9a}$), 115.4 (s, $C_{1/8}$), 108.1 (d, $^{3}J_{P–C}$ = 11.7 Hz, $C_{3/6}$), 47.5 (d, $^{2}J_{C–P}$ = 4.9 Hz, $C_{4/5}NCH(CH_3)_2$), 36.6 (d, $^{4}J_{C–P}$ = 1.7 Hz, C_9), 32.9 (s, $C_9(CH_3)_2$), 22.8 (s, $C_{2/7}(CH_3)$), 18.9 (d, $^{3}J_{C–P}$ = 5.9 Hz, $C_{4/5}NCH(CH_3)_2$).

^{31}P NMR (243 MHz, C_6D_6): δ (ppm) −49.7 (t, $^{3}J_{P–H}$ = 22.5 Hz).

^{31}P{^{1}H} NMR (243 MHz, C_6D_6): δ (ppm) −49.7 (s).

Elemental analysis calcd. (%) for $C_{23}H_{31}Cl_2N_3P$: C 61.34, H 6.71, N 9.33; found: C 60.22, H 5.27, N 8.43. These values fall outside of the expected range, suspected to be on account of an unknown impurity generated during synthesis.

5.7.4 Synthesis of 39



Chlorophosphine **16** (26.4 µmol, 1.0 eq), made *in situ* according to its reported procedure,[33] and sodium iodide (20.0 mg, 0.134 mmol, 5 eq.) were dissolved in acetonitrile and sonicated for 5 minutes, resulting in a yellow solution. The solvent was removed *in vacuo* and the residue extracted into pentane (2 × 5 mL). Slow evaporation of this solution resulted in the formation of large block-like orange crystals of **39** (9.0 mg, 17.7 µmol, 67%).

Heteronuclear NMR spectroscopy was performed on a sample of **39** in d_8-toluene at 85 °C.

^{1}H NMR (600 MHz, d_8-toluene): δ (ppm) 6.99 (1H, s, C_1H), 6.84 (1H, s, C_8H), 6.67 (1H, s, C_3H), 6.58 (1H, s, C_6H), 4.11 (1H, d-sept, $^3J_{P–H}$ = 10.3 Hz, $^3J_{H–H}$ = 6.8 Hz, $C_5NCH(CH_3)_2$), 3.70 (1H, s, NH), 3.30 (1H, sept-d, $^3J_{H–H}$ = 6.4 Hz, $^3J_{H–H}$ = 2.6 Hz, $C_4NCH(CH_3)_2$), 2.26 (3H, s, $C_7(CH_3)$), 2.14 (3H, s, $C_2(CH_3)$), 1.58 (6H, dd, $^3J_{H–H}$ = 6.8 Hz, $^3J_{P–H}$ = 2.1 Hz, $C_5NCH(CH_3)_2$), 1.54 (6H, s, $C_9(CH_3)_2$), 1.14 (6H, d, $^3J_{H–H}$ = 6.4 Hz, $C_4NCH(CH_3)_2$).

^{1}H{^{31}P} NMR (600 MHz, d_8-toluene): as above, except δ (ppm) 4.11 (1H, sept, $^3J_{H–H}$ = 6.8 Hz, $C_5NCH(CH_3)_2$), 1.58 (6H, d, $^3J_{H–H}$ = 6.8 Hz, $C_5NCH(CH_3)_2$).

^{13}C{^{1}H} NMR (151 MHz, d_8-toluene): δ (ppm) 135.9 (d, $^2J_{P–C}$ = 9.5 Hz, C_5), 135.5 (d, $^3J_{P–C}$ = 3.9 Hz, C_{8a}), 134.9 (s, C_4), 133.8 (d, $^4J_{P–C}$ = 1.9 Hz, C_7), 133.8 (s, C_2), 131.8 (s, C_{9a}), 131.7 (d, $^2J_{P–C}$ = 9.5 Hz, C_{4a}), 130.4 (d, $^2J_{P–C}$ = 12.1 Hz, C_{10a}), 119.5 (s, C_8), 109.9 (s, C_6), 49.4 (d, $^{5TS}J_{P–C}$ = 3.6 Hz, $C_4NCH(CH_3)_2$)*, 48.8 (d, $^2J_{C–P}$ = 14.8 Hz, $C_5NCH(CH_3)_2$), 36.8 (s, C_9), 34.3 (br s, $C_9(CH_3)_2$), 22.0 (s, $C_7(CH_3)$), 21.9 (br s, $C_4NCH(CH_3)_2$), 21.2 (s, $C_2(CH_3)$),

* TS = through space coupling to phosphorus in close proximity.[34]

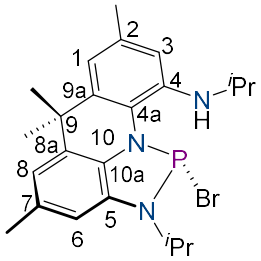
HSQC reveals that resonances for C_1, C_3 and $C_5NCH(CH_3)_2$ are hidden beneath a residual peak for the NMR solvent.

^{31}P NMR (243 MHz, d_8-toluene): δ (ppm) 173.8 (s).

^{31}P{^{1}H} NMR (243 MHz, d_8-toluene): as above.

Elemental analysis calcd. (%) for $C_{23}H_{31}IN_3P$: C 54.44, H 6.16, N 8.28; found: C 54.34, H 6.00, N 7.66.

5.7.5 Synthesis of 42



Chlorophosphine **16** (26.4 µmol, 1.0 eq), made *in situ* according to its reported procedure,[33] and lithium bromide (23 mg, 0.264 mmol, 10 eq.) were dissolved in acetonitrile and sonicated for 5 minutes, resulting in a yellow solution. The solvent was removed *in vacuo* and the residue extracted into pentane (2 × 3 mL). Slow evaporation of this solution resulted in the formation of large block-like orange crystals of **42** (11.3 mg, 24.5 µmol, 93%).

Heteronuclear NMR spectroscopy was performed on a sample of **42** in d_8-toluene at 95 °C.

^{1}H NMR (600 MHz, d_8-toluene): δ (ppm) 7.00 (1H, s, C_1H), 6.80 (1H, s, C_8H), 6.66 (1H, s, C_3H), 6.56 (1H, s, C_6H), 4.10 (1H, d-sept, $^3J_{P–H}$ = 10.8 Hz, $^3J_{H–H}$ = 6.7 Hz, $C_5NCH(CH_3)_2$), 3.44 (1H, br s, N*H*), 3.34 (1H, sept-d, $^3J_{H–H}$ = 6.3 Hz, $^3J_{H–H}$ = 2.2 Hz, $C_5NCH(CH_3)_2$), 2.29 (3H, s, $C_7(CH_3)$), 2.17 (3H, s, $C_2(CH_3)$), 1.57 (6H, dd, $^3J_{H–H}$ = 6.7 Hz, $^3J_{P–H}$ = 1.7 Hz, $C_5NCH(CH_3)_2$), 1.54 (6H, s, $C_9(CH_3)_2$), 1.15 (6H, d, $^3J_{H–H}$ = 6.4 Hz, $C_4NCH(CH_3)_2$).

^{1}H{^{31}P} NMR (600 MHz, d_8-toluene): as above, except δ (ppm) 4.10 (1H, sept, $^3J_{H–H}$ = 6.7 Hz, $C_5NCH(CH_3)_2$), 1.57 (6H, d, $^3J_{H–H}$ = 6.7 Hz, $C_5NCH(CH_3)_2$).

^{13}C{^{1}H} NMR (151 MHz, d_8-toluene): δ (ppm) 135.3–135.2 (m)*, 134.6 (s, C_4), 133.2 (d, $^4J_{P–C}$ = 2.2 Hz, C_7), 133.1 (s, C_2), 131.2 (d, $^2J_{P–C}$ = 8.5 Hz, C_{4a}), 131.1 (s, C_{9a}), 129.9 (d, $^2J_{P–C}$ = 12.1 Hz, C_{10a}), 124.8 (s, $C_{1/3}$)**, 124.7 (s, $C_{1/3}$)**, 118.7 (s, C_8), 109.6 (s, C_6), 49.1 (d, $^{5TS}J_{C–P}$ = 4.1 Hz, $C_4NCH(CH_3)_2$)***, 48.3 (d, $^2J_{P–C}$ = 15.5 Hz, $C_5NCH(CH_3)_2$), 36.7 (s, C_9), 34.2 (br s, $C_9(CH_3)_2$), 22.1 (br s, $C_4NCH(CH_3)_2$), 22.0 (s, $C_7(CH_3)$), 21.5 (br s, $C_5NCH(CH_3)_2$), 21.2 (s, $C_2(CH_3)$).

*Resonances corresponding to C_5 and C_{8a} are contained within this multiplet, revealed by HMBC.

**Overlap of 2D resonances prevent C_1 and C_3 from being distinguished.

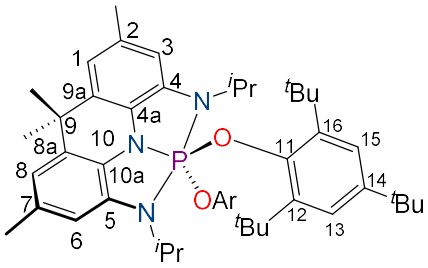
****TS = through space coupling to phosphorus in close proximity.[34]

^{31}P NMR (202 MHz, d_8-toluene): δ (ppm) 150.6 (s).

^{31}P{^{1}H} NMR (202 MHz, d_8-toluene): as above.

Elemental analysis calcd. (%) for $C_{23}H_{31}BrN_3P$: C 60.00, H 6.79, N 9.13; found: C 59.66, H 6.51, N 8.41.

5.7.6 Synthesis of 46



6 (10 mg, 26.4 μmol, 1.0 eq.) and 2,4,6-tri-*tert*-butylphenoxyl radical (14 mg, 52.8 μmol, 2.0 eq.) were dissolved in benzene (0.5 mL), generating a dark green solution. The solvent was removed *in vacuo* to provide a slightly blue residue. Pentane (0.5 mL) was added to this residue, then syphoned off and discarded. The resulting colourless residue was extracted into pentane (5 × 1 mL), slow evaporation of which yielded yellow crystals of **46** (17.5 mg, 19 μmol, 73%).

^{1}H NMR (600 MHz, C_6D_6): δ (ppm) 7.29 (2H, t, $^{4}J_{H-H}$ = 2.9 Hz, $^{5TS}J_{P-H}$ = 2.9 Hz, $C_{12}H$)*, 7.08 (2H, d, $^{4}J_{H-H}$ = 2.9 Hz, $C_{14}H$), 6.63 (2H, s, $C_{1/8}H$), 6.45 (2H, s, $C_{3/6}H$), 4.04 (2H, apparent-octet, $^{3}J_{P-H}$ = 6.7 Hz, $^{3}J_{H-H}$ = 6.7 Hz, $C_{4/5}NCH(CH_3)_2$), 2.26 (6H, s, $C_{2/7}(CH_3)$), 1.89 (6H, s, $C_9(CH_3)_2$), 1.76 (18H, s, $C_{14}(C(CH_3)_3)$), 1.24 (18H, s, $C_{12/16}(C(CH_3)_3)$), 0.93 (18H, s, $C_{12/16}(C(CH_3)_3)$).

* TS = through space coupling to phosphorus in close proximity.[34]

^{1}H{^{31}P} NMR (600 MHz, C_6D_6): as above, except δ (ppm) 7.29 (2H, d, $^{4}J_{H-H}$ = 2.9 Hz, $C_{12}H$), 4.04 (2H, sept, $^{3}J_{H-H}$ = 6.7 Hz, $C_{4/5}NCH(CH_3)_2$).

^{13}C{^{1}H} NMR (151 MHz, C_6D_6): δ (ppm) 148.0 (d, $^{2}J_{P-C}$ = 18.2 Hz, C_{11}), 144.3 (d, $^{3}J_{P-C}$ = 5.2 Hz, $C_{12/16}$), 143.6 (d, $^{5}J_{P-C}$ = 2.7 Hz, C_{14}), 141.1 (d, $^{3}J_{P-C}$ = 5.8 Hz, $C_{12/16}$), 135.0 (d, $^{2}J_{C-P}$ = 16.8 Hz, $C_{4/5}$), 131.6 (s, $C_{2/7}$), 128.6 (s, $C_{8a/9a}$), 126.5 (d, $^{4}J_{P-C}$ = 3.8 Hz, $C_{13/15}$), 125.6 (d, $^{4}J_{P-C}$ = 2.4 Hz, $C_{13/15}$), 119.6

(d, $^{2}J_{C–P}$ = 15.8 Hz, $C_{4a/10a}$), 113.5 (s, $C_{1/8}$), 107.1 (d, $^{3}J_{C–P}$ = 11.3 Hz, $C_{3/6}$), 48.2 (s, $C_{4/5}NCH(CH_3)_2$), 38.7 (s, $C_{12/16}(C(CH_3)_3)$), 38.2 (s, $C_{14}(C(CH_3)_3)$), 36.5 (s, C_9), 34.9 (s, $C_{14}(C(CH_3)_3)$), 34.0–33.8 (overlapping signals)*, 31.4 (s, $C_{12/16}(C(CH_3)_3)$), 23.1 (s, $C_{2/7}(CH_3)$).

*HMBC and HSQC show that these overlapping signals correspond to $C_9(CH_3)$, one $C_{12/16}(C(CH_3)_3)$ signal and one $C_{12/16}(C(CH_3)_3)$ signal.

^{31}P NMR (243 MHz, C_6D_6): δ (ppm) −44.5 (s).

$^{31}P\{^{1}H\}$ NMR (162 MHz, C_6D_6): δ (ppm) −44.5 (t, $^{3}J_{P–H}$ = 6.7 Hz).

Elemental analysis calcd. (%) for $C_{59}H_{88}N_3O_2P$: C 78.53, H 9.83, N 4.66; found: C 78.81, H 9.96, N 4.56.

5.8 References

[1] D. G. Nocera, *Inorg. Chem.* **2009**, *48*, 10001–10017.

[2] N. S. Lewis, D. G. Nocera, *Proc. Natl. Acad. Sci. U S A* **2006**, *103*, 15729–15735.

[3] A. J. Esswein, D. G. Nocera, *Chem. Rev.* **2007**, *107*, 4022–4047.

[4] A. Raphael Karikachery, H. B. Lee, M. Masjedi, A. Ross, M. A. Moody, X. Cai, M. Chui, C. D. Hoff, P. R. Sharp, *Inorg. Chem.* **2013**, *52*, 4113–4119.

[5] A. F. Heyduk, D. G. Nocera, *Science*, **2001**, 293, 1639–1641

[6] A. J. Esswein, A. S. Veige, D. G. Nocera, *J. Am. Chem. Soc.* **2005**, *127*, 16641–16651.

[7] A. J. Esswein, J. L. Dempsey, D. G. Nocera, *Inorg. Chem.* **2007**, *46*, 2362–2364.

[8] T. R. Cook, A. J. Esswein, D. G. Nocera, *J. Am. Chem. Soc.* **2007**, *129*, 10094–10095.

[9] T. R. Cook, Y. Surendranath, D. G. Nocera, *J. Am. Chem. Soc.* **2009**, *131*, 28–29.

[10] T. S. Teets, D. G. Nocera, *J. Am. Chem. Soc.* **2009**, *131*, 7411–7420.

[11] T. A. Perera, M. Masjedi, P. R. Sharp, *Inorg. Chem.* **2014**, *53*, 7608–7621.

[12] S. J. Hwang, D. C. Powers, A. G. Maher, B. L. Anderson, R. G. Hadt, S.-L. Zheng, Y.-S. Chen, D. G. Nocera, *J. Am. Chem. Soc.* **2015**, *137*, 6472–6475.

[13] S. J. Hwang, B. L. Anderson, D. C. Powers, A. G. Maher, R. G. Hadt, D. G. Nocera, *Organometallics* **2015**, *34*, 4766–4774.

[14] B. J. Shields, A. G. Doyle, *J. Am. Chem. Soc.* **2016**, *138*, 12719–12722.

[15] S. K. Kariofillis, A. G. Doyle, *Acc. Chem. Res.* **2021**, *54*, 988–1000.

[16] G. Park, M. Karimi, W.-C. Liu, F. P. Gabbaï, *Angew. Chem., Int. Ed.* **2022**, 61, e202206265.

[17] T.-P. Lin, F. P. Gabbaï, *J. Am. Chem. Soc.* **2012**, *134*, 12230–12238.

[18] H. Yang, F. P. Gabbaï, *J. Am. Chem. Soc.* **2014**, *136*, 10866–10869.

[19] S. Sahu, F. P. Gabbaï, *J. Am. Chem. Soc.* **2017**, *139*, 5035–5038.

[20] M. Karimi, E. S. Tabei, R. Fayad, M. R. Saber, E. O. Danilov, C. Jones, F. N. Castellano, F. P. Gabbaï, *Angew. Chem., Int. Ed.* **2021**, *60*, 22352–22358.

[21] M. Karimi, F. P. Gabbaï, *Organometallics* **2022**, *41*, 642–648.

[22] E. I. Carrera, T. M. McCormick, M. J. Kapp, A. J. Lough, D. S. Seferos, *Inorg. Chem.* **2013**, *52*, 13779–13790.

[23] E. I. Carrera, D. S. Seferos, *Dalton Trans.* **2015**, *44*, 2092–2096.

[24] E. I. Carrera, A. E. Lanterna, A. J. Lough, J. C. Scaiano, D. S. Seferos, *J. Am. Chem. Soc.* **2016**, *138*, 2678–2689.

[25] P.-F. Li, E. I. Carrera, D. S. Seferos, *ChemPlusChem* **2016**, *81*, 917–921.

[26] C. M. Lemon, S. J. Hwang, A. G. Maher, D. C. Powers, D. G. Nocera, *Inorg. Chem.* **2018**, *57*, 5333–5342.

[27] T. P. Robinson, D. De Rosa, S. Aldridge, J. M. Goicoechea, *Chem. Eur. J.* **2017**, *23*, 15455–15465.

[28] F. A. Cotton, P. A. Kibala, *J. Am. Chem. Soc.* **1987**, *109*, 3308–3312.

[29] W.-W. du Mont, M. Bätcher, S. Pohl, W. Saak, *Angew. Chem., Int. Ed.* **1987**, *26*, 912–913.

[30] R. Núñez, F. Teixidor, R. Kivekäs, R. Sillanpää, C. Viñas, *Dalton Trans.* **2008**, 1471–1480.

[31] V. W. Manner, T. F. Markle, J. H. Freudenthal, J. P. Roth, J. M. Mayer, *Chem. Commun.* **2008**, 256–258.

[32] J. Cui, Y. Li, R. Ganguly, R. Kinjo, *Chem. Eur. J.* **2016**, *22*, 9976–9985.

[33] A. J. King, J. Abbenseth, J. M. Goicoechea, *Chem. Eur. J.* **2023**, *29*, e202300818.

[34] J.-C. Hierso, *Chem. Rev.* **2014**, *114*, 4838–4867.

Chapter 6

Conclusions and Future Work

6.1 Conclusions

A stable C_{2v} symmetric, T-shaped, phosphine was synthesised by steric tuning of an acridane-derived NNN-pincer ligand. Due to the inert nature of the aromatic ligand, phosphorus-based reactivity was probed for this system through reaction with small molecule substrates. This revealed the predominantly Lewis acidic, or electrophilic, character of a phosphine in such a geometry, and the diminished nucleophilicity of its phosphorus-based lone pair. This provides experimental validation of the predicted ambiphilic reactivity proposed for such highly constrained systems, and represents a benchmark set of results for reactivity at this degree of geometric constraint.

This phosphine can be used as a ligand to transition metals, displaying conformational flexibility while behaving as a moderate σ-donor and possessing significant π-acceptor properties. The Lewis acidity at phosphorus is maintained on bonding to transition metals, with reactions of one of its gold(I) complexes with E–H bonds occurring solely at the phosphine ligand. These results add to the limited library of examples of phosphine-based activation of E–H bonds whilst bound to a transition metal, and provides a design principle for future work targeting this mode of reactivity. This includes the design of metal-ligand cooperative catalysis towards, for example, hydro-elementation reactions.

Derivatives of this phosphine bearing reduced geometric constraint were shown to activate the N–H bond of ammonia, in some cases doing so more rapidly than the parent phosphine. For these, the observed Lewis acidity at phosphorus was attributed to engaging its lone-pair in the formation of a bond, for instance to a transition metal or an oxidant, demonstrating an alternate methodology to geometric constraint for achieving this reactivity. These results highlight the potential for further work in utilising bond activation reactions with unconstrained phosphorus-based compounds, lowering the

barrier-to-entry for such studies through avoiding the synthetic challenge associated with designing highly constraining ligands.

Dihalogenated phosphorus(V) derivatives of this phosphine were capable of photo-reductively eliminating halogen radicals on irradiation with LEDs. This resulted from excitations populating the $\sigma^*_{P–X}$ antibonding orbital – a transition originating from the extended π-system across the aromatic acridane backbone. This advances the study of halogen photo-elimination towards HX-splitting catalysis by doing so in the absence of precious metals or toxic heavy main-group elements. This highlights an alternative class of compound (i.e. geometrically constrained phosphines) which may prove beneficial for future study of this process.

6.2 Future work

Expanding the library of transition metal complexes of **6** may uncover reactions which utilise the phosphine-based reactivity observed for gold complex **19**. Towards this, preliminary work has shown that rhodium(I), iridium(I), platinum(0) and platinum(II) complexes of **6** all maintain the ability to activate a molecule of ammonia at the phosphine ligand. However, follow-up reactivity towards hydroamination of unsaturated substates using these complexes was not investigated, but poses a promising new line of research.

The work in Chapter 5 concerned only the photoelimination/reduction step of the proposed HX-splitting catalytic cycle. Having shown the applicability of dihalophosphoranes derived from **6** to perform this reaction, the remaining two elementary steps should be addressed next. The addition of a single molecule of HX to **6** was demonstrated in the synthesis of both **16** and **42** (X = Cl and Br, respectively). Their phosphorus(III) oxidation state suggests that reaction with a further molecule of HX may be possible. The resulting compound would likely possess both protic (N–H) and hydridic (P–H) centres, suggesting the possibility of hydrogen elimination from such compounds.

The photoelimination methodology utilised for dihalophosphoranes may be applicable for alternative phosphoranes, such as those possessing organic substituents. Irradiation of such compounds may result in the generation of typically hard-to-access organic radicals with potential for further reactivity in organic transformations. Preliminary work towards this regarded the synthesis of biaryl, or aryl-halide, substituted phosphoranes through reactions of **5** or **38** with reagents of the type ArM (M = alkali metal) in varying stoichiometries. However, photoelimination studies of the resulting compounds was not performed.

Chapter 7

Experimental and Computational Details

7.1 General experimental methods

7.1.1. Synthetic methods

Unless specified otherwise, all reactions and product manipulations were performed using standard Schenk-line techniques under an atmosphere of argon, or in a dinitrogen-filled glovebox (MBraun UNIlab) maintained at <0.1 ppm H_2O and <0.1 ppm O_2. All anhydrous solvents were stored under an atmosphere of nitrogen or argon in gas-tight ampoules over activated 3 Å molecular sieves.

LED irradiation experiments were performed using 456 nm or 390 nm Kessil PR160L LEDs at maximum intensity. J Young NMR tubes sealed under a dinitrogen atmosphere contained the solutions being irradiated. The sample was placed <1 cm away from the centre of the LED block, and a desk fan was placed in close proximity to maintain a constant sample temperature.

Hexane (Sigma Aldrich HPLC grade), pentane (Sigma Aldrich HPLC grade), benzene (Rathburn HPLC grade), dichloromethane (Sigma Aldrich HPLC grade), acetonitrile (Sigma Aldrich HPLC grade) diethyl ether (Sigma Aldrich HPLC grade) and toluene (Sigma Aldrich HPLC grade) were purified using an MBraun SPS-800 solvent system. Ethyl acetate (Sigma Aldrich HPLC grade) and methanol (Sigma Aldrich anhydrous, 99.8%) was used as provided. THF (Sigma Aldrich HPLC grade) was distilled over sodium/benzophenone. C_6D_6 (Sigma Aldrich, 99.5%) and CD_2Cl_2 (Sigma Aldrich, 99.5%) was degassed and dried over CaH_2. d_8-toluene (Sigma Aldrich, 99.5%) and d_8-THF (Sigma Aldrich, 99.5%) was degassed and dried over sodium/potassium alloy.

The following were used as received from their commercial supplier without further purification: palladium on carbon (10 w%, Sigma Aldridge), H_2 (Sigma Aldridge), paraformaldehyde (Merck), sodium methoxide (Sigma Aldridge), sodium borohydride (Sigma Aldridge), phosphorus pentabromide (Acros), trimethylphosphine (Strem), magnesium powder (Sigma Aldridge), potassium *tert*-butoxide

(Sigma Aldridge), 4,7,13,16,21,24-Hexaoxa-1,10-diazabicyclo[8.8.8]hexacosane (Merck), methyl triflate (Apollo Scientific), oxygen (Linde), 2,4-bis(4-methoxyphenyl-1,3,2,4-dithiadiphosphetane-2,4-disulfide (Alfa Aesar), sulfur (Sigma Aldridge), selenium (Sigma Aldridge), 2*H*-1,3,2-benzodioxaborole (Alfa Aesar), 2 M hydrochloric acid in diethyl ether (diluted prior to use, Alfa Aesar), deuterium oxide (Sigma Aldridge), $Au(SMe_2)Cl$ (Sigma Aldrich), tungsten hexacarbonyl (Sigma Aldrich), aniline (Sigma Aldrich), triphenylphosphine oxide (Sigma Aldrich), xenon difluoride (Sigma Aldrich), caesium fluoride (Sigma Aldrich), phosphorus pentachloride (Sigma Aldrich) and TEMPO (Sigma Aldrich). Phosphorus trichloride (Sigma Aldridge) was distilled and degassed prior to use. Triethylamine (TCI) and tetramethylethylene (Sigma Aldrich) was degassed, dried over CaH_2 and distilled prior to use. Benzaldehyde (Sigma Aldridge) was distilled prior to use. Pyridine N-oxide (Sigma Aldridge) was sublimed prior to use. Ammonia (anhydrous, Linde) was stored over activated 3 Å molecular sieves in a gas-tight ampoule. Sodium iodide (Sigma Aldrich) and lithium bromide (Sigma Aldrich) were heated under a dynamic vacuum prior to use. The following were synthesised according to their referenced literature procedure: 2,7,9,9-tetramethyl-4,5-dinitro-9,10-dihydroacridine,[1] **1**$^{i\mathrm{Pr}}$,[1] mesityl azide,[2] $NaBAr^F{}_4$ ($BAr^F{}_4$ = tetrakis(3,5-bis(trifluoromethyl)phenyl)borate),[3] Au(IDipp)Cl,[4] *tert*-butyl azide,[5] and 2,4,6-tri-*tert*-butylphenoxyl radical (**45**).[6]

7.1.2 Characterisation techniques

NMR samples were prepared inside an inert atmosphere glovebox in NMR tubes fitted with a gas-tight valve. NMR spectra were acquired on either a Bruker AVIII 400 MHz NMR spectrometer (^{1}H 400 MHz, ^{11}B 128 MHz, ^{31}P 162 MHz), a Bruker AVIII 500 spectrometer (^{1}H 500 MHz, ^{31}P 202 MHz, ^{19}F 471 MHz, ^{77}Se 95 MHz) or a Bruker Avance NEO 600 MHz NMR spectrometer with a broadband helium cryoprobe (^{1}H 600 MHz, ^{31}P 243 MHz, ^{13}C 151 MHz, ^{11}B 193 MHz). ^{1}H and ^{13}C NMR spectra were referenced to their respective solvent resonance (^{1}H NMR C_6D_6: δ = 7.16 ppm, d_8-toluene: δ = 2.09, CD_2Cl_2: δ = 5.32 ppm, d_8-THF: δ = 3.58 ppm; ^{13}C NMR C_6D_6: δ = 128.1 ppm, d_8-toluene: δ = 20.4 ppm, CD_2Cl_2: δ = 53.8 ppm, d_8-THF: δ = 67.6 ppm). ^{11}B NMR spectra were externally

referenced to $BF_3 \cdot Et_2O$ in C_6D_6. ^{19}F NMR spectra were externally referenced to $CFCl_3$. ^{31}P NMR spectra were externally referenced to an 85% solution of H_3PO_4 in H_2O.

Raman spectra were acquired on a Thermo Scientific DXR3 SmartRaman spectrometer using a 785 nm laser. FT-IR measurements were performed using a Shimadzu IR-Spirit spectrometer (installed inside the glove box) using a single reflection ATR accessory.

High-resolution mass spectrometry was acquired using a Thermo Exactive High-Resolution Orbitrap FTMS instrument equipped with a Acquity TUV Detector, with a Waters Acquity Ultraperformance LC system used for sample delivery.

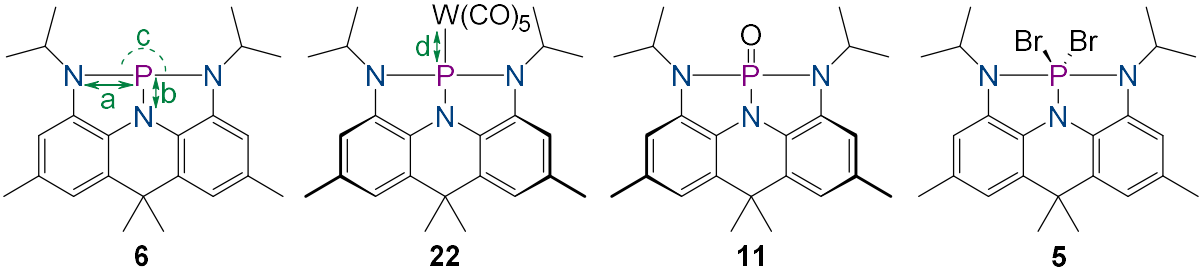
Elemental analyses were carried out by Elemental Analysis Services Team (London Metropolitan University, U.K.). Samples (approximately 5 mg) were submitted in flame sealed glass tubes.

Absorption spectra were recorded on a Jasco V-770 UV-Visible/NIR Spectrophotometer equipped with Peltier temperature controller and stirrer using quartz cuvettes of 1 cm path length. Experiments were conducted at 25°C

7.2 General computational methods

Density functional theory (DFT) calculations were performed using the ORCA 5.0.2 software package.[11–13] All methods were used as implemented. Analytical frequency calculations were carried out to verify all non-fragment geometries as either true minima ($N_{imag} = 0$) or saddle points ($N_{imag} = 1$). Energy decomposition analysis was carried out using the ETS-NOCV approach,[14,15] with difference densities generated by Multiwfn 3.8.[16] Natural Bond Order (NBO) analysis was carried out using the NBO 7.0 program.[17]

Benchmarking: Starting geometries for geometry optimisation calculations were adapted from SCXRD structures of the respective compounds where available, or that of a closely related compound where such was not. Benchmarking was performed through comparison of key bond metric data of the starting structure and that after optimisation to ensure that the calculation provided sensible results. See below for selected examples:



	a (Å)		b (Å)		c (°)		d (Å)	
Compound	Calc.	Exp.	Calc.	Exp.	Calc.	Exp.	Calc.	Exp.
6	1.853	1.860(1)	1.711	1.710(2)	164.7	165.0	-	-
22	1.715	1.718(2)	1.704	1.711(2)	120.5	123.5	2.505	2.498(1)
11	1.692	1.693(3)	1.682	1.678(3)	122.3	121.5	1.467	1.469(2)
5	1.801	1.779(1)	1.651	1.657(1)	171.3	170.6	2.274	2.300(1)

Figure 7.1. Geometry optimisation benchmarking through comparison of bond metric data obtained either through SCXRD, or by DFT

Chapter 3: Geometry optimisation and single point calculations were performed using the ωB97X-D3 functional[18] and the Resolution of Identify approximation (RIJCOSX),[18,19] and corrected for relativistic effects using the zeroth order approximation (ZORA). The segmented all-electron relativistically contracted basis set SARC-ZORA-TZVPP was used for Au and W, and the relativistically contracted basis set ZORA-def2-TZVPP was used for all other atoms, along with the SARC/J auxiliary basis set.[19,20]

Chapter 4: Geometry optimisation and single point calculations were performed using the PBE0 functional and DEF2_TZVP basis set,[21,22] with the Resolution of Identify approximation (RIJCOSX) using the general auxiliary basis set def2/J,[23] accounting for dispersion effects using Grimme's DFT-D3 approach with Becke-Johnson dampening (D3BJ).[24,25] Benchmarking specific to this chapter involved the identification of local or global minimum energy structures and comparing these to species identified experimentally. This included identifying **32** as a local minimum, consistent with its stability in the solid state such that SCXRD analysis could be performed. Additionally, the identification of

reaction products **29** and **31** experimentally aligned with their calculated lower energy in comparison to their respective starting materials, hence confirming their thermodynamic preference.

Chapter 5: Geometry optimisation and single point calculations were performed using the ωB97X-D3 functional[18] and DEF2_TZVPP basis set[22] with the Resolution of Identify approximation (RIJCOSX) using the general auxiliary basis set def2/J.[23] Time-dependant density functional theory (TD-DFT) calculations were performed at the above level of theory. TD-DFT calculations were limited to the 20 highest energy transitions. A scalar energy shift was applied to the resulting simulated spectra to account for the general inaccuracy of TDDFT calculations with this functional, the magnitude of which was determined through comparison to the experimental spectra as performed previously (and references therein).[26] Benchmarking specific to this chapter included the qualitative comparison between the measured UV-Vis spectra of **5** and **38** and those calculated through TD-DFT.

7.3 Single crystal X-ray diffraction data

Single-crystal X-ray diffraction (SCXRD) data were collected using an Oxford Diffraction Supernova dual-source diffractometer equipped with a 135 mm Atlas CCD area detector. Crystals were selected under Paratone-N oil, mounted on micro-mount loops and quench-cooled using an Oxford Cryosystems open flow N_2 cooling device. Data were collected at 150 K or 100 K using mirror monochromated Cu Kα (λ = 1.54184 Å) radiation and processed using the CrysAlisPro package, including unit cell parameter refinement and inter-frame scaling (carried out using SCALE3 ABSPACK).[7] Equivalent reflections were merged and diffraction patterns processed with the CrysAlisPro suite. Structures were subsequently solved using direct methods and refined on F^2 using the SHELXL package.[8–10]

SCXRD data was collected by Aaron J. King and solved by Prof. Jose M. Goicoechea.

Table 7.1. Selected X-ray data collection/refinement parameters for **2, 3** and **5**.

	2	**3**	**5**
Formula	$C_{38}H_{44}N_6P_2$	$C_{19}H_{22}Br_2N_3P$	$C_{23}H_{30}Br_2N_3P$
CCDC	2245882	2245883	2245884
Fw [g mol^{-1}]	646.73	483.18	539.29
Crystal system	monoclinic	monoclinic	monoclinic
Space group	$P2_1/c$	$P2_1/c$	$P2_1/n$
a (Å)	13.6604(1)	10.6582(1)	11.0549(1)
b (Å)	8.6501(1)	20.6927(2)	10.4890(1)
c (Å)	13.9457(1)	17.9575(2)	20.0135(1)
α (°)	90	90	90
β (°)	98.594(1)	103.962(1)	100.466(1)
γ (°)	90	90	90
V (Å^3)	1629.38(3)	3843.46(7)	2282.05(3)
Z	2	8	4
Radiation, λ (Å)	Cu K_α, 1.54184	Cu K_α, 1.54184	Cu K_α, 1.54184
Temp (K)	150(2)	150(2)	150(2)
ρ_{calc} (g cm^{-3})	1.318	1.670	1.570
μ (mm^{-1})	1.503	6.186	5.274
Reflections collected	39989	65795	24074
Indep. reflections	3394	8031	4751
Parameters	214	463	270
R(int)	0.0360	0.0387	0.0566
R1/wR2,[a] $I \geq 2\sigma I$ (%)	3.38/9.59	3.02/7.99	2.08/5.29
R1/wR2,[a] all data (%)	3.80/9.96	3.22/8.15	2.19/5.38
GOF	1.052	1.046	1.069

[a] $R1 = [\Sigma||F_o| - |F_c||]/\Sigma|F_o|$; $wR2 = \{[\Sigma w[(F_o)^2 - (F_c)^2]^2]/[\Sigma w(F_o^2)^2\}^{1/2}$; $w = [\sigma^2(F_o)^2 + (AP)^2 + BP]^{-1}$, where $P = [(F_o)^2 + 2(F_c)^2]/3$ and the A and B values are 0.0578 and 0.633 for **2**, 0.0422 and 3.07 for **3**, and 0.0291 and 0.95 for **5**.

Table 7.2. Selected X-ray data collection/refinement parameters for **6**, **7**[OTf] and **9**.

	6	**7**[OTf]	**9**
Formula	$C_{23}H_{30}N_3P$	$C_{25}H_{33}F_3N_3O_3PS$	$C_{28}H_{42}N_3OP$
CCDC	2245885	2245891	2245886
Fw [g mol^{-1}]	379.47	543.57	467.61
Crystal system	orthorhombic	tetragonal	monoclinic
Space group	$Cmc2_1$	I4/m	C2/c
a (Å)	24.0287(3)	19.7584(1)	17.5219(2)
b (Å)	7.6323(1)	19.7584(1)	18.0163(2)
c (Å)	11.5588(1)	13.4166(2)	19.4088(2)
α (°)	90	90	90
β (°)	90	90	110.154(1)
γ (°)	90	90	90
V (Å^3)	2119.82(4)	5237.77(9)	5751.81(11)
Z	4	8	8
Radiation, λ (Å)	Cu K_α, 1.54184	Cu K_α, 1.54184	Cu K_α, 1.54184
Temp (K)	150(2)	150(2)	150(2)
ρ_{calc} (g cm^{-3})	1.189	1.379	1.080
μ (mm^{-1})	1.224	2.145	1.008
Reflections collected	22420	19103	75436
Indep. reflections	2252	2850	6003
Parameters	147	178	326
R(int)	0.0448	0.0317	0.0374
R1/wR2,[a] $I \geq 2\sigma I$ (%)	2.79/7.29	3.54/9.76	4.13/12.08
R1/wR2,[a] all data (%)	2.95/7.40	4.19/10.30	4.65/12.62
GOF	1.047	1.044	1.046

[a] $R1 = [\Sigma||F_o| - |F_c||]/\Sigma|F_o|$; $wR2 = \{[\Sigma w[(F_o)^2 - (F_c)^2]^2]/[\Sigma w(F_o^2)^2\}^{1/2}$; $w = [\sigma^2(F_o)^2 + (AP)^2 + BP]^{-1}$, where $P = [(F_o)^2 + 2(F_c)^2]/3$ and the A and B values are 0.0515 and 0.31 for **6**, 0.0552 and 5.79 for **7**[OTf], and 0.0729 and 3.46 for **9**.

Table 7.2. Selected X-ray data collection/refinement parameters for **10**, **11**·hex and **12**.

	10	**11**·hex	**12**
Formula	$C_{24}H_{32}N_3P$	$C_{26}H_{37}N_3OP$	$C_{23}H_{30}N_3PS$
CCDC	2245892	2245887	2245888
Fw [g mol^{-1}]	393.49	438.55	411.53
Crystal system	monoclinic	monoclinic	orthorhombic
Space group	$P2_1/n$	C2/c	Pbca
a (Å)	11.5140(3)	30.9090(11)	19.7422(3)
b (Å)	9.5806(3)	9.5766(4)	10.6844(1)
c (Å)	19.8338(7)	34.7072(9)	20.5719(2)
α (°)	90	90	90
β (°)	93.615(3)	106.821(3)	90
γ (°)	90	90	90
V (Å^3)	2183.53(12)	9833.9(6)	4339.30(9)
Z	4	16	8
Radiation, λ (Å)	Cu K_α, 1.54184	Cu K_α, 1.54184	Cu K_α, 1.54184
Temp (K)	150(2)	150(2)	150(2)
ρ_{calc} (g cm^{-3})	1.197	1.185	1.260
μ (mm^{-1})	1.205	1.149	2.112
Reflections collected	24205	35541	4547
Indep. reflections	4543	10142	2252
Parameters	269	621	253
R(int)	0.0800	0.0951	0.0483
R1/wR2,[a] $I \geq 2\sigma I$ (%)	4.38/9.60	5.88/13.26	3.89/11.00
R1/wR2,[a] all data (%)	7.27/11.00	11.34/15.84	4.59/11.63
GOF	1.020	1.020	1.049

[a] $R1 = [\Sigma||F_o| - |F_c||]/\Sigma|F_o|$; $wR2 = \{[\Sigma w[(F_o)^2 - (F_c)^2]^2]/[\Sigma w(F_o^2)^2\}^{1/2}$; $w = [\sigma^2(F_o)^2 + (AP)^2 + BP]^{-1}$, where $P = [(F_o)^2 + 2(F_c)^2]/3$ and the A and B values are 0.0439 and 0.79 for **10**, 0.0576 and 0.00 for **11**-hex, and 0.0629 and 3.49 for **12**.

Table 7.2. Selected X-ray data collection/refinement parameters for **13**, **14** and **16**.

	13	**14**	**16**
Formula	$C_{23}H_{30}N_3PSe$	$C_{32}H_{41}N_4P$	$C_{26}H_{38}ClN_3P$
CCDC	2245889	2245890	2245893
Fw [g mol^{-1}]	458.43	512.66	459.01
Crystal system	orthorhombic	monoclinic	monoclinic
Space group	Pbca	$P2_1/c$	I2/m
a (Å)	10.8791(3)	13.3415(1)	9.7169(2)
b (Å)	20.1396(5)	9.0932(1)	14.3405(3)
c (Å)	20.1643(4)	24.9146(2)	18.4709(5)
α (°)	90	90	90
β (°)	90	104.645(1)	100.148(2)
γ (°)	90	90	90
V (Å^3)	4418.01(19)	2924.36(5)	2533.57(10)
Z	8	4	4
Radiation, λ (Å)	Cu K_α, 1.54184	Cu K_α, 1.54184	Cu K_α, 1.54184
Temp (K)	150(2)	150(2)	150(2)
ρ_{calc} (g cm^{-3})	1.378	1.164	1.203
μ (mm^{-1})	3.076	1.023	2.053
Reflections collected	47384	72843	26919
Indep. reflections	4630	6107	2759
Parameters	261	362	175
R(int)	0.0723	0.0430	0.0425
R1/wR2,[a] $I \geq 2\sigma I$ (%)	3.62/8.71	4.78/14.29	4.25/11.75
R1/wR2,[a] all data (%)	4.92/9.69	5.22/14.86	4.92/12.31
GOF	1.051	1.063	1.051

[a] $R1 = [\Sigma||F_o| - |F_c||]/\Sigma|F_o|$; $wR2 = \{[\Sigma w[(F_o)^2 - (F_c)^2]^2]/[\Sigma w(F_o^2)^2\}^{1/2}$; $w = [\sigma^2(F_o)^2 + (AP)^2 + BP]^{-1}$, where $P = [(F_o)^2 + 2(F_c)^2]/3$ and the A and B values are 0.0421 and 3.48 for **13**, 0.0838 and 1.75 for **14**, and 0.0674 and 2.00 for **16**.

Table 7.2. Selected X-ray data collection/refinement parameters for **17**, **18** and **19**.

	17	**18**	**19**
Formula	$C_{23}H_{32}N_3OP$	$C_{24}H_{34}N_3OP$	$C_{23}H_{30}AuClN_3P$
CCDC	2245894	2245895	2332919
Fw [g mol^{-1}]	397.48	411.51	611.88
Crystal system	triclinic	triclinic	monoclinic
Space group	P–1	P–1	$P2_1/c$
a (Å)	9.7475(2)	9.7300(4)	11.3179(3)
b (Å)	11.4509(2)	11.7503(5)	20.6100(4)
c (Å)	19.9436(4)	11.7696(5)	10.9127(3)
α (°)	96.500(2)	119.932(5)	90
β (°)	101.259(2)	90.877(3)	114.213(3)
γ (°)	98.232(2)	101.004(4)	90
V (Å^3)	2137.75(7)	1134.99(10)	2321.58(11)
Z	4	2	4
Radiation, λ (Å)	Cu K_α, 1.54184	Cu K_α, 1.54184	Cu Kα, 1.54184
Temp (K)	150(2)	150(2)	150(2)
ρ_{calc} (g cm^{-3})	1.235	1.204	1.751
μ (mm^{-1})	1.271	1.213	13.719
Reflections collected	48132	15691	18381
Indep. reflections	8868	4671	4827
Parameters	537	266	270
R(int)	0.0440	0.0280	0.0305
R1/wR2,[a] I ≥ 2σI (%)	4.46/11.79	4.98/14.13	2.93/7.51
R1/wR2,[a] all data (%)	5.47/12.57	5.41/14.52	3.10/7.61
GOF	1.028	1.076	1.143

[a] $R1 = [\Sigma||F_o| - |F_c||]/\Sigma|F_o|$; $wR2 = \{[\Sigma w[(F_o)^2 - (F_c)^2]^2]/[\Sigma w(F_o^2)^2\}^{1/2}$; $w = [\sigma^2(F_o)^2 + (AP)^2 + BP]^{-1}$, where $P = [(F_o)^2 + 2(F_c)^2]/3$ and the A and B values are 0.0666 and 0.97 for **17**, 0.0779 and 0.70 for **18**, and 0.0354 and 6.84 for **19**.

Table 7.2. Selected X-ray data collection/refinement parameters for **20**[BAr^F_4], **21**·0.5C_6H_6 and **22**.

	20[BAr^F_4]	**21**·0.5C_6H_6	**22**
Formula	$C_{82}H_{78}AuBF_{24}N_5P$	$C_{57}H_{78}AuN_5OP$	$C_{28}H_{30}N_3O_5PW$
CCDC	2332920	2332922	2332921
Fw [g mol^{-1}]	1828.24	1077.18	703.37
Crystal system	triclinic	triclinic	monoclinic
Space group	P–1	P–1	$P2_1/c$
a (Å)	12.8519(2)	10.9133(4)	11.83620(10)
b (Å)	18.3376(2)	12.8112(3)	9.34860(10)
c (Å)	18.3422(2)	19.3416(6)	25.4944(2)
α (°)	86.0730(10)	84.481(2)	90
β (°)	77.3920(10)	82.239(3)	91.2200(10)
γ (°)	77.8580(10)	81.453(3)	90
V ($Å^3$)	4123.00(9)	2641.67(14)	2820.36(4)
Z	2	2	4
Radiation, λ (Å)	Cu Kα, 1.54184	Cu Kα, 1.54184	Cu Kα, 1.54184
Temp (K)	150(2)	150(2)	150(2)
ρ_{calc} (g cm^{-3})	1.473	1.354	1.656
μ (mm^{-1})	4.417	5.839	8.475
Reflections collected	52244	31391	53655
Indep. reflections	16986	10901	5862
Parameters	1081	587	351
R(int)	0.0632	0.0464	0.0449
R1/wR2,[a] $I \geq 2\sigma I$ (%)	5.02/13.47	2.75/6.39	1.95/4.65
R1/wR2,[a] all data (%)	5.21/13.76	3.35/6.39	2.33/4.83
GOF	1.040	1.015	1.027

[a] $R1 = [\Sigma||F_o| - |F_c||]/\Sigma|F_o|$; $wR2 = \{[\Sigma w[(F_o)^2 - (F_c)^2]^2]/[\Sigma w(F_o^2)^2\}^{1/2}$; $w = [\sigma^2(F_o)^2 + (AP)^2 + BP]^{-1}$, where $P = [(F_o)^2 + 2(F_c)^2]/3$ and the A and B values are 0.0994 and 1.75 for **20**[BAr^F_4], 0.0277 and 0.00 for **21**·0.5C_6H_6, and 0.0246 and 1.81 for **22**.

Table 7.2. Selected X-ray data collection/refinement parameters for **23**, **24** and **27**.

	23	**24**	**27**
Formula	$C_{24}H_{34}AuClN_3OP$	$C_{29}H_{37}AuClN_4P$	$C_{49}H_{70}N_7P_2$
CCDC	2332923	2332924	-
Fw [g mol^{-1}]	643.93	705.01	819.06
Crystal system	monoclinic	monoclinic	triclinic
Space group	$P2_1/c$	$P2_1/n$	P–1
a (Å)	9.0649(2)	14.07050(10)	13.7540(9)
b (Å)	19.4006(3)	11.92140(10)	14.0991(12)
c (Å)	14.7754(2)	17.7462(2)	15.2637(11)
α (°)	90	90	62.647(8)
β (°)	106.849(2)	110.8640(10)	73.596(6)
γ (°)	90	90	63.879(8)
V (Å^3)	2486.92(8)	2781.56(5)	2348.5(4)
Z	4	4	2
Radiation, λ (Å)	Cu Kα, 1.54184	Cu Kα, 1.54184	Cu Kα, 1.54184
Temp (K)	150(2)	150(2)	150(2)
ρ_{calc} (g cm^{-3})	1.720	1.684	1.158
μ (mm^{-1})	12.871	11.554	1.143
Reflections collected	52244	68877	33873
Indep. reflections	5169	5810	9689
Parameters	293	360	551
R(int)	0.0554	0.0329	0.0782
R1/wR2,[a] $I \geq 2\sigma I$ (%)	3.71/8.48	2.63/5.74	5.39/12.52
R1/wR2,[a] all data (%)	5.10/9.28	2.65/5.75	10.03/14.98
GOF	1.027	1.271	1.007

[a] $R1 = [\Sigma||F_o| - |F_c||]/\Sigma|F_o|$; $wR2 = \{[\Sigma w[(F_o)^2 - (F_c)^2]^2]/[\Sigma w(F_o^2)^2\}^{1/2}$; $w = [\sigma^2(F_o)^2 + (AP)^2 + BP]^{-1}$, where $P = [(F_o)^2 + 2(F_c)^2]/3$ and the A and B values are 0.0357 and 5.17 for **23**, 0.0098 and 7.34 for **24**, and 0.0683 and 0.00 for **27**.

Table 7.2. Selected X-ray data collection/refinement parameters for **28**, **29** and **30**.

	28	**29**	**30**
Formula	$C_{24}H_{35}N_4P$	$C_{23}H_{33}N_4OP$	$C_{27}H_{39}N_4P$
CCDC	-	-	-
Fw [g mol^{-1}]	410.53	412.50	450.59
Crystal system	monoclinic	monoclinic	orthorhombic
Space group	$P2_1/n$	$P2_1/n$	$Pna2_1$
a (Å)	11.1791(2)	9.4131(2)	10.5934(1)
b (Å)	10.1351(1)	10.2263(2)	22.2626(1)
c (Å)	20.0186(3)	23.9723(4)	10.8012(1)
α (°)	90	90	90
β (°)	101.104(2)	93.464(2)	90
γ (°)	90	90	90
V (Å^3)	2225.67(6)	2303.39(8)	2547.32(4)
Z	4	4	4
Radiation, λ (Å)	Cu Kα, 1.54184	Cu Kα, 1.54184	Cu Kα, 1.54184
Temp (K)	150(2)	150(2)	150(2)
ρ_{calc} (g cm^{-3})	1.225	1.190	1.175
μ (mm^{-1})	1.214	1.210	1.103
Reflections collected	22784	27473	59812
Indep. reflections	4617	4791	5297
Parameters	278	288	300
R(int)	0.0377	0.0518	0.0283
R1/wR2,[a] $I \geq 2\sigma I$ (%)	4.69/12.35	4.75/12.10	2.43/6.66
R1/wR2,[a] all data (%)	5.11/12.69	6.33/13.17	2.47/6.71
GOF	1.044	1.028	1.038

[a] $R1 = [\Sigma||F_o| - |F_c||]/\Sigma|F_o|$; $wR2 = \{[\Sigma w[(F_o)^2 - (F_c)^2]^2]/[\Sigma w(F_o^2)^2\}^{1/2}$; $w = [\sigma^2(F_o)^2 + (AP)^2 + BP]^{-1}$, where $P = [(F_o)^2 + 2(F_c)^2]/3$ and the A and B values are 0.0599 and 1.92 for **28**, 0.0658 and 0.54 for **29**, and 0.0442 and 0.32 for **30**.

Table 7.2. Selected X-ray data collection/refinement parameters for **31**, **32** and **37**.

	31	**32**	**37**
Formula	$C_{23}H_{34}N_5P$	$C_{27}H_{42}N_5P$	$C_{23}H_{31}N_3FP$
CCDC	-	-	-
Fw [g mol^{-1}]	411.52	467.62	399.49
Crystal system	monoclinic	triclinic	orthorhombic
Space group	$P2_1/n$	P–1	$Pna2_1$
a (Å)	11.1475(4)	9.7727(3)	19.3382(4)
b (Å)	10.0318(3)	10.2150(3)	15.4324(3)
c (Å)	20.0277(7)	13.4578(5)	7.3135(1)
α (°)	90	100.468(3)	90
β (°)	101.280(3)	93.864(3)	90
γ (°)	90	93.618(3)	90
V (Å^3)	2196.42(13)	1314.21(8)	2182.60(7)
Z	4	2	4
Radiation, λ (Å)	Cu Kα, 1.54184	Cu Kα, 1.54184	Cu Kα, 1.54184
Temp (K)	150(2)	150(2)	100(1)
ρ_{calc} (g cm^{-3})	1.244	1.182	1.216
μ (mm^{-1})	1.245	1.096	1.280
Reflections collected	17282	26553	17460
Indep. reflections	4541	5428	3959
Parameters	278	321	260
R(int)	0.0652	0.0338	0.0376
R1/wR2,[a] $I \geq 2\sigma I$ (%)	4.90/12.31	3.64/9.71	5.60/15.78
R1/wR2,[a] all data (%)	7.20/13.92	4.22/10.15	6.48/16.44
GOF	1.044	1.048	1.268

[a] $R1 = [\Sigma||F_o| - |F_c||]/\Sigma|F_o|$; $wR2 = \{[\Sigma w[(F_o)^2 - (F_c)^2]^2]/[\Sigma w(F_o^2)^2\}^{1/2}$; $w = [\sigma^2(F_o)^2 + (AP)^2 + BP]^{-1}$, where $P = [(F_o)^2 + 2(F_c)^2]/3$ and the A and B values are 0.0711 and 0.4325 for **31**, 0.0560 and 0.3627 for **32**, and 0.1069 and 0.7939 for **37**.

Table 7.2. Selected X-ray data collection/refinement parameters for **38**, **39** and **42**·hex.

	38	**39**	**42**·hex
Formula	$C_{23}H_{30}Cl_2N_3P$	$C_{23}H_{31}N_3PI$	$C_{29}H_{45}N_3PBr$
CCDC	-	-	-
Fw [g mol^{-1}]	450.39	507.38	510.53
Crystal system	monoclinic	monoclinic	monoclinic
Space group	$P2_1/n$	$P2_1/c$	C2/m
a (Å)	11.0297(3)	10.1882(2)	19.2460(1)
b (Å)	10.2691(2)	15.8527(3)	14.4084(1)
c (Å)	20.0534(5)	15.4029(3)	9.8053(1)
α (°)	90	90	90
β (°)	101.182	103.969(2)	110.160(1)
γ (°)	90	90	90
V (Å^3)	2228.23(10)	2414.16(8)	2552.46(4)
Z	4	4	4
Radiation, λ (Å)	Cu K_α, 1.54184	Cu K_α, 1.54184	Cu K_α, 1.54184
Temp (K)	150(2)	150(2)	150(2)
ρ_{calc} (g cm^{-3})	1.343	1.396	1.329
μ (mm^{-1})	3.405	11.132	2.909
Reflections collected	15984	53958	35776
Indep. reflections	4623	5042	2737
Parameters	270	271	161
R(int)	0.0414	0.0530	0.0285
R1/wR2,[a] $I \geq 2\sigma I$ (%)	3.40/8.21	4.03/10.55	3.60/10.74
R1/wR2,[a] all data (%)	4.71/8.85	4.50/10.87	3.68/10.81
GOF	1.030	1.117	1.088

[a] $R1 = [\Sigma||F_o| - |F_c||]/\Sigma|F_o|$; $wR2 = \{[\Sigma w[(F_o)^2 - (F_c)^2]^2]/[\Sigma w(F_o^2)^2\}^{1/2}$; $w = [\sigma^2(F_o)^2 + (AP)^2 + BP]^{-1}$, where $P = [(F_o)^2 + 2(F_c)^2]/3$ and the A and B values are 0.0431 and 0.38 for **38**, 0.0546 and 2.25 for **39**, and 0.0611 and 3.81 for **42**·hex.

Table 7.2. Selected X-ray data collection/refinement parameters for **6**, **7**[OTf] and **9**.

	46
Formula	$C_{59}H_{88}N_3O_2P$
CCDC	-
Fw [g mol^{-1}]	902.29
Crystal system	orthorhombic
Space group	$C222_1$
a (Å)	13.6622(4)
b (Å)	16.3402(4)
c (Å)	24.5509(9)
α (°)	90
β (°)	90
γ (°)	90
V (Å^3)	5480.8(3)
Z	4
Radiation, λ (Å)	Cu K_α, 1.54184
Temp (K)	150(2)
ρ_{calc} (g cm^{-3})	1.093
μ (mm^{-1})	0.757
Reflections collected	17689
Indep. reflections	5445
Parameters	316
R(int)	0.0464
R1/wR2,[a] $I \geq 2\sigma I$ (%)	4.52/10.98
R1/wR2,[a] all data (%)	5.60/11.60
GOF	1.027

[a] $R1 = [\Sigma||F_o| - |F_c||]/\Sigma|F_o|$; $wR2 = \{[\Sigma w[(F_o)^2 - (F_c)^2]^2]/[\Sigma w(F_o^2)^2\}^{1/2}$; $w = [\sigma^2(F_o)^2 + (AP)^2 + BP]^{-1}$, where $P = [(F_o)^2 + 2(F_c)^2]/3$ and the A and B values are 0.059 and 1.09 for **46**.

7.3 References

[1] J. Underhill, E. S. Yang, T. Schmidt-Räntsch, W. K. Myers, J. M. Goicoechea, J. Abbenseth, *Chem. Eur. J.* **2023**, *29*, e202203266.

[2] A. Hubbard, T. Okazaki, K. K. Laali, *J. Org. Chem.* **2008**, *73*, 316–319.

[3] A. J. Martínez-Martínez, A. S. Weller, *Dalton Trans.* **2019**, *48*, 3551–3554.

[4] M. R. Fructos, T. R. Belderrain, P. de Frémont, N. M. Scott, S. P. Nolan, M. M. Díaz-Requejo, P. J. Pérez, *Angew. Chem., Int. Ed.* **2005**, *44*, 5284–5288.

[5] P. Margaretha, S. Solar, O. E. Polansky, *Angew. Chem., Int. Ed.* **1971**, *10*, 412–413.

[6] V. W. Manner, T. F. Markle, J. H. Freudenthal, J. P. Roth, J. M. Mayer, *Chem. Commun.* **2008**, 256–258.

[7] CrysAlisPro, Agilent Technologies, Version 1.171.41.117a.

[8] G. M. Sheldrick, *SHELXL97*, *Programs for Crystal Structure Analysis (Release 97-2)*, Tammanstrasse 4, D-3400 Göttingen, Germany, **1998**.

[9] G. M. Sheldrick, *Acta Crystallogr. A* **1990**, *46*, 467–473.

[10] G. M. Sheldrick, *Acta Crystallogr A* **2008**, *64*, 112–122.

[11] F. Neese, *Wiley Interdiscip. Rev. Comput. Mol. Sci.* **2012**, *2*, 73–78.

[12] F. Neese, *Wiley Interdiscip. Rev. Comput. Mol. Sci.* **2022**, *12*, e1606.

[13] F. Neese, F. Wennmohs, U. Becker, C. Riplinger, *J. Chem. Phys.* **2020**, *152*, 224108.

[14] M. Mitoraj, A. Michalak, *J. Mol. Model.* **2007**, *13*, 347–355.

[15] L. Zhao, M. von Hopffgarten, D. M. Andrada, G. Frenking, *Wiley Interdiscip. Rev. Comput. Mol. Sci.* **2018**, *8*, e1345.

[16] T. Lu, F. Chen, *J. Comput. Chem.* **2012**, *33*, 580–592.

[17] E. D. Glendening, J. K. Badenhoop, A. E. Reed, J. E. Carpenter, J. A. Bohmann, C. M. Morales, P. Karafiloglou, C. R. Landis, F. Weinhold, **2018**.

[18] Y.-S. Lin, G.-D. Li, S.-P. Mao, J.-D. Chai, *J. Chem. Theory Comput.* **2013**, *9*, 263–272.

[19] D. A. Pantazis, X.-Y. Chen, C. R. Landis, F. Neese, *J. Chem. Theory Comput*. **2008**, *4*, 908–919.

[20] M. Bühl, C. Reimann, D. A. Pantazis, T. Bredow, F. Neese, *J. Chem. Theory Comput.* **2008**, *4*, 1449–1459.

[21] C. Adamo, V. Barone, *J. Chem. Phys.* **1999**, *110*, 6158–6170.

[22] F. Weigend, R. Ahlrichs, *Phys. Chem. Chem. Phys.* **2005**, *7*, 3297.

[23] F. Weigend, *Phys. Chem. Chem. Phys.* **2006**, *8*, 1057–1065.

[24] S. Grimme, J. Antony, S. Ehrlich, H. Krieg, *J. Chem. Phys.* **2010**, *132*, 154104.

[25] S. Grimme, S. Ehrlich, L. Goerigk, *J. Comput. Chem.* **2011**, *32*, 1456–1465.

[26] K. Lee, A. V. Blake, A. Tanushi, S. M. McCarthy, D. Kim, S. M. Loria, C. M. Donahue, K. D. Spielvogel, J. M. Keith, S. R. Daly, A. T. Radosevich, *Angew. Chem., Int. Ed.* **2019**, *58*, 6993–6998.